symmetry

Special Issue Reprint

New Power System and Symmetry

Edited by
Yongji Cao, Runjia Sun, Rui Wang and Jin Tan

mdpi.com/journal/symmetry

MDPI

New Power System and Symmetry

New Power System and Symmetry

Guest Editors

Yongji Cao
Runjia Sun
Rui Wang
Jin Tan

MDPI

Basel • Beijing • Wuhan • Barcelona • Belgrade • Novi Sad • Cluj • Manchester

Guest Editors

Yongji Cao
Academy of Intelligent Innovation
Shandong University
Jinan
China

Runjia Sun
School of Electrical Engineering
Shandong University
Jinan
China

Rui Wang
College of Information Science and Engineering
Northeastern University
Shenyang
China

Jin Tan
College of Electrical Engineering
Shanghai University of Electric Power
Shanghai
China

Editorial Office
MDPI AG
Grosspeteranlage 5
4052 Basel, Switzerland

This is a reprint of the Special Issue, published open access by the journal *Symmetry* (ISSN 2073-8994), freely accessible at: https://www.mdpi.com/journal/symmetry/special_issues/OR4CL0F158.

For citation purposes, cite each article independently as indicated on the article page online and as indicated below:

Lastname, A.A.; Lastname, B.B. Article Title. *Journal Name* **Year**, *Volume Number*, Page Range.

ISBN 978-3-7258-8721-7 (Hbk)
ISBN 978-3-7258-8722-4 (PDF)
https://doi.org/10.3390/books978-3-7258-8722-4

© 2026 by the authors. Articles in this reprint are Open Access and distributed under the Creative Commons Attribution (CC BY) license. The reprint as a whole is distributed by MDPI under the terms and conditions of the Creative Commons Attribution-NonCommercial-NoDerivs (CC BY-NC-ND) license (https://creativecommons.org/licenses/by-nc-nd/4.0/).

Contents

About the Editors . . . . . **vii**

Preface . . . . . **ix**

Yongji Cao, Runjia Sun, Rui Wang and Jin Tan
Special Issue: New Power System and Symmetry
Reprinted from: *Symmetry* **2026**, *18*, 1222, https://doi.org/10.3390/sym18071222 . . . . . **1**

Lixue Gao, Shouyuan Wu, Mu Li and Futao Yang
Disturbance Location-Aware Frequency Support in New Power Systems via Heterogeneous Nodal Frequency Response Modeling and Atlas-Based Gain Scheduling
Reprinted from: *Symmetry* **2026**, *18*, 759, https://doi.org/10.3390/sym18050759 . . . . . **7**

Lebing Zhao, Yixuan Peng, Wei Dong, Wen Hua, Ying Yang, Hang Qi and Changgang Li
Hybrid Model and Data-Driven Emergency Load Shedding Optimization for Frequency Security in Receiving-End Power Grids
Reprinted from: *Symmetry* **2026**, *18*, 126, https://doi.org/10.3390/sym18010126 . . . . . **35**

Mu Li and Shouyuan Wu
Self-Adaptive Virtual Synchronous Generator Control for Photovoltaic Hybrid Energy Storage Systems Based on Radial Basis Function Neural Network
Reprinted from: *Symmetry* **2026**, *18*, 70, https://doi.org/10.3390/sym18010070 . . . . . **52**

Yuyue Zhang, Yan Wen, Nan Wang, Zhenhua Yuan, Lina Zhang and Runjia Sun
Construction of Typical Scenarios for Multiple Renewable Energy Plant Outputs Considering Spatiotemporal Correlations
Reprinted from: *Symmetry* **2025**, *17*, 1226, https://doi.org/10.3390/sym17081226 . . . . . **77**

Fan Yang, Xinyi Shao, Bo Zhou, Yuexing Shi, Yunwei Shen and Dongdong Li
Data-Driven Automatic Generation Control Based on Learning to Coordinate and Teach Reinforcement Mechanism
Reprinted from: *Symmetry* **2025**, *17*, 854, https://doi.org/10.3390/sym17060854 . . . . . **95**

Xinyi Chen, Pan Wu, Hongyu He, Bingbing Song, Kangping Qin, Xiaobi Teng, et al.
Optimal Flexibility Dispatching of Multi-Pumped Hydro Storage Stations Considering the Uncertainty of Renewable Energy
Reprinted from: *Symmetry* **2024**, *16*, 1404, https://doi.org/10.3390/sym16101404 . . . . . **110**

Hang Qi, Ruiyang Su, Runjia Sun and Jiongcheng Yan
Data-Driven Dynamic Security Partition Assessment of Power Systems Based on Symmetric Electrical Distance Matrix and Chebyshev Distance
Reprinted from: *Symmetry* **2024**, *16*, 1355, https://doi.org/10.3390/sym16101355 . . . . . **127**

Kaijian Ou, Shilin Gao, Yuhong Wang, Bingjie Zhai and Wei Zhang
Assessment of the Renewable Energy Consumption Capacity of Power Systems Considering the Uncertainty of Renewables and Symmetry of Active Power
Reprinted from: *Symmetry* **2024**, *16*, 1184, https://doi.org/10.3390/sym16091184 . . . . . **149**

About the Editors

Yongji Cao

Yongji Cao is an Associate Professor at the Academy of Intelligent Innovation, Shandong University, China, where he also directs the Shandong University Chongshi Smart Energy Joint Laboratory. His research interests include power system stability analysis and control, artificial intelligence applications in power systems, renewable energy grid integration, and energy storage technologies. He has authored or co-authored over 90 SCI/EI indexed papers, filed more than 20 invention patents, and registered over 10 software copyrights. He has contributed to the development of four group standards and has led two sub-projects under the National Key Research and Development Program, one Shandong Provincial Key Research and Development Project, two Shandong Provincial Natural Science Foundation projects, and more than ten industry-funded technology projects. His work has been recognized with multiple awards, including the 2025 Electric Power Innovation First Prize, the 2025 Shandong Provincial Enterprise Science and Technology Innovation Association Science and Technology Innovation Second Prize, the 2024 State Grid Corporation of China Science and Technology Progress Second Prize, and the 2023 Shandong Electric Power Science and Technology Progress Third Prize.

Runjia Sun

Runjia Sun received his B.S. and Ph.D. degrees from the School of Electrical Engineering, Shandong University, Jinan, China, in 2015 and 2020, respectively. He now serves as an Associate Researcher at the same institution. His research primarily focuses on power system resilience and restoration control. He has acted as Principal Investigator for four research projects funded by the Ministry of Science and Technology, the National Natural Science Foundation of China, and other funding bodies. He has published more than 30 technical papers in leading journals and conference proceedings. He is Treasurer of the IEEE PES Jinan Chapter and Secretary of the AC/DC Hybrid Power Grid Safety and Stability Analysis Subcommittee under the IEEE PES Power System Dynamic Performance Committee China Satellite Committee. He is also a member of IEC SC 8C Working Group 7.

Rui Wang

Rui Wang received his B.S. degree in Electrical Engineering and Automation and his Ph.D. degree in Power Electronics and Power Drive from Northeastern University, Shenyang, China, in 2016 and 2021, respectively. He is currently a Full Professor at Northeastern University. He is an IEEE Senior Member. His research interests include energy routing devices, coordinated control of renewable energy systems, and power system stability analysis. He has made significant contributions to the development of control strategies for renewable energy integration and power electronic devices, with a particular focus on maintaining system stability under high penetration of inverter-based resources. He has authored or co-authored more than 100 articles in leading journals and conference proceedings and holds more than 20 patents. He has led multiple research projects funded by the National Natural Science Foundation of China and other provincial and industry funding bodies. He is actively involved in organizing academic conferences and sessions in the field of power system stability and renewable energy integration.

Jin Tan

Jin Tan is currently an Associate Professor at the School of Electrical Engineering, Shanghai University of Electric Power. She received her Ph.D. in Electrical Engineering from the Technical University of Denmark (DTU) in 2022. Her primary research focuses on integrated energy system planning and operation, capacity configuration of energy storage systems, and uncertainty modeling for renewable energy generation. She has authored over 20 academic papers in recent years. She is currently leading several research projects supported by the National Natural Science Foundation of China, the Science and Technology Commission of Shanghai Municipality, the Shanghai Municipal Education Commission, and the State Grid Corporation of China.

Preface

The global energy landscape is undergoing a profound transformation. Driven by the urgent need to mitigate climate change and reduce dependence on fossil fuels, the integration of renewable energy sources into power grids has accelerated dramatically. This shift has given rise to what is now termed the "new power system," characterized by high penetration of inverter-based resources, distributed generation, and complex, multi-directional power flows. While essential for a sustainable future, these systems present significant engineering challenges, particularly concerning the maintenance of dynamic symmetry, the delicate balance of active and reactive power, frequency stability, and voltage regulation across vast, interconnected networks.

This Reprint addresses these critical challenges by presenting a curated collection of research originally featured in a Special Issue of the journal *Symmetry*. The primary subject of this volume is the intersection of power system engineering and symmetry principles, with a specific focus on the stability, control, and optimization of modern electrical grids.

The scope of this Reprint is comprehensive, encompassing a wide array of cutting-edge topics. These include heterogeneous nodal frequency response modeling, data-driven emergency load shedding, self-adaptive virtual synchronous generator control, and the assessment of renewable energy consumption capacity. Further contributions explore typical scenario construction considering spatiotemporal correlations, optimal flexibility dispatching of multi-pumped hydro storage stations, and dynamic security partition assessment using symmetrical electrical distance matrices. Each of the nine peer-reviewed articles offers a unique perspective, combining theoretical rigor with practical case studies.

The aim of compiling this Reprint is twofold. First, it seeks to provide a consolidated and accessible reference for the latest research advancements in this rapidly evolving field. Second, it aims to foster a deeper understanding of how symmetry principles can be leveraged to design more resilient, flexible, and intelligent power systems. The motivation for this work stems from the collective recognition that traditional grid management approaches are insufficient to handle the variability and uncertainty inherent in high-renewable systems. New methodologies, often drawing on artificial intelligence and advanced signal processing, are urgently required.

This Reprint is addressed to a broad audience of researchers, practicing engineers, graduate students, and policymakers involved in power system planning, operation, and regulation. It serves as a valuable resource for those seeking to understand both the theoretical foundations and the practical applications of next-generation grid technologies. We hope that the insights and innovations presented here will stimulate further research and collaboration, contributing to the global effort to build a sustainable and secure energy future.

The Guest Editors are grateful to all the authors who contributed their work to this project. An accompanying Editorial, which appears first in the Table of Contents, provides a more detailed overview of the individual contributions and their significance.

Yongji Cao, Runjia Sun, Rui Wang, and Jin Tan
Guest Editors

symmetry

MDPI

Editorial

Special Issue: New Power System and Symmetry

Yongji Cao [1], Runjia Sun [2,*], Rui Wang [3] and Jin Tan [4]

[1] Academy of Intelligent Innovation, Shandong University, Jinan 250101, China; yongji@sdu.edu.cn
[2] Key Laboratory of Power System Intelligent Dispatch and Control of the Ministry of Education, Shandong University, Jinan 250061, China
[3] College of Information Science and Engineering, Northeastern University, Shenyang 110819, China; wangrui@ise.neu.edu.cn
[4] College of Electrical Engineering, Shanghai University of Electric Power, Shanghai 200090, China; tanjin@shiep.edu.cn
* Correspondence: sunrunjia@sdu.edu.cn

Global challenges such as fossil energy depletion, environmental pollution, and climate warming are driving the rapid development of renewable energy sources (RESs), including wind power and photovoltaics [1–3]. However, the increasing integration of these RESs has significantly altered the structure and operational characteristics of power systems. The variable and uncertain nature of RES outputs exacerbates disturbances that compromise power symmetry and balance [4,5]. Although power-electronic-interfaced sources offer flexible and fast regulation capabilities, their limited immunity to grid disturbances may further amplify the degree of power asymmetry and imbalance [6–8]. Consequently, maintaining power symmetry and balance poses a substantial challenge in the evolving new power system. To address this pressing issue, this Special Issue, titled "New Power System and Symmetry", presents advanced perception, cognition, and decision-making technologies aimed at restoring and preserving system symmetry.

The contributions assembled in this Special Issue present novel approaches for strengthening power system symmetry and balance from multiple angles. The mechanisms and characteristics underlying power asymmetry and imbalance are thoroughly analyzed. Furthermore, flexible resources within the new power system, particularly energy storage systems, are leveraged to bolster power symmetry and balance. Scenario generation methods are proposed to handle the inherent uncertainty of RESs, thereby enabling the extraction and characterization of disturbances affecting system symmetry. Additionally, data-driven artificial intelligence techniques are employed for precise assessment and robust control. Taken together, these studies deliver profound insights into the origins, assessment, and mitigation of symmetry-related issues in modern power systems.

A total of 14 manuscripts were submitted to this Special Issue. After a thorough and rigorous peer-review process, eight papers were finally accepted for publication. The following paragraphs provide a concise overview of the primary goals and principal results of these selected contributions.

Contribution 1 presents a probabilistic evaluation framework for determining the renewable energy hosting capacity of power grids, explicitly accounting for the stochastic nature of load and wind generation while upholding supply–demand symmetry. A tenth-order Gaussian mixture model is adopted to accurately characterize the probability distributions of load and wind power, achieving a favorable balance between modeling fidelity and computational cost. The Metropolis–Hastings algorithm, grounded in Markov chain Monte Carlo theory, is subsequently applied to generate representative sample spaces, which are then fed into power flow studies to derive the maximum allowable renewable

penetration under static security limits. Validation against Monte Carlo simulations and Gibbs sampling on modified IEEE 39-bus and 102-node AC–DC hybrid testbeds confirm the method's high accuracy and efficiency, yielding maximum hosting capacities of 1054.87 MW and 1250.91 MW, respectively. Additional short-circuit ratio evaluations and N-1 contingency simulations corroborate the system's voltage stability and robustness at elevated renewable penetration levels.

Contribution 2 introduces a data-driven dynamic security assessment (DSA) methodology that leverages a grid partitioning strategy to construct accurate and incrementally updateable DSA models with streamlined architectures. The power network is autonomously segmented into localized zones via the mean shift algorithm, wherein node positions are encoded by a symmetric electrical distance matrix and the Chebyshev distance metric is employed to enhance partitioning quality by approximately 50%. Operating-condition features are subsequently extracted using a stacked denoising autoencoder, while the symmetric electrical distance matrix is tailored to encode fault locations within each subregion, thereby mitigating feature redundancy. Multiple radial basis function neural network (RBFNN)-based DSA models are then established for fault positions per region, complemented by an online incremental update mechanism that prevents catastrophic forgetting. Evaluations on both a 112-bus simplified provincial network and a 2624-bus large-scale practical system in China, conducted with PSS/E, reveal that the partition-based RBFNN model attains 98.96% accuracy, surpassing unified models with more complex architectures. The incremental update strategy preserves over 98% accuracy while curtailing update time to 30 s, underscoring its suitability for online preventive and restorative control applications.

Contribution 3 formulates an optimal dispatching model for multiple pumped hydro storage (PHS) stations to supply operational flexibility across distinct regions of East China's state grid, responding to the escalating randomness and flexibility requirements imposed by high renewable penetration. The credible predictable power of renewables is first derived from forecast data, and system flexibility demand is defined as the net-load variation per unit time, giving rise to a multi-timescale flexibility quantification model. A refined PHS station operation model is subsequently devised, encompassing power limits, mode-transition constraints, start–stop restrictions, minimum run times, and reservoir capacity limits with differentiated hydro-conversion efficiencies. In light of regional allocation constraints, a decentralized multi-PHS model is established, and flexibility provisions to each region are quantified via allocation ratios. The overarching objective is to minimize the mismatch between flexibility supply and demand across all regions. A case study on an East China regional grid comprising 10 PHS stations with a combined capacity of 13,700 MW verifies that the proposed approach effectively aligns flexibility supply with regional demand while respecting actual PHS operating characteristics. Comparative economic analysis further demonstrates that the optimal dispatching strategy substantially lowers flexibility supply costs relative to thermal-only or manual dispatch benchmarks, confirming its effectiveness and superiority.

Contribution 4 puts forward a novel multi-agent deep reinforcement learning (MADRL) framework for automatic generation control (AGC) in interconnected power systems, tackling the dual challenges of active-power symmetry preservation and frequency stability maintenance under high RES penetration and system expansion. The core innovation is a Learning to Coordinate and Teach Reinforcement (LECTR) mechanism, through which expert agents from the original system offer demonstration actions to guide novice agents in newly incorporated regions, expediting strategy-network convergence by 58.73% to 75.01% while enhancing control precision. A double-target critic network with delayed updates is introduced to curb overestimation biases in the target critic, improving

https://doi.org/10.3390/sym18071222

learning stability and yielding higher-quality experience data. The cooperative reward function integrates area control error, frequency deviation, and tie-line power into steer agent training. Simulations on expanding IEEE test systems subject to step-load variations and stochastic renewable disturbances reveal that the proposed method reduces mean absolute area control error (ACE) by 54.93% to 84.80% relative to alternative algorithms, achieves superior reward performance, and sustains robust convergence and control efficacy without necessitating retraining of all regional agents, attesting to its viability for real-time frequency regulation in flexibly extensible power grids.

Contribution 5 presents a scenario construction methodology that preserves spatiotemporal correlations among multiple renewable generation outputs, overcoming the limitations of conventional approaches that neglect such interdependencies and thus inadequately represent the distributional attributes of original data. The framework first defines a symmetric spatial correlation matrix and a temporal autocorrelation matrix to quantitatively encode spatiotemporal relationships. Distributional discrepancies between typical and original scenarios are subsequently characterized across mean, variance, spatial correlation, and temporal autocorrelation dimensions, and a scenario-reduction optimization problem is formulated to minimize these disparities. An enhanced genetic algorithm, featuring adaptive parameter tuning and an elitist preservation strategy, is developed to efficiently derive high-quality representative scenarios. Case studies on five wind farms and fourteen photovoltaic installations in Belgium demonstrate that the improved genetic algorithm achieves accelerated convergence and superior solution quality, producing four representative scenarios within three minutes. The mean absolute percentage error between spatial correlation matrices of original and reduced sets is 2.5% for wind farms and 0.78% for PV plants, while the corresponding errors for first-order temporal autocorrelation coefficients are 2.75% and 2.45%, respectively, confirming that the constructed scenarios faithfully preserve both spatial and temporal dependencies inherent in the original data.

Contribution 6 devises a self-adaptive virtual synchronous generator (VSG) control strategy for PV hybrid energy storage systems (PV-HESS), leveraging a radial basis function (RBF) neural network to dynamically optimize inertia and damping parameters in response to the erosion of dynamic symmetry induced by high renewable penetration. The DC-side storage architecture incorporates a passive filter to decouple high- and low-frequency power components, with supercapacitors mitigating fast fluctuations and batteries smoothing slow variations. A small-signal model of the VSG active-power loop is established to delineate permissible ranges for rotational inertia and damping coefficient, considering cutoff frequency, grid-code requirements, stability margins, and frequency-response time. The RBF network takes angular frequency deviation and its derivative as inputs to adaptively adjust these parameters within optimal bounds, with a sigmoid activation function enforcing physically realizable inertia values and a damping ratio of 0.75 set as the design target. The simulations under power-supply–demand imbalance and grid-frequency disturbance scenarios reveal that the RBF-based strategy substantially outperforms both fixed-parameter and linear adaptive alternatives, achieving respective improvements in power overshoot, settling time, and fluctuation range of 52.7%, 50.1%, and 59.4% under power imbalance, and corresponding frequency-domain enhancements of 68.18%, 41.02%, and 70.37% under frequency disturbances, thereby confirming superior transient response, oscillation damping, and overall system robustness.

Contribution 7 proposes a hybrid model- and data-driven optimization framework for emergency load shedding (ELS) in receiving-end power systems following HVDC blocking incidents, addressing frequency security concerns while honoring transient frequency, rotor-angle, and voltage stability constraints. An ELS decision model is first constructed, incorporating both conventional loads and pumped-storage units, with continuous load-

https://doi.org/10.3390/sym18071222

shedding variables and discrete pumping-cut decisions, and seeks to minimize control costs under dynamic security constraints. The particle swarm optimization (PSO) algorithm is augmented with symmetric opposite learning to boost initial-population diversity and Tent chaotic mapping to broaden the exploration space, thereby elevating solution quality. A hybrid neural-network-based multi-task DSA model is established to rapidly screen candidate ELS schemes during optimization iterations, with time-domain simulations serving as a validation anchor for initial and final solutions to guarantee feasibility. Testing on a provincial receiving-end grid featuring 132 buses, 29 generators, and three HVDC lines totaling 20 GW infeed capacity shows that the enhanced PSO outperforms traditional PSO, adaptive PSO (APSO), hierarchical PSO (HPSO), mutated PSO (MPSO), differential evolution (DE), and genetic algorithm (GA) in solution quality. The hybrid neural network attains a 98.67% assessment accuracy, markedly surpassing artificial neural network (ANN) (93.56%), support vector machine (SVM) (89.00%), and decision tree (DT) (86.77%). The proposed approach yields a viable, least-cost ELS scheme within 0.63 s, representing an approximately 541-fold improvement in optimization efficiency relative to TDS-dependent PSO, while retaining robust generalization to unseen operating conditions with over 92% accuracy at a 1:1 generalization ratio.

Contribution 8 presents a disturbance location-aware coordination framework for frequency support in low-inertia power systems populated by heterogeneous converter types, directly confronting the symmetry-breaking phenomenon whereby post-fault nodal frequency responses are contingent upon disturbance location, network topology, and the coexistence of synchronous generators, grid-forming (GFM) converters, and grid-following (GFL) converters with phase-locked loops (PLLs). The core element is a heterogeneous nodal frequency response (HNFR) state-space model that consolidates SG/GFM electromechanical frequency channels and GFL PLL-estimated frequencies into a unified output matrix, eliminating algebraic network variables via reduced-order representation while explicitly retaining disturbance location as an input dimension for scalable analysis. A reproducible signal-processing protocol is established to compute nodal rate of change of frequency (RoCoF), nadir, and frequency-split indices, facilitating large-scale location sweeps through atlas-ready matrices amenable to high-performance computing. A robust min–max allocation formulation determines GFM virtual-inertia and droop settings across disturbance locations subject to device limits and a fixed aggregate budget. This is complemented by an atlas-based gain-scheduling workflow that obviates online disturbance localization. The atlas functions as a pre-validated repository of frequency-support gain configurations keyed to operating conditions and can be retrieved online without re-optimization. Simulations on a modified IEEE 39-bus system with three wind farms and four tunable GFM buses under a six-location disturbance sweep confirm that the HNFR-based allocation bolsters worst-node security and curtails frequency split while preserving comparable center of inertia (COI) behavior. Under budget-matched conditions, the proposed allocation diminishes worst-node RoCoF by 32.2% and maximum nodal frequency split by 17.8% relative to the COI-oriented benchmark, with a more modest 0.0036 Hz nadir improvement, evidencing that the HNFR formulation effectively resolves localized stress patterns and affords enhanced protection to stressed nodes over aggregated-frequency methods, although RoCoF gains exhibit greater scenario dependence than nadir and split improvements.

Collectively, the eight papers featured in this Special Issue have made notable contributions to the study of power system symmetry. It is our hope that this collection will provide a valuable reference and inspire further inquiry in the field. Future research avenues may include the application of large language models (LLMs) to the assessment and

https://doi.org/10.3390/sym18071222

enhancement of system symmetry, as well as a more detailed consideration of the dynamic effects of power electronic converters, particularly GFM and GFL types.

Funding: This paper is jointly supported by National Major Science and Technology Project on Smart Grid (2024ZD0801100) and Key Research and Development Program of Shandong Province (2025TSGCCZZB0081).

Data Availability Statement: No new data were created or analyzed in this study. Data sharing is not applicable to this article.

Acknowledgments: The guest editors gratefully acknowledge all the authors for their valuable contributions to this Special Issue. We also extend our sincere appreciation to the reviewers for their rigorous and insightful assessments of the submitted manuscripts, and to the editorial team of *Symmetry* for their professional guidance and kind assistance throughout the publication process.

Conflicts of Interest: The authors declare no conflicts of interest.

List of Contributions:

1. Ou, K.; Gao, S.; Wang, Y.; Zhai, B.; Zhang, W. Assessment of the Renewable Energy Consumption Capacity of Power Systems Considering the Uncertainty of Renewables and Symmetry of Active Power. *Symmetry* **2024**, *16*, 1184.
2. Qi, H.; Su, R.; Sun, R.; Yan, J. Data-Driven Dynamic Security Partition Assessment of Power Systems Based on Symmetric Electrical Distance Matrix and Chebyshev Distance. *Symmetry* **2024**, *16*, 1355.
3. Chen, X.; Wu, P.; He, H.; Song, B.; Qin, K.; Teng, X.; Yang, F.; Li, D. Optimal Flexibility Dispatching of Multi-Pumped Hydro Storage Stations Considering the Uncertainty of Renewable Energy. *Symmetry* **2024**, *16*, 1404.
4. Yang, F.; Shao, X.; Zhou, B.; Shi, Y.; Shen, Y.; Li, D. Data-Driven Automatic Generation Control Based on Learning to Coordinate and Teach Reinforcement Mechanism. *Symmetry* **2025**, *17*, 854.
5. Zhang, Y.; Wen, Y.; Wang, N.; Yuan, Z.; Zhang, L.; Sun, R. Construction of Typical Scenarios for Multiple Renewable Energy Plant Outputs Considering Spatiotemporal Correlations. *Symmetry* **2025**, *17*, 1226.
6. Li, M.; Wu, S. Self-Adaptive Virtual Synchronous Generator Control for Photovoltaic Hybrid Energy Storage Systems Based on Radial Basis Function Neural Network. *Symmetry* **2026**, 18, 70.
7. Zhao, L.; Peng, Y.; Dong, W.; Hua, W.; Yang, Y.; Qi, H.; Li, C. Hybrid Model and Data-Driven Emergency Load Shedding Optimization for Frequency Security in Receiving-End Power Grids. *Symmetry* **2026**, *18*, 126.
8. Gao, L.; Wu, S.; Li, M.; Yang, F. Disturbance Location-Aware Frequency Support in New Power Systems via Heterogeneous Nodal Frequency Response Modeling and Atlas-Based Gain Scheduling. *Symmetry* **2026**, *18*, 759.

References

1. Cao, Y.; Song, Y.; Liu, X.; Li, C. Parameter Identification of Synchronous Condenser and Its Excitation System Considering Multivariate Coupling and Symmetry Characteristic. *Symmetry* **2024**, *16*, 1596. [CrossRef]
2. Ma, T.; Pei, W.; Xiao, H.; Yang, Y.; Ma, L. A Joint Power and Renewable Energy Certificate Trading Method in the Peer-to-Peer Market. *IEEE Trans. Smart Grid* **2025**, *16*, 1604–1618. [CrossRef]
3. Cao, Y.; Wu, Q.; Zhang, H.; Li, C.; Zhang, X. Chance-Constrained Optimal Configuration of BESS Considering Uncertain Power Fluctuation and Frequency Deviation Under Contingency. *IEEE Trans. Sustain. Energy* **2022**, *13*, 2291–2303. [CrossRef]
4. Lai, S.; Dong, Z.Y.; Yang, H.; Tao, Y.; Yip, C.; Qiu, J. Renewable Energy Following Strategy via Quantified Aggregated Heterogeneous Electric Vehicle Flexibility. *IEEE Trans. Smart Grid* **2025**, *16*, 3873–3886. [CrossRef]
5. Javadi, M.; Gong, Y.; Chung, C.Y. Frequency Stability Constrained BESS Sizing Model for Microgrids. *IEEE Trans. Power Syst.* **2024**, *39*, 2866–2878. [CrossRef]
6. Wan, C.; Hu, X.; Li, B.; Li, Y.; Liu, H.; Ju, P. A Point-Hyperplane Geometry Method for Operational Security Region of Renewable Energy Generation in Power Systems. *IEEE Trans. Power Syst.* **2026**, *41*, 1308–1320. [CrossRef]

7. Zhang, J.; Wang, J.; Cao, Y.; Li, B.; Li, C. A coordinated control strategy of multi-type flexible resources and under-frequency load shedding for active power balance. *Symmetry* **2024**, *16*, 479. [CrossRef]
8. Rostami, S.M.; Hamzeh, M. An Adaptive Multi-Functional Control Strategy for Power Management and Voltage-Frequency Regulation of PV, BESS, and Hybrid Units in a Microgrid. *IEEE Trans. Smart Grid* **2024**, *15*, 3446–3458. [CrossRef]

Disclaimer/Publisher's Note: The statements, opinions and data contained in all publications are solely those of the individual author(s) and contributor(s) and not of MDPI and/or the editor(s). MDPI and/or the editor(s) disclaim responsibility for any injury to people or property resulting from any ideas, methods, instructions or products referred to in the content.

https://doi.org/10.3390/sym18071222

symmetry

MDPI

Article

Disturbance Location-Aware Frequency Support in New Power Systems via Heterogeneous Nodal Frequency Response Modeling and Atlas-Based Gain Scheduling

Lixue Gao, Shouyuan Wu *, Mu Li and Futao Yang

Key Laboratory of Power System Intelligent Dispatch and Control of Ministry of Education, Shandong University, Jinan 250061, China; lixue_gao@mail.sdu.edu.cn (L.G.); mu_li@mail.sdu.edu.cn (M.L.); 202120611@mail.sdu.edu.cn (F.Y.)

* Correspondence: shouyuan_wu@sdu.edu.cn

Abstract

New power systems with penetration of inverter-based resources (IBRs) exhibit symmetry breaking in post-disturbance frequency, as nodal trajectories depend on disturbance location, network coupling, and heterogeneous frequency channels across synchronous generators (SGs), grid-forming (GFM) converters, and grid-following (GFL) converters with phase-locked loops (PLLs). As a consequence, relying only on aggregated center-of-inertia/center-of-frequency (COI) metrics can underestimate asymmetric local risks, including worst-node rate of change of frequency (RoCoF), worst-node nadir, and nodal frequency split. This paper proposes a disturbance location-aware coordination framework that explicitly models and balances heterogeneous active-power frequency support across the network using an electromechanical-scale state-space formulation. First, a heterogeneous nodal frequency response (HNFR) model yields an explicit state-space input–output mapping from location-specific active power disturbances to nodal frequency outputs for both electromechanical and PLL-estimated channels. Second, a reproducible signal processing protocol computes nodal RoCoF/nadir/split indices and enables large-scale location sweeping via atlas-ready matrices that are naturally parallelizable for high-performance computing. Third, a constrained allocation layer schedules heterogeneous fast frequency response subject to converter limits and finite energy constraints, supporting an atlas-based gain scheduling implementation. Case studies demonstrate that the proposed symmetry-aware design improves worst-node security and suppresses frequency split while maintaining comparable COI behavior. Under budget-matched conditions on the modified IEEE 39-bus system, the proposed allocation reduces worst-node RoCoF by 32.2% and maximum nodal frequency split by 17.8% relative to the COI-based benchmark.

Keywords: renewable generation; spatiotemporal frequency; symmetry breaking; grid-forming converters; frequency stability

1. Introduction

The rapid growth of inverter-based resources (IBRs) is reshaping the dynamical landscape of power systems. Under disturbances, frequency dynamics can exhibit pronounced symmetry breaking across the network. Additionally, as synchronous generators are displaced (see Figure 1), system inertia and governor-based damping decline while converter control and synchronization loops introduce new multi-timescale couplings among angle, frequency, and voltage dynamics [1–5]. As a result, post-disturbance frequency is no longer

well-represented by a single global trajectory: nodal responses can depend strongly on disturbance location and network coupling, leading to spatially heterogeneous RoCoF/nadir and even nodal frequency splitting.

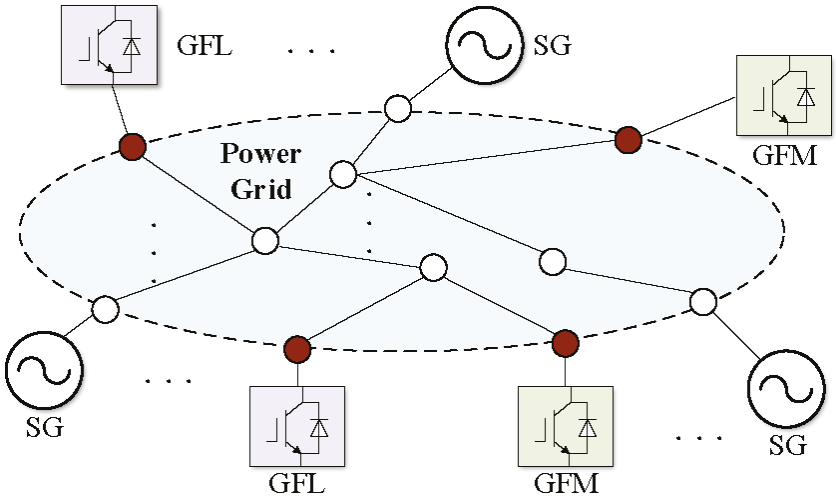


Figure 1. Diagram of an IBR-integrated power system. SG: synchronous generator; GFM: grid-forming converter; GFL: grid-following converter; IBR: inverter-based resource.

Figure 2 illustrates the end-to-end pipeline of the proposed framework. In the offline stage, the HNFR state-space model is assembled from the operating point, network data, and device parameters (step A1), the candidate disturbance location set is swept to evaluate nodal frequency security indices (step A2), and a min–max allocation layer populates an offline atlas with robust gain vectors (step A3). In the online stage, the prevailing operating condition is matched against the atlas (step B1), the stored gains are projected onto current device limits (step B2), and the resulting (H_i, D_i) setpoints are dispatched to the GFM support buses (step B3). Because the atlas already hedges against all candidate disturbance locations, explicit online disturbance localization is not required.

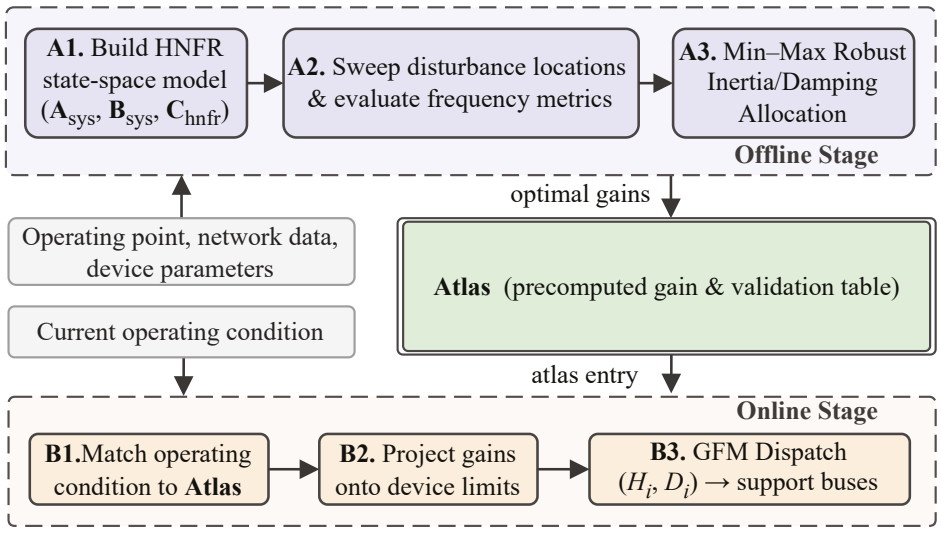


Figure 2. Framework of the proposed atlas-based gain scheduling scheme.

Frequency security in low-inertia grids is commonly evaluated by the rate of change of frequency (RoCoF) and the frequency nadir, both of which are closely related to the available inertia and fast frequency response (FFR) capability [6,7]. In practice, operators are often concerned with worst-node risks rather than averaged behaviors, since local RoCoF and

local nadir can drive protection actions and operational constraints. Moreover, in modern grids these metrics are strongly influenced by measurement and estimation chains (filtering, windowing, noise, and event detection), which motivates the use of reproducible protocols for RoCoF/nadir computation and fair comparison of control strategies [8–10].

A key limitation of many classical frequency studies is the reliance on aggregated indicators such as center-of-inertia/center-of-frequency (COI/COF), which includes the implicit assumption that frequency dynamics are sufficiently homogeneous across the network. Recent analytical and data-driven evidence shows that post-disturbance frequency responses can exhibit pronounced spatial disparities, with certain buses experiencing substantially larger RoCoF or deeper nadirs than those predicted by aggregated models [11–16]. Such spatial heterogeneity becomes more salient when inertia and damping are unevenly distributed and when frequency support actions are geographically concentrated.

Understanding and controlling spatial frequency behavior requires careful definitions of nodal frequency, especially when heterogeneous synchronization mechanisms coexist. While synchronous generators and grid-forming (GFM) converters are naturally associated with electromechanical frequency channels, grid-following (GFL) converters measure frequency through phase-locked loops (PLLs), for which the estimated frequency can deviate from electromechanical notions under weak-grid conditions [17,18]. This coexistence motivates unified yet channel-aware modeling frameworks that can map a location-specific active power disturbance to both mechanical frequency and PLL frequency outputs [19–22].

On the control side, the interplay between GFM and GFL inverters has attracted growing attention, particularly regarding how their parameter choices shape nodal RoCoF/nadir trajectories and stability margins. Analytical design and tuning rules have been proposed to coordinate GFM droop/inertia and GFL PLL bandwidth so as to meet frequency objectives at multiple buses rather than only at the COI [23]. Meanwhile, practical enhancements of GFL control for stiff and weak grids, comprehensive modeling comparisons for PLL-based inverters, and emerging circuit-model augmentations that better capture PLL-driven instabilities collectively highlight that weak-grid frequency behavior is inseparable from PLL dynamics and the associated modeling assumptions [24–27].

Beyond local device tuning, disturbance location-dependent frequency behavior has motivated spatiotemporal analysis tools and placement/design methodologies. Frequency distributions in systems with mixed GFM/GFL populations have been studied from both frequency domain and low-order modeling perspectives, emphasizing that frequency is not a single scalar but a field over buses and time [22,28]. This perspective aligns with spatiotemporal placement and evaluation frameworks for GFM inverters, which explicitly consider where converters are installed and how disturbances propagate through network coupling [29]. Variance-based global sensitivity analysis further provides a scalable route for quantifying locational impacts and screening influential factors under uncertainty [30].

The locational nature of frequency security also raises planning and resource allocation questions around where to place virtual inertia and FFR resources and how to tune them under device limits and finite-energy constraints. One line of work has established optimization-based placement of virtual/synthetic inertia and fast frequency response, including formulations that account for worst-case disturbance locations [31,32]. Storage-based virtual inertia placement and robust allocation of distributed energy storage systems further demonstrate that frequency security requirements can be explicitly locational and that robust methods are often needed to hedge against uncertain contingencies and operating conditions [33–36].

Complementing these planning formulations, hierarchical and distributed FFR coordination strategies prioritize electrically close resources and can reduce the reliance on centralized aggregated frequency signals, leading to improved responsiveness and

scalability [37]. In addition, practical FFR designs for wind and converter-interfaced generation illustrate that fast active power support can be shaped to arrest the nadir and mitigate RoCoF, and in some settings may even offer a low-cost alternative to maintaining high synchronous inertia [38–40].

While the above advances provide important building blocks, two gaps remain critical for IBR-rich low-inertia grids: first, most tractable optimization and tuning approaches still rely on aggregated or homogeneous frequency models, which can underestimate worst-node risks and cannot directly quantify heterogeneous-channel incoherence; second, scalable engineering workflows that sweep disturbance locations, compute nodal RoCoF/nadir/split under a fixed protocol, and translate the resulting sensitivity patterns into deployable gain-scheduling rules remain limited [30]. These gaps motivate a disturbance location-aware framework that (i) builds an explicit heterogeneous nodal frequency response model (HNFR), (ii) evaluates nodal worst-case metrics reproducibly over disturbance location sets, and (iii) coordinates constrained heterogeneous frequency support with an atlas-based gain scheduling deployment in which the atlas serves as a pre-validated library of frequency support gain settings indexed by operating condition and designed to be retrieved online without solving a new optimization at each dispatch.

The main contributions are as follows:

1. A heterogeneous nodal frequency response (HNFR) state-space model that unifies SG and GFM electromechanical frequency channels with GFL PLL-estimated frequency in a single output matrix, eliminates network algebraic variables through a reduced-order representation, and retains disturbance location as an explicit input dimension for scalable nodal frequency analysis.
2. An input–output evaluation protocol that maps each candidate disturbance location to worst-node RoCoF, worst-node nadir, and nodal frequency split through a fixed signal processing chain, enabling reproducible comparison across allocation strategies.
3. A robust min–max allocation formulation that schedules GFM virtual inertia and droop parameters across disturbance locations under device limits and a fixed total budget constraint, together with an atlas-based gain scheduling workflow that does not require explicit online disturbance location identification.

The remainder of the paper is organized as follows: Section 2 derives the HNFR model and the nodal frequency input–output mapping; Sections 3 and 4 formulate the disturbance location-aware frequency support allocation problem and its tractable surrogates; Section 5 reports case studies; and Section 6 concludes the paper.

2. Heterogeneous Nodal Frequency Response Modeling for Spatiotemporal Frequency Dynamics

This section develops an HNFR framework for disturbance location-aware frequency analysis and tuning. The goal is to obtain a reproducible electromechanical-scale linearized state-space model with explicit inputs/outputs, enabling large-scale sensitivity computation and interpretable tuning rules.

Recent analytical frameworks have advanced the understanding of nodal frequency dynamics in bulk power systems. In [13], the developed natural decomposition of nodal frequency responses yielded closed-form solutions for both generation- and load-side disturbances. In [16], a reduced-order bus frequency response model was proposed to preserve spatial distribution characteristics through modal decomposition and a vibrational mechanics analogy, enabling rapid closed-form evaluation. While both frameworks provide valuable analytical insight, neither explicitly distinguishes among SG electromechanical, GFM virtual-swing, and GFL PLL-estimated frequency sources within the output space, and the latter aggregates disturbance location into an equivalent COI power perturbation.

https://doi.org/10.3390/sym18050759

The HNFR model developed below addresses these aspects by unifying heterogeneous frequency channels within a single output matrix while retaining disturbance location as an explicit input dimension.

2.1. Modeling Scope, Frequency Definitions, and Notation

This work targets post-disturbance electromechanical frequency dynamics after fault clearing and other short-term active power disturbances under the quasi-stationary voltage assumption. Buses are partitioned into a support set $\mathcal{S}$ and following set $\mathcal{L}$ according to the dominant frequency channel; $\mathcal{S}$ includes SGs and GFM converters (voltage-source-like synchronization), while $\mathcal{L}$ aggregates GFL converters and frequency-relevant loads for which the measured frequency is dominated by PLL synchronization.

The system state vector $\mathbf{x} \in \mathbb{R}^{3N_S+3N_L}$ is defined as

$$\mathbf{x} = [\Delta\boldsymbol{\delta}_S^T,\ \Delta\boldsymbol{\omega}_S^T,\ \Delta\mathbf{P}_{z,S}^T,\ \Delta\boldsymbol{\theta}_L^T,\ \Delta\boldsymbol{\omega}_{\text{pll}}^T,\ \Delta\mathbf{P}_{\text{inv}}^T]^T. \tag{1}$$

The nodal-frequency output is $\Delta\boldsymbol{\omega}_S$ for $\mathcal{S}$ and $\Delta\boldsymbol{\omega}_{\text{pll}}$ for $\mathcal{L}$, capturing heterogeneous measurement chains that may diverge in weak grids.

For notation, ω_0 denotes the nominal angular frequency (rad/s), $\Delta(\cdot)$ denotes incremental deviations from the operating point, and vectors are stacked by bus ordering within $\mathcal{S}$ and $\mathcal{L}$. Throughout this section, $\Delta\boldsymbol{\omega}$ is in rad/s and RoCoF is in Hz/s, computed as $\text{RoCoF} = \Delta\dot{\omega}/(2\pi)$ after applying a fixed estimation protocol (filtering and sliding-window slope). To avoid notation conflicts across sections, $\mathcal{S}$ and $\mathcal{L}$ are reserved exclusively for the support/following bus sets in this section, while operating condition scenarios and contingency locations are denoted by $\mathcal{O}$ and $\mathcal{K}$, respectively, in the coordination sections.

2.2. Unified Low-Frequency Device Models for SGs, GFM Converters, and GFL Converters with PLLs

At the electromechanical time scale, SGs and GFM converters exhibit frequency support behavior that modulates active power as a function of frequency deviation. Omitting voltage magnitude dynamics, their unified dynamics are

$$\begin{cases} \Delta\dot{\boldsymbol{\delta}}_S = \Delta\boldsymbol{\omega}_S \\ \mathbf{M}_S\Delta\dot{\boldsymbol{\omega}}_S = -\mathbf{D}_S\Delta\boldsymbol{\omega}_S - \Delta\mathbf{P}_{e,S} + \Delta\mathbf{P}_{m,S} \\ \mathbf{T}_S\Delta\dot{\mathbf{P}}_{m,S} = -\Delta\mathbf{P}_{m,S} - \mathbf{R}_S^{-1}\Delta\boldsymbol{\omega}_S - \boldsymbol{\Gamma}_S\Delta\dot{\boldsymbol{\omega}}_S \end{cases}. \tag{2}$$

To remove the dependence on $\Delta\dot{\boldsymbol{\omega}}_S$ on the right-hand side, an auxiliary state $\Delta\mathbf{P}_{z,S}$ is introduced via

$$\begin{cases} \Delta\mathbf{P}_{z,S} = \Delta\mathbf{P}_{m,S} + \mathbf{T}_S^{-1}\boldsymbol{\Gamma}_S\Delta\boldsymbol{\omega}_S, \\ \mathbf{N}_S = \mathbf{M}_S^{-1}\mathbf{T}_S^{-1}\boldsymbol{\Gamma}_S \end{cases}. \tag{3}$$

With diagonal resource parameter matrices, the local state-space model for the support bus can be written as

$$\begin{bmatrix} \Delta\dot{\boldsymbol{\delta}}_S \\ \Delta\dot{\boldsymbol{\omega}}_S \\ \Delta\dot{\mathbf{P}}_{z,S} \end{bmatrix} = \mathbf{A}_S^{\text{loc}}\mathbf{x}_S + \begin{bmatrix} \mathbf{0} \\ -\mathbf{M}_S^{-1} \\ \mathbf{0} \end{bmatrix}\Delta\mathbf{P}_{e,S}, \tag{4}$$

where the local state is $\mathbf{x}_S = [\Delta\boldsymbol{\delta}_S^T, \Delta\boldsymbol{\omega}_S^T, \Delta\mathbf{P}_{z,S}^T]^T$ and $\mathbf{A}_S^{\text{loc}}$ is determined by the component-wise dynamics. The key components are

$$\begin{cases} \Delta\dot{\boldsymbol{\omega}}_S = -\mathbf{M}_S^{-1}\mathbf{D}_S\Delta\boldsymbol{\omega}_S - \mathbf{N}_S\Delta\boldsymbol{\omega}_S - \mathbf{M}_S^{-1}\Delta\mathbf{P}_{e,S} + \mathbf{M}_S^{-1}\Delta\mathbf{P}_{z,S} \\ \Delta\dot{\mathbf{P}}_{z,S} = -\mathbf{T}_S^{-1}\Delta\mathbf{P}_{z,S} + (\mathbf{T}_S^{-2}\boldsymbol{\Gamma}_S - \mathbf{T}_S^{-1}\mathbf{R}_S^{-1})\Delta\boldsymbol{\omega}_S \end{cases}. \tag{5}$$

https://doi.org/10.3390/sym18050759

For following buses, a reduced Type-II proportional–integral (PI) PLL model is

$$\begin{cases} \Delta\dot{\boldsymbol{\theta}}_L = \Delta\boldsymbol{\omega}_{\text{pll}} \\ \Delta\dot{\boldsymbol{\omega}}_{\text{pll}} = -\mathbf{K}_{p,\text{pll}}\Delta\boldsymbol{\omega}_{\text{pll}} + \mathbf{K}_{I,\text{pll}}(\Delta\boldsymbol{\delta}_L - \Delta\boldsymbol{\theta}_L) + \mathbf{K}_{p,\text{pll}}\Delta\dot{\boldsymbol{\delta}}_L \end{cases}. \tag{6}$$

In (6), $\Delta\boldsymbol{\omega}_{\text{pll}}$ is in rad/s. The diagonal gains $\mathbf{K}_{p,\text{pll}}$ and $\mathbf{K}_{I,\text{pll}}$ represent an electromechanical-band reduction of a synchronous reference frame phase-locked loop (SRF-PLL) linearization; a common second-order parameterization is $K_{p,\text{pll}} = 2\zeta\omega_n$ and $K_{I,\text{pll}} = \omega_n^2$ (after normalization by the local voltage observation gain). The term $\Delta\boldsymbol{\delta}_L$ is the following-bus voltage angle induced by network coupling, and is made explicit by the elimination step in (11); when PLL saturation or strong voltage magnitude dynamics are dominant, this reduced channel should be validated against an RMS/DAE model. Under the quasi-stationary voltage assumption, the SRF-PLL tracks the terminal voltage-phase derivative at each following bus. After the network elimination in (11), $\Delta\boldsymbol{\delta}_L$ becomes a linear function of $\Delta\boldsymbol{\delta}_S$, so that both $\Delta\boldsymbol{\omega}_S$ (support-bus electromechanical frequency) and $\Delta\boldsymbol{\omega}_{\text{pll}}$ (following-bus PLL-estimated frequency) are expressed as linear functionals of the same reduced state vector normalized to the same base frequency. This shared representation makes the two heterogeneous frequency channels directly comparable in the common output space defined by $\mathbf{C}_{\text{hnfr}}$ in (25). For the active-power control loop with virtual inertia and droop,

$$\boldsymbol{\tau}_{\text{inv}}\Delta\dot{\mathbf{P}}_{\text{inv}} = -\Delta\mathbf{P}_{\text{inv}} - \mathbf{K}_d\Delta\boldsymbol{\omega}_{\text{pll}} - \mathbf{K}_J\Delta\dot{\boldsymbol{\omega}}_{\text{pll}}. \tag{7}$$

Substituting (6) into (7) and eliminating $\Delta\dot{\boldsymbol{\omega}}_{\text{pll}}$ yields

$$\begin{aligned} \boldsymbol{\tau}_{\text{inv}}\Delta\dot{\mathbf{P}}_{\text{inv}} = -\Delta\mathbf{P}_{\text{inv}} &+ (\mathbf{K}_J\mathbf{K}_{p,\text{pll}} - \mathbf{K}_d)\Delta\boldsymbol{\omega}_{\text{pll}} \\ &+ \mathbf{K}_J\mathbf{K}_{I,\text{pll}}(\Delta\boldsymbol{\theta}_L - \Delta\boldsymbol{\delta}_L) - \mathbf{K}_J\mathbf{K}_{p,\text{pll}}\Delta\dot{\boldsymbol{\delta}}_L. \end{aligned} \tag{8}$$

2.3. Network Elimination and Reduced-Order State-Space Representation

Under the QSS network representation, the linearized active-power balance is

$$\begin{bmatrix} \Delta\mathbf{P}_{\text{inj},S} \\ \Delta\mathbf{P}_{\text{inj},L} \end{bmatrix} = \begin{bmatrix} \mathbf{J}_{SS} & \mathbf{J}_{SL} \\ \mathbf{J}_{LS} & \mathbf{J}_{LL} \end{bmatrix} \begin{bmatrix} \Delta\boldsymbol{\delta}_S \\ \Delta\boldsymbol{\delta}_L \end{bmatrix}. \tag{9}$$

Reproducible construction. Starting from an alternating current (AC) power flow operating point, we form $\mathbf{J}$ under the angle-dominant approximation, select one reference angle per connected component (remove the associated row/column), and partition the reduced $\mathbf{J}$ into (SS, SL, LS, LL) blocks by $(\mathcal{S}, \mathcal{L})$ ordering. In computation, $\mathbf{J}_{LL}^{-1}$ is applied through a sparse linear solver (optionally with mild regularization when $\mathbf{J}_{LL}$ is ill-conditioned). For following buses, the incremental active power injection satisfies

$$\Delta\mathbf{P}_{\text{inj},L} = \Delta\mathbf{P}_{\text{inv}} - \Delta\mathbf{P}_{\text{load},L}. \tag{10}$$

Solving for $\Delta\boldsymbol{\delta}_L$ yields

$$\Delta\boldsymbol{\delta}_L = -\mathbf{Z}_{LL}\mathbf{J}_{LS}\Delta\boldsymbol{\delta}_S + \mathbf{Z}_{LL}\Delta\mathbf{P}_{\text{inv}} - \mathbf{Z}_{LL}\Delta\mathbf{P}_{\text{load},L}, \tag{11}$$

where $\mathbf{Z}_{LL} \triangleq \mathbf{J}_{LL}^{-1}$ denotes the inverse (or equivalently, the linear-solve operator associated with $\mathbf{J}_{LL}$). In implementation, $\mathbf{Z}_{LL}\mathbf{b}$ is obtained by solving $\mathbf{J}_{LL}\mathbf{x} = \mathbf{b}$ with a sparse linear solver, and $\mathbf{J}_{LL} + \epsilon\mathbf{I}$ can be used when regularization is required. Define $\mathbf{K}_{\text{couple}} = \mathbf{Z}_{LL}\mathbf{J}_{LS}$. Differentiating (11) yields

$$\Delta\dot{\boldsymbol{\delta}}_L = -\mathbf{K}_{\text{couple}}\Delta\dot{\boldsymbol{\delta}}_S + \mathbf{Z}_{LL}\Delta\dot{\mathbf{P}}_{\text{inv}} - \mathbf{Z}_{LL}\Delta\dot{\mathbf{P}}_{\text{load},L}. \tag{12}$$

https://doi.org/10.3390/sym18050759

Using $\Delta\dot{\boldsymbol{\delta}}_S = \Delta\boldsymbol{\omega}_S$, an electromechanical-band approximation that avoids derivative-dependent algebraic loops is

$$\Delta\dot{\boldsymbol{\delta}}_L \approx -\mathbf{K}_{\text{couple}}\Delta\boldsymbol{\omega}_S. \tag{13}$$

Within the short RoCoF window $[0, T_{\text{roc}}]$, the remaining net-injection derivative term in (12) is treated as a bounded modeling residual. Define

$$\boldsymbol{\varepsilon}_{\dot{\delta},L}(t) \triangleq \Delta\dot{\boldsymbol{\delta}}_L(t) + \mathbf{K}_{\text{couple}}\Delta\boldsymbol{\omega}_S(t) = \mathbf{Z}_{LL}\big(\Delta\dot{\mathbf{P}}_{\text{inv}}(t) - \Delta\dot{\mathbf{P}}_{\text{load},L}(t)\big). \tag{14}$$

In atlas construction (Section 4), $\|\boldsymbol{\varepsilon}_{\dot{\delta},L}(t)\|_\infty$ over $t \in [0, T_{\text{roc}}]$ is recorded per entry to quantify the conservativeness needed in deployment. The support-side electrical power is

$$\Delta\mathbf{P}_{e,S} = \Delta\mathbf{P}_{\text{inj},S} + \Delta\mathbf{P}_{\text{load},S} = \mathbf{J}_{\text{red}}\Delta\boldsymbol{\delta}_S + \mathbf{C}_{\text{net}}\Delta\mathbf{P}_{\text{inv}} - \mathbf{C}_{\text{net}}\Delta\mathbf{P}_{\text{load},L} + \Delta\mathbf{P}_{\text{load},S}. \tag{15}$$

For clarity, the reduced coupling matrices implied by (9)–(11) are $\mathbf{J}_{\text{red}} \triangleq \mathbf{J}_{SS} - \mathbf{J}_{SL}\mathbf{Z}_{LL}\mathbf{J}_{LS}$, $\mathbf{C}_{\text{net}} \triangleq \mathbf{J}_{SL}\mathbf{Z}_{LL}$, and $\mathbf{K}_{\text{couple}} \triangleq \mathbf{Z}_{LL}\mathbf{J}_{LS}$, which can be formed explicitly or applied as linear operators using sparse solves with $\mathbf{J}_{LL}$. The overall system model is

$$\begin{cases} \dot{\mathbf{x}} = \mathbf{A}_{\text{sys}}\mathbf{x} + \mathbf{B}_{\text{sys}}\mathbf{u}, \\ \mathbf{u} = [\Delta\mathbf{P}_{\text{load},S}^T,\ \Delta\mathbf{P}_{\text{load},L}^T]^T. \end{cases} \tag{16}$$

Physically, the elimination procedure replaces the network algebraic equations with coupling matrices $\mathbf{J}_{\text{red}}$, $\mathbf{C}_{\text{net}}$, and $\mathbf{K}_{\text{couple}}$, which encode how active-power disturbances propagate from the injection bus to each support and following bus through the network impedance structure. The resulting state-space form in (16) is a self-contained linear time-invariant (LTI) system, for which the input is the location-specific active-power disturbance and the output is the full set of heterogeneous nodal frequencies. The system matrix admits a block structure

$$\mathbf{A}_{\text{sys}} = \begin{bmatrix} \mathbf{A}_{11} & \mathbf{A}_{12} \\ \mathbf{A}_{21} & \mathbf{A}_{22} \end{bmatrix}. \tag{17}$$

The submatrices are

$$\mathbf{A}_{11} = \begin{bmatrix} \mathbf{0} & \mathbf{I} & \mathbf{0} \\ -\mathbf{M}_S^{-1}\mathbf{J}_{\text{red}} & -\mathbf{M}_S^{-1}\mathbf{D}_S - \mathbf{N}_S & \mathbf{M}_S^{-1} \\ \mathbf{0} & \mathbf{T}_S^{-2}\boldsymbol{\Gamma}_S - \mathbf{T}_S^{-1}\mathbf{R}_S^{-1} & -\mathbf{T}_S^{-1} \end{bmatrix}, \tag{18}$$

$$\mathbf{A}_{12} = \begin{bmatrix} \mathbf{0} & \mathbf{0} & \mathbf{0} \\ \mathbf{0} & \mathbf{0} & -\mathbf{M}_S^{-1}\mathbf{C}_{\text{net}} \\ \mathbf{0} & \mathbf{0} & \mathbf{0} \end{bmatrix}, \tag{19}$$

$$\mathbf{A}_{21} = \begin{bmatrix} \mathbf{0} & \mathbf{0} & \mathbf{0} \\ -\mathbf{K}_{I,\text{pll}}\mathbf{K}_{\text{couple}} & -\mathbf{K}_{p,\text{pll}}\mathbf{K}_{\text{couple}} & \mathbf{0} \\ \boldsymbol{\Phi}_\delta & \boldsymbol{\Phi}_{\omega_S} & \mathbf{0} \end{bmatrix}, \tag{20}$$

$$\mathbf{A}_{22} = \begin{bmatrix} \mathbf{0} & \mathbf{I} & \mathbf{0} \\ -\mathbf{K}_{I,\text{pll}} & -\mathbf{K}_{p,\text{pll}} & \mathbf{K}_{I,\text{pll}}\mathbf{Z}_{LL} \\ \boldsymbol{\Phi}_\theta & \boldsymbol{\Phi}_\omega & \boldsymbol{\Phi}_p \end{bmatrix}. \tag{21}$$

Let $\boldsymbol{\Lambda} = \boldsymbol{\tau}_{\text{inv}}^{-1}$. The GFL power-loop related coefficients are

$$\begin{cases} \boldsymbol{\Phi}_{\omega_S} = \boldsymbol{\Lambda}\mathbf{K}_J\mathbf{K}_{p,\text{pll}}\mathbf{K}_{\text{couple}} \\ \boldsymbol{\Phi}_\delta = \boldsymbol{\Lambda}\mathbf{K}_J\mathbf{K}_{I,\text{pll}}\mathbf{K}_{\text{couple}} \\ \boldsymbol{\Phi}_\theta = \boldsymbol{\Lambda}\mathbf{K}_J\mathbf{K}_{I,\text{pll}} \end{cases} \tag{22}$$

https://doi.org/10.3390/sym18050759

$$\begin{cases} \boldsymbol{\Phi}_\omega = \boldsymbol{\Lambda}(\mathbf{K}_J\mathbf{K}_{p,\mathrm{pll}} - \mathbf{K}_d) \\ \boldsymbol{\Phi}_p = \boldsymbol{\Lambda}(-\mathbf{I} - \mathbf{K}_J\mathbf{K}_{I,\mathrm{pll}}\mathbf{Z}_{LL}) \end{cases} \tag{23}$$

and the input matrix is

$$\mathbf{B}_{\mathrm{sys}} = \left[\begin{array}{cc} \mathbf{0} & \mathbf{0} \\ -\mathbf{M}_S^{-1} & \mathbf{M}_S^{-1}\mathbf{C}_{\mathrm{net}} \\ \mathbf{0} & \mathbf{0} \\ \hline \mathbf{0} & \mathbf{0} \\ \mathbf{0} & -\mathbf{K}_{I,\mathrm{pll}}\mathbf{Z}_{LL} \\ \mathbf{0} & \boldsymbol{\Lambda}\mathbf{K}_J\mathbf{K}_{I,\mathrm{pll}}\mathbf{Z}_{LL} \end{array}\right]. \tag{24}$$

2.4. Disturbance-to-Nodal-Frequency Mapping and Location Sensitivity Computation

Define the system output as

$$\mathbf{y}(t) \triangleq \begin{bmatrix} \Delta\boldsymbol{\omega}_S(t) \\ \Delta\boldsymbol{\omega}_{\mathrm{pll}}(t) \end{bmatrix} = \mathbf{C}_{\mathrm{hnfr}}\mathbf{x}(t). \tag{25}$$

To keep the units consistent across modeling, optimization, and reporting, we use the Hz-domain nodal frequency output

$$\mathbf{f}(t) \triangleq \frac{1}{2\pi}\mathbf{y}(t) = \begin{bmatrix} \Delta\mathbf{f}_S(t) \\ \Delta\mathbf{f}_{\mathrm{pll}}(t) \end{bmatrix}. \tag{26}$$

For a step disturbance $\mathbf{u}(t) = \mathbf{u}_0 1(t)$ with $\mathbf{x}(0) = \mathbf{0}$, the initial RoCoF relation is

$$\dot{\mathbf{y}}(0^+) = \mathbf{C}_{\mathrm{hnfr}}\mathbf{B}_{\mathrm{sys}}\mathbf{u}_0. \tag{27}$$

If the closed-loop model includes frequency restoration mechanisms such that $\mathbf{A}_{\mathrm{sys}}$ is Hurwitz, then the steady-state output satisfies

$$\mathbf{y}_{\mathrm{ss}} = -\mathbf{C}_{\mathrm{hnfr}}\mathbf{A}_{\mathrm{sys}}^{-1}\mathbf{B}_{\mathrm{sys}}\mathbf{u}_0. \tag{28}$$

The nodal frequency split is

$$\Delta\omega_{\mathrm{split}}(t) \triangleq \max_i y_i(t) - \min_i y_i(t), \tag{29}$$

$$\Delta f_{\mathrm{split}}(t) \triangleq \frac{1}{2\pi}\Delta\omega_{\mathrm{split}}(t) = \max_i f_i(t) - \min_i f_i(t). \tag{30}$$

3. Disturbance Location-Aware Frequency Support Allocation: Theory and Formulation

Sections 3 and 4 form an integrated methodology for location-aware frequency support design. This section develops the system-level allocation model and a tractable formulation. Unlike approaches that optimize only aggregated quantities such as COI, the proposed allocation targets worst-node security and frequency coherence (split) while explicitly accounting for a set of disturbance locations and a set of operating conditions.

Parameter hierarchy and scope. To separate the plant model from the scheduling variables, we distinguish (i) fixed device/network dynamics used to build the HNFR model (Section 2) and (ii) a designated set of externally writable frequency support setpoints coordinated in Sections 3 and 4. The HNFR matrices $(\mathbf{A}_{\mathrm{sys}}, \mathbf{B}_{\mathrm{dist}}, \mathbf{C}_{\mathrm{hnfr}})$ represent the fixed small-signal plant at a given operating point, including internal inverter and PLL dynamics. The coordination layer tunes only setpoints that are available as implementation-

https://doi.org/10.3390/sym18050759

level parameters (e.g., governor droop/FFR gains, GFM frequency–power droop/virtual inertia setpoints, storage/IBR fast frequency support gains, and controllable demand gains). These tunable parameters are stacked in $\mathbf{g}$ in (33) and enter the closed-loop model through an explicit feedback actuation path $\mathbf{B}_{\text{act}}\mathbf{K}(\mathbf{g})\mathbf{C}_{\text{meas}}$ in (34). Internal parameters in Section 2 (e.g., $\mathbf{K}_d, \mathbf{K}_J, \boldsymbol{\tau}_{\text{inv}}, \mathbf{K}_{p,\text{pll}}, \mathbf{K}_{I,\text{pll}}$) are treated as fixed within each atlas bin unless the implementation explicitly supports parameter updates, in which case they are included in $\mathbf{g}$ via the same mapping.

Equivalent inertia/damping parameterization (used in case studies). While $\mathbf{g}$ is written as $(\mathbf{k}_p, \mathbf{k}_J)$ in (32) and (33), the same closed-loop effect can be represented as an effective inertia/damping update on the swing-like support channel dynamics. Consider an (aggregated) support channel frequency equation $\mathbf{M}\Delta\dot{\boldsymbol{\omega}} = -\mathbf{D}\Delta\boldsymbol{\omega} + \Delta\mathbf{P}_a + (\cdots)$ with $\Delta\mathbf{P}_a = -\mathbf{k}_p\Delta\mathbf{f} - \mathbf{k}_J\text{RoCoF}$ and $\Delta\mathbf{f} = \Delta\boldsymbol{\omega}/(2\pi)$. Then, $\Delta\mathbf{P}_a$ is equivalent to updating

$$\mathbf{M}_{\text{eff}} = \mathbf{M} + \frac{1}{2\pi}\mathbf{K}_J, \qquad \mathbf{D}_{\text{eff}} = \mathbf{D} + \frac{1}{2\pi}\mathbf{K}_p, \tag{31}$$

with $\mathbf{K}_p = \text{diag}(\mathbf{k}_p)$ and $\mathbf{K}_J = \text{diag}(\mathbf{k}_J)$ under diagonal actuator sharing. Therefore, provided that constraints are mapped consistently, optimizing $(\mathbf{k}_p, \mathbf{k}_J)$ or optimizing an equivalent $(\mathbf{M}_{\text{eff}}, \mathbf{D}_{\text{eff}})$ represents a change of variables. In our numerical studies, we report the tuned settings in the interpretable (H, D) form for GFM resources, where H is the virtual inertia constant associated with $\mathbf{M}_{\text{eff}}$ and D is the effective damping coefficient. To avoid attributing improvements to "extra inertia", we enforce budgeted tuning that preserves the total effective inertia/damping over the GFM set, i.e., $\sum H_{\text{GFM}}$ and $\sum D_{\text{GFM}}$ are held fixed and only redistributed within per-device bounds.

Because changing H_i modifies the corresponding diagonal entry of $\mathbf{M}_S$, the closed-loop system matrix $\mathbf{A}_{\text{sys}}(\mathbf{g})$ is in general gain-dependent; nonetheless, each atlas entry in Section 4 is computed with the full $\mathbf{A}(\mathbf{g})$-dependence at the optimized gain vector; the "fixed plant" label applies only during the online scaling step between dispatch updates, where the total-budget constraint limits the induced perturbation and keeps the approximation meaningful within the tested envelope.

3.1. Problem Setup: Actuation, Decision Variables, Constraints, and Risk Metrics

The object of allocation in this paper is a system-level configuration of frequency support parameters (gain allocation/scheduling) rather than unit-by-unit power-trajectory commands. We use a unified primary form

$$\Delta P_a(t) = -k_{p,a}\,\Delta f_{m,a}(t) - k_{J,a}\,\text{RoCoF}_{m,a}(t) \tag{32}$$

and stack the tunable gains as

$$\mathbf{g} \triangleq [\mathbf{k}_p^T, \mathbf{k}_J^T]^T, \quad \mathbf{k}_p = [k_{p,1}, \ldots, k_{p,n_a}]^T, \quad \mathbf{k}_J = [k_{J,1}, \ldots, k_{J,n_a}]^T. \tag{33}$$

Implementation mapping and units. We index actuators by $a \in \mathcal{A}$ with $|\mathcal{A}| = n_a$. Throughout the paper, $\mathcal{A}$ denotes the actuator set, while $\mathfrak{A}$ (Section 4) denotes the atlas used to avoid symbol overload. Each actuator a is associated with a bus $b(a)$ and a frequency measurement channel $m(a) \in \{\text{S}, \text{PLL}\}$: for SG/GFM-like support devices, $\Delta f_{m,a}(t) \triangleq \Delta f_{b(a)}(t)$ is the support-channel nodal frequency; for GFL devices with PLL-dominated measurement, $\Delta f_{m,a}(t) \triangleq \Delta f_{\text{pll},b(a)}(t)$. Throughout Sections 3 and 4, Δf is in Hz and RoCoF in Hz/s; therefore, $k_{p,a}$ has unit [MW/Hz] (or [p.u./Hz] on the system base) and $k_{J,a}$ has unit [MW · s/Hz] (or [p.u. · s/Hz] on the system base). Measurement-path realizability. We generate $\Delta f_{m,a}(t)$ and $\text{RoCoF}_{m,a}(t)$ using a fixed measurement chain rather than an assumed ideal. We adopt the protocol in (41) as the implemented chain, that is, a first-order

https://doi.org/10.3390/sym18050759

low-pass $H(s) = \omega_c/(s+\omega_c)$ applied to Δf, followed by a RoCoF estimator. For reproducibility and linear time-invariant (LTI) modeling, the low pass is represented in state space by $\dot{\mathbf{x}}_f = -\omega_c \mathbf{x}_f + \omega_c \mathbf{f}$ and $\mathbf{f}_f = \mathbf{x}_f$; a RoCoF estimate can be represented either (i) by the derivative $\dot{\mathbf{f}}_f$ (continuous-time realization) or (ii) by a fixed-window finite-impulse-response (FIR)/least-squares slope operator in discrete time, which admits an equivalent lifted LTI state-space realization. Accordingly, $\mathbf{C}_{\text{meas}}$ in (34) is defined with respect to an augmented state that includes the filter/estimator realization used by implementation. The same chain is used for all baselines and the proposed method. In the purely feedback realization, $\Delta P_a(t)$ is an active-power injection (or load reduction) applied at bus $b(a)$; hence, it enters the network-reduced model through the corresponding injection channel of $\Delta \mathbf{P}_{\text{inv}}$ (for inverter/storage actuators) or $\Delta \mathbf{P}_{\text{load}}$ (for responsive load). This yields a closed-loop form

$$\dot{\mathbf{x}} = \big(\mathbf{A}_{\text{sys}} + \mathbf{B}_{\text{act}}\mathbf{K}(\mathbf{g})\mathbf{C}_{\text{meas}}\big)\mathbf{x} + \mathbf{B}_{\text{dist}}\mathbf{u}, \quad \mathbf{K}(\mathbf{g}) \triangleq \text{blkdiag}\Big(\begin{bmatrix} -k_{p,a} & -k_{I,a} \end{bmatrix}\Big)_{a\in\mathcal{A}}, \tag{34}$$

where $\mathbf{C}_{\text{meas}}$ extracts the per-actuator $(\Delta f_{m,a}, \text{RoCoF}_{m,a})$ from the state (including any fixed filters) and $\mathbf{B}_{\text{act}}$ maps actuator injections to the corresponding network-reduced state channels. This block form makes explicit that tuning $\mathbf{g}$ primarily modifies $\mathbf{A}_{\text{sys}}(\mathbf{g}) \triangleq \mathbf{A}_{\text{sys}} + \mathbf{B}_{\text{act}}\mathbf{K}(\mathbf{g})\mathbf{C}_{\text{meas}}$, while the disturbance channel remains $\mathbf{B}_{\text{dist}}$ in the pure feedback case. Here, $\mathbf{B}_{\text{dist}}$ denotes the disturbance-to-state channel corresponding to the adopted disturbance encoding; in the open-loop HNFR model (16), one may take $\mathbf{B}_{\text{dist}} \equiv \mathbf{B}_{\text{sys}}$ when $\mathbf{u}$ stacks the active-power disturbances $(\Delta \mathbf{P}_{\text{load},S}, \Delta \mathbf{P}_{\text{load},L})$. Explicit channel mapping. Let n_{inj} denote the dimension of the reduced-network injection vector used by the chosen actuation channels (e.g., inverter/storage injections and responsive-load injections) and define a sparse selector $\mathbf{S}_{\text{act}} \in \mathbb{R}^{n_{\text{inj}} \times n_a}$ that maps actuator commands $\Delta \mathbf{P}_{\text{act}} \triangleq [\Delta P_1, \ldots, \Delta P_{n_a}]^T$ to the corresponding injection entries. Let $\mathbf{B}_{\text{inj}} \in \mathbb{R}^{n_x \times n_{\text{inj}}}$ denote the fixed injection-to-state mapping implied by the HNFR reduction (with n_x as the state dimension, including any measurement-chain states when augmented). We then have $\mathbf{B}_{\text{act}} = \mathbf{B}_{\text{inj}}\mathbf{S}_{\text{act}}$, and $\mathbf{A}_{\text{sys}}(\mathbf{g})$ becomes an explicit affine function of $\mathbf{g}$ once $(\mathbf{B}_{\text{inj}}, \mathbf{S}_{\text{act}}, \mathbf{C}_{\text{meas}})$ are fixed. Each disturbance is represented by a location index $k \in \mathcal{K}$ and deficit magnitude $\Delta P > 0$, encoded as a step input $\mathbf{u}(t) = \mathbf{u}_0\, 1(t)$ with

$$\mathbf{u}_0(k, \Delta P) \triangleq -\Delta P\, \mathbf{e}_k. \tag{35}$$

To balance globality and deployability, we adopt a two-layer decision structure with a baseline gain vector $\mathbf{g}_0$ and a low-dimensional scaling $\mathbf{s}$:

$$\begin{cases} \mathbf{g}(\mathbf{s}) = \mathbf{g}_0 \odot (\mathbf{1} + \mathbf{E}\mathbf{s}), \\ \mathbf{1} + \mathbf{E}\mathbf{s} \geq \mathbf{0} \end{cases} \tag{36}$$

where $\mathbf{s} \in \mathbb{R}^{n_s}$ is the low-dimensional scheduling vector, $\mathbf{E} \in \mathbb{R}^{n_g \times n_s}$ is a fixed embedding/participation matrix that maps $\mathbf{s}$ to actuator-wise gain updates, and $\odot$ denotes the Hadamard (element-wise) product. The non-negativity constraint in (36) prevents the scaling from flipping the sign of the baseline gains in $\mathbf{g}_0$. In a purely feedback realization of (32), actuation is driven by frequency signals generated by the system state; therefore, changing $\mathbf{g}$ primarily modifies the closed-loop dynamics $\mathbf{A}_{\text{sys}}(\mathbf{g})$ rather than the disturbance injection $\mathbf{B}_{\text{sys}}$. In this common case, for step disturbances and zero post-event initial conditions, $\dot{\mathbf{y}}(0^+) = \mathbf{C}_{\text{hnfr}}\mathbf{B}_{\text{sys}}\mathbf{u}_0$ is independent of $\mathbf{g}$ and early-time RoCoF can only be shaped over a short but nonzero window through $\mathbf{A}_{\text{sys}}(\mathbf{g})$. The dependence $\mathbf{B}_{\text{sys}}(\mathbf{g})$ is retained in order to cover implementations with an explicit feedforward/event-triggered

https://doi.org/10.3390/sym18050759

actuation path (e.g., power injection proportional to an estimated ΔP available from system monitoring), in which case gain changes affect the effective disturbance-to-state channel.

To keep the atlas computable and reduce the cost of repeated screening, we adopt an affine matrix parameterization around a reference tuning point $\mathbf{g}_{\mathrm{ref}}$, meaning that the linearized model varies to the first order with $\mathbf{g}$:

$$\begin{cases} \mathbf{A}_{\mathrm{sys}}(\mathbf{g}) = \mathbf{A}_{\mathrm{sys}}(\mathbf{g}_{\mathrm{ref}}) + \sum_{\ell=1}^{n_g} (g_\ell - g_{\ell,ref})\, \mathbf{A}_\ell, \\ \mathbf{B}_{\mathrm{sys}}(\mathbf{g}) = \mathbf{B}_{\mathrm{sys}}(\mathbf{g}_{\mathrm{ref}}) + \sum_{\ell=1}^{n_g} (g_\ell - g_{\ell,ref})\, \mathbf{B}_\ell \end{cases} \tag{37}$$

where $\mathbf{A}_\ell, \mathbf{B}_\ell$ follow from first-order expansions of the explicit device/network-reduced expressions in Section 2. Under diagonal or zone-based parameterizations, $\mathbf{A}_\ell, \mathbf{B}_\ell$ are sparse and affect only the state and input channels associated with the corresponding resource/zone. Consistency with (37): (37) is used as a generic template that also covers implementations where gains affect the disturbance channel (feedforward/event-triggered paths) or where additional gain-dependent blocks are present. For the purely feedback realization (34) with fixed $(\mathbf{B}_{\mathrm{act}}, \mathbf{C}_{\mathrm{meas}})$, $\mathbf{A}_{\mathrm{sys}}(\mathbf{g})$ is exactly affine in $\mathbf{g}$. If g_ℓ denotes one component of $\mathbf{g}$ (either a $k_{p,a}$ or a $k_{J,a}$), then a constant sparse selector $\mathbf{K}_\ell \triangleq \frac{\partial \mathbf{K}(\mathbf{g})}{\partial g_\ell}$ is defined to pick the corresponding entry in $\mathbf{K}(\mathbf{g})$. Then, the exact affine form is

$$\mathbf{A}_{\mathrm{sys}}(\mathbf{g}) = \mathbf{A}_{\mathrm{sys}} + \sum_{\ell=1}^{n_g} g_\ell\, \mathbf{B}_{\mathrm{act}} \mathbf{K}_\ell \mathbf{C}_{\mathrm{meas}}, \quad \mathbf{A}_\ell = \mathbf{B}_{\mathrm{act}} \mathbf{K}_\ell \mathbf{C}_{\mathrm{meas}}. \tag{38}$$

In this case, the disturbance channel is gain-independent ($\mathbf{B}_{\mathrm{sys}}(\mathbf{g}) \equiv \mathbf{B}_{\mathrm{dist}}$) unless an explicit feedforward/event-triggered actuation path is introduced, in which case $\mathbf{B}_\ell$ can be derived from the chosen structure and (37) applies directly.

To map physical limits to admissible gains in a reproducible way, consider $\Delta P(t) \approx -k_p\, \Delta f(t) - k_J\, \mathrm{RoCoF}(t)$. Given available power headroom $\hat{P}_{\max}$ and energy headroom $\hat{E}_{\max}$, conservative bounds can be written as follows:

$$\begin{cases} 0 \le k_p \le \frac{\hat{P}_{\max}}{\Delta f_{\max}}, \\ 0 \le k_J \le \frac{\hat{P}_{\max}}{\mathrm{RoCoF}_{\max}} \end{cases} \tag{39}$$

$$\begin{cases} 0 \le k_p \le \frac{\hat{E}_{\max}}{\Delta f_{\max}\, T_{\mathrm{sup}}}, \\ 0 \le k_J \le \frac{\hat{E}_{\max}}{\mathrm{RoCoF}_{\max}\, T_{\mathrm{sup}}} \end{cases} \tag{40}$$

where $(\Delta f_{\max}, \mathrm{RoCoF}_{\max}, T_{\mathrm{sup}})$ are calibrated bounds/durations recorded in each atlas entry under a fixed evaluation protocol (filtering, RoCoF estimation, and evaluation horizons). In deployment, a tightening factor $0 < \eta \le 1$ can be used to shrink $(\hat{P}_{\max}, \hat{E}_{\max}) \mapsto (\eta \hat{P}_{\max}, \eta \hat{E}_{\max})$ to absorb model mismatch and headroom estimation errors. The admissible gain set $\mathcal{G}$ uses the intersection of (39) and (40) together with any device-specific current and recovery constraints in Section 2. In particular, $\Delta f_{\max}$ and $\mathrm{RoCoF}_{\max}$ are chosen to be consistent with the security limits $(\bar{m}^{\mathrm{nad}}, \bar{m}^{\mathrm{roc}})$ and the RoCoF/nadir evaluation windows $(T_{\mathrm{roc}}, T_{\mathrm{eval}})$ used in (43)–(48), while T_{sup} is selected as the conservative support duration over which the headroom $(\hat{P}_{\max}, \hat{E}_{\max})$ must remain feasible under the adopted recovery policy.

To avoid sign ambiguity in under-frequency events, we define the nodal frequency deviation, RoCoF, and split as follows:

https://doi.org/10.3390/sym18050759

$$\begin{cases} \Delta f_i(t) \triangleq \frac{1}{2\pi}\Delta\omega_i(t), \\ \mathrm{RoCoF}_i(t) \triangleq \frac{d}{dt}\Delta f_i(t), \\ \Delta f_{\mathrm{split}}(t) \triangleq \max_i \Delta f_i(t) - \min_i \Delta f_i(t). \end{cases} \tag{41}$$

Fixed evaluation protocol (reproducible default). All frequency traces are sampled at $f_s = 200$ Hz and pre-filtered by a first-order low-pass $H(s) = \omega_c/(s+\omega_c)$ with $f_c = \omega_c/(2\pi) = 5$ Hz. RoCoF is computed by a sliding window least-squares slope over a window length $T_w = 200$ ms applied to the filtered $\Delta f_i(t)$. Unless otherwise stated, $T_{\mathrm{roc}} = 0.5$ s and $T_{\mathrm{eval}} = 10$ s are used to define the windows in (43)–(48), while $\mathcal{T}_{\mathrm{roc}}$ and $\mathcal{T}$ use uniform grids with $\Delta t = 10$ ms and $\Delta t = 20$ ms, respectively. These protocol parameters are recorded per atlas entry, and must be held fixed across all baselines for fair comparison. Time-grid conservativeness (reproducible bound). Because (43) and (44) use sup over continuous time, the sampled surrogates in (47) and (48) include an additive discretization margin. Let $\mathbf{f}_f(t)$ denote the filtered Hz-domain nodal frequency under the fixed protocol, and define $\dot{\mathbf{f}}_f(t)$ and $\ddot{\mathbf{f}}_f(t)$ accordingly (exact in the continuous-time realization or obtained by a consistent discrete-time differentiation operator used by the implementation). For each atlas entry, compute

$$\bar{d}_{1,\mathcal{I}} \triangleq \sup_{t\in[0,T_{\mathrm{eval}}]} \|\dot{\mathbf{f}}_f(t)\|_\infty, \qquad \bar{d}_{2,\mathcal{I}} \triangleq \sup_{t\in[0,T_{\mathrm{roc}}]} \|\ddot{\mathbf{f}}_f(t)\|_\infty. \tag{42}$$

Then, set $\delta_{\mathcal{I}}^{\mathrm{nad},grid} \triangleq \frac{1}{2}\bar{d}_{1,\mathcal{I}}\Delta t$, $\delta_{\mathcal{I}}^{\mathrm{spl},grid} \triangleq \bar{d}_{1,\mathcal{I}}\Delta t$ (since $\Delta f_{\mathrm{split}} = \max_i \Delta f_i - \min_i \Delta f_i$ has a derivative bounded by $2\|\dot{\mathbf{f}}\|_\infty$) and $\delta_{\mathcal{I}}^{\mathrm{roc},grid} \triangleq \frac{1}{2}\bar{d}_{2,\mathcal{I}}\Delta t$. These values are recorded in the atlas and absorbed into $\delta_{\mathcal{I}}^{x}$ in (55) so that the sampled surrogates are conservative with respect to the continuous-time definitions. Split-node set. In (41) and (44), the max/min are taken over the union of frequency-reporting channels $\mathcal{I}_f \triangleq \mathcal{S} \cup \mathcal{L}$, where $i \in \mathcal{S}$ uses the support-channel nodal frequency Δf_i and $i \in \mathcal{L}$ uses the PLL-estimated nodal frequency $\Delta f_{\mathrm{pll},i}$. This definition intentionally quantifies heterogeneous-channel incoherence; if a study only needs a within-channel split, the same definition is applied on $\mathcal{S}$ or $\mathcal{L}$ separately and reported as an additional metric. Worst-node evaluation metrics (computed by the fixed protocol) are defined as

$$\begin{cases} m_{k,o}^{\mathrm{roc}}(\mathbf{g}) \triangleq \max_i \ \sup_{t\in[0,T_{\mathrm{roc}}]} |\mathrm{RoCoF}_i(t)|, \\ m_{k,o}^{\mathrm{nad}}(\mathbf{g}) \triangleq \max_i \ \sup_{t\in[0,T_{\mathrm{eval}}]} \ (-\Delta f_i(t)) \end{cases} \tag{43}$$

$$m_{k,o}^{\mathrm{spl}}(\mathbf{g}) \triangleq \sup_{t\in[0,T_{\mathrm{eval}}]} \Delta f_{\mathrm{split}}(t). \tag{44}$$

Let $(\bar{m}^{\mathrm{roc}}, \bar{m}^{\mathrm{nad}}, \bar{m}^{\mathrm{spl}})$ denote security limits. To distinguish evaluation metrics from optimization surrogates, the metrics in (43) and (44) are used for reporting, whereas the optimization uses computationally tractable surrogates $\hat{m}_{k,o}^{\mathrm{roc}}(\mathbf{g})$, $\hat{m}_{k,o}^{\mathrm{nad}}(\mathbf{g})$, and $\hat{m}_{k,o}^{\mathrm{spl}}(\mathbf{g})$. We aggregate RoCoF and nadir into a normalized risk:

$$\hat{m}_{k,o}(\mathbf{g}) \triangleq \max\left\{ \frac{\hat{m}_{k,o}^{\mathrm{roc}}(\mathbf{g})}{\bar{m}^{\mathrm{roc}}}, \ \frac{\hat{m}_{k,o}^{\mathrm{nad}}(\mathbf{g})}{\bar{m}^{\mathrm{nad}}} \right\}. \tag{45}$$

Aggregated frequencies such as COI can be reported as baselines for comparability, but are not used as the sole objective because they can mask worst-node risks and nodal incoherence.

https://doi.org/10.3390/sym18050759

Embedding full-network time domain simulation inside the optimization is computationally prohibitive. As a primary surrogate, the initial RoCoF proxy is directly available from the input–output relation:

$$\begin{cases} \dot{\mathbf{y}}(0^+) = \mathbf{C}_{\text{hnfr}}\mathbf{B}_{\text{sys}}(\mathbf{g})\mathbf{u}_0, \\ \hat{m}^{\text{roc0}}_{k,o}(\mathbf{g}) \triangleq \left\| \frac{1}{2\pi}\dot{\mathbf{y}}(0^+) \right\|_\infty \end{cases}. \tag{46}$$

Equation (46) is meaningful when the effective disturbance-to-state channel $\mathbf{B}_{\text{sys}}(\mathbf{g})$ depends on tunable gains (e.g., event-triggered feedforward support proportional to an available ΔP estimate). Unless explicitly stated otherwise, this paper focuses on the purely feedback realization of (32), for which $\mathbf{B}_{\text{sys}}$ is independent of $\mathbf{g}$ and the primary optimization surrogates are the short-horizon and finite-horizon proxies in (47) and (48). For the common purely feedback realization (32), a short-horizon proxy that includes $\mathbf{A}_{\text{sys}}(\mathbf{g})$ is more informative. Using $\mathbf{y}(t) = \mathbf{C}_{\text{hnfr}}e^{\mathbf{A}_{\text{sys}}(\mathbf{g})t}\mathbf{B}_{\text{sys}}\mathbf{u}_0$, define

$$\hat{m}^{\text{roc}}_{k,o}(\mathbf{g}) \triangleq \max_{t\in\mathcal{T}_{\text{roc}}} \left\| \frac{1}{2\pi}\mathbf{C}_{\text{hnfr}}\mathbf{A}_{\text{sys}}(\mathbf{g})e^{\mathbf{A}_{\text{sys}}(\mathbf{g})t}\mathbf{B}_{\text{sys}}\mathbf{u}_0 \right\|_\infty, \tag{47}$$

where $\mathcal{T}_{\text{roc}} \subset [0, T_{\text{roc}}]$ is a fixed sampling set aligned with the RoCoF window used in Section 2. For finite-horizon metrics, $\sup_{t\in[0,T_{\text{eval}}]}$ is approximated by $\max_{t\in\mathcal{T}}$ on a fixed sampling set $\mathcal{T} \subset [0, T_{\text{eval}}]$, and the approximation error is quantified and recorded in the atlas entries as conservative error bounds that guide the selection of margins.

Computational note: the terms $e^{\mathbf{A}t}\mathbf{b}$ and $\mathbf{A}e^{\mathbf{A}t}\mathbf{b}$ are evaluated efficiently via matrix-exponential vector products (e.g., Krylov subspace `expv` routines) using sparse $\mathbf{A}_{\text{sys}}$ and caching across $t \in \mathcal{T}_{\text{roc}}$ and $t \in \mathcal{T}$. For atlas generation, the same cached trajectories are reused to compute $\hat{m}^{\text{roc}}$, $\hat{m}^{\text{nad}}$, and $\hat{m}^{\text{spl}}$; the per-entry cost scales with the number of sampled time points and sparse matvec operations rather than with the dense matrix exponentials.

Using the same sampled trajectories, we define finite-horizon surrogates for nodal nadir and split as

$$\begin{cases} \hat{m}^{\text{nad}}_{k,o}(\mathbf{g}) \triangleq \max_{t\in\mathcal{T}} \left\| \frac{1}{2\pi}\left(-\mathbf{y}(t)\right) \right\|_\infty, \\ \hat{m}^{\text{spl}}_{k,o}(\mathbf{g}) \triangleq \max_{t\in\mathcal{T}} \left(\max_i \Delta f_i(t) - \min_i \Delta f_i(t)\right). \end{cases} \tag{48}$$

Therefore, the split surrogate in (48) uses the same Hz-domain nodal frequency deviation defined in (41) rather than an absolute frequency offset.

3.2. Robust Location-Aware Allocation Formulation

Over $\mathcal{K} \times \mathcal{O}$, we use a min–max risk to represent a security floor. The min–max formulation treats all candidate disturbance locations in $\mathcal{K}$ as equally weighted, meaning that the resulting allocation hedges the worst-case outcome without requiring prior knowledge of disturbance probabilities.

$$\min_{\mathbf{g}\in\mathcal{G}} \max_{(k,o)\in\mathcal{K}\times\mathcal{O}} \hat{m}_{k,o}(\mathbf{g}) \quad \text{s.t.} \quad \hat{m}^{\text{spl}}_{k,o}(\mathbf{g}) \le \bar{m}^{\text{spl}},\ \forall(k,o) \tag{49}$$

Therefore, Equation (49) seeks the gain vector that minimizes the worst-case normalized risk across all candidate disturbance locations and operating conditions, subject to a hard ceiling on the nodal frequency split; the split constraint prevents the optimizer from trading coherence for aggregate security, which would otherwise allow large inter-node frequency deviations to persist unchecked. A probability-weighted or criticality-weighted extension is direct, but is left for future work in order to keep the present revision focused on the

https://doi.org/10.3390/sym18050759

worst-case formulation. An atlas-ready sequential convex approximation (SCA) template can be specified in epigraph form. At iteration r, solve

$$\begin{aligned} \min_{\Delta\mathbf{g},\,\tau}\ & \tau \\ \text{s.t.}\ & \hat{m}_{k,o}(\mathbf{g}^{(r)}) + \nabla_{\mathbf{g}}\hat{m}_{k,o}^{T}(\mathbf{g}^{(r)})\,\Delta\mathbf{g} \le \tau,\ \forall(k,o), \\ & \hat{m}_{k,o}^{\mathrm{spl}}(\mathbf{g}^{(r)}) + \nabla_{\mathbf{g}}\hat{m}_{k,o}^{\mathrm{spl}T}(\mathbf{g}^{(r)})\,\Delta\mathbf{g} \le \bar{m}^{\mathrm{spl}},\ \forall(k,o), \\ & \mathbf{g}^{(r)} + \Delta\mathbf{g} \in \mathcal{G},\ \ \|\Delta\mathbf{g}\|_{\infty} \le \Delta_g \end{aligned} \tag{50}$$

and update $\mathbf{g}^{(r+1)} = \mathbf{g}^{(r)} + \Delta\mathbf{g}$.

To implement (50) under non-smooth surrogates, we evaluate gradients using the sensitivity of the matrix exponential. For $\mathbf{y}(t) = \mathbf{C}e^{\mathbf{A}(\mathbf{g})t}\mathbf{b}$, the directional derivative satisfies

$$\frac{d}{d\theta}\left(e^{\mathbf{A}t}\right) = \int_0^t e^{\mathbf{A}(t-\tau)}\frac{d\mathbf{A}}{d\theta}e^{\mathbf{A}\tau}\,d\tau. \tag{51}$$

In practice, the integral in (51) is approximated by fixed quadrature rules aligned with $\mathcal{T}_{\mathrm{roc}}$ and cached per atlas entry, and the non-smooth $\|\cdot\|_{\infty}$ and max operators in (47) are replaced by smooth upper envelopes during optimization, e.g., $\|\mathbf{v}\|_{\infty} \approx \kappa^{-1}\log\sum_i \exp(\kappa|\mathbf{v}_i|)$. The original non-smooth metrics are retained for reporting and postprocessing checks. The trust region radius Δ_g is chosen per atlas index to preserve the local validity of the affine parameterization (37) and to keep the system within a pre-validated stability region

$$\alpha(\mathbf{g}) \triangleq \max_i \Re\{\lambda_i(\mathbf{A}_{\mathrm{sys}}(\mathbf{g}))\}, \qquad \alpha(\mathbf{g}) \le -\alpha_{\min}, \qquad \alpha_{\min} > 0, \tag{52}$$

where $\alpha(\mathbf{g})$ is the spectral abscissa of the closed-loop matrix and as such has unit s^{-1}, while $\alpha_{\min}$ is the atlas-recorded minimum decay rate margin. Hence, stability screening means that every accepted gain vector must keep all eigenvalues strictly to the left of $-\alpha_{\min}$. To justify the use of a finite trust region, each atlas entry performs local validation on a representative set of points around $\mathbf{g}_0$ (center, axis points, and selected corners); if either the surrogate mismatch or the stability margin changes too quickly over that set, the stored Δ_g is reduced before the entry is released for scheduling. Smooth-envelope gap. The log-sum-exp envelope satisfies $\|\mathbf{v}\|_{\infty} \le \kappa^{-1}\log\sum_i \exp(\kappa|\mathbf{v}_i|) \le \|\mathbf{v}\|_{\infty} + \kappa^{-1}\log(n_v)$, where n_v is the vector dimension. Therefore, we treat $\delta_{\mathcal{I}}^{x,\mathrm{sm}} \triangleq \kappa^{-1}\log(n_v)$ as an explicit conservativeness margin when the smoothed surrogate is used inside SCA, and absorb it into the bound $\delta_{\mathcal{I}}^{x}$ in (55). Reproducible SCA settings. Unless otherwise specified, we use $\kappa = 10$ for smooth upper envelopes, a maximum of 30 SCA iterations, and stop when both (i) the relative objective improvement is below 10^{-3} over three consecutive iterations and (ii) the maximum surrogate constraint violation in (50) is below 10^{-4}. The trust region Δ_g is initialized from stability screening and reduced by a factor 0.5 whenever the validation error bounds $\epsilon_{\mathcal{I}}^{x}$ increase or when the stability margin $\alpha(\mathbf{g})$ approaches $-\alpha_{\min}$.

4. Disturbance Location-Aware Coordination: Atlas-Based Scheduling Workflow

This section converts the allocation formulation into an implementable workflow based on an atlas—a structured collection of pre-validated frequency-support gain configurations, each associated with a specific operating regime and disturbance-location coverage—and gain scheduling execution. The planning stage performs scenario enumeration, surrogate/sensitivity computation, robust allocation, and rule compression. The execution stage applies the scheduled gains associated with the selected atlas entry (and, when used, its low-dimensional scaling). Related online inertia allocation studies

https://doi.org/10.3390/sym18050759

under nadir constraints further motivate the need for deployment-time parameter updates, although they are typically formulated on aggregated frequency models rather than the heterogeneous nodal channels targeted here [41].

4.1. Atlas Construction and Validation

We adopt a binned index for atlas entries that includes short-circuit ratio (SCR) bins:

$$\mathcal{I} \triangleq (k,\ o,\ \text{SCR-bin},\ \text{IBR-penetration-bin},\ \text{availability-bin}) \tag{53}$$

where k is the disturbance location, o denotes an operating point (steady state and device setpoints), and the remaining bins discretize key grid attributes that can be robustly estimated (e.g., short-circuit ratio and IBR penetration). In the case studies in Section 5, the atlas spans the disturbance location axis (Buses 4, 12, 15, 16, 18, and 27) at a fixed operating point; load level, renewable penetration, topology, and unit commitment are identified as future scenario axes. The availability bin encodes actuation availability and headroom regimes (e.g., a joint bin over $\hat{P}_{\max}$ and $\hat{E}_{\max}$ ranges). Each atlas entry stores the following: the baseline gains $\mathbf{g}_0$, low-dimensional structure $\mathbf{E}$, admissible scaling bounds $[\underline{\mathbf{s}}, \bar{\mathbf{s}}]$ and rate limits, evaluation protocol parameters (filters, RoCoF estimation, horizons), a validated disturbance location set $\mathcal{K}(\mathcal{I}) \subseteq \mathcal{K}$, tightened gain constraints induced by (39) and (40), stability screening thresholds $\alpha_{\min}$ and trust region sizes Δ_g, and validation statistics, including conservative surrogate-error bounds for metric safety and ranking consistency. For auditability, each entry additionally records the decomposition of its safety margins (surrogate mismatch, time-grid discretization, smooth-envelope gaps, and optional extra margins). Let $\mathfrak{A}$ denote the atlas, implemented as a keyed collection over indices $\mathcal{I}$. Each entry $\mathfrak{A}(\mathcal{I})$ stores $(\mathbf{g}_0, \mathbf{E}, [\underline{\mathbf{s}}, \bar{\mathbf{s}}], \mathcal{K}(\mathcal{I}), \Delta_g, \alpha_{\min}, \epsilon^x_{\mathcal{I}}, r_{\mathcal{I}}, \eta_{\mathcal{I}})$. This notation is chosen to avoid confusion with the actuator set $\mathcal{A}$ in Section 3. By construction, $\mathcal{K}(\mathcal{I})$ is the explicit disturbance location coverage set on which the entry has been jointly validated; it may reduce to the singleton $\{k\}$, but is recorded explicitly so that a single deployment entry can certify more than one candidate location only when that joint coverage has been validated offline.

To make atlas generation reproducible, a recommended pipeline is as follows: (1) for each operating point o, solve the steady state and construct the explicit HNFR model $(\mathbf{A}_{\text{sys}}, \mathbf{B}_{\text{sys}}, \mathbf{C}_{\text{hnfr}})$ in Section 2 together with the disturbance input encoding; (2) under the fixed evaluation protocol, compute location sensitivity, surrogates, and (optionally) marginal benefit signals; (3) solve the robust allocation over $\mathcal{K} \times \mathcal{O}$ to obtain $\mathbf{g}_0$ and its feasibility/stability margins; (4) compress $\mathbf{g}_0$ into a structured executable form (e.g., zone sharing or clustering), thereby defining the low-dimensional scaling space; and (5) validate surrogate prediction against time domain simulations of the HNFR model (and, when available, higher-fidelity models), quantify conservative error bounds, and label inapplicable regions where linearization errors are amplified (e.g., ill-conditioned $\mathbf{J}_{LL}$, proximity to PLL instability boundaries, or strong current limiting). In addition to metric errors, we explicitly track the validity of the electromechanical-band approximation (13) within each atlas entry. For the same validation set $\mathcal{V}(\mathcal{I})$ and RoCoF window $[0, T_{\text{roc}}]$, define the normalized residual ratio

$$r_{\mathcal{I}} \triangleq \sup_{(k,o)\in\mathcal{V}(\mathcal{I})} \sup_{t\in[0,T_{\text{roc}}]} \frac{\left\|\boldsymbol{\varepsilon}_{\dot{\delta},L}(t)\right\|_\infty}{\left\|\mathbf{K}_{\text{couple}}\Delta\boldsymbol{\omega}_S(t)\right\|_\infty + \varepsilon_0}, \quad \varepsilon_0 > 0, \tag{54}$$

where $\boldsymbol{\varepsilon}_{\dot{\delta},L}(t)$ is defined in (14) and ε_0 prevents division by zero. Entries with $r_{\mathcal{I}}$ above a user-specified threshold (default 0.2) are labeled as "approximation-weak" and

https://doi.org/10.3390/sym18050759

are assigned a smaller trust region Δ_g together with increased margins $\delta_{\mathcal{I}}^{x}$ in (55) to retain conservativeness.

We compute conservative surrogate error bounds per entry and per metric. For $x \in \{\mathrm{roc}, \mathrm{nad}, \mathrm{spl}\}$, let $\mathcal{V}(\mathcal{I}) \subseteq \mathcal{K}(\mathcal{I}) \times \mathcal{O}$ be the validation scenario subset for index $\mathcal{I}$. Define

$$\epsilon_{\mathcal{I}}^{x} \triangleq \sup_{(k,o)\in\mathcal{V}(\mathcal{I})} \Big(m_{k,o}^{x}(\mathbf{g}_0) - \hat{m}_{k,o}^{x}(\mathbf{g}_0) \Big)_{+} + \delta_{\mathcal{I}}^{x}, \tag{55}$$

where $(\cdot)_{+} \triangleq \max\{\cdot, 0\}$ and $\delta_{\mathcal{I}}^{x} \geq 0$ is a user-chosen margin to cover finite sampling and discretization in $\mathcal{T}_{\mathrm{roc}}$ and $\mathcal{T}$. These bounds support conservative screening by ensuring $m_{k,o}^{x}(\mathbf{g}) \leq \hat{m}_{k,o}^{x}(\mathbf{g}) + \epsilon_{\mathcal{I}}^{x}$ for all $(k, o) \in \mathcal{K}(\mathcal{I}) \times \{o\}$ covered by the recorded validation protocol and for all $\mathbf{g}$ within the stored trust region. Hence, $\epsilon_{\mathcal{I}}^{x}$ is jointly valid over the explicit location set $\mathcal{K}(\mathcal{I})$, not only for the anchor index k appearing in (53). Reproducible margin decomposition. We set $\delta_{\mathcal{I}}^{x} \triangleq \delta_{\mathcal{I}}^{x,\mathrm{grid}} + \delta_{\mathcal{I}}^{x,\mathrm{sm}} + \delta_{\mathcal{I}}^{x,\mathrm{add}}$, where $\delta_{\mathcal{I}}^{x,\mathrm{grid}}$ is the time-grid discretization margin (Section 3), $\delta_{\mathcal{I}}^{x,\mathrm{sm}}$ bounds any smooth-envelope gap used inside SCA (Section 3), and $\delta_{\mathcal{I}}^{x,\mathrm{add}}$ is an optional extra conservativeness margin informed by RMS/DAE validation (e.g., bounded nonlinearities, quantization, or delay). Each component is stored in $\mathfrak{A}(\mathcal{I})$ together with the protocol parameters. To avoid extrapolation beyond validation coverage, the bound $\epsilon_{\mathcal{I}}^{x}$ is enforced only for $\mathbf{g}$ within the atlas-recorded trust region $\|\mathbf{g} - \mathbf{g}_0\|_\infty \leq \Delta_g$. In addition, $\delta_{\mathcal{I}}^{x}$ is selected per entry based on validation statistics to cover (i) sampling-set discretization and (ii) residual model mismatch, e.g., by combining a high-quantile of the observed positive error $(m^x - \hat{m}^x)_{+}$ on $\mathcal{V}(\mathcal{I})$ with an extra margin that accounts for the time grid resolution of $\mathcal{T}_{\mathrm{roc}}$ and $\mathcal{T}$. To make explicit this extension from $\mathbf{g}_0$ to the full trust region, $\delta_{\mathcal{I}}^{x,\mathrm{add}}$ is chosen so as to dominate the observed local drift of the positive surrogate error on a representative validation set $\mathcal{N}(\mathcal{I}) \subset \{\mathbf{g} : \|\mathbf{g} - \mathbf{g}_0\|_\infty \leq \Delta_g\}$, i.e.,

$$\delta_{\mathcal{I}}^{x,\mathrm{add}} \geq \sup_{\mathbf{g}\in\mathcal{N}(\mathcal{I})} \big[(m^x(\mathbf{g}) - \hat{m}^x(\mathbf{g}))_{+} - (m^x(\mathbf{g}_0) - \hat{m}^x(\mathbf{g}_0))_{+} \big]_{+}, \tag{56}$$

such that the stored bound remains locally conservative throughout the validated neighborhood. If this drift term is not small, then the entry is re-validated with a smaller Δ_g and/or a larger $\delta_{\mathcal{I}}^{x,\mathrm{add}}$. Atlas parameters for deployment tightening. For each entry, we also record an estimated headroom-estimation relative error bound $\varepsilon_{\mathcal{I}}^{P}, \varepsilon_{\mathcal{I}}^{E} \in [0, 1)$ (from measurement/estimation validation) and an entry-hit confidence $p_{\mathcal{I}}^{\mathrm{hit}} \in [0, 1]$. The latter is defined as a conservative lower confidence bound on the probability that the online localization/bin-classification rule selects an atlas entry with an offline validation set matching the true regime. A conservative default tightening factor for use in deployment can be set as

$$\eta_{\mathcal{I}} \triangleq \Big(1 - \max\{\varepsilon_{\mathcal{I}}^{P}, \varepsilon_{\mathcal{I}}^{E}\}\Big) \cdot p_{\mathcal{I}}^{\mathrm{hit}}, \tag{57}$$

which can be further reduced when the entry is labeled "approximation-weak" (large $r_{\mathcal{I}}$) or when the surrogate error bounds $\epsilon_{\mathcal{I}}^{x}$ are large. Therefore, lower confidence, larger headroom uncertainty, or weaker local validation all decrease $\eta_{\mathcal{I}}$ monotonically and can only shrink the admissible set. Interpretation of $\eta_{\mathcal{I}}$: $\eta_{\mathcal{I}}$ is used to tighten the admissible set $\mathcal{G}(\hat{\boldsymbol{\rho}})$ by shrinking $(\hat{P}_{\max}, \hat{E}_{\max}) \mapsto (\eta\hat{P}_{\max}, \eta\hat{E}_{\max})$ in (39) and (40); hence, decreasing η is monotone-conservative with respect to feasibility under headroom uncertainty.

The full offline procedure is summarized in Algorithm 1.

https://doi.org/10.3390/sym18050759

Algorithm 1: Atlas Construction and Validation

Input : Contingency set $\mathcal{K}$; operating set $\mathcal{O}$; bin definitions; fixed evaluation protocol; actuator models/constraints.

Output: Atlas $\mathfrak{A}$; each index $\mathcal{I}$ stores $(\mathbf{g}_0, \mathbf{E}, [\underline{\mathbf{s}}, \overline{\mathbf{s}}], \mathcal{K}(\mathcal{I}), \Delta_g, \alpha_{\min}, \epsilon^x_{\mathcal{I}}, r_{\mathcal{I}}, \eta_{\mathcal{I}})$.

```
foreach o ∈ O do
    Solve steady state and build (A_sys, B_dist, C_hnfr)
    foreach k ∈ K do
        Encode u_0(k, ΔP) and compute m̂^x_{k,o}(·) under the fixed protocol
    end
end
Solve (49) (e.g., SCA (50)) to obtain g_0 and α(g_0)
Compress g_0 into E and set [s_, s̄] with rate limits
foreach atlas index I do
    Validate on V(I) (time-domain simulation) and compute ε^x_I via (55)
    Compute r_I and the validity label via (54); set Δ_g and η_I via (57)
    Store A(I) and mark inapplicable regions for exclusion/re-selection
end
```

4.2. Execution of Atlas-Based Scheduling

In execution, a set of scheduled gains is selected from the atlas and applied to the designated frequency support actuators. The same fixed measurement and evaluation protocol used in atlas construction is used to compute RoCoF/nadir/split metrics for reporting in Section 5. At each online update, the scheduler receives the current operating condition estimate $\hat{\boldsymbol{\rho}}$ and available headroom estimates. When a real-time localization module is available, it can additionally supply a disturbance location candidate set $\hat{\mathcal{K}}$ with confidence scores and, when the event size is not known exactly, a disturbance magnitude estimate or interval $[\underline{\Delta P}, \overline{\Delta P}]$; these inputs are treated as optional refinements that tighten the atlas selection rather than as prerequisites. In the baseline mode without online localization, $\hat{\mathcal{K}}$ defaults to the full training set $\mathcal{K}$ of the matched atlas entry, meaning that the stored gains remain robust against all covered disturbance locations. Here, the logic is two-stage: $\hat{\mathcal{K}}$ lives in the disturbance location space, while the candidate atlas entry set is obtained by lifting each $k \in \hat{\mathcal{K}}$ to all atlas indices $\mathcal{I} = (k, o, \text{SCR-bin}, \text{IBR-penetration-bin}, \text{availability-bin})$ consistent with the observed bins and $\hat{\boldsymbol{\rho}}$. Denoting this lifted set by $\hat{\mathfrak{I}}$, the scheduler retains only entries for which the lower bound of the hit confidence satisfies $p^{\text{hit}}_{\mathcal{I}} \geq p_{\min}$, the stored location coverage satisfies $\hat{\mathcal{K}} \subseteq \mathcal{K}(\mathcal{I})$, and the validated disturbance magnitude range contains the online estimate (or supports the corresponding conservative endpoint envelope), where $p_{\min} \in (0, 1)$ is a user-chosen acceptance threshold. Disturbance magnitude uncertainty does not create a separate entry index; instead, for every retained $\mathcal{I}$, the online verification is interpreted conservatively over the validated magnitude range associated with that entry, which is implemented by checking the relevant endpoint(s) when no monotonicity certificate is available. If several entries remain, the scheduler verifies them conservatively over the full recorded location set $\mathcal{K}(\mathcal{I})$ together with the retained disturbance magnitude range, then accepts a single deployment entry $\mathcal{I}^\star \in \hat{\mathfrak{I}}$ with the smallest predicted worst-case normalized risk over $\mathcal{K}(\mathcal{I})$. For the accepted entry $\mathcal{I}^\star$, the online adjustment is restricted to the low-dimensional scaling $\mathbf{s}$ in (36). A lightweight execution problem is

https://doi.org/10.3390/sym18050759

$$
\begin{aligned}
\min_{\mathbf{s},\tau}\ & \tau \\
\text{s.t.}\ & \frac{\hat{m}^{\mathrm{roc}}_{k,o}(\mathbf{g}(\mathbf{s})) + \epsilon^{\mathrm{roc}}_{\mathcal{I}^\star}}{\bar{m}^{\mathrm{roc}}} \le \tau,\ \forall k \in \mathcal{K}(\mathcal{I}^\star), \\
& \frac{\hat{m}^{\mathrm{nad}}_{k,o}(\mathbf{g}(\mathbf{s})) + \epsilon^{\mathrm{nad}}_{\mathcal{I}^\star}}{\bar{m}^{\mathrm{nad}}} \le \tau,\ \forall k \in \mathcal{K}(\mathcal{I}^\star), \\
& \frac{\hat{m}^{\mathrm{spl}}_{k,o}(\mathbf{g}(\mathbf{s})) + \epsilon^{\mathrm{spl}}_{\mathcal{I}^\star}}{\bar{m}^{\mathrm{spl}}} \le \tau,\ \forall k \in \mathcal{K}(\mathcal{I}^\star), \qquad \tau \le 1, \\
& \mathbf{g}(\mathbf{s}) \in \mathcal{G}_{\eta_{\mathcal{I}^\star}}(\hat{\boldsymbol{\rho}}),\ \mathbf{s} \in [\underline{\mathbf{s}}_{\mathcal{I}^\star}, \overline{\mathbf{s}}_{\mathcal{I}^\star}],\ \|\mathbf{g}(\mathbf{s}) - \mathbf{g}_{0,\mathcal{I}^\star}\|_\infty \le \Delta_{g,\mathcal{I}^\star}, \\
& \alpha(\mathbf{g}(\mathbf{s})) \le -\alpha_{\min,\mathcal{I}^\star},
\end{aligned}
\tag{58}
$$

where $\mathcal{G}_{\eta_{\mathcal{I}^\star}}(\hat{\boldsymbol{\rho}})$ denotes the admissible set obtained from (39) and (40) after shrinking the headroom bounds by $\eta_{\mathcal{I}^\star}$ and the remaining per-entry quantities in (58) are taken from $\mathfrak{A}(\mathcal{I}^\star)$. In particular, the accepted entry carries an explicit validated location set $\mathcal{K}(\mathcal{I}^\star)$, and the use of $\epsilon^{x}_{\mathcal{I}^\star}$ in (58) is justified jointly over that set rather than only at the anchor location embedded in the index. Because $\dim(\mathbf{s}) \ll n_g$, (58) is intended as a low-dimensional lookup-and-verify step rather than as a full re-optimization of Section 3. When ΔP is uncertain, the same admissibility, metric, and stability checks are interpreted against the validated disturbance magnitude range attached to $\mathcal{I}^\star$, using endpoint evaluation unless a tighter monotonicity certificate has been recorded offline. After the candidate-set envelope check has selected $\mathcal{I}^\star$, the acceptance sequence is intentionally strict: (1) check bin consistency, $p^{\mathrm{hit}}_{\mathcal{I}^\star}$, and the coverage condition $\hat{\mathcal{K}} \subseteq \mathcal{K}(\mathcal{I}^\star)$; (2) confirm that the online disturbance magnitude estimate lies inside the validated range of $\mathcal{I}^\star$ (or else use its conservative endpoint envelope); (3) solve or clip $\mathbf{s}$ inside $[\underline{\mathbf{s}}_{\mathcal{I}^\star}, \overline{\mathbf{s}}_{\mathcal{I}^\star}]$; (4) verify the trust region condition $\|\mathbf{g} - \mathbf{g}_{0,\mathcal{I}^\star}\|_\infty \le \Delta_{g,\mathcal{I}^\star}$; (5) verify the metric bounds through $\hat{m}^x + \epsilon^x_{\mathcal{I}^\star}$ over all $k \in \mathcal{K}(\mathcal{I}^\star)$; and (6) verify stability through (52). If any step fails, the scheduler first retries with a smaller η or a more conservative candidate entry. If feasibility or stability is still not recovered or if all candidate entries have low confidence, the policy falls back to a location-agnostic pre-certified safe gain vector $\mathbf{g}^{\mathrm{glob}}_{\mathrm{safe}}(o, \mathrm{bins})$ stored offline with the atlas (or a companion safe table) and validated against all $k \in \mathcal{K}$ under the same protocol and over the same disturbance magnitude range. This fallback closes the online loop when localization is uncertain and prevents trust region claims from being used outside their validated domain.

An important practical consequence of the min–max formulation in (49) is that the online stage does not require explicit real-time identification of the disturbance bus. Because each atlas entry is optimized over the full candidate location set $\mathcal{K}(\mathcal{I})$, the stored gain vector is already robust to any disturbance within that set for the indexed operating condition. Therefore, online execution selects the atlas entry by matching only the prevailing operating condition key. If real-time disturbance localization becomes available, it can serve as an optional refinement to narrow the conservativeness of the min–max hedge rather than as a prerequisite.

Regarding computational cost, the HNFR assembly scales as $O(n_S^3 + n_L^3)$ for the network elimination step, which is dominated by the sparse solver with $\mathbf{J}_{LL}$. Although atlas construction involves repeated matrix-exponential evaluations, the per-entry cost remains tractable because the affine gain parameterization and low-dimensional scaling structure limit the number of required trajectory re-evaluations. For the IEEE 39-bus system, the full offline atlas construction completes within one minute on a standard workstation; by comparison, the online lookup and gain projection are instantaneous, requiring only a key-matching step and a bounded scaling operation. Communication requirements are limited to dispatching a small number of scalar gain setpoints to the GFM support buses at

https://doi.org/10.3390/sym18050759

each dispatch update, which is compatible with existing supervisory control infrastructure operating on 5–15 min refresh cycles.

5. Case Studies

This section validates the framework developed in Sections 2–4 through three coordinated case studies: sensitivity to disturbance location, comparative coordination performance, and atlas-based online scheduling.

5.1. Test System

All studies are carried out on the modified IEEE 39-bus system shown in Figure 3. Relative to the benchmark network, three wind farms (WF1–WF3) are placed at Buses 10, 23, and 29 as GFL converter stations with PLL-based synchronization, with four tunable GFM-support buses (31, 33, 35, and 37) serving as the decision-variable locations for the (H_i, D_i) allocation. In Figure 3, circles labeled WF1–WF3 denote the wind-farm GFL stations, GFM-icon buses 31, 33, 35, and 37 denote the tunable grid-forming support locations, red arrows denote the candidate disturbance buses (4, 12, 15, 16, 18, and 27), and solid black lines denote transmission corridors. The network is further partitioned into three areas following the conventional New England boundary, as indicated by the dashed zones in Figure 3. This partitioning groups the ten support buses (30–39) by electrical proximity, and is used later in the area-wise comparison in Section 5 to interpret how the optimized allocations redistribute inertia and damping across the system. The comparative studies then reuse the same three parameter files, namely, the Original setting, the HNFR-optimized setting, and the COI-optimized setting, meaning that the reported differences reflect coordination logic rather than inconsistent data preparation.

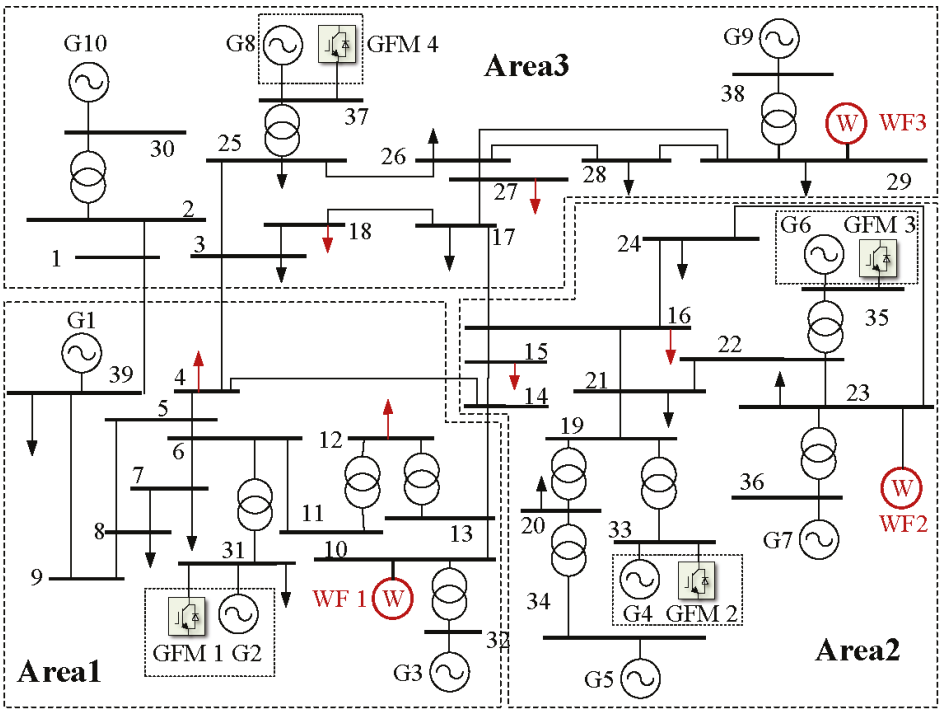


Figure 3. Structure of the modified IEEE 39-bus system.

Two disturbance families are used. First, all waveform comparisons are locked to a single prescribed event, namely, a 250 MW active power increase at load Bus 4 injected at $t = 2.0$ s. Second, the location sensitivity and atlas-audit studies sweep the disturbance location over Buses 4, 12, 15, 16, 18, and 27 under the same disturbance magnitude. In every case, the compared methods share the same support portfolio, the same 0.005 s

simulation grid, and the same RoCoF/nadir/split definitions, providing a common basis for interpreting nodal and aggregated responses.

Table 1 fixes the common protocol used by all case study comparisons in this section. Table 2 then reports the three GFM-side parameter configurations used throughout the case studies, namely, the Original setting taken from the baseline model, the HNFR-optimized setting obtained from the proposed location-aware tuning, and the COI-optimized setting obtained from the aggregated-frequency benchmark. Consistent with Section 3, the listed H/D values are effective coefficients mapped from the writable GFM frequency support setpoints in (32) and (33). Therefore, the differences among the three columns represent different closed-loop support allocations across Buses 31, 33, 35, and 37 rather than changes to all internal converter-control parameters in the Section 2 device model.

Table 1. Compact case study protocol.

Item	Setting
Network	Modified IEEE 39-bus test system; wind farms WF1/WF2/WF3 at Buses 10, 23, and 29; tunable support buses at 31, 33, 35, and 37.
Fixed waveform case	Bus 4, 250 MW step at $t = 2.0$ s on a 0.005 s simulation grid; used for waveform and budget-matched comparisons.
Location sweep	Disturbance buses 4, 12, 15, 16, 18, and 27 under the same disturbance magnitude.

Table 2. GFM-side H/D settings.

Bus	Original		HNFR		COI	
	H	D	H	D	H	D
31	4.329	2.800	5.115	5.366	3.463	2.926
33	3.575	6.500	3.719	2.600	5.248	9.750
35	4.350	7.600	3.877	18.079	6.525	11.400
37	3.471	3.400	7.732	1.360	5.207	2.720

5.2. Disturbance Location Sensitivity and Heterogeneous Nodal Responses

The six disturbance buses (4, 12, 15, 16, 18, and 27) used in this subsection constitute the candidate location set $\mathcal{K}$ over which the atlas in Section 4 is constructed. Therefore, the following waveform and metric comparisons simultaneously serve as cross-scenario evidence and atlas training set diagnostics.

The first study characterizes how disturbance location reshapes heterogeneous nodal frequency behavior under a common disturbance magnitude and common support portfolio. A fixed Bus 4 event is used for waveform inspection, then the disturbance location is swept over six buses for metric comparison. The resulting evidence quantifies whether worst-node RoCoF, nadir, and nodal split are governed primarily by a system-average response or by spatially localized stress patterns that require explicit disturbance location modeling.

The trajectory comparison in Figure 4 shows that the early transient was much more pronounced at the stressed GFM-side Bus 31 than at the remote synchronous-machine Bus 38. Figure 4a shows that at Bus 31, the Original, HNFR, and COI responses separated clearly during the first few seconds after the event; the inset confirms that the largest inter-method deviation was concentrated in the early post-disturbance window rather than in the late quasi-steady segment. Figure 4b shows that the Bus 38 traces remained comparatively smooth and stayed closer to the COI reference. This two-panel comparison identifies a localized transient burden that is only weakly reflected by the aggregated COI trajectory.

https://doi.org/10.3390/sym18050759

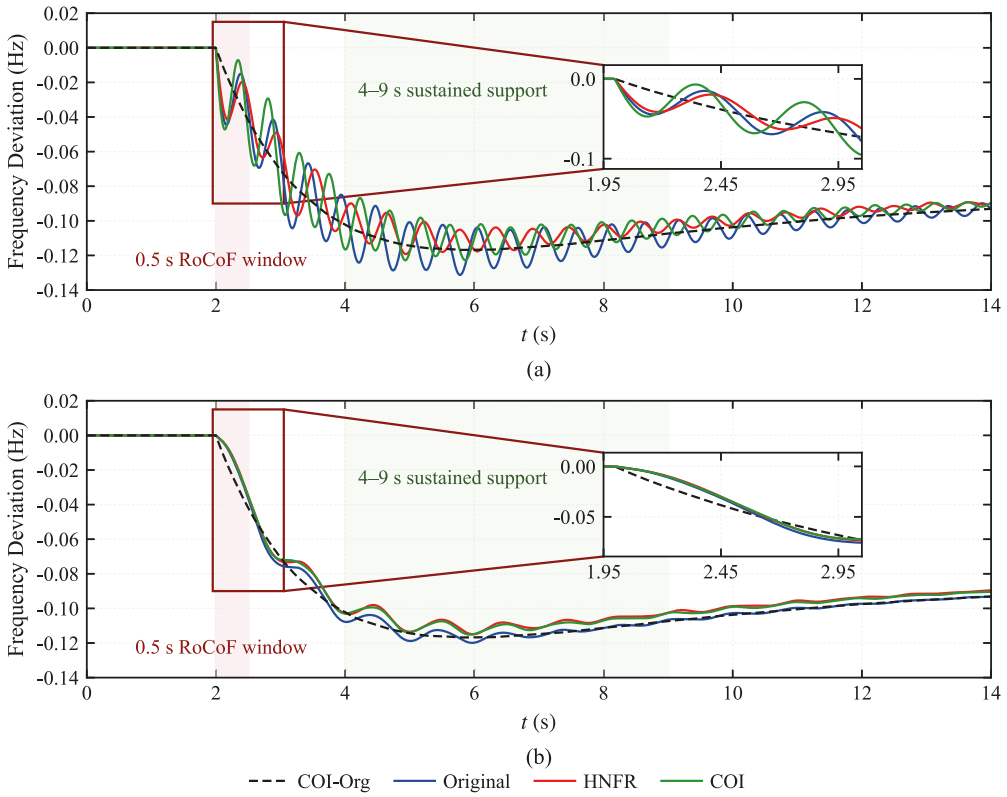


Figure 4. (**a**) Representative trajectories at the stressed GFM-side Bus 31 under the fixed Bus 4, 250 MW disturbance; (**b**) representative trajectories at the remote SG Bus 38 under the same disturbance.

Figure 5 compares the Original, HNFR, and COI parameter sets over the same six-bus disturbance sweep under a unified simulation chain. Figure 5a shows that the worst-node RoCoF burden remained strongly location dependent and was not minimized by the same method at every disturbance bus: the most adverse RoCoF occurred at Bus 16 for the Original and HNFR settings, but shifted to Bus 12 for the COI setting. Figure 5b,c shows an even clearer concentration pattern. For all three parameter sets, Bus 12 produced both the deepest worst-node nadir and the largest maximum nodal frequency split; thus, the dominant stress concentration remained tied to a specific disturbance location instead of being distributed uniformly over the network.

Across the three curves, the HNFR setting consistently reduces the most restrictive nadir and split outcomes relative to the COI tuning, limiting the minimum nadir to 49.8800 Hz and the maximum split to 0.0440 Hz, whereas the corresponding COI results are 49.8749 Hz and 0.0473 Hz. The advantage of RoCoF remains more scenario-dependent, but the overall ranking in Figure 5 shows a smaller nodal risk envelope under the location-aware heterogeneous formulation than under the aggregated tuning objective.

The location-dependent patterns in Figure 5 can be traced analytically to the initial RoCoF relation in (27): for a unit disturbance at bus k, the initial RoCoF at each observation node is determined by $[\mathbf{C}_{\text{hnfr}}\mathbf{B}_{\text{sys}}]_{i,k}$, which encodes the electrical coupling between the disturbance bus and each observation bus through the network admittance and effective inertia distribution. Within the test system, the dominant factor is the electrical distance to the nearest GFM-support unit: Buses 4 and 12 produce the most severe worst-node responses because they are electrically remote from the support cluster at Buses 33, 35, and 37 and are primarily served by Bus 31 alone.

https://doi.org/10.3390/sym18050759

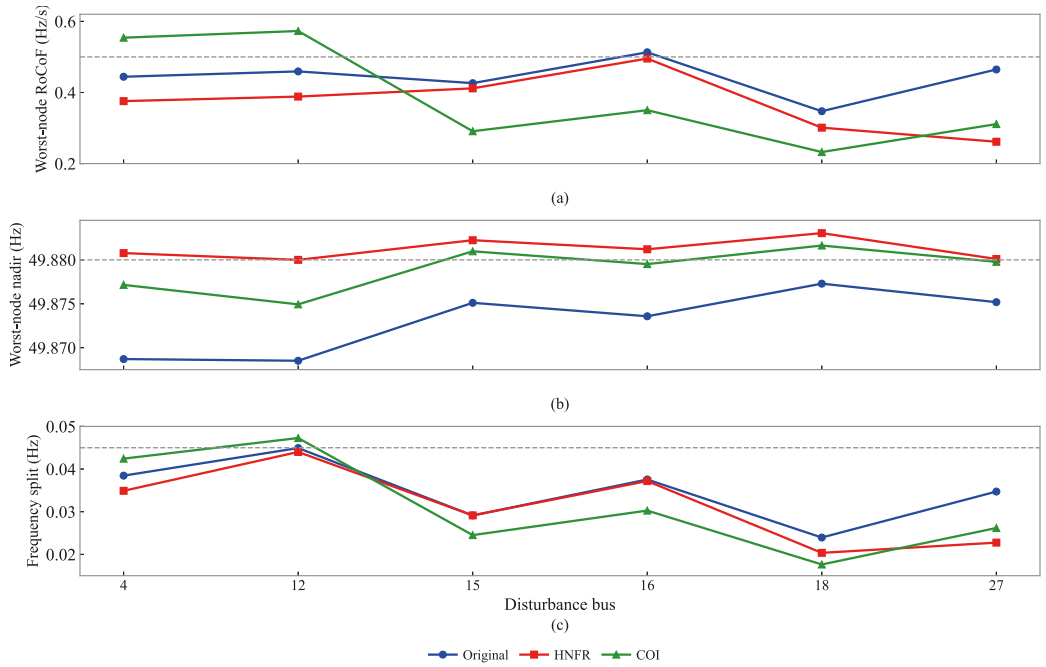


Figure 5. (**a**) Location sweep of worst-node RoCoF over the six candidate disturbance buses, (**b**) location sweep of worst-node nadir over the same disturbance set, and (**c**) location sweep of the maximum nodal frequency split. The horizontal dashed lines indicate the corresponding design/security thresholds used as references for comparison across the three parameter settings.

For practical context, the observed worst-node RoCoF values across all six disturbance locations remain below 0.56 Hz/s, and the worst-node nadir deviation remains within 0.13 Hz of nominal. These values are well within standard RoCoF relay thresholds (typically 0.5–1.0 Hz/s) and first-stage under-frequency load shedding levels (typically 49.0–49.2 Hz). The security constraints used in the min–max allocation are design-level specifications set tighter than the protection thresholds, meaning that the inter-method gap between HNFR and COI in Figure 5 reflects differences in margin utilization rather than proximity to system protection limits.

5.3. Comparative Performance of Location-Aware Coordination

The second study compares the Original, HNFR, and COI parameter settings under the same fixed disturbance, simulation grid, and response-processing pipeline. The comparison is carried out under a matched total GFM support budget, meaning that differences among the three methods are attributable to allocation strategy rather than support quantity. Waveform traces at the dominant stressed buses and event-level security metrics are evaluated jointly under the same event.

Under the budget-matched comparison in Figure 6, the dominant nodal stress remained concentrated around Bus 31, whereas the aggregated COI trajectory changed much less across methods. Figure 6a shows that the COI-tuned case preserved the system-average response but left a deeper dip at the stressed node and a larger separation between the local and aggregated trajectories. Figure 6b shows that the HNFR-tuned case reduced the depth of the stressed-node excursion and tightened the separation between the nodal and COI traces while maintaining a comparable aggregate response. Therefore, under the same total support budget, the HNFR setting corresponds to a stronger redistribution of support toward the electrically stressed location and a smaller local security burden than the COI-oriented allocation.

https://doi.org/10.3390/sym18050759

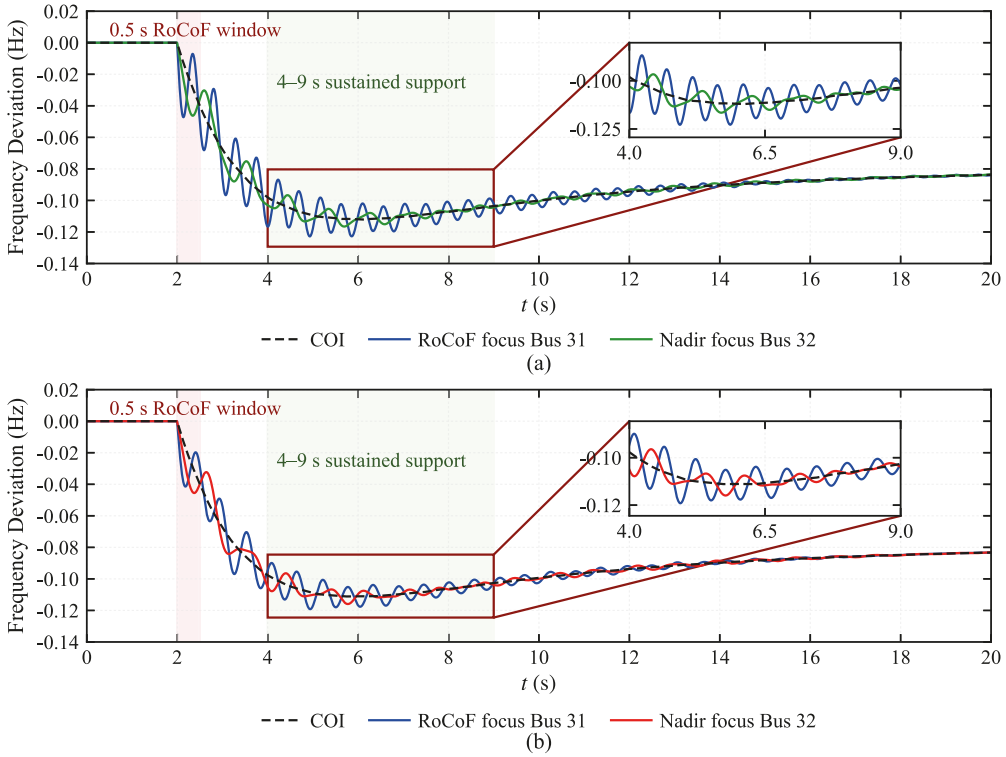


Figure 6. (**a**) Budget-matched COI response under the fixed Bus 4, 250 MW disturbance and (**b**) budget-matched HNFR response under the same disturbance.

Table 3 quantifies the fixed-disturbance comparison among the three parameter sets. Relative to the Original setting, HNFR reduced the worst-node RoCoF by 15.43%, improved the worst-node nadir by 0.0121 Hz, and reduced the maximum frequency split by 9.25%. Relative to the COI setting, HNFR further reduced the worst-node RoCoF by 32.20%, improved the worst-node nadir by 0.0036 Hz, and reduced the maximum split by 17.78%, while the COI nadir changed only marginally. The largest performance separation appears in the nodal-security metrics, whereas the aggregated COI nadir remains comparatively close across the tuned cases.

Table 3. Comparison of the three parameter sets under the fixed Bus 4 250 MW disturbance.

Method	Worst-Node RoCoF (Hz/s)	Worst-Node Nadir (Hz)	Max Frequency Split (Hz)	COI Nadir (Hz)
Original	0.4442	49.8687	0.0385	49.8832
HNFR	0.3757	49.8808	0.0349	49.8888
COI	0.5541	49.8771	0.0424	49.8879

Figure 7 shows how the three parameter sets redistribute effective inertia and droop across the three areas. The inertia bars indicate that the HNFR and COI solutions allocate inertia differently from the Original setting and from each other, with the HNFR solution shifting more effective support toward the electrically stressed area rather than preserving the baseline distribution. The damping bars show the same non-uniform trend for the droop, where the HNFR-tuned configuration concentrates damping support more selectively than the COI benchmark. These area-wise allocation changes are consistent with the smaller stressed-node excursions observed in Figures 4 and 6, and show that the HNFR improvement is achieved through spatial reallocation rather than through uniform increase of all GFM support parameters.

https://doi.org/10.3390/sym18050759

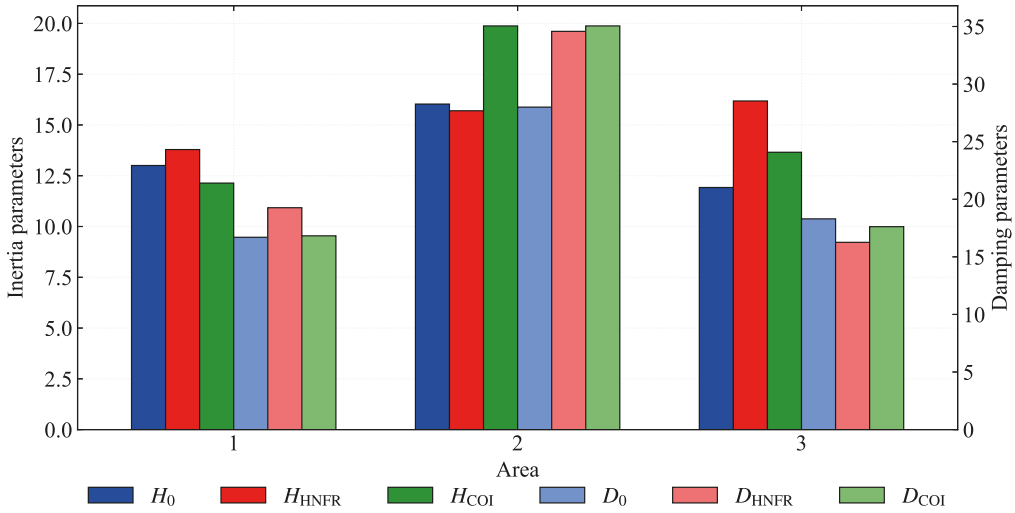


Figure 7. Area-wise comparison of effective inertia and droop allocation under the Original, HNFR, and COI parameter settings.

Across the broader set of representative scenarios in Figure 8, the aggregated COI trajectories remain relatively close, but the nodal trajectories separate more visibly during the initial dip and in the recovery-stage inset. Therefore, the same pattern observed for the fixed Bus 4 disturbance is retained across multiple disturbance locations; inter-method differences remain modest in the aggregate trajectory, and become more pronounced in the stressed nodal responses.

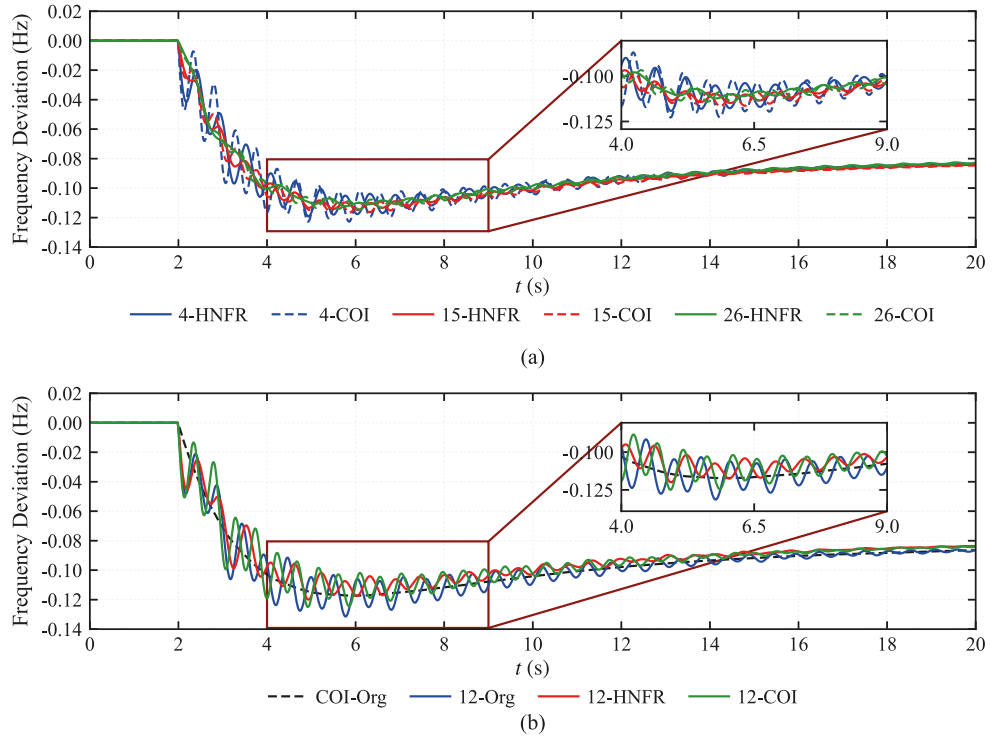


Figure 8. (**a**) Representative nodal frequency response comparison across selected disturbance scenarios and (**b**) close-up comparison of the Original, HNFR, and COI responses under the most severe representative scenario.

The nadir-oriented cross-scenario comparison in Figure 9 extends the comparison from a single event to the full six-bus disturbance set, focusing on the most restrictive

frequency deviation outcome in each scenario. In Figure 9, the red dashed line denotes the design-level frequency-deviation threshold used as a security reference, and the paired bars at each disturbance location correspond to the HNFR and COI settings, respectively. Across all reported locations, the HNFR setting yielded smaller worst-node deviations than the COI setting, with the most severe case occurring at Bus 12 and being limited to 0.119989 Hz under HNFR versus 0.124978 Hz under COI. Therefore, the nadir ordering remains unchanged when the disturbance location is swept systematically.

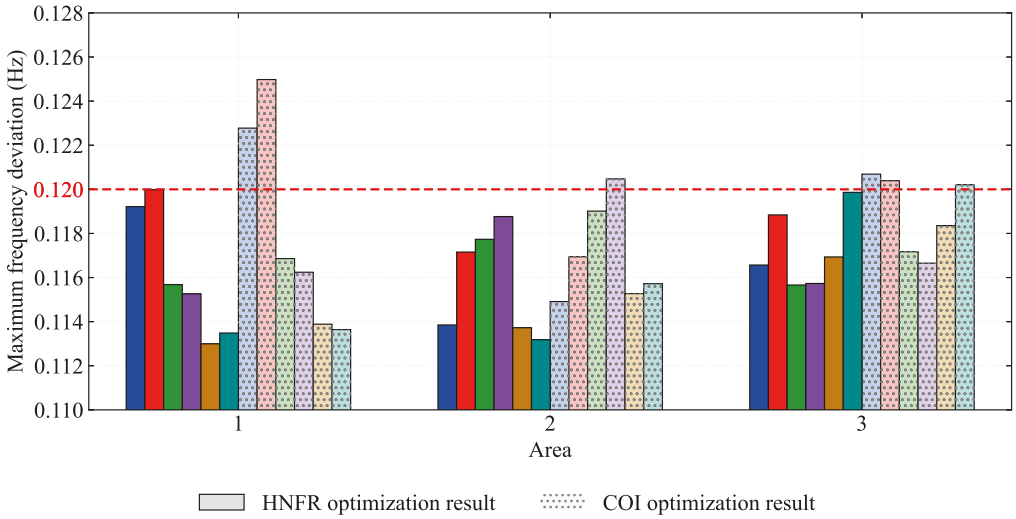


Figure 9. Cross-scenario comparison of maximum frequency deviations under the HNFR and COI parameter settings.

The RoCoF-oriented evidence in Figure 10 complements the nadir comparison by examining the fastest local transient over the same six disturbance locations. In Figure 10, the red dashed line denotes the design-level RoCoF threshold used as a security reference, and the paired bars at each disturbance location correspond to the HNFR and COI settings, respectively. Figure 10 shows that the RoCoF ranking is more scenario-dependent than the nadir ranking: HNFR reduces the worst-node RoCoF at Buses 4 and 12, whereas the COI setting remains slightly better at several other disturbance locations. For both methods, the spread across the curves remains strongly location-dependent. Among the cross-scenario results, the most consistent HNFR advantage appears in nadir and split, while the RoCoF benefit depends more strongly on the disturbance location and the spatial distribution of transient stress.

To assess the sensitivity of the scheduled gains to parameter uncertainty, the HNFR-optimized (H, D) vector was perturbed by independent uniform random factors drawn from $[0.85, 1.15]$ across all four GFM buses, then the worst-node metrics were re-evaluated over the same six disturbance locations for 20 random samples. The 95th-percentile worst-node nadir deviation remained within 1.6% of the baseline value and the 95th-percentile maximum split variation remained within 1.9%, indicating that the allocation is not sensitive to moderate gain uncertainty in the reported operating regime.

Taken together, the case studies show strong dependence on disturbance location, clear separation among heterogeneous nodal frequency channels, and systematic benefits from worst-node-oriented coordination in low-inertia systems. Aggregated COI behavior alone does not reveal the most restrictive transient risk, whereas the HNFR-based formulation provides stronger stressed-node security than the Original and COI parameter settings across the reported waveform and metric comparisons.

https://doi.org/10.3390/sym18050759

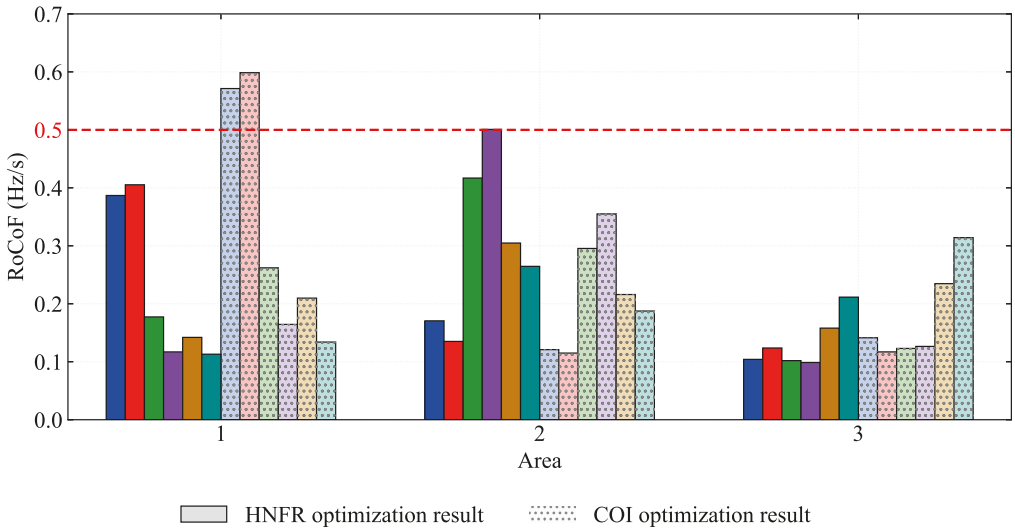


Figure 10. Cross-scenario comparison of worst-node RoCoF under the HNFR and COI parameter settings.

6. Discussion

This paper develops a disturbance location-aware frequency support framework for low-inertia systems with heterogeneous frequency channels. The proposed HNFR model preserves the distinction among SG/GFM electromechanical frequencies and GFL PLL-estimated frequencies, enabling reproducible evaluation of worst-node RoCoF, nadir, and nodal frequency split under location-specific disturbances. The main implication of the reported results is that frequency security in low-inertia systems with heterogeneous converter channels is governed by nodal stress concentration rather than by a single aggregate indicator. Across the waveform comparisons, disturbance location sweep, and budget-matched tuning study, the most restrictive transient burden remains concentrated at a small set of buses and is not represented faithfully by the COI trajectory alone. By preserving the separation among SG electromechanical frequencies, GFM-controlled responses, and GFL PLL-estimated frequencies, the HNFR formulation resolves the nodal stress patterns that determine whether support allocation is protective at those buses that experience the most severe transients.

The case studies also delimit the present engineering scope of the method. The HNFR setting improves stressed-node nadir and reduces nodal split more consistently than the competing settings, whereas the RoCoF comparison remains scenario-dependent, indicating that different transient objectives continue to impose competing design pressures. Extending the method toward faster online scheduling would require further progress in model refinement, uncertainty handling, and implementation-level acceleration.

The HNFR model is derived under the quasi-stationary voltage assumption and electromechanical-scale linearization around a given operating point. These assumptions exclude large-signal voltage dynamics, converter current-limiting behavior, and nonlinear saturation effects that may become significant under severe disturbances. Within the moderate disturbance range used in the case studies (250 MW active-power step), the reported results remain internally consistent across the presented scenarios; broader validation against EMT-class or large-disturbance simulation is identified as future work.

Regarding parameter sensitivity, the min–max formulation provides an inherent hedge against worst-case disturbance locations within the candidate set. A full Monte Carlo sensitivity study covering parameter uncertainty, measurement noise, and communication delay is identified as future work. Extending the atlas to span additional scenario axes such as

https://doi.org/10.3390/sym18050759

load level, renewable energy penetration, and network topology would further strengthen the robustness characterization, and is a natural next step for larger-scale deployments.

Author Contributions: Conceptualization, L.G., S.W., M.L. and F.Y.; methodology, L.G., S.W., M.L. and F.Y.; software, L.G., S.W., M.L. and F.Y.; validation, L.G., S.W., M.L. and F.Y.; formal analysis, F.Y. and S.W.; investigation, F.Y. and S.W.; resources, M.L. and S.W.; data curation, L.G., S.W., M.L. and F.Y.; writing—original draft, L.G., S.W., M.L. and F.Y.; writing—review and editing, L.G., S.W., M.L. and F.Y. All authors have read and agreed to the published version of the manuscript.

Funding: This research was funded by State Grid Science & Technology Project in China, grant number 4000-202316071A-1-1-ZN.

Data Availability Statement: The data supporting the reported results are contained within the article and the generated case study assets included in this project.

Conflicts of Interest: The authors declare that this study received funding from the State Grid Science & Technology Project in China. The funders had no role in the design of the study; in the collection, analyses, or interpretation of data; in the writing of the manuscript; or in the decision to publish the results.

References

1. Gu, Y.; Green, T.C. Power System Stability with a High Penetration of Inverter-Based Resources. *Proc. IEEE* **2023**, *111*, 832–853. [CrossRef]
2. Yan, K.; Li, G.; Zhang, R.; Xu, Y.; Jiang, T.; Li, X. Frequency Control and Optimal Operation of Low-Inertia Power Systems with HVDC and Renewable Energy: A Review. *IEEE Trans. Power Syst.* **2024**, *39*, 4279–4295. [CrossRef]
3. Al Kez, D.; Foley, A.M.; Ahmed, F.; Morrow, D.J. Overview of frequency control techniques in power systems with high inverter-based resources: Challenges and mitigation measures. *IET Smart Grid* **2023**, *6*, 447–469. [CrossRef]
4. Khan, M.; Wu, W.; Li, L. Grid-forming control for inverter-based resources in power systems: A review on its operation, system stability, and prospective. *IET Renew. Power Gener.* **2024**, *18*, 887–907. [CrossRef]
5. Sajadi, A.; Rañola, J.A.; Kenyon, R.W.; Hodge, B.M.; Mather, B. Dynamics and Stability of Power Systems with High Shares of Grid-Following Inverter-Based Resources: A Tutorial. *IEEE Access* **2023**, *11*, 29591–29613. [CrossRef]
6. Tan, B.; Zhao, J.; Netto, M.; Krishnan, V.; Terzija, V.; Zhang, Y. Power system inertia estimation: Review of methods and the impacts of converter-interfaced generations. *Int. J. Electr. Power Energy Syst.* **2022**, *134*, 107362. [CrossRef]
7. Chen, X.; Jiang, Y.; Terzija, V.; Lu, C. Review on measurement-based frequency dynamics monitoring and analyzing in renewable energy dominated power systems. *Int. J. Electr. Power Energy Syst.* **2024**, *155*, 109520. [CrossRef]
8. Deng, X.; Mo, R.; Wang, P.; Chen, J.; Nan, D.; Liu, M. Review of RoCoF Estimation Techniques for Low-Inertia Power Systems. *Energies* **2023**, *16*, 3708. [CrossRef]
9. Yin, H.; Wu, Y.; Qiu, W.; Zeng, C.; You, S.; Tan, J.; Hoke, A.; Kruse, C.J.; Rockwell, B.W.; Kawamura, K.A.; et al. Precise ROCOF estimation algorithm for low inertia power grids. *Electr. Power Syst. Res.* **2022**, *209*, 107968. [CrossRef]
10. Azizi, S.; Sun, M.; Liu, G.; Terzija, V. Local Frequency-Based Estimation of the Rate of Change of Frequency of the Center of Inertia. *IEEE Trans. Power Syst.* **2020**, *35*, 4948–4951. [CrossRef]
11. Wang, T.; Ma, S.; Wang, S.; Hou, W.; Gao, J.; Guo, J.; Zhou, X. Modal Analysis-Based Analytical Method for Frequency Estimation During Inertia Response Stage of Power Systems. *IEEE J. Emerg. Sel. Top. Circuits Syst.* **2023**, *13*, 692–701. [CrossRef]
12. Wang, L.; Ren, J.; Huang, G.; Xie, L.; Feng, C.; Zhang, Y. Identifying the Largest RoCoF and Its Implications. *IEEE Trans. Power Syst.* **2025**, *40*, 1164–1167. [CrossRef]
13. Wang, J.; Zhang, J.; Hou, Q.; Jiang, H.; Strbac, G.; Teng, F.; Zhang, N. Analytical Decomposition of Nodal Frequency Responses. *IEEE Trans. Power Syst.* **2025**, *40*, 1176–1179. [CrossRef]
14. Badesa, L.; Teng, F.; Strbac, G. Conditions for Regional Frequency Stability in Power System Scheduling—Part I: Theory. *IEEE Trans. Power Syst.* **2021**, *36*, 5558–5566. [CrossRef]
15. Kerci, T.; Milano, F. Asymmetry of Frequency Distribution in Power Systems: Sources, Estimation, Impact and Control. *IEEE Open Access J. Power Energy* **2025**, *12*, 135–145. [CrossRef]
16. Wang, X.; Li, W.; Shen, J.; Ding, Q. Reduced-Order Bus Frequency Response Model for Bulk Power Systems. *J. Mod. Power Syst. Clean Energy* **2025**, *13*, 1127–1138. [CrossRef]
17. Milano, F.; Ortega, A. Frequency Divider. *IEEE Trans. Power Syst.* **2016**, *32*, 1493–1501. [CrossRef]
18. Gao, H.; Xin, H.; Huang, L.; Li, Z.; Huang, W.; Wu, C.; Ju, P. Common-Mode Frequency in Converter-Integrated Power Systems: Definition, Analysis, and Quantitative Evaluation. *IEEE Trans. Power Syst.* **2022**, *37*, 4846–4860. [CrossRef]

19. Li, J.; Li, Y.; Li, W.; Yang, S.; Du, Z. System Power Imbalance Estimation Utilizing Linear Component of Local Frequency. *IEEE Trans. Power Syst.* **2024**, *39*, 2373–2376. [CrossRef]
20. Liu, J.; Wang, C.; Bi, T. Revisiting the Effect of Grid-Following Converter on Frequency Dynamics - Part I: Center of Inertia. *IEEE Trans. Power Syst.* **2026**, *41*, 1441–1458. [CrossRef]
21. Liu, J.; Wang, C.; Bi, T. Revisiting the Effect of Grid-Following Converter on Frequency Dynamics - Part II: Spatial Difference. *IEEE Trans. Power Syst.* **2026**, *41*, 1459–1472. [CrossRef]
22. Trujillo, M.; Sajadi, A.; Shaw, J.; Hodge, B.M. Analytical Models of Frequency and Voltage in Large-Scale All-Inverter Power Systems. *IEEE Trans. Power Syst.* **2026**, 1–12. [CrossRef]
23. Ducoin, E.A.S.; Gu, Y.; Chaudhuri, B.; Green, T.C. Analytical Design of Contributions of Grid-Forming and Grid-Following Inverters to Frequency Stability. *IEEE Trans. Power Syst.* **2024**, *39*, 6345–6358. [CrossRef]
24. Askarian, A.; Park, J.; Salapaka, S. Enhanced Grid-Following (E-GFL) Inverter: A Unified Control Framework for Stiff and Weak Grids. *IEEE Trans. Power Electron.* **2024**, *39*, 5089–5107. [CrossRef]
25. Zhou, W.; Mohammed, N.; Bahrani, B. Comprehensive Modeling, Analysis, and Comparison of State-Space and Admittance Models of PLL-Based Grid-Following Inverters Considering Different Outer Control Modes. *IEEE Access* **2022**, *10*, 30109–30146. [CrossRef]
26. Carreño, M.; Velasco-Falguera, O.; Arévalo-Soler, J.; Gomis-Bellmunt, O. RMS+: Augmenting the Traditional Circuit Model to Capture PLL Instability. *IEEE Trans. Power Deliv.* **2026**, *41*, 364–374. [CrossRef]
27. Shang, L.; Hua, Z.; Liu, C.; Dong, X.; Jiao, F.; Li, Y. Modelling and analysis of grid frequency dynamics with equivalent inertia characteristic of grid-forming voltage source converters. *CSEE J. Power Energy Syst.* **2024**, 1–13. [CrossRef]
28. Wang, Z.; Shan, Y.; Zhu, Y.; Liu, R.; Gu, Y. Spatio-Temporal Frequency Distribution Analysis in Systems with Grid-Forming and Grid-Following Inverters: A New Perspective From Frequency Domain. *IEEE Access* **2025**, *13*, 87999–88011. [CrossRef]
29. Liyanage, C.; Meegahapola, L.; Nutkani, I.; Jalili, M. Strategic Placement of Grid-Forming Inverters Considering Spatiotemporal Dynamics and Composite Stability Index. *IEEE Open J. Ind. Electron. Soc.* **2025**, *6*, 290–308. [CrossRef]
30. Ni, F.; Nijhuis, M.; Nguyen, P.H.; Cobben, J.F.G. Variance-Based Global Sensitivity Analysis for Power Systems. *IEEE Trans. Power Syst.* **2018**, *33*, 1670–1682. [CrossRef]
31. Poolla, B.K.; Bolognani, S.; Dorfler, F. Optimal Placement of Virtual Inertia in Power Grids. *IEEE Trans. Autom. Control* **2017**, *62*, 6209–6220. [CrossRef]
32. Poolla, B.K.; Gross, D.; Dorfler, F. Placement and Implementation of Grid-Forming and Grid-Following Virtual Inertia and Fast Frequency Response. *IEEE Trans. Power Syst.* **2019**, *34*, 3035–3046. [CrossRef]
33. Golpira, H.; Atarodi, A.; Amini, S.; Messina, A.R.; Francois, B.; Bevrani, H. Optimal Energy Storage System-Based Virtual Inertia Placement: A Frequency Stability Point of View. *IEEE Trans. Power Syst.* **2020**, *35*, 4824–4835. [CrossRef]
34. Zhao, T.; Parisio, A.; Milanovic, J.V. Location-dependent distributed control of battery energy storage systems for fast frequency response. *Int. J. Electr. Power Energy Syst.* **2021**, *125*, 106493. [CrossRef]
35. Han, R.; Hu, Q.; Zhang, H.; Ge, Y.; Quan, X.; Wu, Z. Robust allocation of distributed energy storage systems considering locational frequency security. *Int. J. Electr. Power Energy Syst.* **2024**, *157*, 109903. [CrossRef]
36. Liu, D.; Yang, Q.; Chen, Y.; Chen, X.; Wen, J. Optimal Parameters and Placement of Hybrid Energy Storage Systems for Frequency Stability Improvement. *Prot. Control Mod. Power Syst.* **2025**, *10*, 40–53. [CrossRef]
37. Ekomwenrenren, E.; Tang, Z.; Simpson-Porco, J.W.; Farantatos, E.; Patel, M.; Hooshyar, H. Hierarchical Coordinated Fast Frequency Control Using Inverter-Based Resources. *IEEE Trans. Power Syst.* **2021**, *36*, 4992–5005. [CrossRef]
38. Zhao, X.; Xue, Y.; Zhang, X.P. Fast Frequency Support From Wind Turbine Systems by Arresting Frequency Nadir Close to Settling Frequency. *IEEE Open Access J. Power Energy* **2020**, *7*, 191–202. [CrossRef]
39. Lyu, X.; Gross, D. Grid Forming Fast Frequency Response for PMSG-Based Wind Turbines. *IEEE Trans. Sustain. Energy* **2024**, *15*, 23–38. [CrossRef]
40. Lavi, Y.; Apt, J. Inverter fast frequency response is a low-cost alternative to system inertia. *Electr. Power Syst. Res.* **2023**, *221*, 109422. [CrossRef]
41. Peng, Z.; Peng, Q.; Zhang, Y.; Han, H.; Yin, Y.; Liu, T. Online Inertia Allocation for Grid-Connected Renewable Energy Systems Based on Generic ASF Model With Frequency Nadir Constraint. *IEEE Trans. Power Syst.* **2024**, *39*, 1615–1627. [CrossRef]

Disclaimer/Publisher's Note: The statements, opinions and data contained in all publications are solely those of the individual author(s) and contributor(s) and not of MDPI and/or the editor(s). MDPI and/or the editor(s) disclaim responsibility for any injury to people or property resulting from any ideas, methods, instructions or products referred to in the content.

symmetry

MDPI

Article

Hybrid Model and Data-Driven Emergency Load Shedding Optimization for Frequency Security in Receiving-End Power Grids

Lebing Zhao [1], Yixuan Peng [2], Wei Dong [1], Wen Hua [1], Ying Yang [1], Hang Qi [2,*] and Changgang Li [2]

[1] State Grid Zhejiang Electric Power Co., Ltd., Research Institute, Hangzhou 310014, China; eezhaolb@163.com (L.Z.); eedongwei@163.com (W.D.); huawenpin@126.com (W.H.); yang_ying02@163.com (Y.Y.)
[2] School of Electrical Engineering, Shandong University, Jinan 250061, China; pengyixuan_pyx@mail.sdu.edu.cn (Y.P.); lichgang@sdu.edu.cn (C.L.)
* Correspondence: qi_hang@mail.sdu.edu.cn

Abstract

Aiming at the receiving-end power grid frequency security after HVDC blocking events, this paper proposes a hybrid model and data-driven optimization method of emergency load shedding (ELS). Firstly, a decision-making model of ELS considering multiple dynamic security constraints, e.g., frequency and rotor angle, is constructed. Then, the particle swarm optimization (PSO) algorithm is improved by integrating with symmetric opposite learning and Tent chaotic mapping to obtain high-quality ELS schemes. Finally, to boost the optimization efficiency, a data-driven dynamic security assessment model based on the hybrid neural network is constructed and introduced into the solution process of PSO. To ensure the feasibility of the final ELS scheme, the model-driven time-domain simulation method is adopted for validation. The effectiveness of the proposed ELS optimization method is verified on a receiving-end power grid with multi-infeed HVDC lines. It can obtain a high-quality and feasible ELS scheme within 0.7 s.

Keywords: HVDC blocking; receiving-end power grid; emergency load shedding; particle swarm optimization; hybrid neural network

1. Introduction

In a receiving-end power grid with multi-infeed high voltage direct current (HVDC) lines, the proportion of power transmitted via HVDC lines is substantial. The blocking of large-capacity HVDC transmission channels can result in severe power deficiency in the receiving-end power grid, which can lead to a significant frequency drop [1] and even widespread power outages [2]. Therefore, for a receiving-end power grid with multi-infeed HVDC lines, it is essential to implement defense measures to mitigate the impact of HVDC blocking. It is difficult to handle the large power loss caused by HVDC blocking events by preventive control measures. Moreover, the probability of the HVDC blocking is typically low. It is economically infeasible to implement preventive control measures for such low-probability events. It is required to adopt emergency control measures after such an event occurs to ensure the stable operation of the receiving-end power grid [3].

There is a large amount of load in the receiving-end power grid. Therefore, the emergency load shedding (ELS) is a crucial control method for maintaining the frequency security of the receiving-end power grid following a large-capacity HVDC blocking event. The

decision-making of ELS schemes needs to consider multiple dynamic security constraints, such as minimum transient frequency, maximum transient rotor angle difference, and minimum transient voltage. It is a high-dimensional and nonlinear optimization problem.

Conventional analytical methods for ELS optimization include linear programming [4,5], interior-point method [6], and branch-and-bound algorithm [7], etc. These methods transform nonlinear constraints into linear forms based on trajectory sensitivities [8]. However, the solution quality may be low due to its high dependence on the initial solution and the convexity of the optimization problem. Metaheuristic algorithms, such as particle swarm optimization (PSO) [9], differential evolution (DE) [10], and genetic algorithms (GA) [11], can offer superior global optimization capabilities for nonlinear optimization problems. According to a specific rule, they conduct a random search in the solution space to obtain high-quality schemes. Metaheuristic algorithms have been widely applied in ELS optimization [12–15]. However, during the iterative optimization process, metaheuristic algorithms rely on time-domain simulation (TDS) to repeatedly evaluate the feasibility of each candidate ELS scheme [16]. The TDS is time-consuming, severely deteriorating the optimization efficiency of ELS.

With the development of artificial intelligence, data-driven machine learning methods can directly extract the mapping relationship between input features and outputs. Data-driven dynamic security assessment (DSA) methods have been widely studied [17–21]. Replacing the TDS in the ELS optimization with machine learning can significantly improve optimization efficiency. In terms of the type of input features, the DSA methods based on machine learning can be categorized into two classes. The first type is the DSA employing post-fault dynamic response features as inputs [22,23]. Since dynamic features can only be obtained after a fault occurs, the ELS optimization based on this DSA method has to be real-time, i.e., executed after a fault occurs. The system frequency drop following an HVDC blocking event is rapid. Such real-time ELS optimization requires high efficiency in both optimization and data transmission. The second type is the DSA using pre-fault steady-state features as inputs [24–26]. This can conduct dynamic security scanning in advance for various operating conditions and potential contingencies. The ELS optimization based on the second type of DSA can be performed in advance for a specific power loss event. Compared with post-fault real-time optimization, it has less strict requirements on efficiency. The second type of DSA is adopted in this paper.

In this paper, the PSO algorithm is employed for ELS optimization due to its good adaptivity and extensibility. The steady-state feature-based DSA is integrated with PSO algorithm to improve optimization efficiency. The DSA model needs to consider different operating conditions and ELS schemes. Therefore, a hybrid neural network is designed to incorporate the two types of information for high assessment accuracy. Due to the inherent errors of the data-driven DSA, the TDS is conducted to validate the feasibility of the final ELS scheme. The contributions of this paper are as follows.

(1) A decision-making model of ELS incorporating common loads and pumped storage power stations is constructed. It considers multiple dynamic security constraints, including transient frequency drop, rotor angle instability, and voltage instability.
(2) An improved particle swarm optimization (PSO) by integrating with symmetric opposite learning and Tent chaotic mapping is proposed to solve the ELS decision-making model. Opposite learning and Tent chaotic mapping can broaden the search space of PSO in terms of particle initialization and updating, thereby improving the solution quality.
(3) A data-driven multi-task DSA model is constructed on a hybrid neural network. It aims to improve the PSO optimization efficiency by rapidly assessing whether the

https://doi.org/10.3390/sym18010126

candidate ELS schemes satisfy dynamic security constraints. Initial and final output ELS schemes are validated by TDS to ensure the feasibility.

The structure of this paper is organized as follows. The optimization framework and execution mode of ELS are introduced in Section 2. A decision-making model of ELS is constructed in Section 3. In Section 4, an improved PSO algorithm is proposed for solving the decision-making model. A DSA model based on a hybrid neural network is constructed in Section 5. A case study of a receiving-end power grid with multi-infeed HVDC lines is presented in Section 6 to verify the effectiveness of the proposed method.

2. The Proposed Methodology

2.1. Optimization Framework of ELS

The proposed optimization framework of ELS is shown in Figure 1. It consists of two stages: model training and ELS optimization. In the stage of model training, a dataset for model training is first generated based on TDS. The features of a sample in the dataset include the power grid operating condition and ELS scheme information. The sample label represents the feasibility of the ELS scheme under the corresponding operating condition. In the stage of ELS optimization, the ELS scheme under a latest operating condition is optimized based on the metaheuristic algorithm, i.e., the PSO algorithm in this paper. During the iterative optimization process, the trained hybrid neural network, instead of TDS, is invoked to rapidly evaluate the feasibility of candidate schemes in each generation, thereby improving the optimization efficiency of ELS schemes.

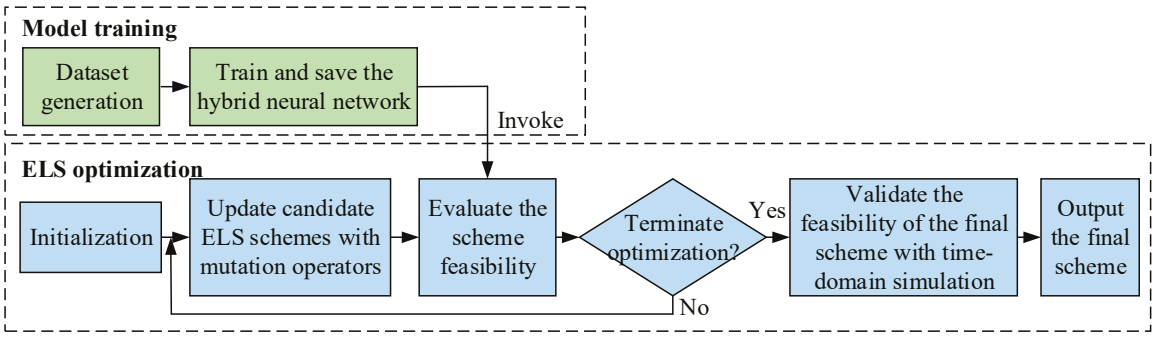


Figure 1. Proposed optimization framework of ELS.

Due to the inevitable errors of the machine learning model, the ELS optimization completely relying on the machine learning model may obtain unfeasible schemes. To ensure feasibility, the TDS is adopted to validate the final ELS scheme. The final ELS scheme is output if it is feasible. If not, this scheme is discarded, and the globally sub-optimal scheme is validated next, and so on, until a feasible scheme is found and output.

When applied in the large-scale power grid, the searching space of the PSO algorithm becomes broader. To ensure the quality of the ELS scheme, the population size needs to be larger and the number of particle evaluations is thereby increased. Due to the rapid evaluation of the hybrid neural network, the ELS optimization time is not significantly increased. Moreover, the parallel computation technique can be further adopted to improve the optimization efficiency in the large-scale power grid.

The proposed ELS optimization framework is applicable for different metaheuristic algorithms. Each metaheuristic algorithm has its own scenario of application. With the development of metaheuristic algorithms, the PSO algorithm can be replaced with other state-of-the-art metaheuristic algorithms and the proposed optimization framework can still be transferred.

https://doi.org/10.3390/sym18010126

2.2. Execution Mode of Event-Driven ELS

The ELS in this paper is event-driven [8,27]. It is triggered instantaneously when a specific HVDC blocking event occurs without waiting for the system frequency to violate a threshold. Therefore, it has a faster action speed than the response-driven under-frequency/voltage load shedding [28].

Traditionally, the execution mode of the ELS is "offline decision and online matching". For a specific HVDC blocking event, an ELS scheme is first determined offline considering various operating conditions of the receiving-end power grid. Then, it is sent and stored in load substations. Once the corresponding HVDC event occurs, the power grid dispatching center issues a load shedding command. With the penetration of renewable energy generation, the uncertainty in power system operating conditions is increasing. Offline operating conditions cannot completely cover the actual operating conditions of the power system, leading to the mismatch of offline ELS schemes. Worse, it may be unfeasible, failing to maintain the stable operation of the post-fault power system.

To address the above issue, an execution mode of "online and early decision, rolling updating" is adopted in this paper. Firstly, a predicted operating condition in the next dispatching cycle is obtained in the dispatching center. Then, an ELS scheme is formulated online and in advance based on the newly predicted information and a specific HVDC blocking event. It is updated in a rolling way to adapt to constantly varying operating conditions, such as every quarter of an hour. The updated ELS scheme is sent to load substations periodically. Finally, the action of the ELS scheme is triggered immediately once the responding event is detected. The adopted execution mode can improve the matching degree between the ELS scheme and actual operating conditions.

3. Decision-Making Model of Emergency Load Shedding Following HVDC Blocking

3.1. Objective Function

Emergency load shedding is a crucial emergency control strategy for maintaining frequency security in receiving-end power grids following an HVDC blocking event. Traditional ELS considers only common load available for shedding. The amount of load shedding is treated as a discrete variable [29,30]. In addition to common loads, a pumped storage power station operating in pumping mode can be treated as a special type of load. Cutting a pumped storage power station in pumping mode has similar effects to shedding common loads on maintaining frequency security. In this paper, the decision-making model incorporates both common loads and pumped storage power stations. The amount of load shedding is regarded as a continuous variable and the cutting amount of pumped storage power stations is a discrete variable. The decision-making of ELS aims to minimize the control cost while satisfying constraints. The optimization objective function can be represented as:

$$\min F = \boldsymbol{\alpha}_{\mathrm{P}} \Delta \boldsymbol{P}_{\mathrm{P}} + \boldsymbol{\alpha}_{\mathrm{L}} \Delta \boldsymbol{P}_{\mathrm{L}} \tag{1}$$

where F denotes the control cost of ELS. $\boldsymbol{\alpha}_{\mathrm{P}}$ denotes a vector composed of the unit shedding cost of each pumped storage power station. $\boldsymbol{\alpha}_{\mathrm{P}} = [\alpha_{\mathrm{P},1},\ldots,\alpha_{\mathrm{P},n\mathrm{P}}]$. n_{P} denotes the number of pumped storage power stations. $\Delta \boldsymbol{P}_{\mathrm{P}}$ denotes a vector composed of the shedding power of each pumped storage power station. $\Delta \boldsymbol{P}_{\mathrm{P}} = [\Delta P_{\mathrm{P},1},\ldots,\Delta P_{\mathrm{P},n\mathrm{P}}]$. $\boldsymbol{\alpha}_{\mathrm{L}}$ denotes a vector composed of the unit shedding cost of each load. $\boldsymbol{\alpha}_{\mathrm{L}} = [\alpha_{\mathrm{L},1},\ldots,\alpha_{\mathrm{L},n\mathrm{L}}]$. n_{L} is the number of loads available for shedding. $\Delta \boldsymbol{P}_{\mathrm{L}}$ denotes a vector composed of the shedding power of each load. $\Delta \boldsymbol{P}_{\mathrm{L}} = [\Delta P_{\mathrm{L},1},\ldots,\Delta P_{\mathrm{L},n\mathrm{L}}]$.

https://doi.org/10.3390/sym18010126

3.2. Constraints

The constraints of ELS optimization can be categorized into two types: constraints of control variables and dynamic security constraints. The constraints of control variables are represented as:

$$\begin{cases} 0 \le \Delta P_{\mathrm{P},i} \le \Delta P_{\mathrm{P},i}^{\max} \\ 0 \le \Delta P_{\mathrm{L},i} \le \Delta P_{\mathrm{L},i}^{\max} \end{cases} \tag{2}$$

where $\Delta P_{\mathrm{P},i}^{\max}$ denotes the upper limit of the shedding power of the i-th pumped storage power station; $\Delta P_{\mathrm{L},i}^{\max}$ denotes the upper limit of the shedding power of the i-th load.

In practice, load shedding is achieved by tripping the outgoing feeders of load substations, and the amount $\Delta P_{\mathrm{L},i}$ is discrete. The receiving-end power grid with multi-infeed HVDC lines is typically a load-intensive center and has a large number of terminal loads. Moreover, the development of communication technology makes the fast demand side management and precise load control a reality [31]. It can conduct the precise tripping of load feeders at a lower voltage level. The continuous variation in $\Delta \mathrm{P}_{\mathrm{L},i}$ can be achieved by combinations of different terminal loads and precise load control [7]. Therefore, the amount $\Delta P_{\mathrm{L},I}$ of load shedding is assumed to be a continuous variable. Unlike common loads, the number of pumped storage power stations is small, and $\Delta P_{\mathrm{P},i}$ is a discrete variable. It can take two values of 0 and rated power. 0 indicates that no shedding for the i-th pumped storage power station. The rated power indicates that the whole pumped storage power station is cut off.

Stability is the basis of secure operation of the power grid. Transient rotor angle, voltage, and frequency are the core aspects of power system stability during the transient process. A severe power loss event, such as the blocking of a large-capacity HVDC line, typically leads to transient frequency drops. It is also important to note that the severe power loss can cause large-scale power flow transfer. The large fluctuations in transmission section power flows may lead to transient rotor angle and rotor instability. As an emergency control measure, the emergency load shedding (ELS) needs to consider the stability and security simultaneously. In this paper, the above three constraints are called "dynamic security constraints". Considering the above three constraints in the optimization process of ELS is a widely used approach [8,32,33]. Each constraint is elaborated as follows.

Minimum transient frequency is a key indicator for the power grid security. A frequency below this threshold can trigger under-frequency load shedding and under-frequency protection actions of generators. This paper adopts the system minimum frequency as the metric for frequency security assessment. The specific transient frequency security constraint is as follows:

$$f_{\min} \ge f_{\min}^{\mathrm{th}} \tag{3}$$

where $f_{\min}$ denotes the minimum frequency of the receiving-end power grid following an HVDC blocking event; $f_{\min}^{\mathrm{th}}$ denotes the allowable minimum frequency threshold.

Transient rotor angle stability represents the capability of generators to maintain synchronous operation after a large disturbance. The transient rotor angle instability is judged to occur when the maximum rotor angle difference between synchronous generators exceeds 180°. The transient rotor angle stability constraint is represented as:

$$\Delta\delta_{\max} \le 180^{\circ} \tag{4}$$

where $\Delta\delta_{\max}$ denotes the maximum rotor angle difference between generators during the transient process. When $\Delta\delta_{\max}$ is less than 180°, the system is deemed to be transiently stable; otherwise, the system is deemed to be transiently instable.

https://doi.org/10.3390/sym18010126

Transient voltage stability refers to the capability of the power system to maintain stable bus voltages following a significant disturbance [34]. Existing practical criteria for transient voltage stability mainly include two categories. The first type determines voltage instability by checking whether the bus voltage remains below a threshold for a period of time. It requires continuous monitoring over a time window, leading to a complex execution logic. The second type determines voltage stability by checking whether the load bus voltage recovers above a threshold in a period of time following the disturbance. It only requires monitoring at a time point. The second type has a simple execution logic and is thereby adopted in this paper. At 10 s after an HVDC blocking event, all load buses need to satisfy:

$$u_i \geq 0.8 \text{ p.u.}, i = 1, \ldots, n_{\text{LB}} \tag{5}$$

where u_i denotes the voltage at load bus i at 10 s following the disturbance; n_{LB} denotes the number of load buses.

The optimization for Equations (1)–(5) is a mixed integer nonlinear programming (MINLP) problem with a single objective and multiple constraints. This paper adopts the PSO algorithm to solve this problem due to its straightforward logic and high adaptability to complex MINLP problems. To enhance solution quality, the PSO algorithm is improved by integrating opposite learning and the Tent chaotic mapping. To improve optimization efficiency, a hybrid neural network model is employed to rapidly assess whether the candidate ELS scheme satisfies constraints at each iteration. To ensure the feasibility of the final ELS scheme, the TDS is adopted to generate initial schemes and validate final schemes.

4. ELS Optimization Based on Improved PSO Algorithm

The solution quality of the PSO algorithm is closely related to its particle initialization and position updating strategy. This paper improves the PSO algorithm from two aspects: particle initialization and updating strategy.

4.1. Particle Swarm Optimization Based on Opposite Learning

In the PSO algorithm, a particle represents an ELS scheme. The solution quality of PSO depends on the distribution of initial particles. The traditional PSO algorithm initializes the particle swarm randomly. A diverse distribution that contains superior initial particles contributes to high-quality solutions. This paper introduces the opposite learning into particle swarm initialization. By simultaneously considering current particles and their opposite particles, this approach can enhance the diversity of particle distribution and broaden the searching scope. The solution quality of the PSO algorithm can be thereby improved.

The process of opposite learning is described as follows: let P be a real number in the range $[l, u]$. Its opposite number P' is $u + l - P$. Assuming the position vector of the i-th particle is $\boldsymbol{P}_i = [P^1{}_i, \ldots, P^d{}_i]$, where $P^j{}_i \epsilon [l_j, u_j]$. then the vector of its opposite particle is $\boldsymbol{P}'_i = [P^1{}_i{}', \ldots, P^d{}_i{}']$. The fitness values $f(\boldsymbol{P}_i)$ and $f(\boldsymbol{P}_i{}')$ of the two particles are compared, and the particle with the superior fitness is selected for subsequent iterations.

The flowchart for particle swarm initialization based on opposite learning is shown in Figure 2. s denotes the population size. Firstly, the initial particle swarm satisfying constraints is generated using a completely random method. Secondly, the opposite particles are generated according to the opposite learning process described in the above paragraph. If an opposite particle satisfies constraints, its control cost is compared with that of the corresponding initial particle, and the particle with the lower cost is selected as the updated initial particle; if the opposite particle violates one of constraints, the initial particle remains unchanged. Finally, the initial particle swarm processed by opposite learning is output, and the particle swarm initialization stage finishes. To ensure that initialization

https://doi.org/10.3390/sym18010126

satisfies dynamic security constraints, each particle after initialization needs to be validated with TDS.

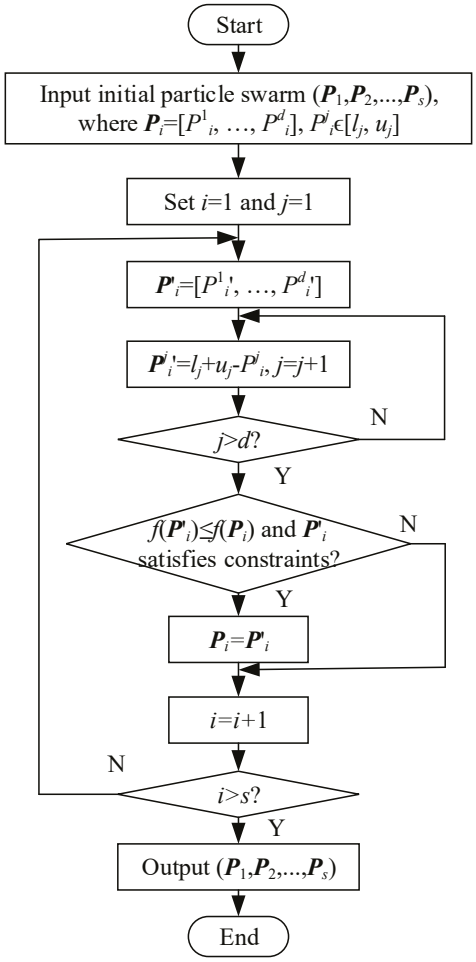


Figure 2. Flowchart of particle swarm initialization based on opposite learning.

The opposite learning can also be applied in the subsequent optimization process. After each iterative updating, the opposite particle $\boldsymbol{P}'_i$ is generated for the current particle $\boldsymbol{P}_i$. Assuming the particle and its opposite particle after the t-th iteration are denoted as $\boldsymbol{P}_i(t)$ and $\boldsymbol{P}'_i(t)$, the particle updating process is performed according to the following rules:

(1) If $\boldsymbol{P}_i(t)$ satisfies dynamic security constraints and $\boldsymbol{P}'_i(t)$ does not, then $\boldsymbol{P}_i(t)$ remains unchanged.

(2) If $\boldsymbol{P}_i(t)$ violates dynamic security constraints but $\boldsymbol{P}'_i(t)$ satisfies them, then $\boldsymbol{P}_i(t)$ is updated to $\boldsymbol{P}'_i(t)$.

(3) If both $\boldsymbol{P}_i(t)$ and $\boldsymbol{P}'_i(t)$ satisfy dynamic security constraints, and if $f(\boldsymbol{P}'_i(t)) \leq f(\boldsymbol{P}_i(t))$, $\boldsymbol{P}_i(t)$ is updated to $\boldsymbol{P}'_i(t)$; otherwise, $\boldsymbol{P}_i(t)$ remains unchanged.

(4) If both $\boldsymbol{P}_i(t)$ and $\boldsymbol{P}'_i(t)$ violate dynamic security constraints, then $\boldsymbol{P}_i(t)$ remains consistent with the previous generation $\boldsymbol{P}_i(t-1)$.

During the optimization process, if the load shedding amount of a particle violates the boundary limits, the exceeding amount is directly set to the boundary value. The PSO paths based on opposite learning are symmetric in the searching space. It enhances the exploration range by broadening the particle swarm distribution, thereby improving the quality of the final ELS scheme.

https://doi.org/10.3390/sym18010126

4.2. Particle Updating Strategy Based on Tent Chaotic Mapping

In each iteration, the updating of the velocity and position of the *i*-th particle can be represented as:

$$\boldsymbol{v}_i(t+1) = \omega \boldsymbol{v}_i(t) + c_1 r_1 (\boldsymbol{P}_{i,\mathrm{b}} - \boldsymbol{P}_i(t)) + c_2 r_2 (\boldsymbol{P}_{\mathrm{b}} - \boldsymbol{P}_i(t)) \tag{6}$$

$$\boldsymbol{P}_i(t+1) = \boldsymbol{P}_i(t) + \boldsymbol{v}_i(t+1) \tag{7}$$

where $v_i(t + 1)$ denotes the velocity vector of the *i*-th particle in the $(t + 1)$-th iteration; $v_i(t)$ denotes the velocity vector of the *i*-th particle in the previous iteration; ω denotes the inertia coefficient; c_1 and c_2 denote the learning factors, usually set such that $c_1 = c_2$ and ranging in [0, 4]; r_1 and r_2 denote random factors uniformly distributed in [0, 1], used to increase the randomness of particle movement; $\boldsymbol{P}_i(t)$ denotes the updated position of the *i*-th particle in the *t*-th iteration; $\boldsymbol{P}_{i,b}$ denotes the historical best position of the *i*-th particle; and $\boldsymbol{P}_b$ denotes the global best position of the entire particle swarm.

As shown in Equation (6), the diversity of particle updating is related to the random factors r_1 and r_2. However, the random search has a disadvantage of insufficient global exploration and is prone to the risk of falling into local optimal solutions. The chaotic sequences have ergodicity and non-repetition. This paper introduces the Tent chaotic mapping to conduct the particle velocity updating, thereby achieving a broader searching space than completely random methods. The chaotic sequence generated based on the Tent chaotic mapping can be represented as:

$$r(t) = \begin{cases} \frac{r(t-1)}{\mu}, 0 \le r(t-1) < \mu \\ \frac{1-r(t-1)}{1-\mu}, \mu \le r(t-1) \le 1 \end{cases} \tag{8}$$

where the parameter $\mu \in [0, 1]$, and is set to 0.7 in this paper; $r(t - 1)$ denotes the output value of the chaotic sequence at the $(t - 1)$-th iteration. It serves as the input for generating the *t*-th chaotic value; $r(t)$ denotes the output value of the chaotic sequence in the *t*-th iteration. By replacing the random factors r_1 and r_2 in Equation (6) with the chaotic sequence values, the particle velocity can be represented as:

$$\boldsymbol{v_i}(t+1) = \omega \boldsymbol{v}_i(t) + c_1 r(t) (\boldsymbol{P}_{i,\mathrm{b}} - \boldsymbol{P_i}(t)) + c_2 (1 - r(t)) (\boldsymbol{P}_{\mathrm{b}} - \boldsymbol{P_i}(t)) \tag{9}$$

Compared with the traditional PSO, the improved PSO algorithm requires the evaluation for a larger number of particles. Using the TDS to evaluate whether the particles in each iteration satisfy dynamic security constraints has a heavy computational burden, leading to low ELS optimization efficiency. Machine learning has the advantages of high efficiency. Replacing the TDS with machine learning can significantly reduce evaluation time and the ELS optimization efficiency is thereby improved.

5. Rapid Assessment of Emergency Load Shedding Scheme Based on Hybrid Neural Network

A DSA model for a specific HVDC blocking event is constructed based on the hybrid neural network. It aims to determine whether the candidate ELS scheme satisfies each dynamic security constraint under a given operating condition.

5.1. Feature Selection

In this paper, the DSA model needs to adapt to the variations in operating conditions and ELS schemes. Therefore, the input features of the DSA model need to contain information of operating conditions and ELS schemes. Dynamic response features, such as bus

https://doi.org/10.3390/sym18010126

voltage and generator rotor angle after a fault occurs, can reflect implicitly the variations in operating conditions and ELS schemes. However, these response features are typically obtained after a fault occurs and cannot be used for the decision-making of the ELS scheme in advance.

Without dynamic response information, this paper directly employs the steady-state power flow features and ELS schemes as inputs. The steady-state power flow features include voltage magnitude and phase angle at each bus, injected power at each bus, and power flow on each branch. These steady-state features contain initial and sufficient information of operating conditions, which have been widely adopted in the data-driven DSA [24–26]. The data structure of a sample can be represented as:

$$\left(\boldsymbol{P}_{\text{gen}}, \boldsymbol{Q}_{\text{gen}}, \boldsymbol{P}_{\text{load}}, \boldsymbol{Q}_{\text{load}}, \boldsymbol{P}_{\text{line}}, \boldsymbol{Q}_{\text{line}}, \boldsymbol{V}_{\text{bus}}, \boldsymbol{\theta}_{\text{bus}}, \Delta\boldsymbol{P}_{\text{P}}, \Delta\boldsymbol{P}_{\text{L}}, y_{\text{f}}, y_{\text{a}}, y_{\text{v}}\right) \tag{10}$$

where $\boldsymbol{P}_{\text{gen}}$, $\boldsymbol{Q}_{\text{gen}}$, $\boldsymbol{P}_{\text{load}}$, $\boldsymbol{Q}_{\text{load}}$, $\boldsymbol{P}_{\text{line}}$, $\boldsymbol{Q}_{\text{line}}$, $\boldsymbol{V}_{\text{bus}}$, and $\boldsymbol{\theta}_{\text{bus}}$ are steady-state power flow feature vectors; $\Delta\boldsymbol{P}_{\text{P}}$, and $\Delta\boldsymbol{P}_{\text{L}}$ are feature vectors of an ELS scheme; $\boldsymbol{y}_{\text{f}}$, $\boldsymbol{y}_{\text{a}}$, and $\boldsymbol{y}_{\text{v}}$ denote multiple labels. $\boldsymbol{P}_{\text{gen}}$ and $\boldsymbol{Q}_{\text{gen}}$ denote the vectors composed of the active and reactive output of each generator; $\boldsymbol{P}_{\text{load}}$ and $\boldsymbol{Q}_{\text{load}}$ denote the vectors composed of the active and reactive power of each load; $\boldsymbol{P}_{\text{line}}$ and $\boldsymbol{Q}_{\text{line}}$ denote the vectors composed of the active and reactive power on each line; Vbus and θbus denote the vectors composed of the voltage magnitude and phase angle of each bus; $\Delta\boldsymbol{P}_{\text{P}}$ denotes a vector composed of the shedding power of each pumped storage power station. $\Delta\boldsymbol{P}_{\text{L}}$ denotes a vector composed of the shedding power of each load. $\boldsymbol{y}_{\text{f}}$, $\boldsymbol{y}_{\text{a}}$, and $\boldsymbol{y}_{\text{v}}$ denote the assessment results for transient frequency, rotor angle, and voltage constraints, respectively.

Each assessment for each dynamic security constraint can be treated as a binary classification problem. Transient frequency, rotor angle, and voltage are highly coupled. Constructing separate assessment models for each constraint fails to fully utilize their inherent correlations. Moreover, the model structures for each dynamic security constraint are similar, resulting in wasted storage and computational resources. This paper addresses these three dynamic security constraints by constructing a multi-task assessment model. By using the loss functions of each task to jointly adjust the shared model parameters, the strong correlations between these three dynamic security constraints can be fully leveraged, thereby improving the assessment accuracy and saving computational resources [35].

5.2. Construction of the Multi-Task DSA Model Based on Hybrid Neural Network

To fully learn the mapping relationship between inputs and outputs, it is essential to construct a large-scale training set containing sufficient operating conditions and ELS schemes. Moreover, the feature dimension of the operating condition is proportional to the system scale, leading to a high-dimensional input feature set. It is difficult for traditional shallow machine learning models to achieve high assessment accuracy in high-dimensional, large-scale, and highly nonlinear datasets. Compared with shallow machine learning, the convolutional neural network (CNN) has stronger learning capabilities. This paper constructs a hybrid neural network by combining multi-channel CNNs and shallow neural networks, serving as a multi-task DSA model. The detailed model structure is shown in Figure 3.

The multi-task DSA model structure is composed of a feature construction module, a feature extraction layer, a feature concatenation layer, and a logical judgment layer. Initial input features are prepared in the feature construction module. In the feature extraction layer, different types of input features are processed by different feature extractors. The operating condition features are processed by multi-channel CNNs due to the high dimensionality. The feature dimensionality of the ELS scheme is equal to the sum of loads and pumped storage power stations to be shed. It is relatively low-dimensional and processed

https://doi.org/10.3390/sym18010126

by a single-layer neural network. The high-level abstract features extracted from multi-channel CNNs and the single-layer neural network are concatenated into a feature vector in the feature concatenation layer, serving as the inputs to the final logical judgment layer. In the logical judgment layer, the concatenated feature vector passes through separate fully connected layers to output the assessment results for each dynamic security constraint. Each assessment result is a 0–1 value. The value "0" represents that the dynamic security constraint is satisfied. The value "1" represents that the constraint is not satisfied. Each channel of CNNs and the single-layer neural network are trained simultaneously and not affected by each other, significantly improving the training efficiency of the hybrid neural network.

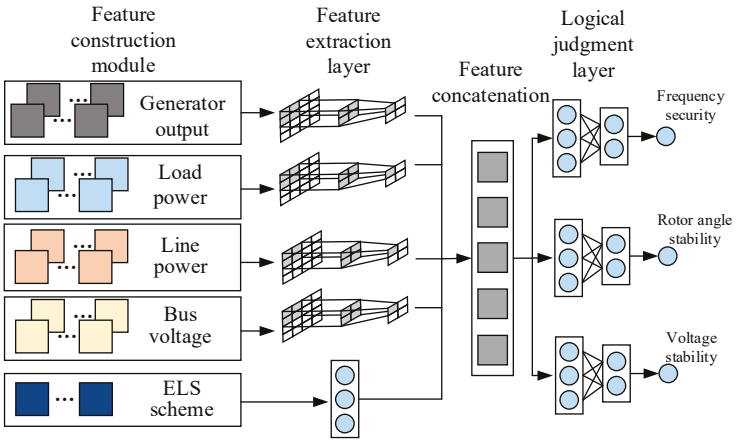


Figure 3. Structure of multi-task DSA model based on hybrid neural network.

The particle is in the feasible region only if all constraints are satisfied. This paper defines a comprehensive value y to represent whether the ELS scheme is feasible:

$$y = y_{\mathrm{f}} || \, y_{\mathrm{a}} || \, y_{\mathrm{v}} \tag{11}$$

where $||$ denotes the operation "OR"; y_{f}, y_{a}, y_{v} denote the assessment results for transient frequency, rotor angle, and voltage constraints, respectively. $y = 0$ represents that all dynamic security constraints are satisfied and the ELS scheme is feasible; $y = 1$ represents that at least one constraint is not satisfied and the ELS scheme is unfeasible.

Based on the comprehensive value y and the confusion matrix, the following metrics, i.e., accuracy I_{AC}, false alarm rate I_{FA}, and missed alarm rate I_{MA}, are defined for the performance evaluation of the DSA model. The confusion matrix is shown in Table 1.

$$I_{\mathrm{AC}} = \frac{n(\mathrm{TP})+n(\mathrm{TN})}{n(\mathrm{TP})+n(\mathrm{FP})+n(\mathrm{FN})+n(\mathrm{TN})} \times 100\% \tag{12}$$

$$I_{\mathrm{FA}} = \frac{n(\mathrm{FN})}{n(\mathrm{TP})+n(\mathrm{FN})} \times 100\% \tag{13}$$

$$I_{\mathrm{MA}} = \frac{n(\mathrm{FP})}{n(\mathrm{FP})+n(\mathrm{TN})} \times 100\% \tag{14}$$

Table 1. Confusion matrix.

Predicted \ Actual	0	1
0	TP	FP
1	FN	TN

It should be noted that the purpose of the DSA model in this section is to rapidly judge whether the PSO particles are located within the feasible region. The judgment is determined by the comprehensive result y. Therefore, the parameter tuning process of the DSA model mainly considers the three metrics I_{AC}, I_{FA}, and I_{MA} defined on the comprehensive result y.

6. Case Study

6.1. Descriptions of the Power Grid

To validate the effectiveness of the proposed method, a provincial receiving-end power grid with multi-infeed HVDC lines is employed. The topology diagram can be found in Ref. [24]. It includes 132 buses, 29 generators, 65 loads, 201 500-kV AC lines, and 11 1000-kV AC lines. There are three HVDC lines with a total infeed power of 20 GW. Nine wind farms are added. Among these, six have a rated output power of 1000 MW, two of 1500 MW, and one of 1300 MW.

The dynamic models of the synchronous generators, HVDC lines, wind turbines, and loads are modelled by software PSS/E 34. The generator rotor model is set as "GENROU", which is a 6-order non-salient pole machine model. The exciter model is set as "SEXS". The turbine governor is set as "IEESGO". The model of the dual-terminal LCC-HVDC is set as "CDC4T". The doubly-fed induction generator model of the wind turbine is set as "WT3G1". The "IEEL" models are adopted to represent static load models, and all static load models are set as constant power loads. The dynamic load model is set as the induction motor model "CIM6".

Four pumped storage units are set and each unit has a rated capacity of 300 MW and is operated in the pumping mode. Twenty load buses available for shedding are set. The upper shedding limit of each load is set to 50%. The total power available for load shedding is 10.385 GW. The unit shedding cost of each pumped storage power station is set to 0.1. The unit shedding cost of each load is selected in [0.3, 0.7].

All simulations, optimizations and model training are conducted on a server with a 24-core Intel Xeon Gold 6148 CPU (2.40 GHz) and 64 GB of RAM. The machine learning models are constructed based on the "Keras" module of Python 3.7.

6.2. Optimization of Emergency Load Shedding

The blocking of HVDC #2 with a capacity of 8 GW is simulated as a severe power loss event. The time step of the simulation is set to 0.005 s, and the total simulation duration is 15 s. The HVDC blocking fault occurs at 0.5 s. The allowable minimum frequency threshold is set to 49.8 Hz. If the ELS is not executed after the DC blocking event, the system frequency response curve is shown in Figure 4. The minimum system frequency drops to 49.3 Hz, indicating that the ELS must be implemented to ensure transient frequency security.

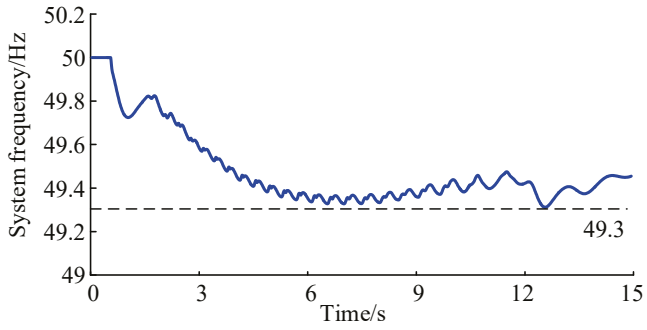


Figure 4. Frequency response curve without ELS after HVDC#2 blocking.

The ELS optimization model is solved using different optimization algorithms, including traditional PSO, adaptive PSO (APSO), hierarchical PSO (HPSO), mutated PSO (MPSO), DE, and GA. The iterative solution processes of the above algorithms are shown in Figure 5. Among the above algorithms, the same random factors are set to initialize population. The size of population is set to 10. The maximum number of iterations is 30. Learning factors c_1 and c_2 are set to 1. Except for APSO and HPSO, the inertia weight ω in other PSO algorithms is set to 1. During the optimization process, the TDS is adopted to determine whether the particle satisfies dynamic security constraints.

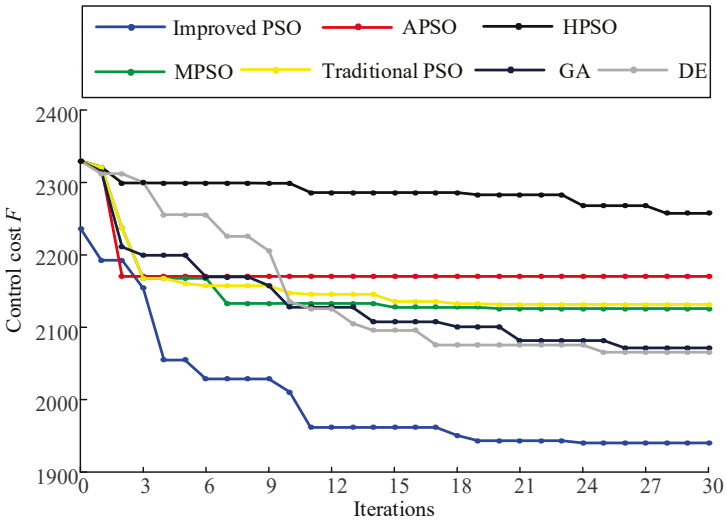


Figure 5. Comparisons of solution processes based on different optimization algorithms.

As shown in Figure 5, the improved PSO algorithm can obtain the solution with the highest quality within 30 iterations. Moreover, compared with other algorithms, it can obtain superior initial solutions during initialization. Therefore, the improved PSO algorithm is applicable for the ELS optimization. The obtained ELS scheme is shown in Table 2. The total shedding power of loads and pumped storage is 5546 MW. The ELS scheme is executed 0.2 s after the HVDC blocking event occurs. The system frequency response curve after the ELS acts is shown in Figure 6, and the voltage response curves of load buses are shown in Figure 7. The simulation results indicate that the frequency of the receiving-end power grid remains above the threshold of 49.8 Hz, while satisfying the constraints for transient rotor angle and voltage stability.

Table 2. Shedding power of each load and pumped storage.

Load bus	6	7	8	13	15	16
Shedding power/MW	0	0	942	63	0	487
Load bus	17	35	36	37	38	41
Shedding power/MW	185	352	0	418	0	0
Load bus	71	72	73	74	75	89
Shedding power/MW	551	0	0	0	0	294
Load bus	90	92	Pumped storage 1	Pumped storage 2	Pumped storage 3	Pumped storage 4
Shedding power/MW	710	944	300	300	0	0

https://doi.org/10.3390/sym18010126

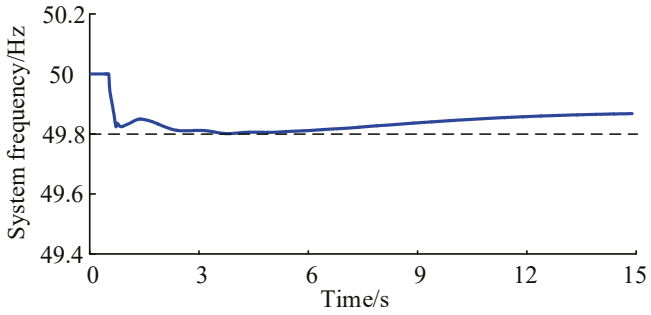


Figure 6. Frequency response curve with ELS after HVDC#2 blocking.

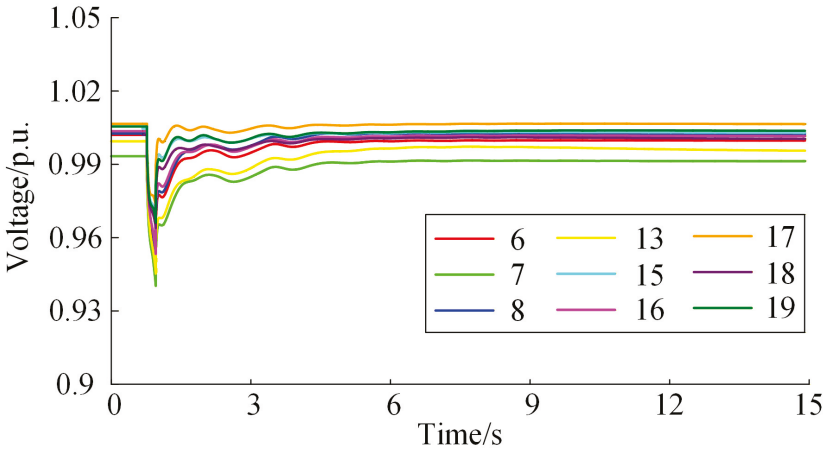


Figure 7. Voltage response curves of load buses with ELS after HVDC#2 blocking.

6.3. Optimization of Emergency Load Shedding Integrated with Hybrid Neural Network

The power at each load bus is randomly varied between 80% and 120% of the base level. The output power of each wind farm fluctuates between 25% and 35% of the rated output power. The power imbalance introduced by loads and wind power generation is distributed among generators according to the spinning reserve. A total of 500 operating conditions are generated. Upon each operating condition and the blocking of HVDC#2, 100 ELS schemes are randomly generated. A total of 50,000 samples are generated, including 19,869 feasible samples and 30,131 unfeasible samples. Approximately 70% of the samples are randomly selected as the training set, and the remaining samples constitute the test set.

The multi-task DSA model is trained based on the hybrid neural network. Each convolution channel includes two convolution layers and one pooling layer. The convolution layer includes ten convolution cores with the size of 3. The number of neurons in the single-layer neural network is the same as the dimensionality of an ELS scheme. The logical judgment layer for each output is composed of two fully connected layers (100, 20). The activation functions of all neurons are set as "ReLU" and the activation function of the output layer is set as "Sigmoid." A batch training strategy is adopted, and the batch size is set to 100. The optimizer for adjusting model parameters is "Adam." The default learning rate is 0.001. Training epochs are set to 100. The callback function is adopted to save the optimal DSA model. The evaluation performance of the model is described by the metrics defined as Equation (12) to Equation (14).

The comparisons between hybrid neural network, single-layer neural network (ANN), support vector machine (SVM), and decision tree (DT) are shown in Table 3. The hybrid neural network has the best evaluation metrics in terms of accuracy, false alarm rate, and missed alarm rate. Its evaluation accuracy reaches 98.67%. In contrast, the evaluation accuracy of simple machine learning methods is low. It indicates that the traditional simple

https://doi.org/10.3390/sym18010126

machine learning methods struggle to address the DSA problem considering operating conditions and ELS schemes simultaneously.

Table 3. Performance metrics of DSA model based on different machine learning methods.

Methods	Accuracy	False Alarm Rate	Missed Alarm Rate
Hybrid neural network	98.67%	1.09%	1.83%
ANN	93.56%	5.97%	7.14%
SVM	89.00%	9.53%	13.20%
DT	86.77%	12.01%	15.05%

The generalization performance of the DSA model is important. A generalization test on unlearned operating conditions, i.e., operating conditions not in the training set, is further conducted. A total of 50,000 samples are divided into a training set and a test set according to different generalization ratios of operating conditions. The generalization ratio is equal to the number of operating conditions in the test set divided by the number of operating conditions in the training set. The operating conditions in the training set and test set are not overlapped. The variation of evaluation accuracy under different generalization ratios is shown in Figure 8. Although the evaluation accuracy decreases with the increasing of generalization ratio, the evaluation accuracy with the generalization ratio of 1:1 remains more than 92%. It demonstrates that the DSA model based on hybrid neural network has good generalization performance on unlearned operating conditions.

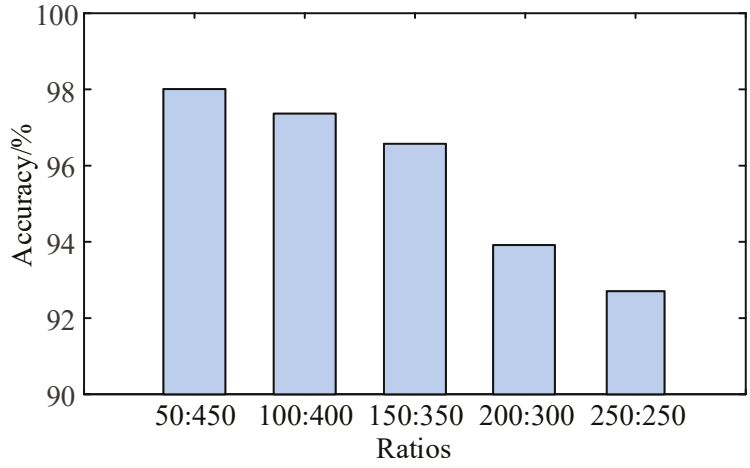


Figure 8. Variation of evaluation accuracy of hybrid neural network under different ratios.

The trained hybrid neural network is adopted to assess the feasibility of particles during the optimization process. The output ELS scheme is validated by TDS. The comparative results with the PSO completely relying on TDS are shown in Figure 9. The results indicate that both methods yield ELS schemes with nearly equivalent costs. Compared with Table 2, the shedding loads at buses 13 and 16 are reduced to 0 MW, and the shedding load at bus 15 is changed to 524 MW. Other shedding load power remains unchanged. Further comparison of computational time is conducted. The PSO integrated with the hybrid neural network can obtain the final ELS scheme within 0.63 s. In contrast, the PSO completely depending on TDS requires 341 s to finish the optimization process. The optimization efficiency is improved by approximately 541 times.

The optimization results on ten different operating conditions are further given in Figure 10. The deviation between TDS and hybrid neural network is low. It demonstrates that the proposed ELS optimization method has high adaptivity for operating conditions.

https://doi.org/10.3390/sym18010126

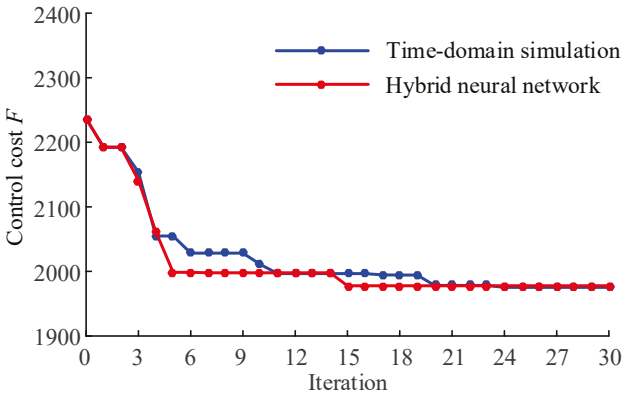


Figure 9. Solution processes of PSO with time-domain simulation and hybrid neural network.

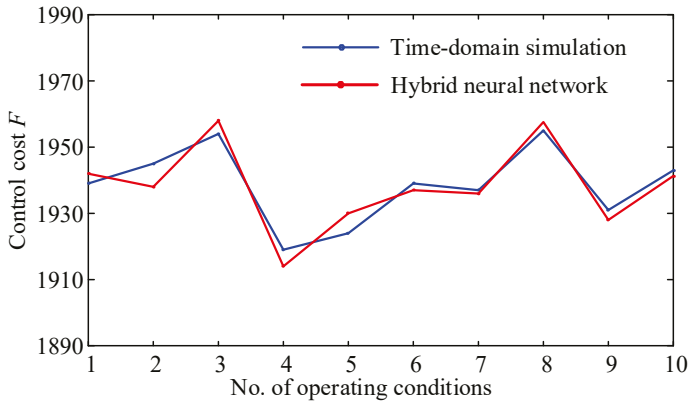


Figure 10. Optimization results on ten different operating conditions.

7. Conclusions

This paper proposes a hybrid model and data-driven ELS optimization method for frequency security in receiving-end power grids, aiming to rapidly obtain a feasible and high-quality ELS scheme. By integrating symmetric opposite learning and Tent chaotic mapping into the PSO algorithm, the quality of the final ELS scheme can be significantly boosted. A data-driven DSA model based on a hybrid neural network is constructed to assess the feasibility of each candidate scheme, enhancing the optimization efficiency of ELS. The time-domain simulation is adopted for validation in initialization and final outputs, ensuring the feasibility of the final ELS scheme. The test results on a practical receiving-end power grid demonstrate that the proposed optimization method can obtain the lowest-cost and feasible ELS scheme within 0.7 s. The optimization efficiency is 541 times greater than that of time-domain simulation.

In this paper, the ELS optimization is conducted for only one predicted operating condition in the next dispatching cycle. Due to the uncertainty induced by renewable generation, the number of predicted operating conditions in a long cycle may be more than one. It is worth further studying an ELS optimization method adaptive for multiple predicted operating conditions. Moreover, the ELS scheme needs to be updated online in a rolling way. It requires coordination with fast and reliable data communication devices.

Author Contributions: Conceptualization, L.Z.; methodology, L.Z.; software, Y.P.; validation, Y.P.; formal analysis, W.D.; investigation, W.H.; data curation, Y.Y.; writing—original draft preparation, L.Z. and C.L.; writing—review and editing, H.Q.; supervision, C.L. All authors have read and agreed to the published version of the manuscript.

Funding: The authors declare that this study received funding from the Science and Technology Project of State Grid Zhejiang Electric Power Co., Ltd. "Research on Development Trends and Support Requirements of Stability Characteristics for New-Type Power Systems in Receiving-End Provincial Regions" under Grant B311DS24000X. The funder had the following involvement with the study: methodology, writing—original draft preparation, and data curation.

Data Availability Statement: The raw data supporting the conclusions of this article will be made available by the authors on request.

Conflicts of Interest: Authors Lebing Zhao, Wei Dong, Wen Hua, and Ying Yang were employed by the State Grid Zhejiang Electric Power Co., Ltd., Research Institute. The authors declare that this study received funding from the Science and Technology Project of State Grid Zhejiang Electric Power Co., Ltd. "Research on Development Trends and Support Requirements of Stability Characteristics for New-Type Power Systems in Receiving-End Provincial Regions" under Grant B311DS24000X. The funder had the following involvement with the study: methodology, writing—original draft preparation, and data curation.

References

1. Sun, Z.; Han, J.; Chen, W.; Zhang, R.; Liu, Y.; Levron, Y.; Belikov, J. Decentralized coordinated emergency frequency control strategy for renewables-rich power systems based on multi-agent reinforcement learning. *Int. J. Electr. Power Energy Syst.* **2025**, *171*, 111035. [CrossRef]
2. Yan, R.; Masood, N.A.; Kumar Saha, T.; Bai, F.; Gu, H. The anatomy of the 2016 South Australia blackout: A catastrophic event in a high renewable network. *IEEE Trans. Power Syst.* **2018**, *33*, 5374–5388. [CrossRef]
3. Chen, Y.; Liao, S.; Xu, J. Emergency load-shedding optimization control method based on reinforcement learning assistance. *Energy Rep.* **2022**, *8*, 1051–1061. [CrossRef]
4. Reveles-Pinedo, A.; Fuerte-Esquivel, C.R.; Pizano-Martínez, A.; Ramirez-Betancour, R. Selective optimal under-frequency load shedding based on trajectory sensitivities. *Electr. Power Syst. Res.* **2024**, *234*, 110810. [CrossRef]
5. Tang, L.; McCalley, J. Two-stage load control for severe under-frequency conditions. *IEEE Trans. Power Syst.* **2016**, *31*, 1943–1953. [CrossRef]
6. Gan, G.; Zhu, Z.; Geng, G.; Jiang, Q. An efficient parallel sequential approach for transient stability emergency control of large-scale power system. *IEEE Trans. Power Syst.* **2018**, *33*, 5854–5864. [CrossRef]
7. Liu, J.; Zhuan, X.; Shang, L.; Su, S.; Xie, Q. A load-shedding preplan strategy for unplanned microgrid islanding considering frequency security constraints. *Int. J. Electr. Power Energy Syst.* **2025**, *170*, 110932. [CrossRef]
8. Xu, X.; Zhang, H.; Li, C.; Liu, Y.; Li, W.; Terzija, V. Optimization of the event-driven emergency load-shedding considering transient security and stability constraints. *IEEE Trans. Power Syst.* **2017**, *32*, 2581–2592. [CrossRef]
9. Arya, L.D.; Singh, P.; Titare, L.S. Differential evolution applied for anticipatory load shedding with voltage stability considerations. *Int. J. Elect. Power Energy Syst.* **2012**, *42*, 644–652. [CrossRef]
10. Hong, Y.; Nguyen, M. Multiobjective multiscenario under-frequency load shedding in a standalone power system. *IEEE Syst. J.* **2020**, *14*, 2759–2769. [CrossRef]
11. Yao, L.; Chang, W.; Yen, R. An iterative deepening genetic algorithm for scheduling of direct load control. *IEEE Trans. Power Syst.* **2005**, *20*, 1414–1421. [CrossRef]
12. Sheikhzadehbaboli, P.; Samimi, A.; Ebadi, M.; Bayat, M.; Pirayesh, A. Frequency control in standalone renewable based-microgrids using steady state load shedding considering droop characteristic. *Int. J. Electr. Power Energy Syst.* **2022**, *142*, 108351. [CrossRef]
13. Singh, P.; Arya, R.; Titare, L.S. Value aided optimal load shedding accounting voltage stability consideration employing Crow Search Algorithm with modification based on Lampinen's criterion. *Appl. Soft Comput.* **2023**, *143*, 110391. [CrossRef]
14. Hong, Y.Y.; Hsiao, C.Y. Under-frequency load shedding in a standalone power system with wind-turbine generators using fuzzy PSO. *IEEE Trans. Power Deliv.* **2022**, *37*, 1140–1150. [CrossRef]
15. Sun, G.; Yuan, G.; Deng, L.; Li, C.; Zheng, M. An adaptive differential evolution algorithm based on individual-level intervention strategy for global optimization. *Expert. Syst. Appl.* **2025**, *286*, 128054. [CrossRef]
16. Lara, J.D.; Henriquez-Auba, R.; Ramasubramanian, D.; Dhople, S.; Callaway, D.S. Revisiting power systems time-domain simulation methods and models. *IEEE Trans. Power Syst.* **2023**, *39*, 2421–2437. [CrossRef]
17. Lal, M.D.; Varadarajan, R. A review of machine learning approaches in synchrophasor technology. *IEEE Access* **2023**, *11*, 33520–33541. [CrossRef]
18. Alimi, O.A.; Ouahada, K.; Abu-Mahfouz, A.M. A review of machine learning approaches to power system security and stability. *IEEE Access* **2020**, *8*, 113512–113531. [CrossRef]

19. Chen, H.; Guan, L.; Lin, B.; Chen, L.; Huang, J.; Li, Y. A continual learning scheme for data-driven transient stability assessment via clustered memory replay and hierarchical embedding constraint. *Electr. Power Syst. Res.* **2025**, *247*, 111704. [CrossRef]
20. Boričić, A.; Popov, M. Voltage vulnerability curves: Data-driven dynamic security assessment of voltage stability and system strength in modern power systems. *Int. J. Electr. Power Energy Syst.* **2025**, *168*, 110636. [CrossRef]
21. Wang, Y.; Wu, J. Resnet-based power system frequency security assessment considering frequency spatiotemporal distribution characteristics. *Energy Rep.* **2023**, *9*, 125–134. [CrossRef]
22. Shahriyari, M.; Khoshkhoo, H.; Guerrero, J.M. A novel fast transient stability assessment of power systems using fault-on trajectory. *IEEE Syst. J.* **2022**, *16*, 4334–4344. [CrossRef]
23. Zhu, L.; Lu, C.; Luo, Y. Time series data-driven batch assessment of power system short-term voltage security. *IEEE Trans. Ind. Inf.* **2020**, *16*, 7306–7317. [CrossRef]
24. Qi, H.; Su, R.; Sun, R.; Yan, J. Data-driven dynamic security partition assessment of power systems based on symmetric electrical distance matrix and Chebyshev distance. *Symmetry* **2024**, *16*, 1355. [CrossRef]
25. Liu, X.; Min, Y.; Chen, L.; Zhang, X.; Feng, C. Data-driven transient stability assessment based on kernel regression and distance metric learning. *J. Mod. Power Syst. Clean Energy* **2020**, *9*, 27–36. [CrossRef]
26. An, J.; Yu, J.; Li, Z.; Zhou, Y.; Mu, G. A data-driven method for transient stability margin prediction based on security region. *J. Mod. Power Syst. Clean Energy* **2020**, *8*, 1060–1069. [CrossRef]
27. Hu, Z.; Yao, W.; Shi, Z.; Shuai, H.; Gan, W.; Wen, J. Intelligent and rapid event-based load shedding pre-determination for large-scale power systems: Knowledge-enhanced parallel branching dueling Q-network approach. *Appl. Energy* **2023**, *347*, 121468. [CrossRef]
28. Yang, J.; Zhou, S.; Cai, G.; Liu, C.; Jiang, C. Response-driven adaptive under frequency load shedding scheme based on energy model. *Electr. Power Syst. Res.* **2025**, *238*, 111150. [CrossRef]
29. Ceja-Gomez, F.; Qadri, S.S.; Galiana, F.D. Under-frequency load shedding via integer programming. *IEEE Trans. Power Syst.* **2012**, *27*, 1387. [CrossRef]
30. Lukas, S.; Luis, R.; Francisco, M.E. A review of the state of the art of UFLS schemes for isolated power system. *International. Int. J. Electr. Power Energy Syst.* **2018**, *99*, 525–539.
31. Acharya, S.; EI Moursi, M.S.; Al-Hinai, A. Coordinated frequency control strategy for an islanded microgrid with demand side management capability. *IEEE Trans. Energy Convers.* **2018**, *33*, 639–651. [CrossRef]
32. Yuan, H.; Xu, Y.; Zhang, C. Robustly coordinated generation dispatch and load shedding for power systems against transient instability under uncertain wind power. *IEEE Trans. Power Syst.* **2022**, *37*, 1032–1043. [CrossRef]
33. Gao, Q.; Zhang, J.; Yang, H.; Xia, S.; Li, P.; Jiang, T. Power system emergency load shedding strategy based on improved POA-GWO algorithm. In Proceedings of the 2024 9th Asia Conference on Power and Electrical Engineering, Shanghai, China, 11–13 April 2024; pp. 145–150.
34. Hatziargyriou, N.; Milanovic, J.; Rahmann, C.; Ajjarapu, V.; Canizares, C.; Erlich, I.; Hill, D.; Hiskens, I.; Kamwa, I.; Pal, B.; et al. Definition and classification of power system stability–revisited & extended. *IEEE Trans. Power Syst.* **2020**, *36*, 3271–3281.
35. Huang, J.; Guan, L.; Su, Y.; Yao, H.; Guo, M.; Zhong, Z. Recurrent graph convolutional network-based multi-task transient stability assessment framework in power system. *IEEE Access* **2020**, *8*, 93283–93296. [CrossRef]

Disclaimer/Publisher's Note: The statements, opinions and data contained in all publications are solely those of the individual author(s) and contributor(s) and not of MDPI and/or the editor(s). MDPI and/or the editor(s) disclaim responsibility for any injury to people or property resulting from any ideas, methods, instructions or products referred to in the content.

symmetry

MDPI

Article

Self-Adaptive Virtual Synchronous Generator Control for Photovoltaic Hybrid Energy Storage Systems Based on Radial Basis Function Neural Network

Mu Li * and Shouyuan Wu

Key Laboratory of Power System Intelligent Dispatch and Control of Ministry of Education, Shandong University, Jinan 250061, China; shouyuan_wu@sdu.edu.cn
* Correspondence: 202434727@mail.sdu.edu.cn

Abstract

Renewable energy's growing penetration erodes traditional power systems' inherent dynamic symmetry—balanced inertia, damping, and frequency response. This paper proposes a self-adaptive virtual synchronous generator (VSG) control strategy for a photovoltaic hybrid energy storage system (PV-HESS) based on a radial basis function (RBF) neural network. The strategy establishes a dynamic adjustment framework for inertia and damping parameters via online learning, demonstrating enhanced system stability and robustness compared to conventional VSG methods. In the structural design, the DC-side energy storage system integrates a passive filter to decouple high- and low-frequency power components, with the supercapacitor attenuating high-frequency power fluctuations and the battery stabilizing low-frequency power variations. A small-signal model of the VSG active power loop is developed, through which the parameter ranges for rotational inertia (J) and damping coefficient (D) are determined by comprehensively considering the active loop cutoff frequency, grid connection standards, stability margin, and frequency regulation time. Building on this analysis, an adaptive parameter control strategy based on an RBF neural network is proposed. Case studies show that under various conditions, the proposed RBF strategy significantly outperforms conventional methods, enhancing key performance metrics in stability and dynamic response by 16.98% to 70.37%.

Keywords: dynamic symmetry; PV-HES; VSG; RBF neural network; passive filter; frequency deviation

1. Introduction

Driven by power electronics, rising renewable penetration accelerates the shift toward distributed generation, critically reducing system inertia and damping and directly compromising transient stability. In high-renewable systems, insufficient inertia and damping pose primary stability threats, as improper parameter coordination triggers sustained oscillations or collapse. VSG technology addresses this by emulating inertia and damping characteristics, optimizing dynamic response in inverter-dominated grids through symmetrical electrical-mechanical mapping, thereby restoring generation–grid interaction symmetry and enhancing grid support capabilities, establishing VSG as the key enabler for transient stability in modern power systems.

References [1–5] provide comprehensive reviews of VSGs, covering their mathematical models, operational principles, research advancements, demonstration projects, and technical challenges. However, conventional VSG control strategies with fixed parameters exhibit

limitations in complex and variable operating conditions. Studies [6,7] propose inertia-damping coordinated adaptive algorithms that dynamically adjust control parameters to improve frequency stability and response speed, addressing the rigidity of traditional fixed-parameter approaches. Nevertheless, these algorithms lack sufficient experimental validation in multi-source system environments with high renewable penetration. Regarding dynamic coupling mechanisms, reference [8] investigates voltage-frequency coupling dynamics in VSG systems and establishes a unified small-signal model, providing important theoretical foundations for system analysis. However, it does not address the coordinated frequency regulation mechanism between energy storage systems and VSGs under low-inertia conditions, thereby limiting its theoretical guidance for integrated "storage–VSG" frequency regulation system design. In terms of transient stability, while references [9–12] enhance the transient stability of the system from perspectives such as synchronization preservation under severe faults, adaptive parameter optimization, reactive power–frequency coupling control, and multi-objective coordinated control, they lack a systematic analysis of dynamic performance under frequent, small-magnitude power fluctuations caused by renewable intermittency. Existing research highlights two key challenges in VSG-based systems under low inertia and high volatility: First, current dynamic coupling models inadequately guide energy storage coordination, especially in heterogeneous multi-storage systems; Second, a systematic approach for dynamic parameter tuning and effective storage support is lacking, hindering coordinated power sharing and stability. This gap reflects a disconnect between control theory and practical "source–storage–grid" interactions.

Under this context, coordinated control of energy storage systems with VSGs has emerged as a pivotal strategy. References [13–15] focus on coordinated control incorporating energy storage physical constraints and optimal configuration considerations, effectively addressing the parameter design problem considering practical engineering limitations. Reference [16] establishes an islanded microgrid model containing diesel generators, photovoltaic arrays, and energy storage systems, proposing a cascade control method combining droop control with VSG techniques that uses battery energy storage to estimate active power for frequency fluctuation suppression. Reference [17] introduces an adaptive VSG characteristic and state-of-charge coordinated control strategy for primary frequency regulation in PV-HESS, solving the coordination problem between virtual inertia and actual energy storage state. Reference [18] presents a decentralized adaptive coordinated control strategy based on VSGs that adaptively adjusts droop characteristics, enabling local controllers to automatically switch operation modes according to inverter ratings, photovoltaic maximum output, and battery charge/discharge limits, effectively solving the power distribution optimization problem.

References [19–21] propose improved virtual synchronous control strategies to enhance photovoltaic system stability and response capabilities in microgrids, providing solutions for renewable energy integration reliability. Reference [22] develops a virtual inertia control strategy based on bidirectional grid-connected converters (BGCs) that enhances DC microgrid (DC-MG) inertia while employing DC output current feedforward disturbance suppression methods, addressing DC system stability challenges. Studies [23,24] focus on off-grid diesel generator microgrids, designing VSG control strategies based on real-time parameter optimization by simulating inertia and damping characteristics through energy storage inverters, effectively suppressing frequency fluctuations in isolated systems. Reference [25] proposes an adaptive neural predictive control (ANPC) scheme for ultrabattery energy storage systems (UBESSs) in autonomous wind–diesel power systems, enhancing operational stability through VSGs behavior emulation and real-time parameter optimization. Reference [26] introduces a neural-network-based adaptive VSG

https://doi.org/10.3390/sym18010070

control strategy that tunes virtual inertia by learning the nonlinear relationship between inertia and angular velocity, thereby effectively damping power oscillations. Reference [27] presents a three-phase grid-connected inverter control method using adaptive dynamic programming (ADP), achieving adaptive optimal control through value iteration strategies while incorporating virtual impedance to enhance system stability.

To address system inertia reduction and frequency stability issues caused by high photovoltaic penetration, this study proposes a PV-HESS based on an improved VSG control strategy. This strategy employs an adaptive RBF neural network to dynamically optimize system inertia and damping parameters. A simulation model was developed in Simulink to validate the approach. Results demonstrate that hybrid energy storage units can actively participate in grid frequency regulation and power support under complex operating conditions such as irradiance fluctuations. Compared to traditional methods, the RBF neural network-based VSG control strategy exhibits faster response, smaller overshoot, and weaker DC-side disturbances. These improvements significantly enhance the stability and robustness of PV-energy storage systems.

The remainder of this paper is organized as follows: Section 2 describes the PV-HESS structure. Section 3 presents the modeling of VSG. Section 4 proposes an adaptive RBF-based J and D parameter optimization. Section 5 validates the strategy through specific operational scenarios. Section 6 summarizes key findings and future research directions.

2. Model of PV-HESS

2.1. PV-HESS Structure

The DC side of the PV-HESS consists of a photovoltaic array, energy storage system, boost converter, and bidirectional DC/DC converter connected to the DC bus, as shown in Figure 1. This DC structure is linked to loads and the grid through a DC/AC inverter and filter circuit. The actual voltage and current of the PV array are denoted as U_{pv} and i_{pv}, respectively. U^*_{pv} represents the reference voltage at the PV array's maximum power point. The DC bus voltage is labeled as u_{dc}, with the DC bus capacitor marked as C_{dc}. In the grid-side LCL filter circuit, C_f, R_f, and L_f correspond to the filter capacitor, resistor, and inductor, respectively. R_g and L_g represent the equivalent resistance and inductance on the grid side.

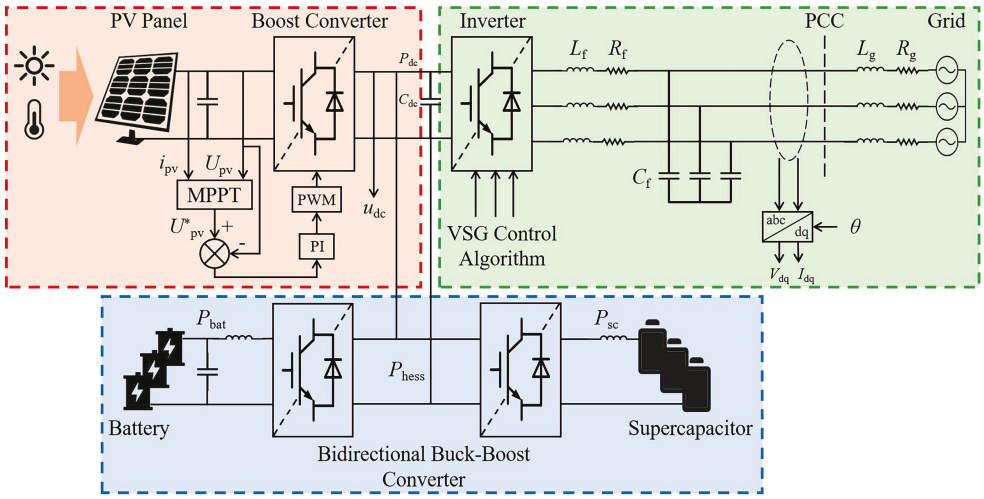


Figure 1. Structure of PV-HESS-VSG integrated system.

The power relationship on the DC side of the system is expressed by Equation (1):

$$P_{dc} = P_{pv} + P_{hess} \tag{1}$$

where P_{pv} denotes the power supplied by the PV modules to the system. P_{dc} represents the power required to maintain DC bus voltage stability. P_{hess} denotes the power absorbed or delivered by the hybrid energy storage system during the charging and discharging process.

The HESS consists of a battery and a supercapacitor, which are functionally complementary. The battery primarily supplies base-load power to meet sustained energy demands, while the supercapacitor responds to transient power fluctuations due to its high power density and fast dynamic response. The power balance within the HESS is given by Equation (2):

$$P_{hess} = P_{bat} + P_{sc} \tag{2}$$

where P_{bat} and P_{sc} are the battery and supercapacitor power, respectively, defined as positive during discharging and negative during charging.

Integrating Equations (1) and (2) gives:

$$P_{dc} = P_{pv} + P_{hess} = P_{pv} + P_{bat} + P_{sc} \tag{3}$$

2.2. Constant DC Bus Voltage Control Model

The effective current on the DC bus, denoted as i_{dc}, can be expressed as:

$$i_{dc} = C_{dc}\frac{du_{dc}}{dt} \tag{4}$$

The power P_{dc} required to maintain DC bus voltage stability can be expressed as:

$$P_{dc} = C_{dc}u_{dc}\frac{du_{dc}}{dt} \tag{5}$$

When the actual DC bus voltage u_{dc} is lower than the reference voltage u_{dcref}, the PI controller outputs a positive i_{dcref}, indicating that the DC bus capacitor requires charging. Conversely, if u_{dc} exceeds u_{dcref}, the PI controller generates a negative i_{dcref}, signaling the capacitor to discharge. The reference power P_{dcref}, which represents the power absorbed or delivered by the DC bus capacitor to maintain voltage stability, is calculated from i_{dcref} and u_{dc}.

2.3. Hybrid Energy Storage Power Allocation Strategies

The power allocation between the battery and the supercapacitor is realized through a low-pass filter (LPF). Based on the respective characteristics of the battery and supercapacitor, the battery handles the low-frequency components of power variations, while the supercapacitor manages the high-frequency power fluctuations. The transfer function of the first-order low-pass filter is given by:

$$H(s) = \frac{1}{1+Ts} \tag{6}$$

where T denotes the time constant of the filter, and s represents the differential operator.

Based on the power balance equations of the DC system units and the operational principle of the LPF, the power distribution strategy between the battery and the supercapacitor is implemented as shown in Figure 2.

The power borne by the hybrid energy storage system is obtained according to Equation (7):

$$P_{hess} = P_{bat} + P_{sc} = P_{dc} - P_{pv} \tag{7}$$

https://doi.org/10.3390/sym18010070

The power P_{hess} assumed by the hybrid energy storage system is passed through a LPF to obtain a smoothed portion, which is used as the battery reference power command P_{batref}, as shown in Equation (8):

$$P_{\text{batref}} = \frac{1}{1+Ts} P_{\text{hess}} \tag{8}$$

where the filtering time constant T can be determined according to the frequency band in which the battery needs to flatten the power fluctuation. And the supercapacitor reference power command P_{scref} is shown in Equation (9):

$$P_{\text{scref}} = P_{\text{hess}} - P_{\text{batref}} = \frac{Ts}{1+Ts} P_{\text{hess}} \tag{9}$$

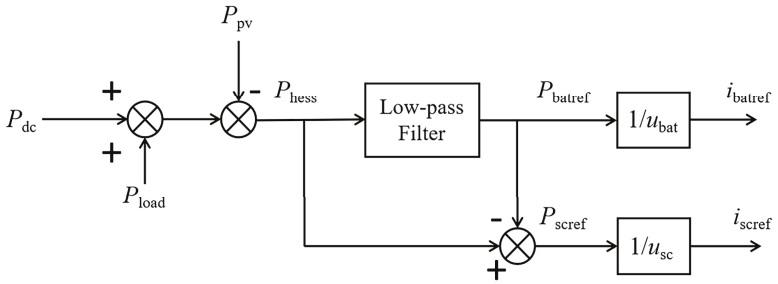


Figure 2. Power distribution diagram of the energy storage system.

3. VSG Control Strategy

3.1. Conventional VSG Control Strategy

The active power control of VSG emulates the active-power-frequency characteristics of SGs. Virtual mechanical power is generated by simulating the rotor mechanical equations, as shown in Equations (10) and (11). The reactive power control follows the excitation regulation characteristics of SGs. This control strategy utilizes the reactive power-voltage relationship to maintain voltage stability in the system, as expressed in Equation (12).

$$\begin{cases} P_{\text{m}} - P_{\text{e}} = J\omega_0 \frac{\text{d}\omega}{\text{d}t} + D\omega_0(\omega - \omega_0) \\ \theta = \int (\omega - \omega_0)\text{d}t \end{cases} \tag{10}$$

$$P_{\text{m}} = P_{\text{ref}} - K_{\text{p}}(\omega - \omega_0) \tag{11}$$

$$E = E_0 + \frac{1}{K_{\text{v}}s}[Q_{\text{ref}} - Q + K_{\text{q}}(U_{\text{ref}} - U)] \tag{12}$$

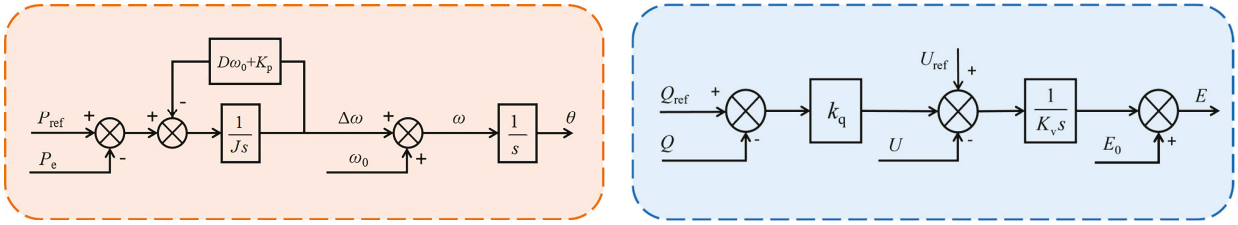
The control strategy comprises two functionally symmetrical blocks. The active power control block emulates the active power-frequency characteristics of SGs by simulating the rotor's mechanical equations, as detailed in Equations (10) and (11). Similarly, the reactive power control block replicates the excitation regulation characteristics using the reactive power-voltage relationship, formulated in Equation (12), to maintain voltage stability. This architectural symmetry, where both loops emulate the corresponding physical laws of SGs and utilize structurally analogous proportional feedback, simplifies multi-variable coordination and enhances system robustness. Based on these equations, the structural diagrams for active power-frequency and reactive power–voltage interactions are established and illustrated in Figure 3a and Figure 3b, respectively.

3.2. Small Signal Analysis of VSG

The VSG in the grid-connected inverter system topology as shown in Figure 1 is treated as an ideal voltage source. The grid-connected model is simplified. The equivalent circuit

https://doi.org/10.3390/sym18010070

of VSG in grid-connected mode is shown in Figure 4. E and U denote the inverter output voltage and grid voltage, respectively. R and L represent the combined filter impedance and grid-connected line resistance and inductance of the inverter. A small-signal analysis is performed to evaluate the influence of virtual inertia and virtual damping parameters on the VSG output response.



(**a**) (**b**)

Figure 3. Schematic diagram of active and reactive power control: (**a**) VSG active-frequency control structure diagram; (**b**) VSG reactive power-voltage control structure diagram.

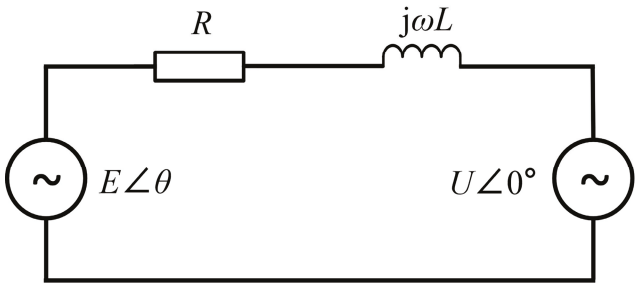


Figure 4. Equivalent circuit in phasor domain for VSG grid-connected operation.

Based on the circuit configuration in Figure 4 and the principles of power transmission, the VSG operates in coordination with the grid. Assuming a symmetric three-phase grid voltage with balanced amplitude and 120° phase separation, the active power transfer can be simplified to a single-phase equivalent model, as given by Equation (13). This ensures uniform virtual inertia and damping action across all phases:

$$P = \frac{EU\cos(\delta-\theta)}{Z} - \frac{U^2\cos\delta}{Z} \tag{13}$$

where Z and δ are as shown in Equations (14) and (15):

$$Z = \sqrt{R^2+(\omega L)^2} \tag{14}$$

$$\delta = \arctan(\omega L/R) \tag{15}$$

According to the rotor motion equation and the VSG active power-frequency droop equation, and using the small-signal modeling approach for approximation with reference to paper [20], the active closed-loop transfer function of the VSG is given by Equation (16).

$$G(s) = \frac{P_{out}(s)}{P_{ref}(s)} = \frac{\frac{1}{J\omega_0}\frac{EU}{Z}}{s^2+\left(\frac{D}{J}+\frac{K_P}{J\omega_0}\right)s+\frac{1}{J\omega_0}\frac{EU}{Z}} \tag{16}$$

The active-frequency link open-loop transfer function is shown in Equation (17):

$$G_o(s) = \frac{\frac{EU}{Z}}{J\omega_0 s^2+(D\omega_0+K_P)s} \tag{17}$$

https://doi.org/10.3390/sym18010070

The active power closed-loop transfer function $G_o(s)$ reveals that the VSG system exhibits second-order dynamics. Based on the standard second-order system model, the natural oscillation angular frequency ω_n and damping ratio ξ of VSG are demonstrated in Equation (18):

$$\begin{cases} \omega_n = \sqrt{\frac{EU}{J\omega_0 Z}} \\ \xi = D\sqrt{\frac{\omega_0 Z}{4JEU}} + K_p\sqrt{\frac{Z}{4J\omega_0 EU}} \end{cases} \tag{18}$$

Figure 5 presents the root locus of the active power loop under varying J and D parameters. When J is constant: increasing D shifts the complex conjugate poles toward the real axis, which elevates the damping ratio ξ. This suppresses overshoot and enhances dynamic stability. However, the increased pole real part slows the system response. Exceeding the critical D value drives the system into overdamped states, where the settling time is dominated by the real pole near the imaginary axis, potentially prolonging the regulation duration. When D is constant: increasing J moves the conjugate poles toward the imaginary axis, reducing ξ. This lowers oscillation frequency, increases overshoot, and degrades stability. In extreme cases, the poles approaching the imaginary axis may render the system marginally stable or even divergent.

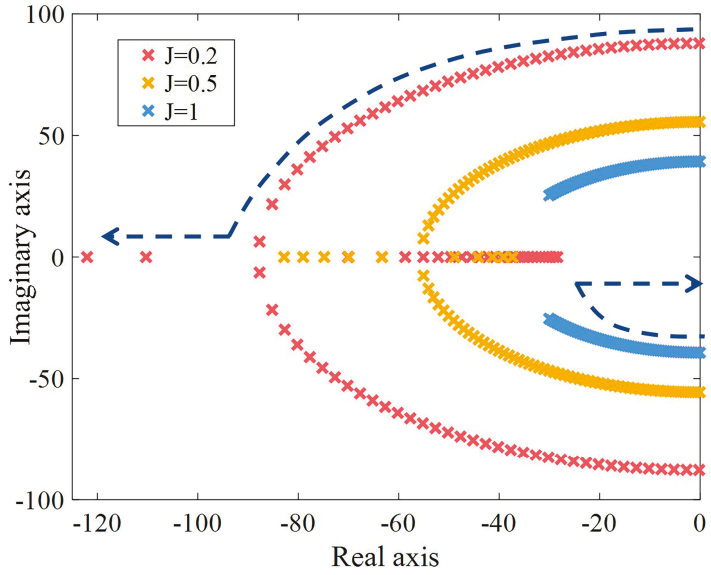


Figure 5. Pole distribution of VSG active power system when J and D change.

Figure 6a demonstrates that when the virtual inertia parameter J is fixed at 0.2, increasing the damping coefficient D gradually reduces the rising speed of the system step response. The active power overshoot significantly decreases, and the oscillation amplitude diminishes. The overall settling time shortens. This phenomenon arises because higher D values enhance the damping ratio ξ, strengthening the system's ability to dissipate oscillation energy. This mechanism effectively suppresses power oscillations. Peak power trends marked by red arrows further indicate that at low D values, the response curve exhibits noticeable oscillations after the peak. However, with increased D, both oscillation amplitude and frequency are substantially mitigated.

Figure 6b demonstrates that when the damping coefficient D is fixed at 10, increasing the virtual inertia parameter J gradually reduces the rising speed of the system response. However, the active power overshoot increases, and the oscillation amplitude significantly rises. This leads to intensified transient fluctuations before reaching steady state, prolonging the settling time. Peak power trends marked by red arrows indicate that at low J values, the response curve decays rapidly after the peak with minimal oscillation amplitude and

short settling time. When J increases, the rising phase response slows down, accompanied by sustained and pronounced oscillations. Both oscillation amplitude and settling time increase substantially. This behavior arises from the enhanced system inertia caused by higher J values, which decelerates dynamic response and intensifies oscillation characteristics.

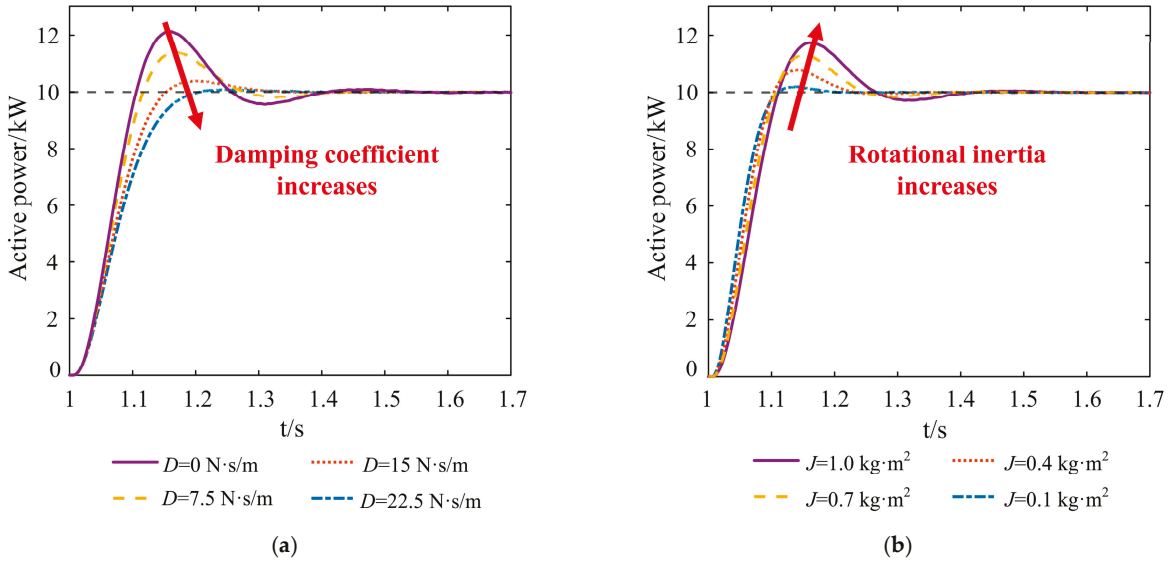


Figure 6. Active power step response curve with different parameters: (**a**) J = 0.2, different D corresponds to the step response; (**b**) D = 10, different J corresponds to the step response.

The interplay between J and D reflects a symmetrical trade-off: a large J enhances disturbance rejection but slows the response, while a small D permits oscillation and overshoot. Adjusting D suppresses transients at the cost of rise speed, whereas increasing J slows dynamics and amplifies overshoot. Thus, an optimal J and D pair achieves temporal symmetry in the step response by proportionally balancing the rise time, peak time, and settling time, which together minimize both undershoot and overshoot.

3.3. VSG Parameter Tuning

To ensure system stability, relevant parameters must be adjusted within appropriate ranges. This section discusses the selection of inertia and damping coefficients from four aspects: cutoff frequency, grid connection standards, stability margins, and frequency adjustment time.

K_p serves as the primary frequency regulation coefficient, characterizing the capability and response characteristics of VSG participating in primary frequency regulation. It quantifies the power support magnitude under unit frequency deviation. Equation (19) is employed in this study for its quantification:

$$K_p = \frac{S_{rate}}{1\%\omega_0} = 6.43 \tag{19}$$

where S_{rate} denotes the rated capacity of the VSG and 1% ω_0 denotes the 1% deviation of the system angular frequency.

Based on the open-loop transfer function $G_o(s)$ of the active power loop, the conditions for the active frequency loop at the cutoff frequency f_c are derived and presented in Equation (20):

$$|G_o(j2\pi f_c)| = \frac{EU}{2\pi f_c Z} \cdot \frac{1}{\sqrt{(J\omega_0 2\pi f_c)^2 + (D\omega_0 + K_P)^2}} = 1 \tag{20}$$

Further derivation yields the inertia J as shown in Equation (21):

$$J = \frac{D\omega_0 + K_\mathrm{p}}{2\pi\omega_0 f_c} \cdot \sqrt{\left[\frac{\frac{EU}{Z}}{2\pi f_c(D\omega_0 + K_\mathrm{p})}\right]^2 - 1} \tag{21}$$

To ensure the moment of inertia J has a clear physical meaning, its expression must be valid and non-zero. Additionally the expression inside the square root must be greater than zero. This determines the maximum cutoff frequency f_{cmax} as Equation (22):

$$f_{\mathrm{cmax}} = \frac{\frac{EU}{Z}}{2\pi(D\omega_0 + K_\mathrm{p})} \tag{22}$$

Then the range of values of the cutoff frequency f_c is shown in Equation (23):

$$f_c \triangleq \frac{\frac{EU}{Z}}{2\pi(D\omega_0 + K_\mathrm{p})} \leq f_{\mathrm{cmax}} \tag{23}$$

The standard [28] mandates the restriction of dynamic coupling effects in power systems. To achieve this, the frequency-domain decoupling control principle is employed, which imposes a key constraint: the maximum cutoff frequency of the power-voltage dual-loop control must satisfy $f_{\mathrm{cmax}} \leq 0.1 \times 2f_0$. The purpose of this constraint is to limit the bandwidth to 10% of the second harmonic frequency, thereby suppressing dynamic coupling between the power and voltage loops. Consequently, for a typical 50 Hz grid, this establishes a design boundary of f_{cmax} = 10 Hz. Applying this boundary, a parameter boundary analysis then yields the critical minimum damping coefficient D_{min}, as formulated in Equation (24):

$$D \geq D_{\mathrm{min}} = \frac{\frac{3EU}{Z} - 2\pi K_\mathrm{p} f_{\mathrm{cmax}}}{2\pi\omega_0 f_{\mathrm{cmax}}} \approx 11.2 \tag{24}$$

In addition, according to the standard [29], when the frequency changes by 1 Hz, the active power output of the inverter should vary from 40–100% of the rated capacity to provide power support:

$$D = \frac{\Delta t}{\Delta\omega_{\mathrm{max}}} = \frac{\Delta P}{\omega\Delta\omega_{\mathrm{max}}} \approx \frac{\Delta P}{\omega_0\Delta\omega_{\mathrm{max}}} \tag{25}$$

where ΔT is the torque variation; $\Delta\omega_{\mathrm{max}}$ is the maximum angular frequency variation; ΔP is the active power variation; ω_0 is the rated angular frequency; and ω is the angular frequency.

According to the design requirements of system stability in the automatic control principle, the steady-state parameters of the virtual inertia J need to satisfy the phase margin and magnitude margin constraints at the same time: the typical design range of the phase margin γ should be controlled at (30°, 80°), and the magnitude margin needs to be kept strictly positive.

Also from the open-loop transfer function $G_\mathrm{o}(s)$, the phase at the cutoff frequency ω_c (ω_c = 2πf_c) can be expressed as Equation (26):

$$G_o(\mathrm{j}\omega_c) = -\frac{EU}{\mathrm{X}} \cdot \frac{[J\omega_0\omega_c^2 + \mathrm{j}(D\omega_0 + K_\mathrm{p})\omega_c]}{(J\omega_0\omega_c^2)^2 + (D\omega_0 + K_p)^2\omega_c^2} \tag{26}$$

The phase margin γ can be obtained as shown in Equation (27):

$$\gamma = \arctan\frac{D\omega_0 + K_\mathrm{p}}{J\omega_0\omega_c}, \gamma \in [30^\circ, 80^\circ] \tag{27}$$

https://doi.org/10.3390/sym18010070

Further derivation leads to Equation (28):

$$\frac{D\omega_0 + K_\mathrm{p}}{J\omega_0\omega_c} \geq tan\gamma \tag{28}$$

In this paper, $\gamma = 45^\circ$ is selected as the design basis, under which the virtual inertia J is derived to satisfy Equation (29):

$$J \leq \frac{D\omega_0 + K_\mathrm{p}}{\omega_0\omega_c} cot\gamma \tag{29}$$

Since the regulation time of the system is closely related to the position of the closed-loop pole. Specifically, when the closed-loop pole is farther away from the imaginary axis, the regulation time of the system will be shorter. Therefore, in order to meet the requirement of fast response, the closed-loop pole of the system needs to be configured at a position farther away from the imaginary axis, and the detailed derivation is shown in Equation (30):

$$\mathrm{Re}(s_\mathrm{i}) = -\omega_\mathrm{n}\xi = -\frac{D\omega_0 + K_\mathrm{p}}{2J\omega_0} \leq -15 \tag{30}$$

Based on the above calculations and analysis, the moment of inertia J falls within the interval (0.045, 0.65]. The damping coefficient D lies within the range [11.2, 26.7].

4. RBF Neural Network-Based Control Strategy

RBF neural networks exhibit a compact structure and strong generalization capability. They efficiently handle complex nonlinear mappings between parameters and frequency. These properties make them suitable for VSG controller parameter tuning. They support both fast response and nonlinear optimization requirements.

Figure 7 shows the input-output structure of the RBF neural network. The two inputs correspond to the angular frequency variation $\Delta\omega$ and its rate of change $\mathrm{d}\omega/\mathrm{d}t$ in the VSG. The two output nodes represent the virtual inertia J and damping coefficient D. Since inertia cannot be negative in physical systems, a sigmoid activation function is applied at the output layer. The parameters j, i, and l denote the number of nodes in the input, hidden, and output layers, respectively. To cover the input space while maintaining computational efficiency and generalization capability, the hidden layer contains 5 neurons. The RBF neural network adopts a 2-5-1 structure.

For clarity, variables in the equations are denoted with superscripts (1), (2), and (3) to represent the input layer, hidden layer, and output layer, respectively. As shown in Figure 7, the neural network inputs are defined as the change in angular frequency and its rate of change. The output of the input layer is expressed as Equation (36):

$$O_\mathrm{j}^{(1)} = x_\mathrm{j}, \mathrm{j} = 1, 2 \tag{31}$$

where $x_1 = \omega - \omega_0 = \Delta\omega$, $x_2 = \mathrm{d}\omega/\mathrm{d}t$, and $O_\mathrm{j}^{(1)}$ corresponds to the output function of the input layer.

The input to the hidden layer is:

$$net_\mathrm{i}^{(2)}(k) = \vec{x}, \vec{x} = [x_1, x_2]^T \tag{32}$$

where $net_\mathrm{i}^{(2)}(K)$ is the input function of the neural network.

The output of the hidden layer is:

$$O_\mathrm{i}^{(2)}(k) = g(net_\mathrm{i}^{(2)}(k)), \mathrm{i} = 1, 2, \ldots, 5 \tag{33}$$

https://doi.org/10.3390/sym18010070

where $O_i^{(2)}(k)$ is the output function of the implicit layer and $g(x)$ is the Gaussian function:

$$g(x) = \exp(-\frac{\| \vec{x} - \vec{C_i} \|^2}{2b_i^2}), i = 1, 2, \ldots, 5 \tag{34}$$

where b_i is the width vector of the Gaussian function and c_i is the center vector of the ith hidden layer neuron. The Gaussian basis function g(x) exhibits radial symmetry about its center c_i, meaning its output depends solely on the Euclidean distance between input vector x and c_i, not on the direction of deviation. This inherent symmetry ensures that the RBF network treats bidirectional dynamic perturbations, such as positive/negative frequency deviations ($\Delta\omega$) and acceleration/deceleration ($d\omega/dt$), in a balanced and unbiased manner, thereby preserving input-output symmetry in adaptive parameter tuning.

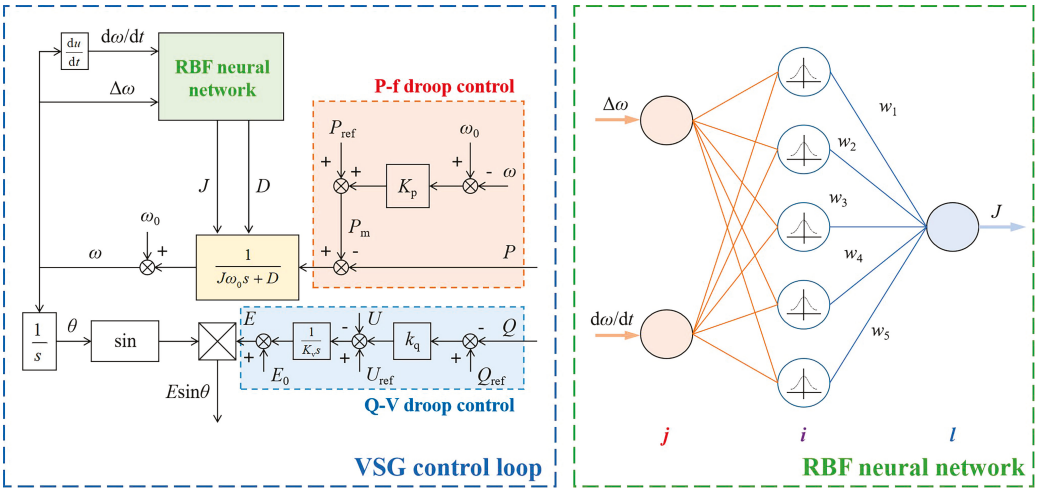


Figure 7. Adaptive control structure for VSG system based on RBF neural network.

The input to the output layer of the neural network is:

$$net_i^{(3)}(k) = \sum_{i=1}^{5} w_i^{(3)} O_i^{(2)}(k) \tag{35}$$

where $w_i^{(3)}$ is the weights of the RBF neural network.

The virtual inertia J as the output of the output layer can be expressed as:

$$J = O^{(3)}(k) = f(net_i^{(3)}(k)) \tag{36}$$

The output function of the neural network is taken as:

$$f(x) = \frac{ue^x}{e^x + e^{-x}} \tag{37}$$

where u is the upper limit of the rotational inertia.

The performance evaluation function of this NN is:

$$E(k) = \frac{1}{2}(\omega_0(k) - \omega(k))^2 \tag{38}$$

The gradient descent method is used to adjust the weights in the hidden layer, while the inertia link is introduced to accelerate the convergence rate of the algorithm, and the weights can be expressed as:

$$\Delta w_i^{(3)}(k) = -\eta \frac{\partial E(k)}{\partial w_i^{(3)}} + \alpha \Delta w_i^{(3)}(k-1) \tag{39}$$

where η and α, respectively, represent the learning rate and inertia coefficient.

The algorithm flow of the proposed control strategy is illustrated in Figure 8. The single inertia parameter adaptive control strategy discussed previously fails to account for the coupling relationship between the damping coefficient and system power-frequency oscillations. A theoretical analysis is subsequently conducted to determine the optimal damping ratio ξ. This parameter optimization aims to enhance the dynamic response characteristics of the second-order system.

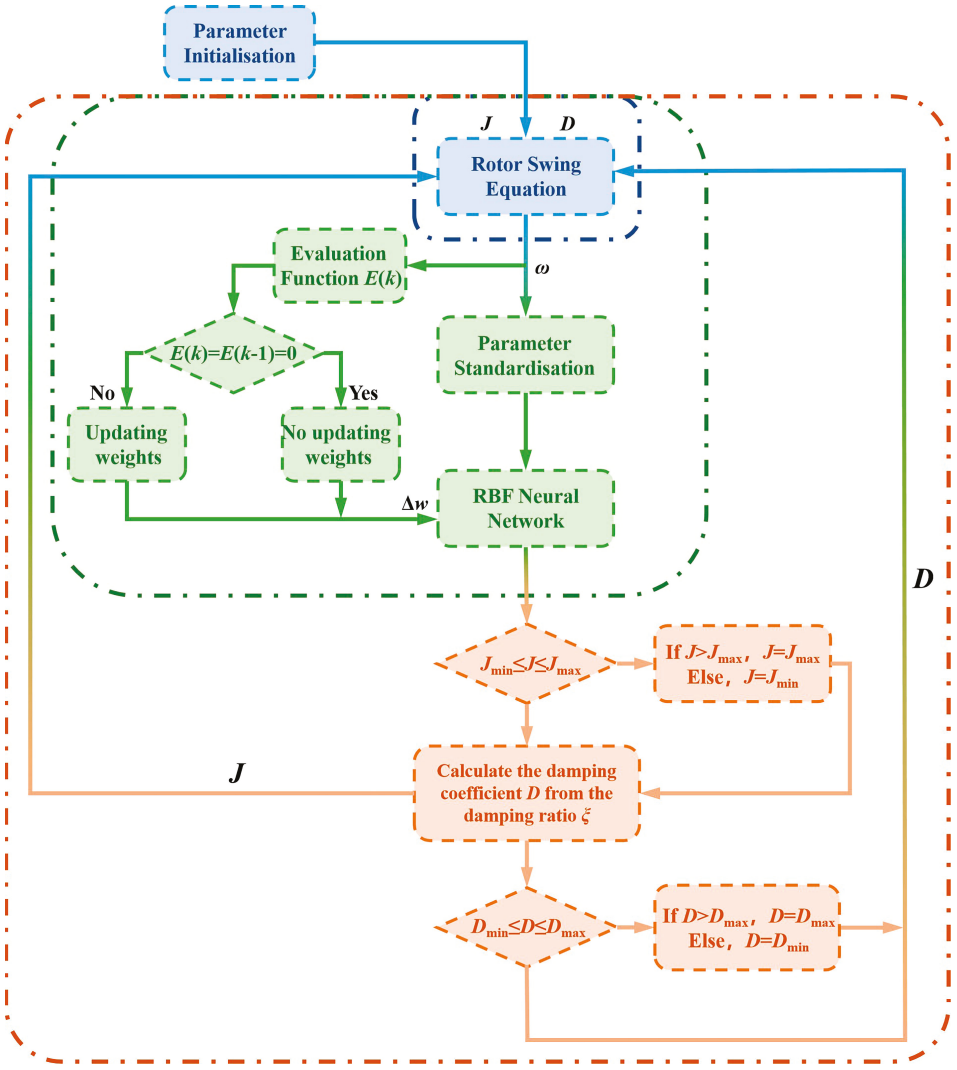


Figure 8. Flowchart of RBF algorithm.

In the typical second-order system, Equation (18) reveals the coupling relationship among inertia parameter J, damping coefficient D, and damping ratio ξ. When the damping ratio ξ remains fixed, the damping coefficient D can be determined based on the inertia parameter J.

The analysis of the VSG active power loop small-signal model demonstrates inherent trade-offs among system dynamic performance indicators: overshoot magnitude, settling

time, and response speed cannot be simultaneously optimized through single parameter tuning. In conventional VSG control frameworks, inertia parameter J and damping coefficient D exhibit strong coupling effects. This nonlinear parameter interaction prevents independent regulation strategies from achieving both overshoot suppression and rapid response requirements. Considering the fundamental constraint of limited overload capacity in power electronic devices, this study establishes a tuning principle prioritizing overshoot suppression over response speed optimization. Consequently, a damping ratio ξ value of 0.75 is selected as the design reference.

In summary, the proposed RBF-VSG control topology is shown in Figure 9. The system operates as follows. First, active power P and reactive power Q are measured at the point of common coupling. These measurements are used together with active power–frequency and reactive power–voltage control schemes. The mechanical power P_m, reference voltage magnitude E, and phase angle θ are then computed.

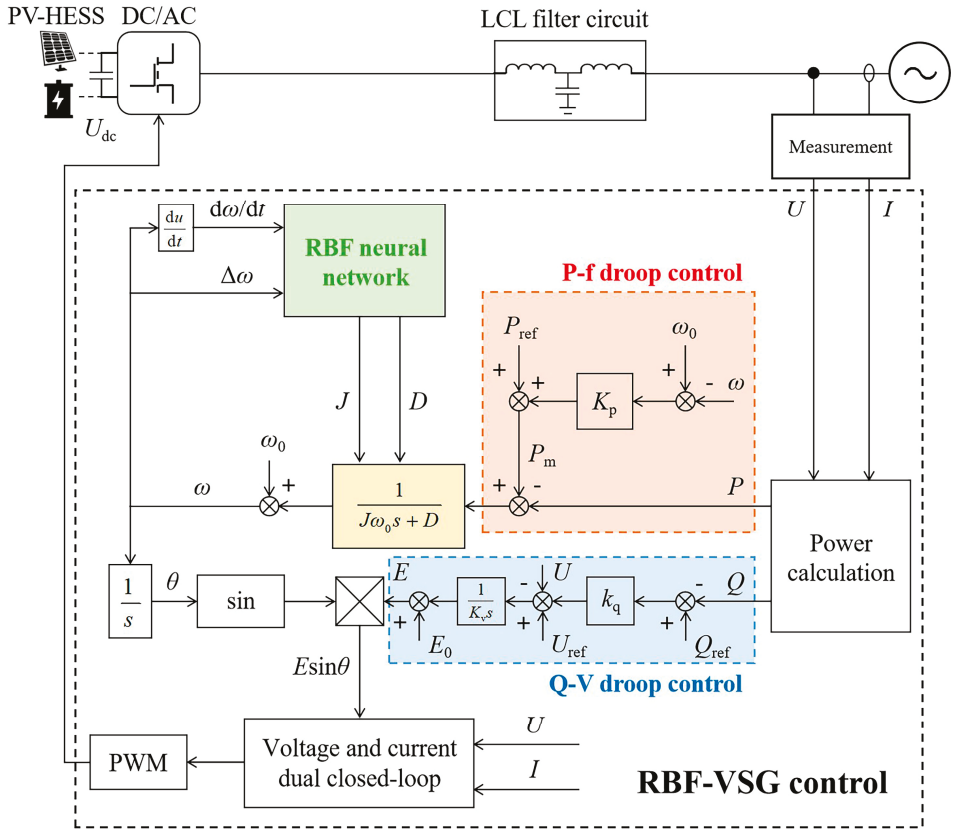


Figure 9. VSG control structure of PV-HESS based on RBF neural network.

Secondly, the VSG controller transmits the angular frequency ω and the angular frequency change rate $d\omega/dt$ to the RBF neural network, which calculates the error results according to the current inputs $\Delta\omega$ and $d\omega/dt$ by substituting them into the evaluation function and adjusts the size of the weights in the implicit layer, and then calculates the rotational inertia and damping coefficient at this time.

The adjusted rotational inertia and damping coefficients are reapplied to the VSG controller, and the updated controller sends the frequency signal at this moment to the integration link to obtain the phase angle θ. Finally, the output voltage amplitude E and phase angle θ generate a reference voltage to produce a modulating signal through the voltage-current control loop, which is sent to the PWM signal generator to produce a pulse signal to control the DC-AC converter.

https://doi.org/10.3390/sym18010070

5. Case Study

To verify the operational safety and control stability of the proposed PV-HESS under environmental variations and grid disturbances, a simulation model was developed in MATLAB/Simulink. A series of test scenarios were designed to evaluate the effectiveness of the proposed control strategy. Through calculation and tuning, the system simulation parameters are as shown in Table 1:

Table 1. Configuration table of system simulation parameters.

Definition	Parameter	Parameter Value
DC Bus Voltage	U_{dc}	750 V
Grid Voltage	U_g	380 V
Grid Angular Frequency	ω_g	314 rad/s
Filter Inductance	L_f	0.7 mH
Filter Capacitance	C_f	2250 uF
Learning Rate	η	0.65
Inertia Coefficient	α	0.05
Carrier Frequency	f_c	10,000 Hz

In subsequent cases, this study compares the performance of the RBF neural network-based VSG algorithm with that of the conventional fixed parameter VSG algorithm in the system. The piecewise linear parameter adaptive algorithm is also introduced for comparison. This algorithm is referred to as the linear algorithm. The specific expressions are given by Equations (40) and (41):

$$J = \begin{cases} J_0 & \Delta\omega(\mathrm{d}\omega/\mathrm{dt}) \le 0 \\ J_0 & \left|\mathrm{d}\omega/\mathrm{dt}\right| \le T_j \\ J_0 + K_j \left|\mathrm{d}\omega/\mathrm{dt}\right| & \Delta\omega(\mathrm{d}\omega/\mathrm{dt}) > 0 \cap \left|\mathrm{d}\omega/\mathrm{dt}\right| > T_j \end{cases} \tag{40}$$

$$D = \begin{cases} D_0 & \Delta\omega(\mathrm{d}\omega/\mathrm{dt}) \ge 0 \\ D_0 & \left|\mathrm{d}\omega/\mathrm{dt}\right| \le T_d \\ D_0 + K_d|\Delta\omega| & \Delta\omega(\mathrm{d}\omega/\mathrm{dt}) < 0 \cap \left|\mathrm{d}\omega/\mathrm{dt}\right| > T_d \end{cases} \tag{41}$$

where J_0 and D_0 are the value of rotational inertia and damping coefficient when the VSG is in stable operation, respectively; K_j and K_d are the adjustment coefficients of rotational inertia and damping coefficient, respectively; and T_j and T_d are the change thresholds. Based on the theoretical calculations, the specific parameter values are listed in Table 2.

Table 2. Configuration table of linear algorithm parameters.

Definition	Parameter	Parameter Value
Inertia Adjustment Coefficient	K_j	0.025 Kg·m^2·s^2·rad^{-1}
Damping Adjustment Coefficient	K_d	2.35 (N·s)·m^{-1}·rad^{-1}
Inertia Threshold	T_j	1.125 rad·s^{-2}
Damping Threshold	T_d	0.84 rad·s^{-2}
Initial Inertia Value	J_0	0.28 Kg·m^2
Initial Damping Value	D_0	21.6 (N·s)/m

5.1. Verification of Steady State Power Balance Characteristics

Case 1: The total simulation duration is 2 s. The grid-side active power reference is set to 15 kW, the reactive power reference is 0, and the frequency reference is 50 Hz. At 1 s, the solar irradiance increases from 800 W/m^2 to 1000 W/m^2, and simultaneously the grid-side

https://doi.org/10.3390/sym18010070

active power reference steps up from 15 kW to 20 kW and remains constant. At 1.5 s, the solar irradiance decreases back to 800 W/m^2.

Figure 10 shows that from 0.5 s to 1 s, the photovoltaic output is 7 kW, the battery output is 8 kW, and the inverter output is 15 kW. The system operates stably during this period. At 1 s, solar irradiance increases, raising the photovoltaic output to 10 kW. Simultaneously, the inverter power reference steps up to 20 kW, creating a power deficit. The energy storage system responds automatically. The battery handles low frequency fluctuations, increasing its output to 10 kW. The supercapacitor provides fast response to high frequency fluctuations, reducing stress on the battery. At 1.5 s, solar irradiance decreases, causing the photovoltaic output to drop back to 7 kW. The inverter power reference remains at 20 kW, further increasing the power deficit. The energy storage system compensates by increasing its output. The battery output rises to 13 kW to manage low frequency fluctuations. The supercapacitor maintains power stability through rapid charge and discharge to address high frequency fluctuations.

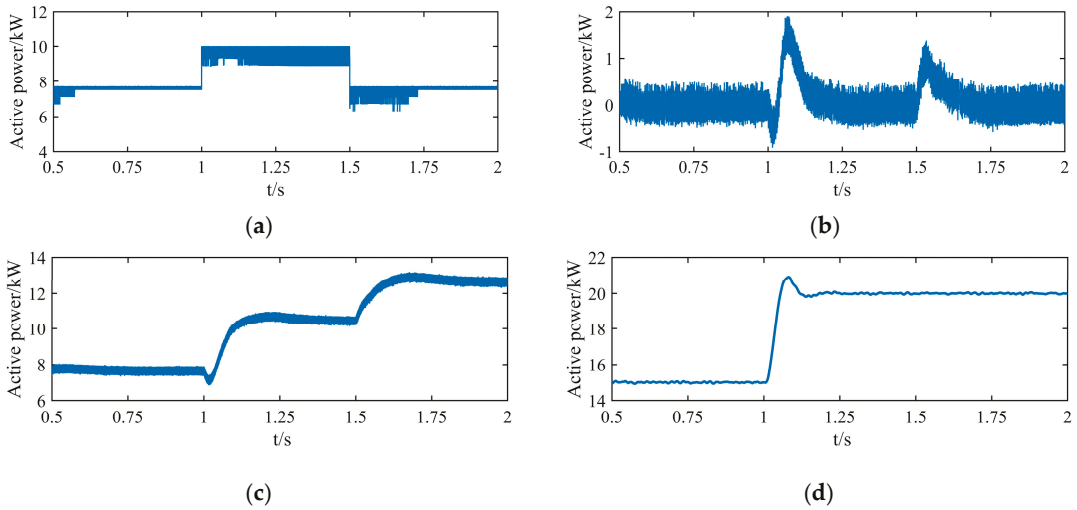


Figure 10. Output power of each component in the PV-HESS: (**a**) Photovoltaic output power; (**b**) Supercapacitor output power; (**c**) Battery output power; (**d**) Converter output power.

5.2. Transient Power Impact Response Verification

Case 1 verifies the system's steady-state power balance capability. To investigate the dynamic impact of grid-side power fluctuations, Case 2 is designed. Grid-side power fluctuations are introduced in Case 2. The effects on the DC side and grid side are analyzed. System response characteristics are also evaluated.

Case 2 details are as follows: The simulation duration is 2 s. The frequency remains constant at 50 Hz. The irradiance is maintained at 1000 W/m^2. The photovoltaic output remains steady at 10 kW. The grid-side active power command steps up from 15 kW to 20 kW at 1 s. Reactive power is kept at 0.

5.2.1. Analysis of Hybrid Energy Storage System Power Response

The analysis of Case 1 shows that the hybrid energy storage system needs to increase its output to compensate for the power deficit. The output power rises from the original 5 kW to 10 kW. The battery power increases from 5 kW to 10 kW during this process. However, the dynamic response and stability performance of the three control methods show distinct differences.

The battery output power under different control strategies is shown in Figure 11. The fixed parameter method exhibits the most significant power fluctuations. The peak power reaches 11,276 W. The overshoot is 12.76%. The output continues to oscillate after

returning to the steady-state value. This indicates poor system stability. In contrast, the linear control algorithm achieves a peak power of 10,986 W. The overshoot is 9.86%. The oscillation amplitude decreases significantly after stabilization. The stability performance is notably better than the fixed parameter method. The RBF neural network algorithm demonstrates the best performance. It has the shortest adjustment time. The overshoot is nearly zero. The output stabilizes at 10,732 W. The overshoot is 7.32%. The dynamic response curve is smooth. Power fluctuations are almost negligible. The comparison results demonstrate that the RBF neural network algorithm enhances battery output power. It also ensures better system stability and dynamic response performance. This makes it a more ideal control strategy.

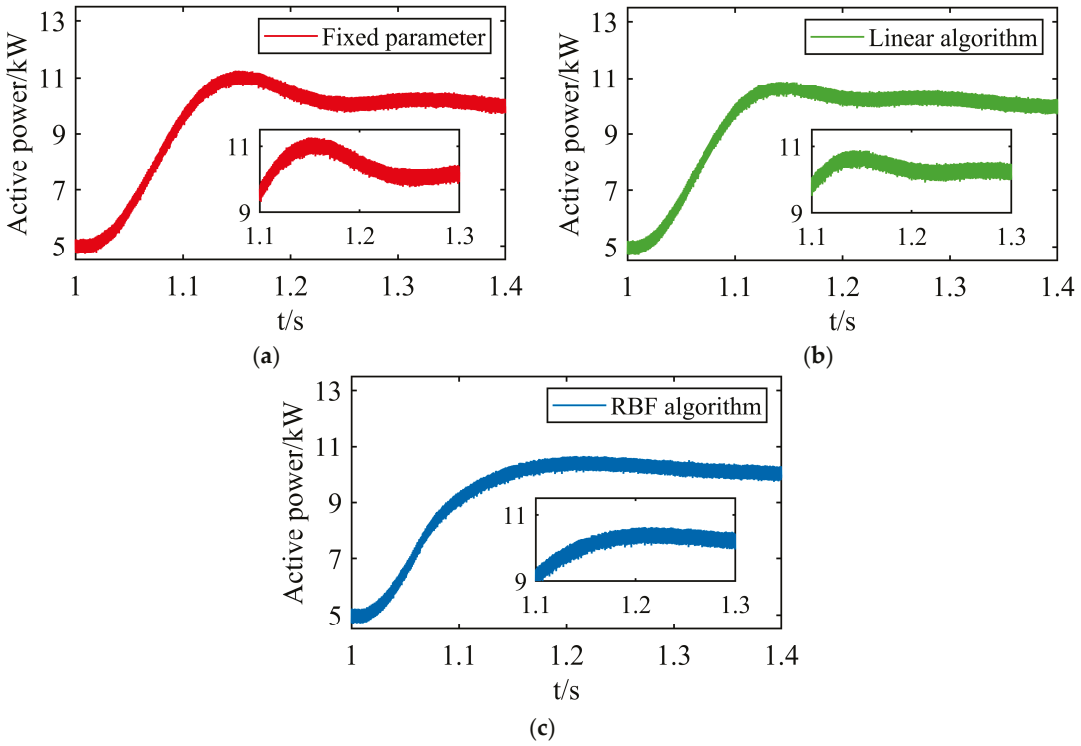


Figure 11. Battery output power under different control strategies: (**a**) Battery output power under fixed parameters; (**b**) Battery output power under linear algorithm; (**c**) Battery output power under the RBF algorithm.

Figure 12 compares the supercapacitor output power under different control strategies. The supercapacitor only exhibits significant power fluctuations during abrupt changes in power commands, demonstrating its role in mitigating power shocks and protecting the battery. The dynamic responses of three control methods are characterized as follows: The fixed-parameter method shows the largest fluctuations with peak power reaching 2488 W, accompanied by severe oscillations during steady-state recovery. The linear control algorithm achieves slightly lower peak power at 2483 W with reduced oscillation amplitude compared to the fixed-parameter method. The RBF algorithm demonstrates superior performance with peak power further reduced to 2363 W and negligible oscillations during transient recovery. These results confirm that the RBF algorithm effectively suppresses power fluctuations and delivers the best dynamic response. The comparative analysis indicates that the RBF algorithm can better handle grid-side power variations, thereby minimizing disturbances to the DC-side energy storage system and significantly enhancing overall system efficiency and reliability.

https://doi.org/10.3390/sym18010070

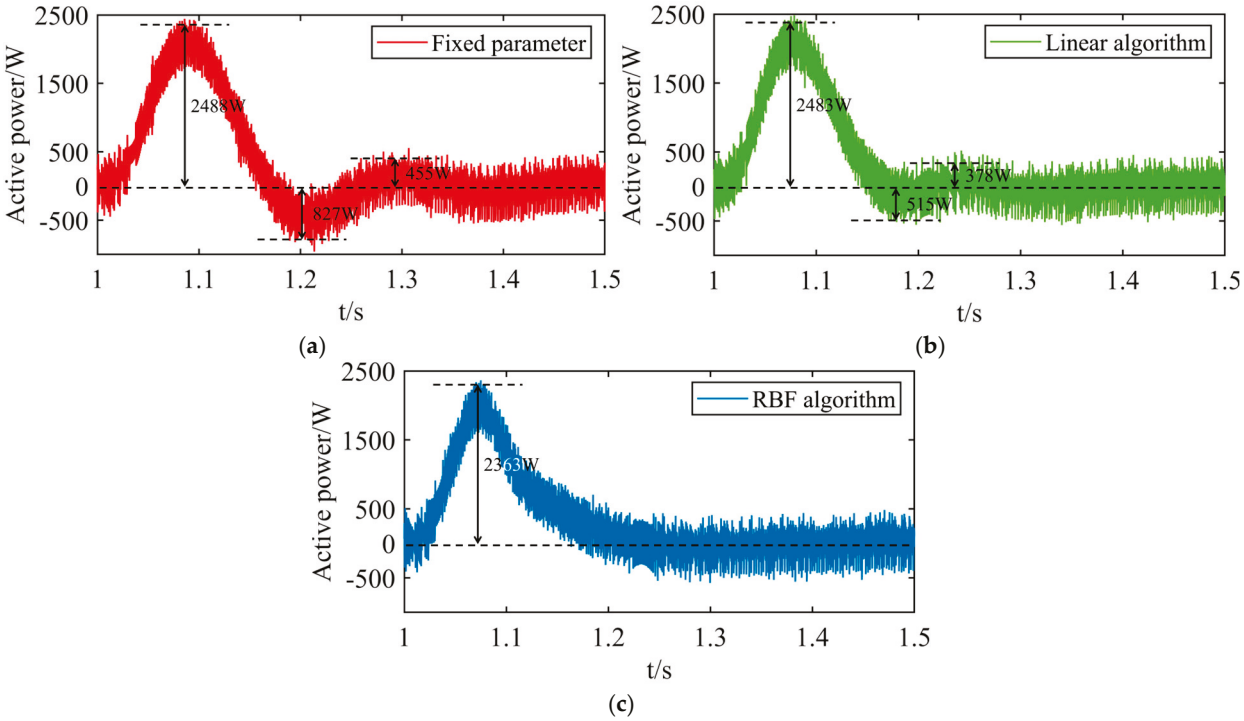


Figure 12. Supercapacitor output power under different control strategies: (**a**) Supercapacitor output power under fixed parameters; (**b**) Supercapacitor output power under linear algorithm; (**c**) Supercapacitor output power under the RBF algorithm.

5.2.2. Analysis of Fluctuations in DC Bus Voltage

The DC bus voltage fluctuations under different control strategies are shown in Figure 13. During the steady state operation of the system, the DC bus voltage is maintained stably at 750 V. When the step surge of the grid-side power occurs at the moment of 1 s, the DC bus voltage will fall instantaneously, and the dynamic response characteristics of different parameter regulation methods show significant differences. Under fixed-parameter control, the voltage drops to 736.77 V at the lowest level, and there are many oscillations during the recovery process, which reveals that the fixed-parameter control has insufficient dynamic regulation capability and cannot effectively suppress the voltage fluctuations. The linear parameter adaptive control raises the minimum voltage to 737.48 V, which is a slight improvement over the fixed parameter. In contrast, the RBF parameter adaptive control shows optimal performance, and the minimum voltage value only drops to 739.17 V, with the smallest fluctuation.

5.2.3. Analysis of Three-Phase Currents on the Grid Side of AC Power Systems

Figure 14 compares grid current fluctuations under different control strategies. Simulation results demonstrate that traditional fixed-parameter control causes significant surge current spikes in grid-side three-phase currents during active power step change cases. The peak surge current reaches 48 A with current overshoot lasting approximately 0.2 s, revealing limitations in conventional VSG control strategies caused by fixed virtual inertia and damping parameters, which prevent the system from adapting flexibly and rapidly to dynamically changing operating conditions. The linear algorithm reduces peak current to 47 A and shortens overshoot duration to 0.15 s, indicating preliminary effectiveness of parameter self-tuning strategies, though transient characteristics remain partially unmitigated. The proposed RBF algorithm achieves superior performance by restricting surge current peaks below 45 A and compressing overshoot duration to 0.1 s. This demonstrates

the RBF algorithm's capability to effectively suppress transient current disturbances while maintaining system stability.

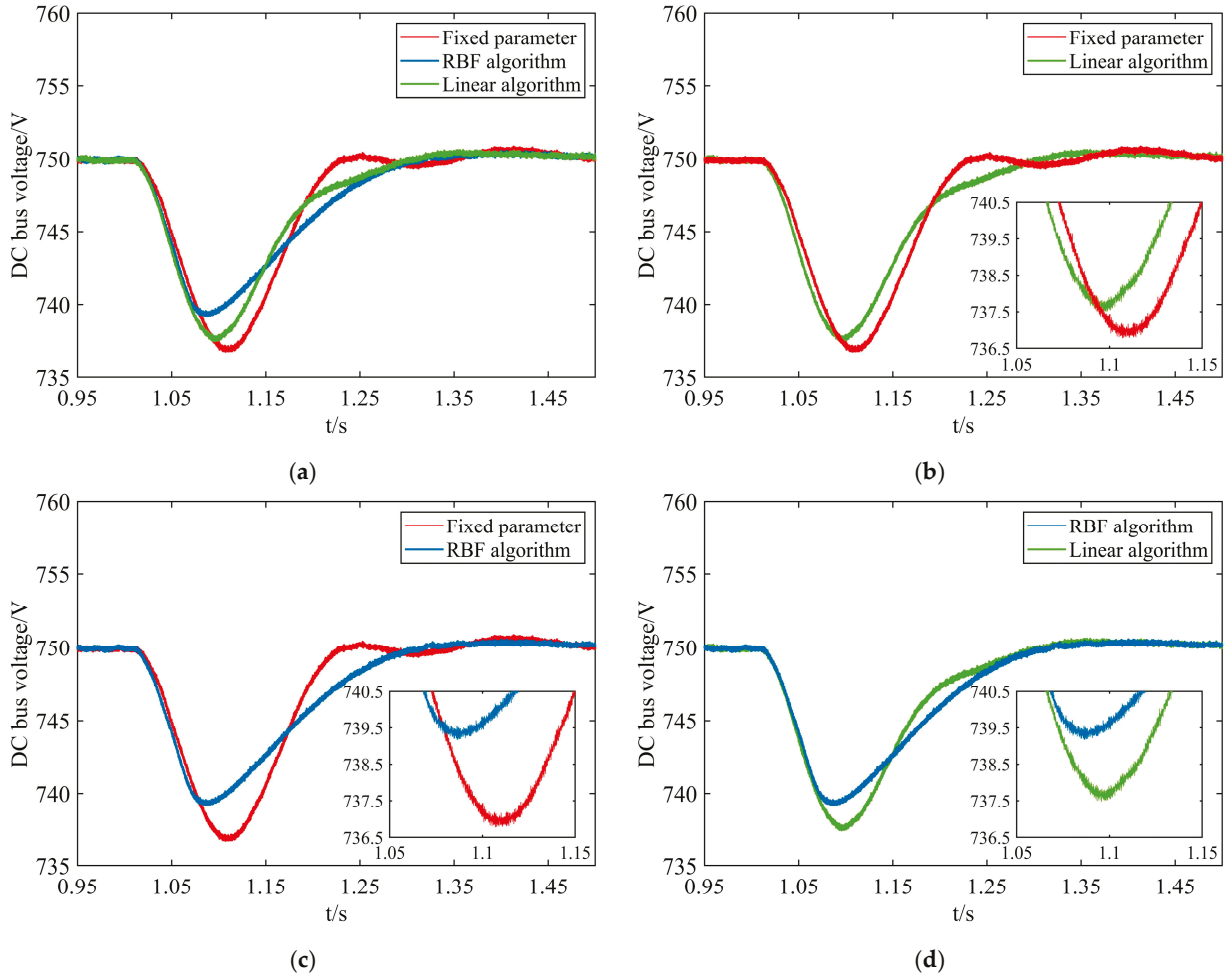


Figure 13. Comparison of DC bus voltage fluctuations under different control strategies: (**a**) Overview of DC bus voltage fluctuations; (**b**) Comparison of fixed parameters and linear algorithm; (**c**) Comparison of fixed parameters and RBF algorithm; (**d**) Comparison of linear algorithm and RBF algorithm.

5.3. Frequency-Power Regulation Performance Verification

Case 2 establishes the impact of grid power transients on the DC-side stability. Case 3 subsequently focuses on evaluating the dynamic regulation capability of the grid-side inverter. Given the clarity of DC-side power response characteristics from Case 2, this case specifically investigates the inverter's dynamic response performance during grid power and frequency adjustment processes.

Case 3 includes two subcases. Case 3a: Step changes in inverter active power commands induce system supply–demand mismatches. Case 3b: Grid-side frequency perturbations lead to system fluctuations.

5.3.1. Power Supply–Demand Imbalance

Case 3a: The grid-side active power command undergoes a step in 1 s, from 15 kW to 20 kW.

As shown in Figure 15, fixed-parameter control achieves a frequency regulation time of 0.207 s, an overshoot of 0.0784 Hz, and an offset of 0.0961 Hz, while power regulation reaches 0.514 s, 2037.4 W, and 2885 W, respectively. The linear algorithm reduces frequency regulation time to 0.203 s, lowers overshoot to 0.0731 Hz, and narrows the offset

https://doi.org/10.3390/sym18010070

to 0.0889 Hz; for power regulation, it decreases the time to 0.351 s, reduces overshoot to 1574.2 W, and shrinks the offset to 2123.1 W. Further adoption of the RBF algorithm shortens frequency regulation time to 0.192 s (compared to 0.203 s with the linear algorithm), lowers overshoot to 0.0615 Hz, and narrows the offset to 0.0779 Hz. Concurrently, power regulation time is reduced to 0.257 s, overshoot drops to 964.4 W, and the offset decreases to 1170.1 W, demonstrating consistent improvements over the linear algorithm.

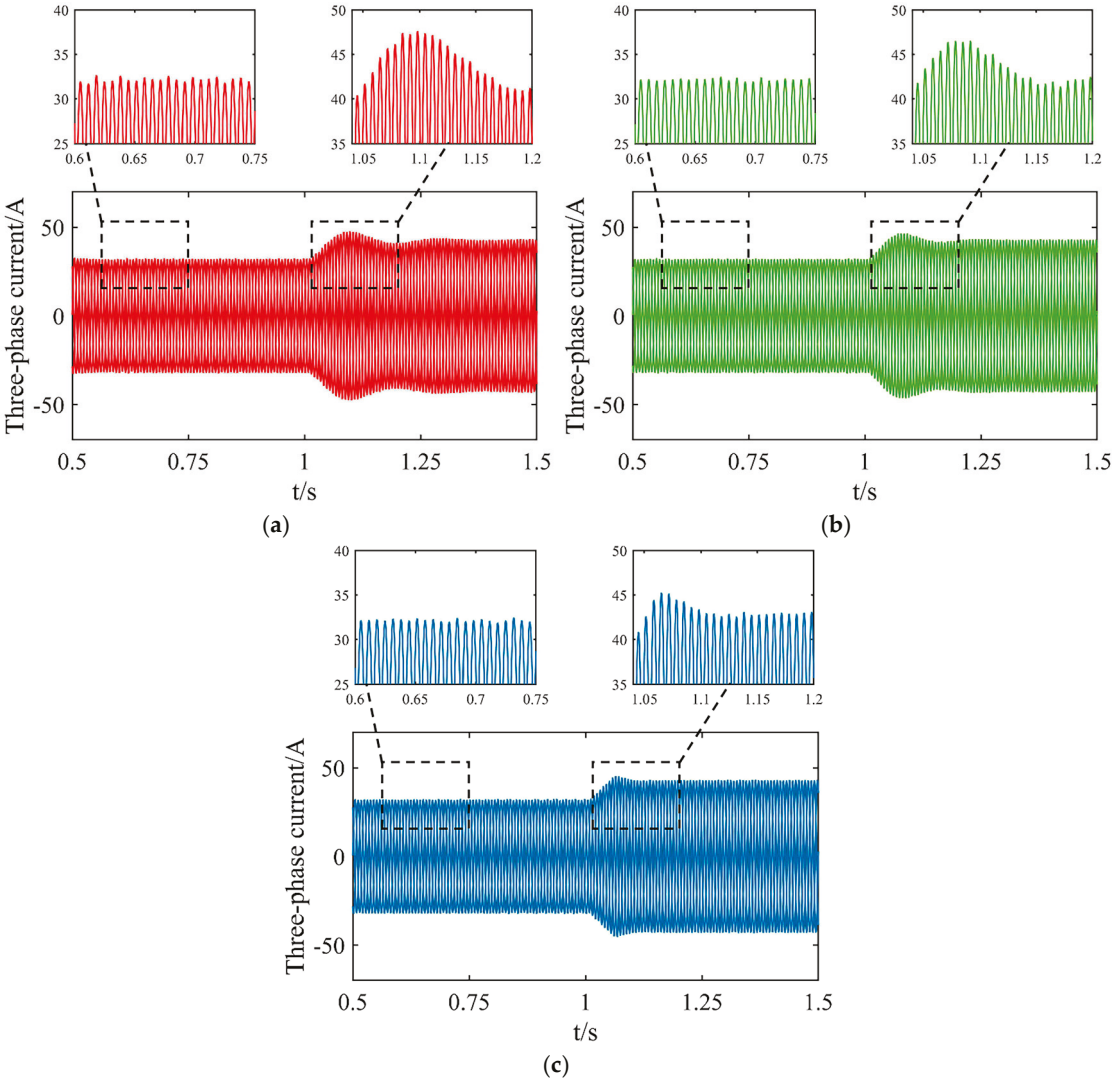
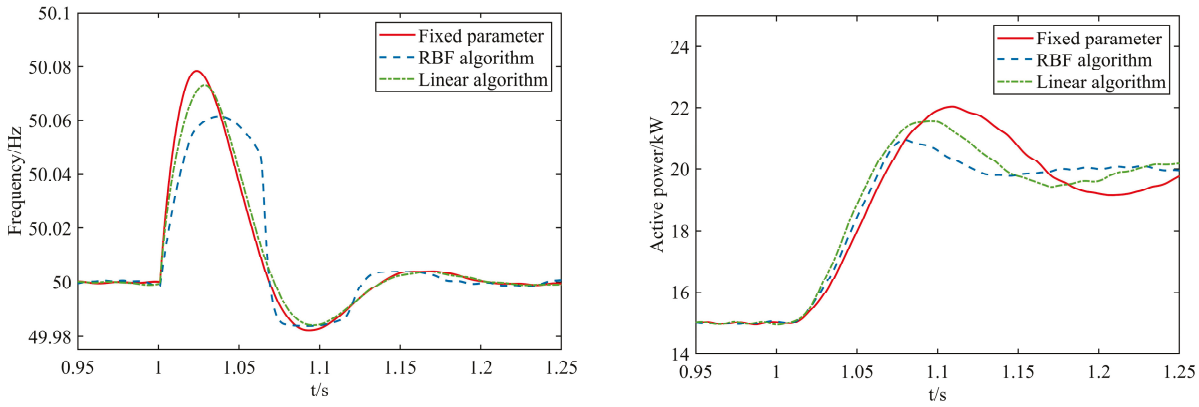


Figure 14. Grid current under different control strategies: (**a**) Fixed parameters; (**b**) Linear algorithm; (**c**) RBF algorithm.

The detailed data for Figure 15 are presented in Table 3. Under conditions of power supply–demand imbalance, the RBF algorithm simultaneously reduces both frequency and power overshoot, shortens the settling time, and minimizes the fluctuation ranges of frequency and power compared to fixed-parameter and linear algorithms. Specifically, under power imbalance conditions, in response to system power mismatch, the RBF algorithm achieves improvements of 52.7%, 50.1%, and 59.4% in power overshoot, settling time, and power fluctuation range, respectively, compared to the fixed-parameter algorithm. When compared to the linear algorithm, the corresponding improvements are 39.1%, 26.8%, and 44.9%. These results demonstrate that the RBF algorithm, through dynamic adaptive adjustment of control parameters, significantly suppresses power overshoot, considerably shortens settling time, and effectively narrows power fluctuation range. Its advantage

in suppressing power fluctuations is particularly prominent, fully demonstrating the superior performance of the RBF neural network in optimizing the dynamic response of nonlinear systems.



(**a**) (**b**)

Figure 15. Comparison of frequency and power fluctuations under different control strategies during power supply–demand imbalance: (**a**) Comparison of frequency fluctuations; (**b**) Comparison of power fluctuations.

Table 3. Frequency and power response performance metrics for different control strategies under power supply–demand imbalance.

	Fixed Parameters	Linear Algorithm	RBF Algorithm
Frequency Overshoot/Hz	0.078	0.073	0.062
Frequency Settling Time/s	0.207	0.203	0.192
Frequency Fluctuation Range/Hz	0.096	0.089	0.078
Power Overshoot/kW	2.037	1.574	0.964
Power Settling Time/s	0.514	0.351	0.257
Power Fluctuation Range/kW	2.885	2.123	1.170

Figure 16a,b present the dynamic adjustment characteristics of rotational inertia J and damping coefficient D under power supply–demand imbalance. In the conventional VSG control strategy, J and D remain constant at 0.25 and 21, respectively, lacking adaptive capability to system dynamics. In the linear adaptive algorithm, rotational inertia J is adjusted only when power fluctuates drastically and the rate of change in electrical angular frequency $\mathrm{d}\omega/\mathrm{d}t$ exceeds a critical threshold, with its peak value reaching 0.8. This value exceeds the previously determined optimal range of (0.045, 0.65], reflecting the algorithm's insufficient adaptability. When the fluctuation does not meet the condition, J remains stable at 0.28. The adjustment of the damping coefficient D is highly dependent on the electrical angular frequency deviation $\Delta\omega$, resulting in a relatively slow response speed.

In contrast, the RBF algorithm demonstrates superior dynamic response: when frequency fluctuations occur, J exhibits a brief delay but quickly activates and continuously optimizes to effectively suppress system oscillations. Throughout the adjustment process, the values of J and D are strictly confined within the optimal range, eliminating the need

https://doi.org/10.3390/sym18010070

for predefined fixed thresholds, thereby achieving precise real-time adaptation and efficient regulation of the system state.

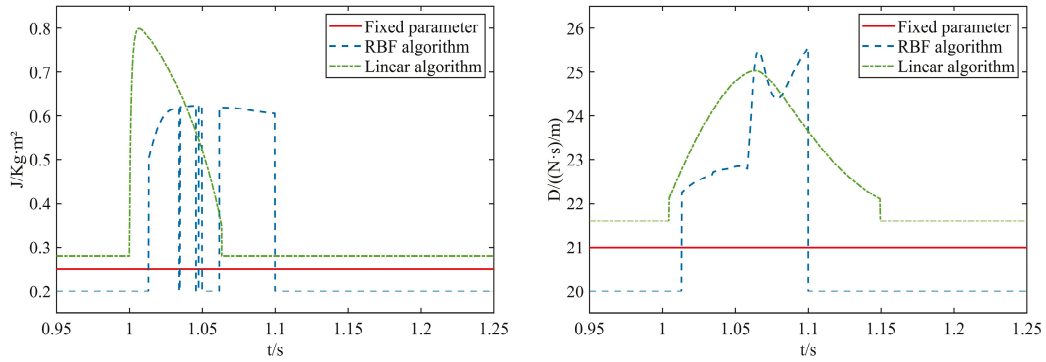


Figure 16. Comparison of rotational inertia and damping coefficients under different control strategies during power supply–demand imbalance: (**a**) Comparison of rotational inertia; (**b**) Comparison of damping coefficients.

5.3.2. Grid Frequency Disturbances

Case 3b describes a frequency drop on the grid side at 1 s, decreasing from 50 Hz to 49.9 Hz.

As shown in Figure 17, the fixed-parameter system achieves a frequency regulation time of 0.256 s, an overshoot of 0.0216 Hz, and an offset of 0.0272 Hz for frequency regulation, while power regulation reaches 0.36 s, 2166.3 W, and 2950.5 W, respectively. The linear algorithm reduces frequency regulation time to 0.182 s, lowers overshoot to 0.0145 Hz, and narrows the offset to 0.0171 Hz; for power regulation, it decreases time to 0.24 s, reduces overshoot to 1275.1 W, and shrinks the offset to 1719.7 W. The RBF algorithm further enhances performance: frequency regulation time shortens to 0.151 s, overshoot decreases to 0.0071 Hz, and offset narrows to 0.0084 Hz. Concurrently, power regulation time drops to 0.13 s, overshoot reduces to 309.8 W, and offset decreases to 466.3 W, demonstrating consistent improvements over the linear algorithm.

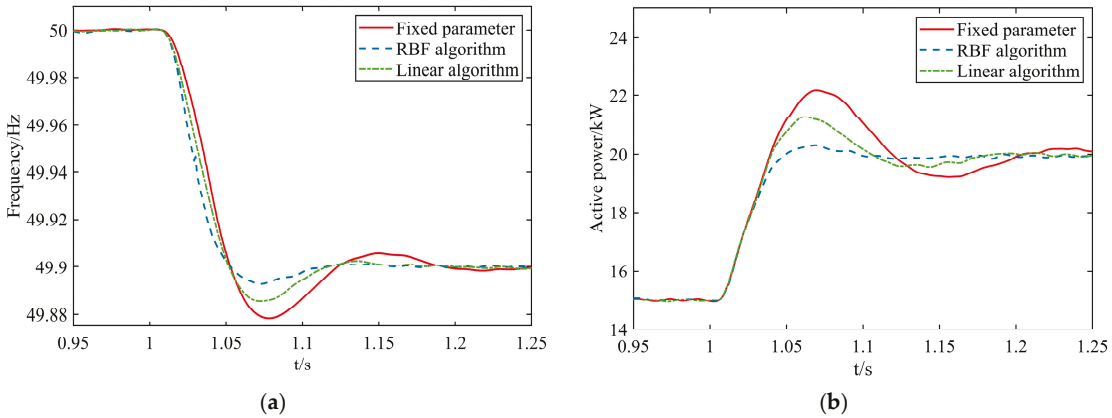


Figure 17. Comparison of frequency and power fluctuations under different control strategies during grid frequency disturbances: (**a**) Comparison of frequency fluctuations; (**b**) Comparison of power fluctuations.

The detailed data for Figure 17 are presented in Table 4. Under conditions of sudden grid frequency variations, the RBF algorithm can simultaneously reduce both frequency and power overshoot, shorten the settling time, and minimize the fluctuation ranges of both frequency and power compared to the fixed-parameter and linear algorithms. Specifically,

under sudden grid frequency variations, the RBF algorithm achieves improvements of 68.18%, 41.02%, and 70.37% in frequency overshoot, settling time, and fluctuation range, respectively, compared to the fixed-parameter VSG. When compared to the linear algorithm VSG, the corresponding improvements are 53.33%, 16.98%, and 52.94%. These results indicate that the RBF algorithm, through dynamic adaptive adjustment of parameters, significantly suppresses frequency overshoot, substantially shortens the settling time, and effectively narrows the frequency fluctuation range. Its advantage in suppressing frequency fluctuations is particularly prominent, fully demonstrating the superior performance of the RBF neural network in optimizing the dynamic response of nonlinear systems.

Table 4. Frequency and power response performance metrics for different control strategies under grid frequency disturbances.

	Fixed Parameters	Linear Algorithm	RBF Algorithm
Frequency Overshoot/Hz	0.022	0.015	0.007
Frequency Settling Time/s	0.256	0.182	0.151
Frequency Fluctuation Range/Hz	0.027	0.017	0.008
Power Overshoot/kW	2.166	1.275	0.310
Power Settling Time/s	0.360	0.240	0.130
Power Fluctuation Range/kW	2.951	1.720	0.466

Figure 18a,b illustrate the adaptive adjustment processes of rotational inertia J and damping coefficient D under grid frequency disturbances. In conventional VSG control strategies, both J and D remain fixed at 0.25 and 21, respectively, lacking the ability to respond to dynamic variations in the system. In the linear adaptive algorithm, J is adjusted only when the rate of change in the electrical angular frequency $\mathrm{d}\omega/\mathrm{d}t$ exceeds a critical threshold and the frequency deviation shows an increasing trend. The magnitude of adjustment is determined by the absolute value of $\mathrm{d}\omega/\mathrm{d}t$, reaching a maximum of 0.63. If the rate of frequency change remains below the threshold or enters a declining phase, J stays fixed at 0.28. The damping coefficient D is primarily regulated based on the magnitude of the electrical angular frequency deviation $\Delta\omega$, resulting in delayed responses under minor deviations and constrained overall dynamic performance.

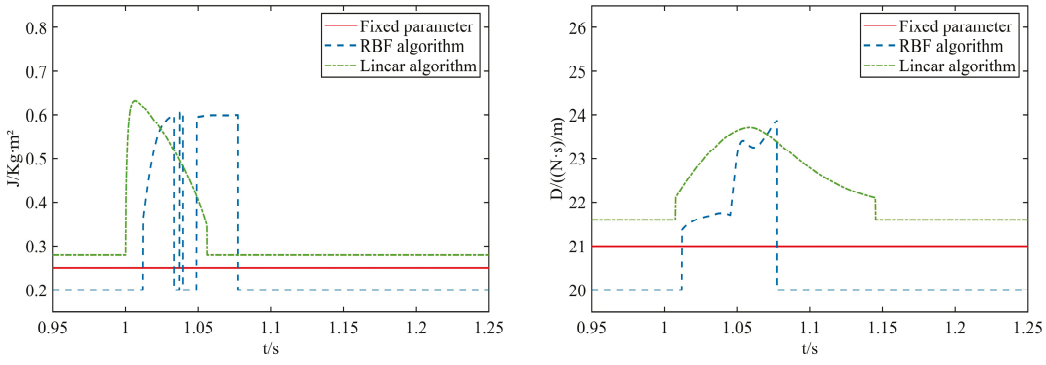


Figure 18. Comparison of rotational inertia and damping coefficients under different control strategies during grid frequency disturbances: (**a**) Comparison of rotational inertia; (**b**) Comparison of damping coefficients.

https://doi.org/10.3390/sym18010070

In contrast, the RBF algorithm demonstrates higher sensitivity and adaptability: despite a slight initial delay, rotational inertia J rapidly activates and continuously optimizes to effectively suppress system oscillations. This method eliminates reliance on predefined thresholds and enables continuous parameter adjustment based on real-time operating conditions. With enhanced nonlinear fitting capability and dynamic tracking performance, the system achieves significantly improved stability and robustness under complex operating conditions.

6. Conclusions

This paper proposes a PV-HESS topology based on an enhanced VSG control strategy. The structure employs a constant DC bus voltage control, utilizes a filtering unit to decouple high- and low-frequency power components, and integrates a VSG with real-time optimization of inertia and damping parameters through an RBF neural network. This approach enhances system stability and robustness under complex operating conditions. The main conclusions are summarized as follows:

(1) Within the VSG control framework, the virtual inertia J and damping coefficient D exhibit a trade-off relationship: increasing D enhances damping and suppresses oscillations, but slows dynamic response and prolongs settling time; conversely, higher J improves inertia support but reduces damping, shifting system poles closer to the imaginary axis, thereby increasing overshoot and compromising stability. Therefore, a balanced design of J and D is essential to achieve optimal transient performance and stability. This balance embodies the restoration of dynamic symmetry in inverter-dominated grids.

(2) The proposed DC-side energy storage control strategy achieves steady-state power balance through automatic compensation of power imbalances via constant DC bus voltage regulation. Imbalance power is dynamically allocated based on frequency characteristics: the supercapacitor mitigates high-frequency fluctuations, while the battery handles low-frequency components to stabilize system output. This frequency-based coordination enhances the overall dynamic regulation capability of the system.

(3) The RBF neural network-based adaptive control strategy demonstrates superior performance compared to fixed-parameter and linear adaptive methods. It effectively mitigates the impact of DC-side power imbalance and reduces surge current in the AC grid. Furthermore, during frequency and power regulation, the strategy significantly suppresses oscillations and overshoot, thereby enhancing system stability and dynamic response performance. Specifically, under power imbalance conditions, the RBF algorithm improves power overshoot, settling time, and fluctuation range by 52.7%, 50.1%, and 59.4%, respectively, compared to the fixed-parameter VSG, and by 39.1%, 26.8%, and 44.9% compared to the linear algorithm. Under grid frequency fluctuation conditions, it achieves improvements of 68.18%, 41.02%, and 70.37% in frequency overshoot, settling time, and fluctuation range over the fixed-parameter VSG, and 53.33%, 16.98%, and 52.94% over the linear algorithm.

Future work will focus on enhanced VSG-based control strategies for photovoltaic hybrid energy storage systems, particularly in multi-source DC-side integration scenarios. The study will center on optimizing the RBF neural network algorithm and developing a SOC parameter fusion mechanism for the energy storage system. A hardware-in-the-loop simulation platform will be established to evaluate the dynamic response and robustness of the proposed control strategy under complex operating conditions.

Author Contributions: Conceptualization, M.L. and S.W.; methodology, M.L. and S.W.; software, M.L. and S.W.; validation, M.L. and S.W.; formal analysis, M.L. and S.W.; investigation, M.L. and

S.W.; resources, M.L. and S.W.; data curation, M.L. and S.W.; writing—original draft, M.L. and S.W.; writing—review and editing, M.L. and S.W. All authors have read and agreed to the published version of the manuscript.

Funding: This research was funded by State Grid Science & Technology Project in China, grant number 4000-202316071A-1-1-ZN.

Data Availability Statement: The original contributions presented in this study are included in the article. Further inquiries can be directed to the corresponding author.

Conflicts of Interest: The authors declare that this research was conducted in the absence of any commercial or financial relationships that could be construed as a potential conflict of interest. The authors declare that this study received funding from the State Grid Science & Technology Project in China, grant number 4000-202316071A-1-1-ZN. The funders had no role in the design of this study; in the collection, analyses, or interpretation of data; in the writing of the manuscript; or in the decision to publish the results.

Abbreviations

The following abbreviations are used in this manuscript:

VSG	Virtual synchronous generator
PV-HESS	Photovoltaic hybrid energy storage system
RBF	Radial basis function
BGCs	Bidirectional grid-connected converters
DC-MG	DC microgrid
ANPC	Adaptive neural predictive control
UBESSs	Ultrabattery energy storage systems
ADP	Adaptive dynamic programming

References

1. Zhong, Q.C. Power-Electronics-Enabled Autonomous Power Systems: Architecture and Technical Routes. *IEEE Trans. Ind. Electron.* **2017**, *64*, 5907–5918. [CrossRef]
2. Pan, D.; Wang, X.; Liu, F.; Shi, R. Transient Stability of Voltage-Source Converters with Grid-Forming Control: A Design-Oriented Study. *IEEE J. Emerg. Sel. Top. Power Electron.* **2020**, *8*, 1019–1033. [CrossRef]
3. Li, C.; Yang, Y.Q.; Mao, X.; Xiong, X.H.; Dragicevic, T. Modeling, control and stabilization of virtual synchronous generator in future power electronics-dominated power systems: A survey of challenges, advances, and future trends. *Int. J. Electron. Power Energy Syst.* **2025**, *171*, 111001. [CrossRef]
4. Liu, K.Y.; Qian, T.; Zhang, W.; Wu, S.H.; Han, R.S.; Hou, K.; Wu, Z.J.; Hu, Q.R. Review on small-signal stability of multiple virtual synchronous generators. *Renew. Sustain. Energy Rev.* **2025**, *215*, 115543. [CrossRef]
5. Al-Kaoaz, H.N.A.; Alsammak, A.N.B. Utilizing Hybrid Renewable Energy Systems for Enhancing Transient Stability in Power Grids: A Comprehensive Review. *J. Eur. Syst. Autom.* **2023**, *56*, 687–696. [CrossRef]
6. Li, D.; Zhu, Q.; Lin, S.; Bian, X.Y. A Self-Adaptive Inertia and Damping Combination Control of VSG to Support Frequency Stability. *IEEE Trans. Energy Convers.* **2017**, *32*, 397–398. [CrossRef]
7. Ren, M.; Li, T.; Shi, K.; Xu, P.; Sun, Y. Coordinated Control Strategy of Virtual Synchronous Generator Based on Adaptive Moment of Inertia and Virtual Impedance. *IEEE Jour. Emer. Select. Top. Circu. Syst.* **2021**, *11*, 99–110. [CrossRef]
8. Cheng, H.; Li, C.; Ghias, A.M.Y.M.; Blaabjerg, F. Dynamic Coupling Mechanism Analysis Between Voltage and Frequency in Virtual Synchronous Generator System. *IEEE Trans. Power Syst.* **2024**, *39*, 2365–2368. [CrossRef]
9. Chen, S.M.; Sun, Y.; Han, H.; Fu, S.Q.; Luo, S.H.; Shi, G.Z. A Modified VSG Control Scheme with Virtual Resistance to Enhance Both Small-Signal Stability and Transient Synchronization Stability. *IEEE Trans. Power Electron.* **2023**, *38*, 6005–6014. [CrossRef]
10. Chen, M.; Zhou, D.; Blaabjerg, F. Enhanced Transient Angle Stability Control of Grid-Forming Converter Based on Virtual Synchronous Generator. *IEEE Trans. Ind. Electron.* **2022**, *69*, 9133–9144. [CrossRef]
11. Ge, P.J.; Xiao, F.; Tu, C.M.; Guo, Q.; Gao, J.Y.; Song, Y.F. Transient Stability Enhancement Control for VSG Considering Power Angle Stability and Fault Current Limitation. *CSEE J. Power Energy Syst.* **2025**, *11*, 173–183.
12. Salleh, Z.M.; Alsammak, A.N.B.; Mohammed, H.A. Enhancing Power System Transient Stability Using Static Var Compensator Based on a Fuzzy Logic Controller. *J. Eur. Syst. Autom.* **2024**, *57*, 1565–1572. [CrossRef]

13. Chen, X.; Ma, M.; Yan, Z. An improved parameter boundary calculation method for virtual synchronous generator with capacity constraints of energy storage system. *Electron. Power Syst. Res.* **2025**, *241*, 111391. [CrossRef]
14. Chen, J.; Donnell, T.O. Parameter Constraints for Virtual Synchronous Generator Considering Stability. *IEEE Trans. Power Syst.* **2019**, *34*, 2479–2481. [CrossRef]
15. Liu, J.; Hou, Y.; Guo, J.; Liu, X.; Liu, J. A Cost-Efficient Virtual Synchronous Generator System Based on Coordinated Photovoltaic and Supercapacitor. *IEEE Trans. Power Electron.* **2023**, *38*, 16219–16229. [CrossRef]
16. Lamaouche, Z.; Hamadi, A.; Ndtoungou, A.; Gustave, K.; Al-Haddad, K. Cascade Droop-Virtual Synchronous Generator Control Approach to Improve Frequency Deviation. In Proceedings of the IECON 2023—49th Annual Conference of the IEEE Industrial Electronics Society, Singapore, 16–19 October 2023; pp. 1–6.
17. Yang, D.-Q.; Li, M.-J.; Ma, T.; Ni, J.-W.; Han, Z.-Y. Study on adaptive VSG parameters and SOC control strategy for PV-HESS primary frequency regulation. *Energy* **2025**, *314*, 133909. [CrossRef]
18. Mao, M.; Qian, C.; Ding, Y. Decentralized coordination power control for islanding microgrid based on PV/BES-VSG. *CPSS Trans. Power Electron. Appl.* **2018**, *3*, 14–24. [CrossRef]
19. Singh, A.K.; S, K. Active Damping Control using Virtual Synchronous Generator and Sliding Mode Technique for Solar PV and BES based Isolated Microgrid. In Proceedings of the 2024 IEEE 11th Power India International Conference (PIICON), Jaipur, India, 10–12 December 2024; pp. 1–6.
20. Xia, Y.; Wang, Y.; Chen, Y.; Shi, J.H.; Yang, Y.Q.; Li, W.; Li, K. A Cooperative Adaptive VSG Control Strategy Based on Virtual Inertia and Damping for Photovoltaic Storage System. *Energies* **2025**, *18*, 1505. [CrossRef]
21. Papageorgiou, P.G.; Oureilidis, K.O.; Christoforidis, G.C. Adaptive frequency regulation in a low-inertia low-voltage AC microgrid with multiple hybrid storage systems and photovoltaics. *Sustain. Energy Grids Netw.* **2025**, *44*, 102040. [CrossRef]
22. Wu, W.; Chen, Y.; Luo, A.; Zhou, L.; Zhou, X.; Yang, L.; Dong, Y.; Guerrero, J.M. A Virtual Inertia Control Strategy for DC Microgrids Analogized with Virtual Synchronous Machines. *IEEE Trans. Ind. Electron.* **2017**, *64*, 6005–6016. [CrossRef]
23. Shi, R.; Zhang, X.; Hu, C.; Xu, H.; Gu, J.; Cao, W. Self-tuning virtual synchronous generator control for improving frequency stability in autonomous photovoltaic-diesel microgrids. *J. Mod. Power Syst. Clean Energy* **2018**, *6*, 482–494. [CrossRef]
24. Mohamed, M.M.; El Zoghby, H.M.; Sharaf, S.M.; Mosa, M.A. Optimal virtual synchronous generator control of battery/supercapacitor hybrid energy storage system for frequency response enhancement of photovoltaic/diesel microgrid. *J. Energy Storage* **2022**, *51*, 104317. [CrossRef]
25. Mir, A.S.; Senroy, N. Self-Tuning Neural Predictive Control Scheme for Ultrabattery to Emulate a Virtual Synchronous Machine in Autonomous Power Systems. *IEEE Trans. Neural Netw. Learn. Syst.* **2020**, *31*, 136–147. [CrossRef] [PubMed]
26. Yao, F.; Zhao, J.; Li, X.; Mao, L.; Qu, K. RBF Neural Network Based Virtual Synchronous Generator Control with Improved Frequency Stability. *IEEE Trans. Ind. Inform.* **2021**, *17*, 4014–4024. [CrossRef]
27. Wang, Z.; Yu, Y.; Gao, W.; Davari, M.; Deng, C. Adaptive, Optimal, Virtual Synchronous Generator Control of Three-Phase Grid-Connected Inverters Under Different Grid Conditions—An Adaptive Dynamic Programming Approach. *IEEE Trans. Ind. Inform.* **2022**, *18*, 7388–7399. [CrossRef]
28. *IEEE Std 1547-2018*; IEEE Standard for Interconnection and Interoperability of Distributed Energy Resources with Associated Electric Power Systems Interfaces. IEEE Standards Association: New York, NY, USA, 2018.
29. *EN 50438:2013*; Requirements for Micro-Generating Plants to be Connected in Parallel with Public Low-Voltage Distribution Networks. CENELEC: Brussels, Belgium, 2013.

Disclaimer/Publisher's Note: The statements, opinions and data contained in all publications are solely those of the individual author(s) and contributor(s) and not of MDPI and/or the editor(s). MDPI and/or the editor(s) disclaim responsibility for any injury to people or property resulting from any ideas, methods, instructions or products referred to in the content.

symmetry

MDPI

Article

Construction of Typical Scenarios for Multiple Renewable Energy Plant Outputs Considering Spatiotemporal Correlations

Yuyue Zhang [1], Yan Wen [1], Nan Wang [1], Zhenhua Yuan [1], Lina Zhang [1] and Runjia Sun [2,*]

[1] Economic & Technology Research Institute of State Grid Shandong Electric Power Company, Jinan 250021, China; hitzhangyuyue@163.com (Y.Z.); gwsdjyybgs@163.com (Y.W.); wangnan@jyy.sd.sgcc.com.cn (N.W.); yuanzhenhua@jyy.sd.sgcc.com.cn (Z.Y.); zhanglina@jyy.sd.sgcc.com.cn (L.Z.)

[2] School of Electrical Engineering, Shandong University, Jinan 250061, China

* Correspondence: sunrunjia@sdu.edu.cn

Abstract

A high-quality set of typical scenarios is significant for power grid planning. Existing construction methods for typical scenarios do not account for the spatiotemporal correlations among renewable energy plant outputs, failing to adequately reflect the distribution characteristics of original scenarios. To address the issues mentioned above, this paper proposes a construction method for typical scenarios considering spatiotemporal correlations, providing high-quality typical scenarios for power grid planning. Firstly, a symmetric spatial correlation matrix and a temporal autocorrelation matrix are defined, achieving quantitative representation of spatiotemporal correlations. Then, distributional differences between typical and original scenarios are quantified from multiple dimensions, and a scenario reduction model considering spatiotemporal correlations is established. Finally, the genetic algorithm is improved by incorporating adaptive parameter adjustment and an elitism strategy, which can efficiently obtain high-quality typical scenarios. A case study involving five wind farms and fourteen photovoltaic plants in Belgium is presented. The rate of error between spatial correlation matrices of original and typical scenario sets is lower than 2.6%, and the rate of error between temporal autocorrelations is lower than 2.8%. Simulation results demonstrate that typical scenarios can capture the spatiotemporal correlations of original scenarios.

Keywords: typical scenario; renewable energy plant outputs; spatiotemporal correlation; scenario reduction; genetic algorithm

1. Introduction

Over the past decade, the installed capacity of renewable energy generation has continued to grow and is expected to maintain an upward trend in the foreseeable future [1]. However, the inherent uncertainty of renewable energy plant outputs can lead to challenges in matching power generation with real-time load demand, thereby posing risks to the secure and stable operation of the power system [2]. To address the uncertainty of renewable energy, multi-scenario planning based on stochastic programming theory is a commonly employed approach in power system planning.

A high-quality set of typical scenarios is a prerequisite for obtaining optimal solutions in multi-scenario planning [3]. To ensure the optimality of solutions, it is essential to construct a typical scenario set that accurately reflects the distribution characteristics of renewable energy plant power outputs [4]. The construction of a typical scenario set mainly

consists of two steps: scenario generation and scenario reduction [5]. An original scenario set is first generated to capture the output patterns of renewable energy plants, then this original set is reduced to obtain the final set of typical scenarios.

Directly utilizing historical output data from renewable energy plants for original scenarios is a commonly used approach for scenario generation. When historical data are insufficient, original scenarios can be expanded using methods such as probabilistic sampling [6,7], artificial intelligence techniques [8–12], and time-series production simulation [13,14]. However, using a large number of original scenarios for power grid planning can significantly increase computational complexity and hinder the optimization process. To reduce computational complexity, scenario reduction is required to construct a high-quality set of typical scenarios that accurately reflect the output characteristics of renewable energy plants.

The most commonly used scenario reduction methods are divided into selection methods, mathematical programming methods, clustering algorithms and heuristic algorithms. The selection-based reduction methods, including forward selection [15] and backward reduction, construct typical scenarios by incrementally adding or removing scenarios [16]. Mathematical programming methods formulate scenario reduction as a mixed-integer programming problem, and the mathematical optimization model is solved to determine whether the original scenario is selected as a typical scenario [17]. These two types of scenario reduction methods have high computational complexity when processing massive original scenarios. Clustering-algorithm-based reduction methods, such as K-means [18,19] and agglomerative clustering algorithms [20], employ similarity metrics to select typical scenarios that characterize the distribution of original scenarios. The heuristic search algorithm is employed to obtain optimal typical scenarios in [21]. Compared to the former two categories, the latter two scenario reduction methods are more computationally efficient and more suitable for processing massive original scenarios.

The power output of a single renewable energy plant exhibits inherent temporal correlation, while significant spatial correlation also exists among multiple renewable energy plants [22]. Typical scenarios for power grid planning should reflect spatiotemporal correlations to ensure the planning scheme quality. Although such correlations have been considered in the scenario generation stage [23], most studies on scenario reduction do not focus on them. During the process of scenario reduction, spatiotemporal correlation information may be lost as the number of scenarios decreases, leading to discrepancies between typical scenarios and actual conditions, thereby affecting the quality of the subsequent planning schemes.

To ensure that typical scenarios accurately reflect the characteristics of renewable energy plant outputs, spatiotemporal correlations need to be considered in scenario reduction. In this paper, a construction method of typical scenarios for multiple renewable energy plant outputs, considering spatiotemporal correlations, is proposed. Firstly, the spatial correlation and temporal autocorrelation matrices are defined, achieving an explicit quantitative representation of spatiotemporal correlations. Secondly, distributional differences between typical and original scenarios are quantified in terms of mean, variance, spatial correlation, and temporal autocorrelation, and an optimization model for scenario reduction considering spatiotemporal correlations is constructed. Thirdly, an improved genetic algorithm is developed by incorporating adaptive hyperparameter adjustment and an elitism-based evolutionary strategy. It aims to obtain high-quality typical scenarios. A case study involving multiple renewable energy plants in Belgium shows that constructed typical scenarios can effectively reflect the spatiotemporal correlations of original scenarios.

2. Description of Spatiotemporal Correlations Among Multiple Renewable Energy Plant Outputs

2.1. Temporal Scenario Description of Multiple Renewable Energy Plant Outputs

In this paper, the 24 h power outputs of multiple renewable energy plants are regarded as a temporal scenario $\boldsymbol{x}$, which can be represented as follows:

$$\boldsymbol{x} = \begin{bmatrix} x_{1,1} & x_{1,2} & \cdots & x_{1,T} \\ x_{2,1} & x_{2,2} & \cdots & x_{2,T} \\ \vdots & \vdots & \ddots & \vdots \\ x_{N,1} & x_{N,2} & \cdots & x_{N,T} \end{bmatrix} \tag{1}$$

where N is the number of renewable energy plants; T is the length of the time series; $x_{i,t}$ is the power output of the i-th renewable energy plant in scenario $\boldsymbol{x}$ at time t. In this paper, the time resolution of the renewable energy plant output is set to one hour, so T is equal to 24.

2.2. Description of Spatial Correlation

The spatial correlation among multiple renewable energy plant power outputs in a scenario $\boldsymbol{x}$ is characterized by a spatial correlation matrix $\boldsymbol{\rho}$. It is a symmetric matrix with dimensions of $N \times N$ and can be represented as follows:

$$\boldsymbol{\rho} = \begin{bmatrix} 1 & \rho_{1,2} & \cdots & \rho_{1,N} \\ \rho_{2,1} & 1 & \cdots & \rho_{2,N} \\ \vdots & \vdots & \ddots & \vdots \\ \rho_{N,1} & \rho_{N,2} & \cdots & 1 \end{bmatrix} \tag{2}$$

where $\rho_{i,j}$ is the Pearson correlation coefficient [24] between the power outputs of the i-th and j-th renewable energy plants in a scenario $\boldsymbol{x}$:

$$\rho_{i,j} = \frac{\sum_{t=1}^{T}\left[(x_{i,t} - \frac{\chi_i}{T})(x_{j,t} - \frac{\chi_j}{T})\right]}{\sqrt{\sum_{t=1}^{T}(x_{i,t} - \frac{\chi_i}{T})^2 \times \sum_{t=1}^{T}(x_{j,t} - \frac{\chi_j}{T})^2}} \tag{3}$$

where $\chi_i = \sum_{t=1}^{T} x_{i,t}$, $\chi_j = \sum_{t=1}^{T} x_{j,t}$.

2.3. Description of Temporal Autocorrelation

The power output of the renewable energy plant exhibits temporal autocorrelation [25,26]. In order to characterize this, a temporal autocorrelation matrix $\boldsymbol{A}$ is introduced and can be represented as follows:

$$\boldsymbol{A} = \begin{bmatrix} a_{1,1} & a_{1,2} & \cdots & a_{1,N_{\text{lag}}} \\ a_{2,1} & a_{2,2} & \cdots & a_{2,N_{\text{lag}}} \\ \vdots & \vdots & \ddots & \vdots \\ a_{N,1} & a_{N,2} & \cdots & a_{N,N_{\text{lag}}} \end{bmatrix} \tag{4}$$

where $a_{i,l}$ is the l-th-order temporal autocorrelation coefficient [27] of the i-th renewable energy plant power output in scenario $\boldsymbol{x}$, and N_{lag} represents the maximum order of the temporal autocorrelation. The matrix element $a_{i,l}$ can be represented as follows:

$$a_{i,l} = \sum_{t=l+1}^{T} \frac{(x_{i,t} - \chi_i)(x_{i,t-l} - \chi_i)}{\sum_{t=1}^{T}(x_{i,t} - \chi_i)^2} \tag{5}$$

3. Construction of A Scenario Reduction Model Considering Spatiotemporal Correlations

3.1. Difference Metric Between Typical Scenarios and Original Scenarios

N_{org} denotes the number of original scenarios, and N_{typ} denotes the number of typical scenarios. $\boldsymbol{x}_k^{\text{org}}$ denotes the k-th original scenario, and $\boldsymbol{x}_k^{\text{typ}}$ denotes the k-th typical scenario:

$$\boldsymbol{x}_k^{\text{org}} = \begin{bmatrix} x_{1,1,k}^{\text{org}} & x_{1,2,k}^{\text{org}} & \cdots & x_{1,T,k}^{\text{org}} \\ x_{2,1,k}^{\text{org}} & x_{2,2,k}^{\text{org}} & \cdots & x_{2,T,k}^{\text{org}} \\ \vdots & \vdots & \ddots & \vdots \\ x_{N,1,k}^{\text{org}} & x_{N,2,k}^{\text{org}} & \cdots & x_{N,T,k}^{\text{org}} \end{bmatrix} \tag{6}$$

$$\boldsymbol{x}_k^{\text{typ}} = \begin{bmatrix} x_{1,1,k}^{\text{typ}} & x_{1,2,k}^{\text{typ}} & \cdots & x_{1,T,k}^{\text{typ}} \\ x_{2,1,k}^{\text{typ}} & x_{2,2,k}^{\text{typ}} & \cdots & x_{2,T,k}^{\text{typ}} \\ \vdots & \vdots & \ddots & \vdots \\ x_{N,1,k}^{\text{typ}} & x_{N,2,k}^{\text{typ}} & \cdots & x_{N,T,k}^{\text{typ}} \end{bmatrix} \tag{7}$$

where $x_{i,t,k}^{\text{org}}$ and $x_{i,t,k}^{\text{typ}}$ denote the power output of the i-th renewable energy plant at time t in the k-th original scenario and typical scenario, respectively.

(1) Mean difference

The mean matrices of the original and the typical scenario set, denoted as $\boldsymbol{M}_{\text{org}}$ and $\boldsymbol{M}_{\text{typ}}$, both have the dimensions of $N \times T$. The elements in the i-th row and t-th column, denoted as $m_{i,t}^{\text{org}}$ and $m_{i,t}^{\text{typ}}$, represent the average power output of the i-th renewable energy plant at time t in the original and typical scenario set, respectively. They can be represented as follows:

$$m_{i,t}^{\text{org}} = \sum_{k=1}^{N_{\text{org}}} x_{i,t,k}^{\text{org}} \tag{8}$$

$$m_{i,t}^{\text{typ}} = \sum_{k=1}^{N_{\text{typ}}} x_{i,t,k}^{\text{typ}} \tag{9}$$

The mean difference between the original and the typical scenario set is measured using the mean square error (MSE). It is denoted as MSE_{mean}:

$$\text{MSE}_{\text{mean}} = \frac{1}{NT} \sum_{i=1}^{N} \sum_{t=1}^{T} \left(m_{i,t}^{\text{org}} - m_{i,t}^{\text{typ}} \right)^2 \tag{10}$$

(2) Variance difference

The variance matrices of the original and the typical scenario set, denoted as $\boldsymbol{V}_{\text{org}}$ and $\boldsymbol{V}_{\text{typ}}$, both have the dimensions of $N \times T$. The elements in the i-th row and t-th column, denoted as $v_{i,t}^{\text{org}}$ and $v_{i,t}^{\text{typ}}$, represent the variance in the power output of the i-th renewable energy plant at time t in the original and the typical scenario set, respectively. They can be represented as follows:

$$v_{i,t}^{\text{org}} = \frac{1}{N_{\text{org}} - 1} \sum_{k=1}^{N_{\text{org}}} \left(x_{i,t,k}^{\text{org}} - m_{i,t}^{\text{org}} \right)^2 \tag{11}$$

$$v_{i,t}^{\text{typ}} = \frac{1}{N_{\text{typ}} - 1} \sum_{k=1}^{N_{\text{typ}}} \left(x_{i,t,k}^{\text{typ}} - m_{i,t}^{\text{typ}} \right)^2 \tag{12}$$

The variance difference between the original and the typical scenario set is measured using the MSE. It is denoted as $\mathrm{MSE}_{\mathrm{var}}$.

$$\mathrm{MSE}_{\mathrm{var}} = \frac{1}{NT}\sum_{i=1}^{N}\sum_{t=1}^{T}\left(v_{i,t}^{\mathrm{org}} - v_{i,t}^{\mathrm{typ}}\right)^2 \tag{13}$$

(3) Spatial correlation difference

The spatial correlation matrices of the k-th original scenario and typical scenario are denoted as $\boldsymbol{\rho}_k^{\mathrm{org}}$ and $\boldsymbol{\rho}_k^{\mathrm{typ}}$, respectively. Both are $N \times N$-dimensional matrices and can be represented as follows:

$$\boldsymbol{\rho}_k^{\mathrm{org}} = \begin{bmatrix} 1 & \rho_{1,2,k}^{\mathrm{org}} & \cdots & \rho_{1,N,k}^{\mathrm{org}} \\ \rho_{2,1,k}^{\mathrm{org}} & 1 & \cdots & \rho_{2,N,k}^{\mathrm{org}} \\ \vdots & \vdots & \ddots & \vdots \\ \rho_{N,1,k}^{\mathrm{org}} & \rho_{N,2,k}^{\mathrm{org}} & \cdots & 1 \end{bmatrix} \tag{14}$$

$$\boldsymbol{\rho}_k^{\mathrm{typ}} = \begin{bmatrix} 1 & \rho_{1,2,k}^{\mathrm{typ}} & \cdots & \rho_{1,N,k}^{\mathrm{typ}} \\ \rho_{2,1,k}^{\mathrm{typ}} & 1 & \cdots & \rho_{2,N,k}^{\mathrm{typ}} \\ \vdots & \vdots & \ddots & \vdots \\ \rho_{N,1,k}^{\mathrm{typ}} & \rho_{N,2,k}^{\mathrm{typ}} & \cdots & 1 \end{bmatrix} \tag{15}$$

where $\rho_{i,j,k}^{\mathrm{org}}$ is the Pearson correlation coefficient between the power outputs of the i-th and j-th renewable energy plants in the k-th original scenario; $\rho_{i,j,k}^{\mathrm{typ}}$ is the Pearson correlation coefficient between the power outputs of the i-th and j-th plants in the k-th typical scenario.

The spatial correlation matrices of the original scenario set and the typical scenario set, denoted as $\boldsymbol{\rho}^{\mathrm{org}}$ and $\boldsymbol{\rho}^{\mathrm{typ}}$, are obtained by averaging the spatial correlation matrices across all scenarios, and can be represented as follows:

$$\boldsymbol{\rho}^{\mathrm{org}} = \frac{1}{N_{\mathrm{org}}}\sum_{k=1}^{N_{\mathrm{org}}}\boldsymbol{\rho}_k^{\mathrm{org}} \tag{16}$$

$$\boldsymbol{\rho}^{\mathrm{typ}} = \frac{1}{N_{\mathrm{typ}}}\sum_{k=1}^{N_{\mathrm{typ}}}\boldsymbol{\rho}_k^{\mathrm{typ}} \tag{17}$$

The spatial correlation difference between the original scenario set and the typical scenario set is measured using the MSE. It is denoted as $\mathrm{MSE}_{\mathrm{space}}$.

$$\mathrm{MSE}_{\mathrm{space}} = \frac{1}{N^2}\sum_{i=1}^{N}\sum_{j=1}^{N}\left(\rho_{i,j}^{\mathrm{org}} - \rho_{i,j}^{\mathrm{typ}}\right)^2 \tag{18}$$

where $\rho_{i,j}^{\mathrm{org}}$ and $\rho_{i,j}^{\mathrm{typ}}$ are the elements in the i-th row and j-th column of $\boldsymbol{\rho}^{\mathrm{org}}$ and $\boldsymbol{\rho}^{\mathrm{typ}}$, respectively. Equation (18) is a commonly used method for quantifying the difference between two correlation matrices [28].

(4) Temporal autocorrelation difference

The power output of a renewable energy plant exhibits temporal autocorrelation. The N_{lag}-order temporal autocorrelation matrices of the k-th original scenario and the k-th typical scenario are denoted as $\boldsymbol{A}_k^{\text{org}}$ and $\boldsymbol{A}_k^{\text{typ}}$, which can be represented as follows:

$$\boldsymbol{A}_k^{\text{org}} = \begin{bmatrix} a_{1,1,k}^{\text{org}} & a_{1,2,k}^{\text{org}} & \cdots & a_{1,N_{\text{lag}},k}^{\text{org}} \\ a_{2,1,k}^{\text{org}} & a_{2,2,k}^{\text{org}} & \cdots & a_{2,N_{\text{lag}},k}^{\text{org}} \\ \vdots & \vdots & \ddots & \vdots \\ a_{N,1,k}^{\text{org}} & a_{N,2,k}^{\text{org}} & \cdots & a_{N,N_{\text{lag}},k}^{\text{org}} \end{bmatrix} \tag{19}$$

$$\boldsymbol{A}_k^{\text{typ}} = \begin{bmatrix} a_{1,1,k}^{\text{typ}} & a_{1,2,k}^{\text{typ}} & \cdots & a_{1,N_{\text{lag}},k}^{\text{typ}} \\ a_{2,1,k}^{\text{typ}} & a_{2,2,k}^{\text{typ}} & \cdots & a_{2,N_{\text{lag}},k}^{\text{typ}} \\ \vdots & \vdots & \ddots & \vdots \\ a_{N,1,k}^{\text{typ}} & a_{N,2,k}^{\text{typ}} & \cdots & a_{N,N_{\text{lag}},k}^{\text{typ}} \end{bmatrix} \tag{20}$$

where $a_{i,l,k}^{\text{org}}$ is the l-th-order temporal autocorrelation coefficient of the power output of the i-th renewable energy plant in the k-th original scenario; $a_{i,l,k}^{\text{typ}}$ is the corresponding coefficient in the k-th typical scenario.

The temporal autocorrelation matrices of the original scenario set and the typical scenario set, denoted as $\boldsymbol{A}^{\text{org}}$ and $\boldsymbol{A}^{\text{typ}}$, are obtained by averaging the temporal autocorrelation matrices across all scenarios, and can be represented as follows:

$$\boldsymbol{A}^{\text{org}} = \frac{1}{N_{\text{org}}} \sum_{k=1}^{N_{\text{org}}} \boldsymbol{A}_k^{\text{org}} \tag{21}$$

$$\boldsymbol{A}^{\text{typ}} = \frac{1}{N_{\text{typ}}} \sum_{k=1}^{N_{\text{typ}}} \boldsymbol{A}_k^{\text{typ}} \tag{22}$$

The temporal autocorrelation difference between the original scenario set and the typical scenario set is measured using the MSE. It is denoted as MSE_{time}.

$$\text{MSE}_{\text{time}} = \frac{1}{N N_{\text{lag}}} \sum_{i=1}^{N} \sum_{j=1}^{N_{\text{lag}}} \left(a_{i,j}^{\text{org}} - a_{i,j}^{\text{typ}} \right)^2 \tag{23}$$

where $a_{i,j}^{\text{org}}$ and $a_{i,j}^{\text{typ}}$ are the elements in the i-th row and j-th column of $\boldsymbol{A}^{\text{org}}$ and $\boldsymbol{A}^{\text{typ}}$, respectively.

3.2. Modeling of Scenario Reduction

Scenario reduction aims to approximate a large number of original scenarios with several typical scenarios [29]. Under the premise of minimizing the distributional discrepancy between the original and typical scenario sets, N_{typ} scenarios are selected from the original set to form the typical scenario set. The process of scenario reduction can be modeled as follows:

$$\begin{aligned} &\min F = \alpha_1 \text{MSE}_{\text{mean}} + \alpha_2 \text{MSE}_{\text{var}} + \alpha_3 \text{MSE}_{\text{space}} + \alpha_4 \text{MSE}_{\text{time}} \\ &\text{s.t. } X_{N_{\text{typ}}} \subseteq \{ \boldsymbol{x}_1^{\text{org}}, \boldsymbol{x}_2^{\text{org}}, \ldots, \boldsymbol{x}_{N_{\text{org}}}^{\text{org}} \} \end{aligned} \tag{24}$$

where α_1, α_2, α_3, and α_4 are weighting coefficients of the mean difference, variance difference, spatial correlation difference, and temporal autocorrelation difference, respectively. $X_{N\text{typ}}$ is a set composed of N_{typ} typical scenarios. To facilitate the optimization of F, the

power output data in the original scenarios need to be normalized in advance. The target function F is reduced by adjusting the combination of typical scenarios.

4. Solution of Typical Scenarios Based on Improved Genetic Algorithm

The selection of typical scenarios belongs to a large-scale nonlinear combinatorial optimization problem. When solving nonlinear combinatorial optimization problems, metaheuristic algorithms have advantages such as fast computation, strong adaptability, and ease of implementation [30,31]. Various classical and cutting-edge metaheuristic algorithms have exhibited excellent performance, such as the genetic algorithm [32], particle swarm optimization [33], differential evolution [34], Red Fox Optimizer [35], and Mountain Gazelle Optimizer [36]. A combination scheme of typical scenarios is suitable to be represented as a discrete encoding form, which is a common representation form of populations in genetic algorithms. Therefore, the genetic algorithm is naturally suited to solve the abovementioned combinatorial optimization problems due to its discrete encoding form. In this section, the performance of the genetic algorithm is further improved by incorporating adaptive parameter adjustment and an elitism-based evolutionary strategy. The typical scenario set is then obtained using the improved genetic algorithm.

4.1. Improved Genetic Algorithm

(1) Adaptive adjustment of parameters

In the genetic algorithm, the early stage of evolution should focus on enhancing population diversity to improve global search capability, while the later stage should emphasize local exploitation for superior individuals to enhance convergence performance. As shown in Equations (25) and (26), the crossover and mutation rates are dynamically adjusted throughout the evolutionary process to achieve a dynamic balance between global search and local exploitation capabilities.

$$p_{\mathrm{c}}(g) = p_{\mathrm{c_max}} + \frac{g}{g_{\max}}(p_{\mathrm{c_min}} - p_{\mathrm{c_max}}) \tag{25}$$

$$p_{\mathrm{m}}(g) = p_{\mathrm{m_max}} + \frac{g}{g_{\max}}(p_{\mathrm{m_min}} - p_{\mathrm{m_max}}) \tag{26}$$

where $p_{\mathrm{c}}(g)$ is the population crossover rate at the g-th generation; $g_{\max}$ is the maximum number of generations; $p_{\mathrm{c_min}}$ and $p_{\mathrm{c_max}}$ are the minimum and maximum crossover rates, respectively. $p_{\mathrm{m}}(g)$ is the mutation rate at the g-th generation; $p_{\mathrm{m_min}}$ and $p_{\mathrm{m_max}}$ are the minimum and maximum mutation rates, respectively.

(2) Elitism-based evolutionary strategy

The schematic diagram of the elitism-based evolutionary strategy in the genetic algorithm is shown in Figure 1. The population size is N_{pop}. After calculating the fitness of all individuals in the current generation, the top N_{e} individuals in fitness ranking are identified as elite individuals. These elite individuals are retained directly into the next generation without undergoing selection, crossover, or mutation operations. The elitism-based evolutionary strategy ensures that high-quality individuals are not lost during the evolutionary process, thereby improving the optimization efficiency of the genetic algorithm.

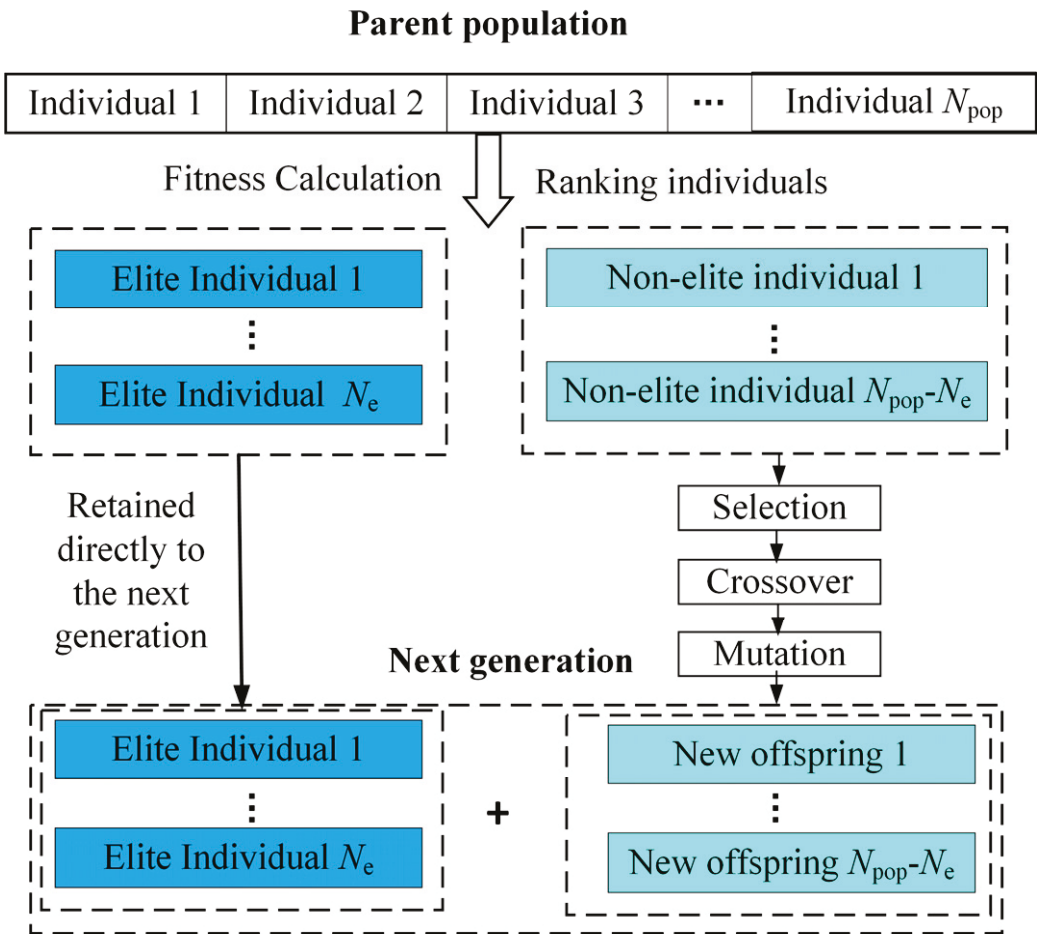


Figure 1. Diagram of the elitism-based evolutionary strategy.

4.2. Solution Procedure of Typical Scenarios Based on Improved Genetic Algorithm

The solution procedure of typical scenarios based on the improved genetic algorithm can be divided into six steps as follows:

(1) Population initialization

The solved scenario scheme is encoded as an integer vector of length N_{typ}, denoted as $\boldsymbol{ind} = [id_1, id_2, \ldots, id_{Ntyp}]$. Each element is a unique integer within the range $\{1, 2, \ldots, N_{org}\}$. A total of N_{pop} individuals are generated to form the initial population.

(2) Calculation and ranking of fitness

The fitness of each individual is calculated according to Equation (24). Individuals are then ranked in ascending order according to their fitness values. The top N_e individuals are identified as elite individuals, which are directly retained in the next generation without undergoing crossover or mutation operations.

(3) Selection operation for non-elite individuals

The tournament selection strategy is used for selecting non-elite individuals. N_{ts} is the tournament size. The offspring population is generated through the following steps: randomly select N_{ts} candidate individuals from the non-elite population, and choose the one with the best fitness value as the offspring individual. This selection process is repeated iteratively until $N_{pop} - N_e$ offspring individuals are generated.

(4) Crossover operation for non-elite individuals

The process of the crossover operation is shown in Figure 2. Different colors represent gene segments from different parents. Arrows represent that the gene segments from the

parents are retained in the offspring. Dashed arrows represent that the gene segments are not retained. For a pair of parent individuals, a random number r is generated from a uniform distribution within the range [0, 1]. The crossover probability $p_c(g)$ is calculated according to Equation (25). If $r < p_c(g)$, the crossover operation is performed; otherwise, it is skipped. For two parent individuals to perform a crossover operation, two crossover points k_1 and k_2 are randomly generated so that $1 < k_1 < k_2 < N_{typ}$. A segment between k_1 and k_2 is extracted from Parent 1. Offspring 1 inherits this segment, and the remaining positions are filled in order with non-conflicting genes from Parent 2. Offspring 2 is generated symmetrically by reversing the roles of the parents.

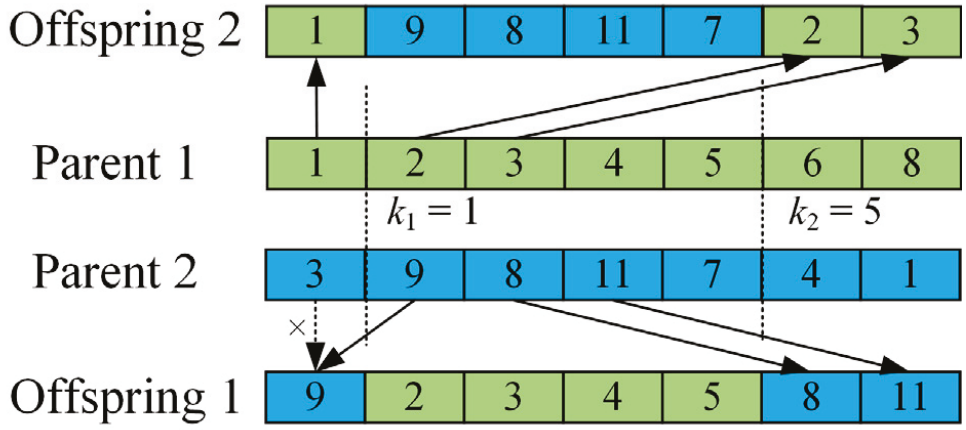


Figure 2. Schematic diagram of crossover operation.

(5) Mutation operation for non-elite individuals

For each non-elite individual, a random number r is generated from a uniform distribution within the range [0, 1]. The mutation rate $p_m(g)$ is calculated according to Equation (26). If $r < p_m(g)$, the mutation operation is performed. For individuals undergoing mutation, a new index value is randomly selected from the set $\{1, 2, \ldots, N_{typ}\}$ that satisfies the uniqueness constraint of an individual (i.e., all elements in the individual are unique). The original gene at the selected position is then replaced with the new index value.

(6) Iteration termination judgment

The new offspring individuals, including both elite and non-elite individuals after selection, crossover, and mutation, form the next-generation population. If the maximum number of evolution generations is reached, the optimization process is terminated and the solved typical scenarios are output; otherwise, the procedure returns to step 2.

The solution flowchart of typical scenarios based on the improved genetic algorithm is shown in Figure 3.

The computational burden for solving typical scenarios increases as the size of the original scenario set grows. When dealing with large-scale original scenario sets, the solution process for typical scenarios becomes highly time-consuming. Due to the inherent compatibility of genetic algorithms with parallel computing techniques, the efficiency of extracting typical scenarios can be enhanced by increasing the number of parallel computation cores.

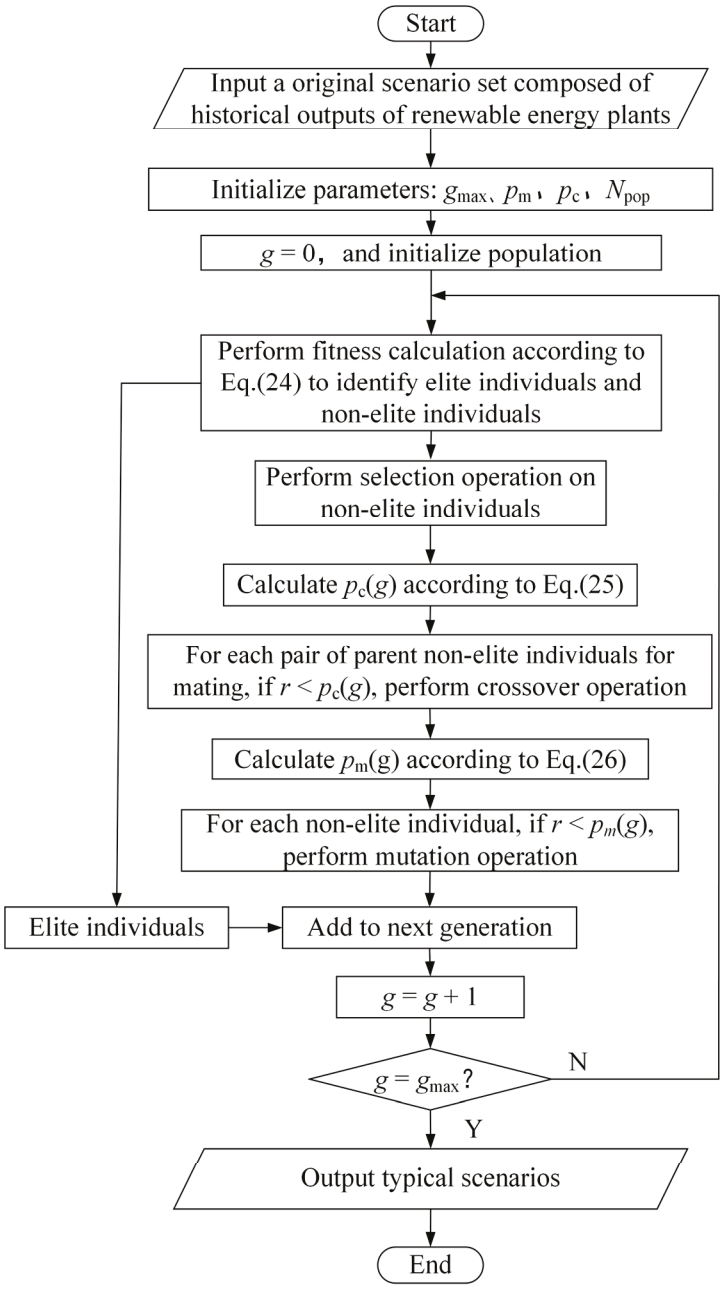


Figure 3. Flowchart of scenario reduction based on an improved genetic algorithm.

5. Case Study

The proposed construction method of typical scenarios is verified in multiple renewable energy plants in Belgium, including five wind farms (WFs) and fourteen photovoltaic (PV) plants. For scenario generation, historical output data from plants recorded over a period of one year serve as the original scenario set, including a total of 365 historical scenarios. The power outputs of all plants are normalized to eliminate potential large differences among different plants.

5.1. Scenario Reduction of Multiple WF Outputs

Typical scenarios for multiple WFs are solved using the improved genetic algorithm. Weighting coefficients α_1, α_2, α_3, and α_4 are set to 1. The number of typical scenarios N_{typ} is set to 4. The maximum iteration number g_{max} is set to 200. p_{c_max} is set to 0.8. p_{c_min} is 0.2. p_{m_max} is 0.4. p_{m_min} is 0.1. Objective function value F with different population sizes and

N_e are shown in Figures A1 and A2 in Appendix A. After the population size reaches 20, the optimization results no longer exhibit significant changes. Moreover, the optimal results are achieved when the number N_e of elite individuals is set to 2.

With a population size of 20 and N_e = 2, the fitness value variation curves of the improved and standard genetic algorithms during the optimization process are shown in Figure 4. The *X*-axis denotes the number of iterations in the genetic algorithm. The *Y*-axis fitness value is the objective function *F*. With 10 parallel computation cores, the standard genetic algorithm requires 177 iterations to obtain the optimal solution, which takes 234 s. The improved genetic algorithm achieves a higher-quality solution in just 125 iterations, which takes 165 s. Therefore, compared to the standard genetic algorithm, the improved genetic algorithm demonstrates faster convergence and superior solution quality. The four typical scenarios for WF 1 are shown in Figure 5. The *X*-axis denotes the sampling time points in one day. The *Y*-axis denotes the normalized power output of WF 1 on a single time point.

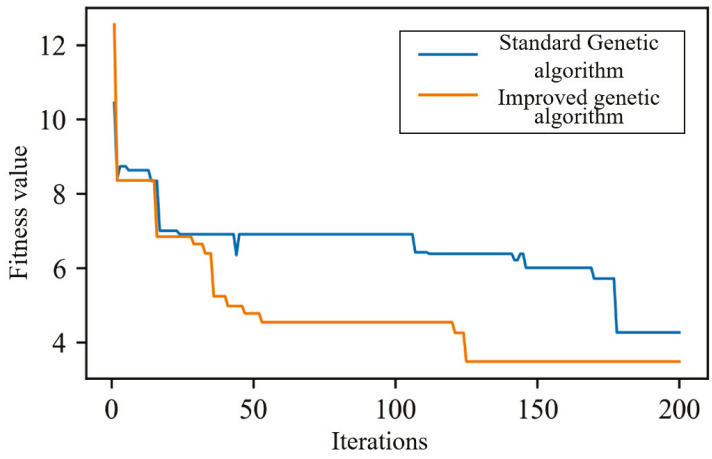


Figure 4. The fitness variation curves of the standard and improved genetic algorithms.

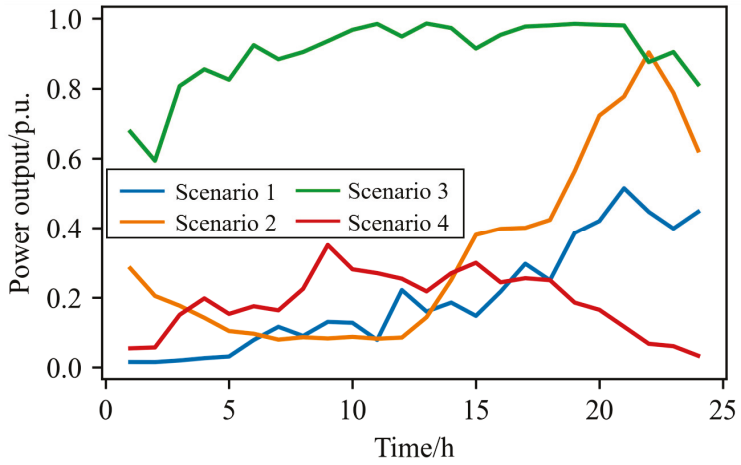


Figure 5. Typical scenario set for WF 1.

The mean and variance differences between original and typical scenarios across the five WFs are given in Table 1. As shown in Table 1, the constructed typical scenario set maintains statistical similarity to the original scenario set in terms of mean and variance. Further comparisons of the spatial correlations of power outputs between the original and typical scenario sets are presented in Figures 6 and 7. The numbers in Figures 6 and 7 denote the spatial correlation coefficients between WF outputs.

Table 1. Means and variances between the original and typical scenario sets for five WFs.

	Original Scenario Set		Typical Scenario Set	
	Mean/p.u.	Variance	Mean/p.u.	Variance
WF 1	0.4121	0.0308	0.4723	0.0319
WF 2	0.2455	0.0096	0.2765	0.0066
WF 3	0.2477	0.0089	0.2975	0.0092
WF 4	0.2374	0.0084	0.2532	0.0071
WF 5	0.1852	0.0087	0.1609	0.0081

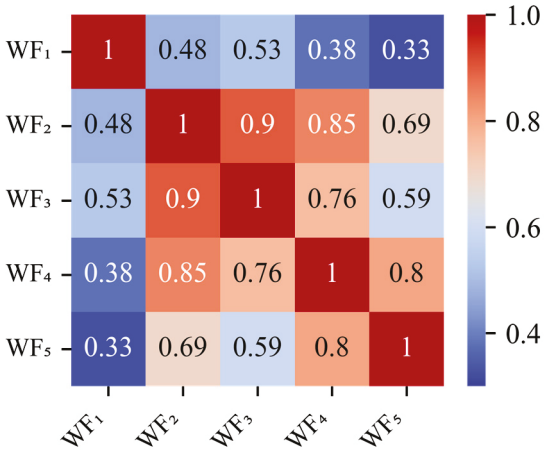


Figure 6. Heatmap of spatial correlations in the original scenario set for five WFs.

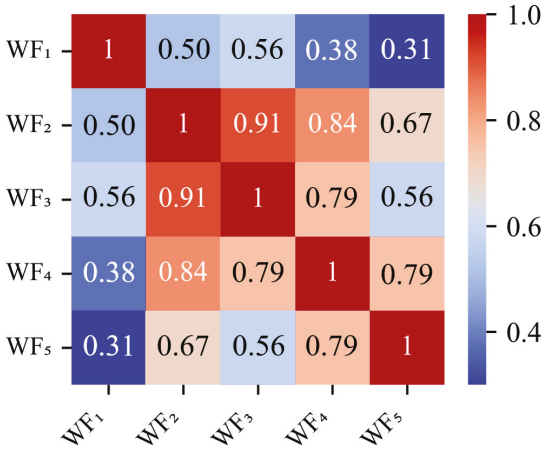


Figure 7. Heatmap of spatial correlations in the typical scenario set for five WFs.

It can be seen that the spatial correlation heatmaps of power outputs across the five WFs in the original and typical scenario sets are highly similar. The mean absolute percentage error (MAPE) between spatial correlation matrices of the original and typical scenario sets is 2.5%, indicating that the obtained typical scenario set can effectively preserve the spatial correlations among multiple WFs. Furthermore, a comparison of the average temporal autocorrelation coefficient curves between the original and typical scenario sets for WF 1 is presented in Figure 8. The *X*-axis denotes the order of temporal autocorrelation. The *Y*-axis denotes the average autocorrelation coefficients of WF 1 across all scenarios. The percentage error between the first-order temporal autocorrelation coefficients of the original and typical scenario sets is 2.75%. The consistency between the two curves demonstrates that typical scenarios can also preserve the temporal autocorrelation of WF outputs.

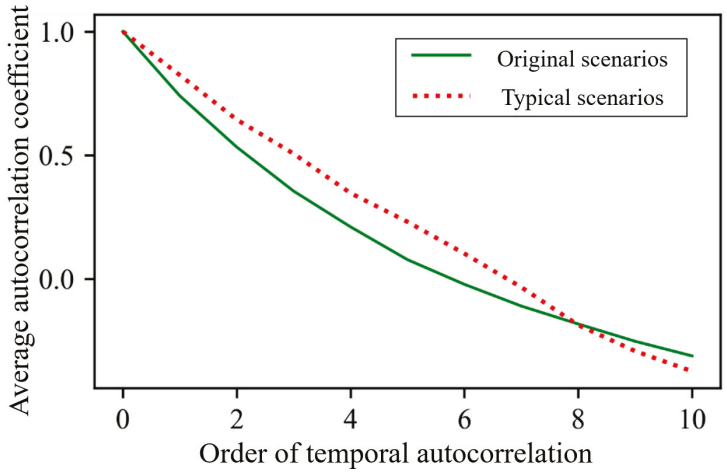


Figure 8. Average autocorrelation coefficients of original and typical scenarios for WF 1.

5.2. Scenario Reduction of Multiple PV Plant Outputs

A typical scenario set for 14 PV plants is obtained using the improved genetic algorithm. Among these, the four typical output scenarios for PV plant 1 are shown in Figure 9. The *Y*-axis denotes the normalized power output of PV plant 1 on a single time point. It can be seen that the scenarios are distributed across distinct output intervals. The mean and variance differences between the original and typical scenario sets for the 14 PV plants are given in Table 2. The results indicate that the constructed typical scenario set retains mean and variance characteristics that are close to the original scenario set.

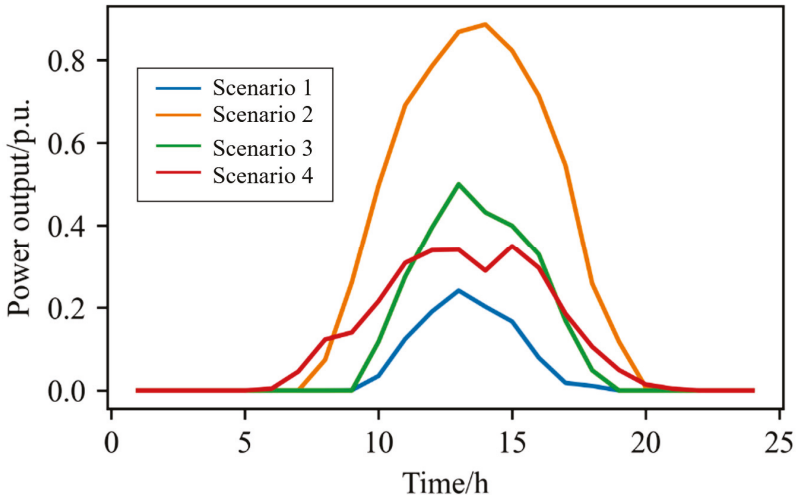


Figure 9. Typical scenario set for PV plant 1.

The spatial correlation heatmaps of power outputs among 14 PV plants in the original and typical scenario sets are shown in Figures 10 and 11, respectively. The MAPE between spatial correlation matrices of the original and typical scenario sets is 0.78%. The high similarity in correlation distributions between the two sets indicates that the constructed typical scenario set can effectively capture the spatial correlations among the historical outputs of 14 PV plants. As shown in Figures 10 and 11, the spatial correlation coefficients between PV plants are generally above 0.9. Compared to WFs, PV plants exhibit stronger spatial correlation. This is attributed to the large-scale, uniform, and gradual nature of solar irradiance variations, which lead to consistent power output changes among PV plants within the same region.

Table 2. Means and variances between original and typical scenario sets for 14 PV plants.

	Original Scenario Set		Typical Scenario Set	
	Mean/p.u.	**Variance**	**Mean/p.u.**	**Variance**
PV 1	0.1275	0.0358	0.1361	0.0415
PV 2	0.1268	0.0343	0.1347	0.0397
PV 3	0.1236	0.0335	0.13167	0.0390
PV 4	0.1335	0.0387	0.1410	0.0444
PV 5	0.1317	0.0372	0.1394	0.0430
PV 6	0.1315	0.0379	0.1420	0.0451
PV 7	0.1151	0.0285	0.1185	0.0311
PV 8	0.1265	0.0353	0.1376	0.0413
PV 9	0.1145	0.0287	0.1272	0.0343
PV 10	0.1090	0.0258	0.1235	0.0321
PV 11	0.1106	0.0268	0.1126	0.0271
PV 12	0.1138	0.0277	0.1221	0.0317
PV 13	0.1157	0.0293	0.1216	0.0329
PV 14	0.1383	0.0412	0.1413	0.0447

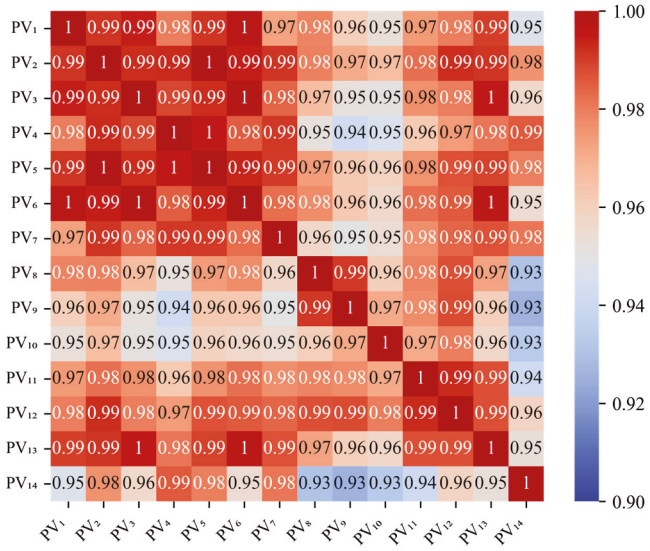


Figure 10. Heatmap of spatial correlations in the original scenario set for 14 PV plants.

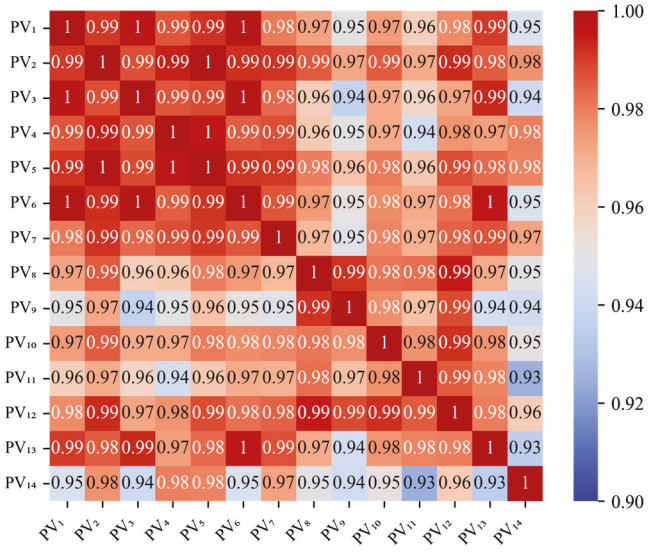


Figure 11. Heatmap of spatial correlations in the typical scenario set for 14 PV plants.

A further comparison of the average temporal autocorrelation coefficients between the original and typical scenario sets for PV plant 1 is shown in Figure 12. The *Y*-axis denotes the average autocorrelation coefficients of PV plant 1 across all scenarios. The percentage error between the first-order temporal autocorrelation coefficients of the original and typical scenario sets is 2.45%. The high degree of alignment between the two curves demonstrates that the constructed typical scenario set can effectively preserve the temporal autocorrelation of the historical outputs from PV plant 1.

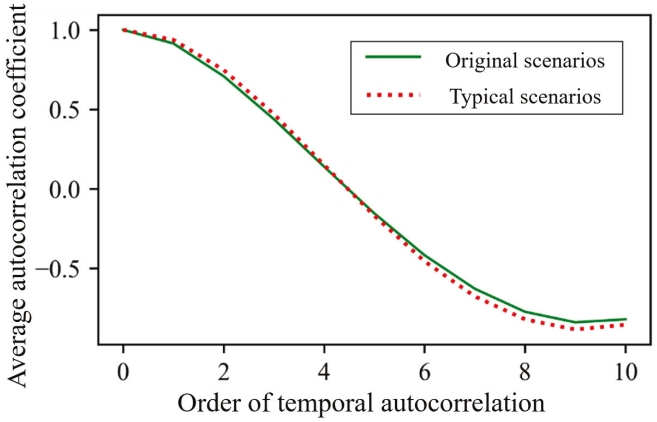


Figure 12. Average autocorrelation coefficients between the original and typical scenario sets for PV plant 1.

In summary, the proposed construction method for typical scenarios for multiple renewable energy plant outputs based on the improved genetic algorithm can effectively preserve the statistical characteristics of the original scenario set, including the mean, variance, spatial correlation, and temporal correlation.

6. Conclusions

A construction method for typical scenarios considering spatiotemporal correlations among multiple renewable energy plant outputs is proposed in this paper. A symmetric spatial correlation matrix and a temporal autocorrelation matrix are defined, achieving quantitative representation of the spatiotemporal correlations. Distributional differences between the typical and original scenario sets are quantified in terms of mean, variance, spatial correlation, and temporal autocorrelation, and an optimization model for scenario reduction is constructed. The model is solved based on the improved genetic algorithm in order to obtain high-quality typical scenarios. The proposed method in this paper can provide typical scenarios that reflect distributional characteristics of original scenarios, thereby contributing to the optimality of the power grid planning schemes. The case study on multiple renewable energy plants in Belgium gives the following conclusions:

(1) By incorporating adaptive parameter adjustment and an elitism strategy, the solution quality and efficiency of the improved genetic algorithm are enhanced significantly. Four high-quality typical scenarios can be obtained in 3 min.

(2) The MAPE between spatial correlation matrices of the original and typical scenario sets for wind farms is 2.5%. The MAPE for photovoltaic plants is 0.78%. These simulation results demonstrate that the constructed typical scenarios can effectively capture the spatial correlations of the original scenarios.

(3) The percentage error between first-order temporal autocorrelation coefficients of original and typical scenarios for wind farms is 2.75%. The MAPE for photovoltaic plants is 2.45%. The low errors demonstrate that typical scenarios can also capture the temporal correlations of the original scenarios.

While increasing the size of the typical scenario set can more accurately reflect the distributional characteristics of the original scenario set, it also increases the complexity of subsequent planning solutions. Future research should incorporate subsequent power grid planning solutions into the construction of typical scenarios, aiming to construct a minimal-sized typical scenario set that is well-suited for power grid planning.

Author Contributions: Conceptualization, Y.Z. and Y.W.; methodology, Y.Z.; software, N.W.; validation, Z.Y. and R.S.; formal analysis, R.S.; investigation, L.Z.; data curation, Y.W.; writing—original draft preparation, Y.Z.; writing—review and editing, R.S.; supervision, R.S. All authors have read and agreed to the published version of the manuscript.

Funding: The authors declare that this study received funding from Science and Technology Project of State Grid Shandong Electric Power Company "Research on the Optimal Configuration of Grid-Forming Energy Storage in New Energy Station Cluster for Unconventional Security Risks" under Grant 520625240005. The funder had the following involvement with the study: methodology, writing—original draft preparation, and data curation.

Data Availability Statement: The raw data supporting the conclusions of this article will be made available by the authors on request.

Conflicts of Interest: Authors Yuyue Zhang, Yan Wen, Nan Wang, Zhenhua Yuan, and Lina Zhang were employed by the Economic & Technology Research Institute of the State Grid Shandong Electric Power Company. The remaining authors declare that the research was conducted in the absence of any commercial or financial relationships that could be construed as a potential conflict of interest.

Appendix A

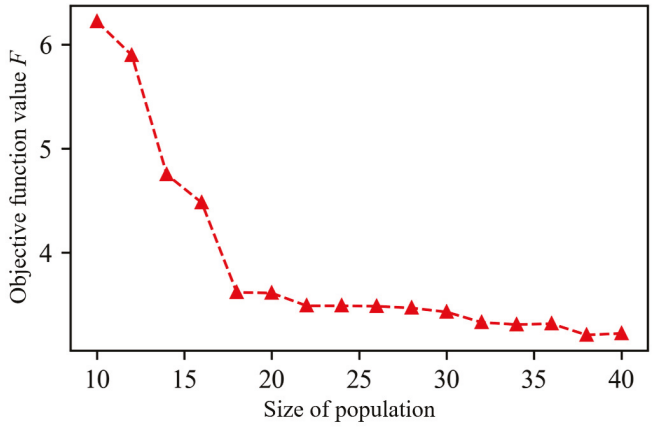


Figure A1. Objective function value F under different population sizes.

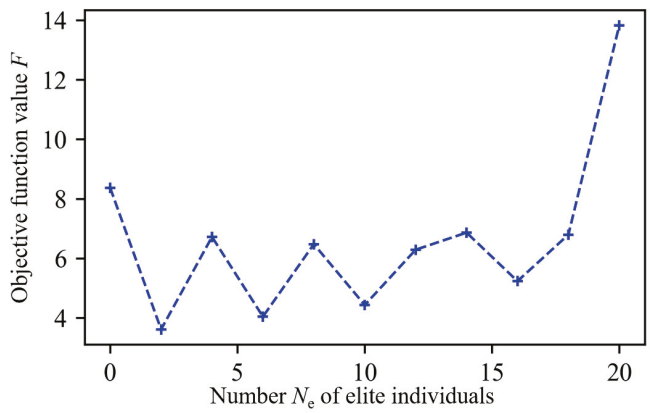


Figure A2. Objective function value F under different N_e in the elitism strategy.

References

1. Khaleel, M.; Yusupov, Z.; Rekik, S. Exploring trends and predictions in renewable energy generation. *Energy 360* **2025**, *4*, 100030. [CrossRef]
2. Wang, L.; Xie, L.; Yang, Y.; Zhang, Y.; Wang, K.; Cheng, S. Distributed online voltage control with fast PV power fluctuations and imperfect communication. *IEEE Trans. Smart Grid* **2023**, *14*, 3681–3695. [CrossRef]
3. Zhao, L.; Huang, Y.; Dai, Q.; Yang, L.; Chen, F.; Wang, L.; Sun, K.; Huang, J.; Lin, Z. Multistage active distribution network planning with restricted operation scenario selection. *IEEE Access* **2019**, *7*, 121067–121080. [CrossRef]
4. Li, H.; Ren, Z.; Fan, M.; Li, W.; Xu, Y.; Jiang, Y.; Xia, W. A review of scenario analysis methods in planning and operation of modern power systems: Methodologies, applications, and challenges. *Electr. Power Syst. Res.* **2022**, *205*, 107722. [CrossRef]
5. Stappers, B.; Paterakis, N.G.; Kok, K.; Gibescu, M. A class-driven approach based on long short-term memory networks for electricity price scenario generation and reduction. *IEEE Trans. Power Syst.* **2020**, *35*, 3040–3050. [CrossRef]
6. Gazijahani, F.S.; Salehi, J. Stochastic multi-objective framework for optimal dynamic planning of interconnected microgrids. *IET Renew. Power Gener.* **2017**, *11*, 1749–1759. [CrossRef]
7. Safdarian, A.; Fotuhi-Firuzabad, M.; Aminifar, F. Compromising wind and solar energies from the power system adequacy viewpoint. *IEEE Trans. Power Syst.* **2012**, *27*, 2368–2376. [CrossRef]
8. Chen, Y.; Wang, Y.; Kirschen, D.; Zhang, B. Model-free renewable scenario generation using generative adversarial networks. *IEEE Trans. Power Syst.* **2018**, *33*, 3265–3275. [CrossRef]
9. Yuan, R.; Wang, B.; Sun, Y.; Song, X.; Watada, J. Conditional style-based generative adversarial networks for renewable scenario generation. *IEEE Trans. Power Syst.* **2022**, *38*, 1281–1296. [CrossRef]
10. Song, Z.; Huang, Y.; Xie, H.; Li, X. Generation method of multi-regional photovoltaic output scenarios-set using conditional generative adversarial networks. *IEEE J. Emerg. Sel. Top. Circuits Syst.* **2023**, *13*, 861–870. [CrossRef]
11. Kang, M.; Zhu, R.; Chen, D.; Li, C.; Gu, W.; Qian, X.; Yu, W. A cross-modal generative adversarial network for scenarios generation of renewable energy. *IEEE Trans. Power Syst.* **2024**, *39*, 2630–2640. [CrossRef]
12. Dong, W.; Chen, X.; Yang, Q. Data-driven scenario generation of renewable energy production based on controllable generative adversarial networks with interpretability. *Appl. Energy* **2022**, *308*, 118387. [CrossRef]
13. Yao, W.; Huo, Z.; Zou, J.; Wu, C.; Wang, J.; Wang, X.; Lu, S.; Xie, Y.; Zhuo, Y.; Liang, J.; et al. Medium- and long-term power system planning method based on source-load uncertainty modeling. *Energies* **2024**, *17*, 5088. [CrossRef]
14. Suo, X.; Zhao, S.; Ma, Y. Multipoint layout planning method for multi-energy sources based on time-series production simulation. *Int. J. Energy Res.* **2022**, *46*, 9323–9344. [CrossRef]
15. Liu, D. An improved wind power scenario reduction method considering spatial-temporal correlation and cyber attacks. In Proceedings of the 3rd Asia Energy and Electrical Engineering Symposium (AEEES 2021), Chengdu, China, 26–29 March 2021; pp. 730–734.
16. Terrén-Serrano, G.; Ludkovski, M. Extreme day-ahead renewables scenario selection in power grid operations. *Appl. Energy* **2025**, *391*, 125747. [CrossRef]
17. Li, Z.; Li, Z. Linear programming-based scenario reduction using transportation distance. *Comput. Chem. Eng.* **2016**, *88*, 50–58. [CrossRef]
18. Sannigrahi, S.; Ghatak, S.R.; Acharjee, P. Multi-scenario based Bi-level coordinated planning of active distribution system under uncertain environment. *IEEE Trans. Ind. Appl.* **2019**, *56*, 850–863. [CrossRef]
19. Qiu, Y.; Li, Q.; Pan, Y.; Yang, H.; Chen, W. A scenario generation method based on the mixture vine copula and its application in the power system with wind/hydrogen production. *Int. J. Hydrogen Energy* **2019**, *44*, 5162–5170. [CrossRef]
20. Kile, H.; Uhlen, K.; Kjølle, G. Scenario selection in composite reliability assessment of deregulated power systems. *Int. J. Electr. Power Energy Syst.* **2014**, *63*, 124–131. [CrossRef]
21. Li, J.; Lan, F.; Wei, H. A scenario optimal reduction method for wind power time series. *IEEE Trans. Power Syst.* **2016**, *31*, 1657–1658. [CrossRef]
22. Zhou, H.; Wu, H.; Ye, C.; Xiao, S.; Zhang, J.; He, X.; Wang, B. Integration capability evaluation of wind and photovoltaic generation in power systems based on temporal and spatial correlations. *Energies* **2019**, *12*, 171. [CrossRef]
23. Tang, C.; Wang, Y.; Xu, J.; Sun, Y.; Zhang, B. Efficient scenario generation of multiple renewable power plants considering spatial and temporal correlations. *Appl. Energy* **2018**, *221*, 348–357. [CrossRef]
24. Poncelet, K.; Höschle, H.; Delarue, E.; Virag, A.; D'haeseleer, W. Selecting representative days for capturing the implications of integrating intermittent renewables in generation expansion planning problems. *IEEE Trans. Power Syst.* **2017**, *32*, 1936–1948. [CrossRef]
25. Zhu, N.; Wang, Y.; Yuan, K.; Yan, J.; Li, Y.; Zhang, K. GGNet: A novel graph structure for power forecasting in renewable power plants considering temporal lead-lag correlations. *Appl. Energy* **2024**, *364*, 123194. [CrossRef]
26. Raik, B. Generation of time-coupled wind power infeed scenarios using pair-copula construction. *IEEE Trans. Sustain. Energy* **2018**, *9*, 1298–1306.

27. Sharma, K.; Bhakar, R.; Tiwari, H.P.; Chawda, S. Scenario based uncertainty modeling of electricity market prices. In Proceedings of the 6th International Conference on Computer Applications in Electrical Engineering-Recent Advances (CERA 2017), Roorkee, India, 5–7 October 2017; pp. 164–168.
28. He, Y.; Wu, H.; Ding, M.; Bi, R.; Hua, Y. Reduction method for multi-period time series scenarios of wind power. *Electr. Power Syst. Res.* **2023**, *214*, 108813. [CrossRef]
29. Cheng, D.; Xing, F.; Su, R.; Qi, H.; Ma, L.; Ma, H.; Wang, T.; Zhou, N.; Li, C. Multiple wind farms power generation scenario generation and reduction based on multivariate copula function and greedy strategy. In Proceedings of the 7th International Conference on Power and Energy Engineering (ICPEE 2023), Chengdu, China, 22–24 December 2023; pp. 337–342.
30. Toaza, B.; Esztergaz-Kiss, D. A review of metaheuristic algorithms for solving TSP-based scheduling optimization problems. *Appl. Soft Comput.* **2023**, *148*, 110908. [CrossRef]
31. Shoaei, M.; Noorollahi, Y.; Hajinezhad, A.; Moosavian, S.F. A review of the applications of artificial intelligence in renewable energy systems: An approach-based study. *Energy Convers. Manag.* **2024**, *306*, 118207. [CrossRef]
32. Katoch, S.; Chauhan, S.S.; Kumar, V. A review on genetic algorithm: Past, present, and future. *Multimed. Tools Appl.* **2021**, *80*, 8091–8126. [CrossRef]
33. Hong, Y.; Nguyen, M. Multi-objective multi-scenario under-frequency load shedding in a standalone power system. *IEEE Syst. J.* **2020**, *14*, 2759–2769. [CrossRef]
34. Tang, L.; Dong, Y.; Liu, J. Differential evolution with an individual-dependent mechanism. *IEEE Trans. Evol. Comput.* **2015**, *19*, 560–574. [CrossRef]
35. Pandey, A.K.; Jadoun, V.K.; Jayalakshmi, N.S. Profit maximization based optimal scheduling of a virtual power plant using red fox optimizer. In Proceedings of the IEEE 10th Power India International Conference (PIICON 2022), New Delhi, India, 25–27 November 2022; pp. 1–6.
36. Pandey, A.K.; Jadoun, V.K.; Sabhahit, J.N.; Sharma, S. Interconnected operation and economic feasibility-based sustainable planning of virtual power plant in multi-area context. *Smart Cities* **2025**, *8*, 37. [CrossRef]

Disclaimer/Publisher's Note: The statements, opinions and data contained in all publications are solely those of the individual author(s) and contributor(s) and not of MDPI and/or the editor(s). MDPI and/or the editor(s) disclaim responsibility for any injury to people or property resulting from any ideas, methods, instructions or products referred to in the content.

symmetry

MDPI

Article

Data-Driven Automatic Generation Control Based on Learning to Coordinate and Teach Reinforcement Mechanism

Fan Yang [1], Xinyi Shao [2], Bo Zhou [1,*], Yuexing Shi [1], Yunwei Shen [1] and Dongdong Li [1]

[1] College of Electric Engineering, Shanghai University of Electric Power, Shanghai 200090, China; smartgridcontrol@163.com (F.Y.); syx16622323736@163.com (Y.S.); ywshen@shiep.edu.cn (Y.S.); powerldd@163.com (D.L.)
[2] Pudong Power Supply Branch State Grid, Shanghai Electric Power Company, Shanghai 200120, China; m13585642006@163.com
* Correspondence: zhoubo@shiep.edu.cn

Abstract: Large-scale integration of renewable energy introduces significant random perturbations to the power system, disrupting the symmetry and balance of active power, which complicates the stabilization of the system's frequency. Inter-regional energy cooperation plays a crucial role in maintaining the symmetry and balance of the overall power system's active power. However, when the power system area is expanded, automatic generation control (AGC) based on reinforcement learning faces the challenge of not being able to leverage the prior experience of the original system topology to train the new area, making it difficult to quickly develop an effective control strategy. To address these challenges, this paper proposes a novel data-driven AGC method that employs a multi-agent reinforcement learning algorithm with a learning to coordinate and teach reinforcement (LECTR) mechanism. Specifically, under the LECTR mechanism, when the power system region expands, agents in the original region will instruct the agents in the newly merged region by providing demonstration actions. This accelerates the convergence of their strategy networks and improves control accuracy. Additionally, the proposed algorithm introduces a double critic network to mitigate the issue of target critic network value overestimation in reinforcement learning, thereby obtaining higher-quality empirical data and improving algorithm stability. Finally, simulations are conducted to evaluate the method's effectiveness in scenarios with an increasing number of IEEE interconnected grid areas.

Keywords: automatic generation control; double critic network delay update strategy; interconnected power system; multi-agent reinforcement learning; learning to coordinate and teach reinforcement mechanism

1. Introduction

In order to solve the fossil fuel crisis and environmental pollution, a new power system primarily based on renewable energy has been rapidly developing in recent years [1–3]. The integration of a high proportion of large-capacity renewable energy sources into the grid leads to significant fluctuations in grid frequency, which undermines the stability of the grid system.

To ensure the safe and stable operation of the power system, researchers proposed automatic generation control (AGC) [4–8] as a secondary frequency regulation strategy. AGC maintains power system frequency stability by achieving "symmetry" between the amount of power generated by the system and the amount of power required on the load side, ensuring that both the two are fully matched in quantity and highly synchronized in

time. The AGC controller typically takes power system frequency deviation and tie-line power deviation as inputs, and outputs power adjustment commands for each frequency-regulating unit. It maintains the frequency stability of the power system by regulating the "symmetry" between the generated power and the load demand, namely that the two are fully matched in quantity and highly synchronized in time. In [9], a new two-degree-of-freedom combined proportional–integral–derivative control scheme is applied to an interconnected power system to minimize frequency deviations. In [10], the authors present a novel sliding mode control method for load frequency control, which offers advantages such as reduced overshoot and faster response compared to traditional PID control. These aforementioned AGCs are generally designed on the basis of accurate physical system models. However, they face challenges in accurately controlling systems with inherent uncertainties [11] and in coordinating multi-area controllers [12].

As an alternative, data-driven algorithms—particularly reinforcement learning [13–15]—have been increasingly applied in the field of AGC due to their powerful search and learning capabilities. This data-driven AGC method constructs a decision-making agent centered around neural networks, allowing the agent to dynamically interact with the interconnected power system environment during the offline training phase. By combining a reward function to quantitatively assess the effectiveness of generation control commands, the agent's parameters are gradually optimized, ultimately approaching the global optimal solution. After training, the agent can directly generate generation control commands upon acquiring data from the interconnected power system environment, significantly enhancing the computational efficiency of online decision-making.

In [16], the authors proposed a data-driven method for continuous-action AGC; however, this approach relies on single-agent reinforcement learning, which neglects cooperation among areas, leading to unstable training outcomes. In [17], the authors analyzed how positioning agents in each area to obtain global information can stabilize the training environment. Consequently, implementing a multi-agent control algorithm to regulate interconnected power systems has become essential. In [18], the authors proposed a multi-agent deep reinforcement learning method based on continuous action space, where multiple agents are trained to be able to independently output optimal power generation control commands so as to effectively respond to the control demands in complex power system environments. In [19], the authors introduced networks with varying exploration rates during the exploration process and employed categorical experience replay to enhance the utilization of experience. In [20], the authors proposed a centralized learning and decentralized execution automatic generation control framework based on a global action-value function multi-agent deep reinforcement learning algorithm, which can adaptively obtain the optimal coordinated control strategy for multiple LFC controllers. These studies demonstrate the successful application of multi-agent reinforcement learning in AGC, yielding significant results.

However, when a new area is integrated into the original interconnected power system, the previously mentioned algorithms become inefficient, and the training time increases as additional areas are incorporated. Meanwhile, the agents discussed in the aforementioned paper utilize only a single critic network. The AGC based on this method encounters challenges related to increased estimation errors [21] and overfitting during the training process. Consequently, the agent may mistakenly perceive certain actions as more beneficial for long-term rewards, leading to the adoption of suboptimal strategies.

To address the challenges associated with data-driven AGC, a MADRL control method based on the LECTR mechanism [22] is proposed for interconnected power systems. The approach introduces a double-target critic network delay update strategy to prevent the overestimation of target critic network value and enhance learning efficiency. Simultane-

ously, the newly integrated regional agents function as novice agents and interact with the expert agents of the original interconnected power system. The LeCTR mechanism introduces dynamic switching of agent roles, building upon the teach reinforcement mechanism. This enhanced interaction method further facilitates the learning of agents to collaborate and accelerates the optimization of the novice agent network. Ultimately, the trained agents are deployed within the power system environment to generate power commands in real-time.

The main contributions of this paper are as follows:

(1) A novel multi-agent distributed coordinated control framework based on the LECTR mechanism is proposed. This framework improves the training speed of the newly added area agent when the regions of the power system are expanded.
(2) During the training of the agents, we employed a double-target critic network architecture in place of a single critic network. This structure reduces the variance in target critic network value estimation, thereby enhancing the learning performance of the multi-agent system and facilitating superior control strategies.
(3) We developed a cooperative reward function considering the control error of each region within the interconnected system, effectively guiding the training of the reinforcement learning algorithm.

The paper is structured as follows: In Section 2, we provide a detailed description of the interconnected power system model. Section 3 introduces a novel data-driven AGC framework. Section 4 describes the training process of the AGC agent utilizing the LECTR mechanism. Section 5 evaluates the effectiveness of this method in an expandable power system through simulation. Finally, in Section 6, we summarize the conclusions derived from this study.

2. Muti-Area Power System Model

Figure 1 presents a typical linearized interconnected power system model [23], expressed in transfer function form. The power system consists of various components, including generators, governors, steam turbines, renewable energy sources, and loads. The agents in each area manage the total power signal for that region, with the goal of minimizing frequency deviations and tie-line power fluctuations. They achieve this by adjusting the output of each unit within the area to optimize control performance. The dynamics of the system within the i-th area of a multi-area power system can be represented by a set of differential equations.

$$\Delta \dot{f}_i = \frac{1}{2H_i}(\Delta P_{\mathrm{m}i} + \Delta P_{\mathrm{RES}i} - \Delta P_{\mathrm{L}i} - \Delta P_{\mathrm{tie},i}) - \frac{D_i}{2H_i}\Delta f_i \tag{1}$$

$$\Delta \dot{P}_{\mathrm{m}i} = \frac{1}{T_{\mathrm{t}i}}\Delta P_{\mathrm{g}i} - \frac{1}{T_{\mathrm{t}i}}\Delta P_{\mathrm{m}i} \tag{2}$$

$$\Delta \dot{P}_{\mathrm{g}i} = \frac{1}{T_{\mathrm{g}i}}\Delta P_{ci} - \frac{1}{R_i T_{\mathrm{g}i}}\Delta f_i - \frac{1}{T_{\mathrm{g}i}}\Delta P_{\mathrm{g}i} \tag{3}$$

$$\Delta \dot{P}_{\mathrm{tie},i} = 2\pi \sum_{j=1, j\neq i}^{N} T_{ij}(\Delta f_i - \Delta f_j) \tag{4}$$

$$T_{ij} = \frac{|V_i V_j|}{X_{ij}} cos\left(\delta_i^0 - \delta_j^0\right) \tag{5}$$

where δ_i^0, V_i are power angle and terminal voltage of equivalent machines for area i. X_{ij}, T_{ij} are tie-line reactance and synchronous coefficient between area i and j. ΔP_{mi}, ΔP_{gi} are generator mechanical output and valve position for i-th area. T_{gi}, T_{ti} are governor time

constant and turbine time constant for i-th area. D_i, H_i, R_i are the machine damping coefficient, synchronous machine inertia, and speed drop for i-th area. $\Delta P_{\mathrm{L}i}$, $\Delta P_{\mathrm{RES}i}$ represent the load disturbance and the random disturbance caused by the renewable energy. The generation commands, denoted as P_{ci}, are typically determined based on the area control error (ACE) signal, which is denoted by $ACE = B_i \Delta f_i + \Delta P_{\mathrm{tie},i}$. The bias factor B_i is determined using the equation $B_i = \left(\frac{1}{R_i}\right) + D_i$.

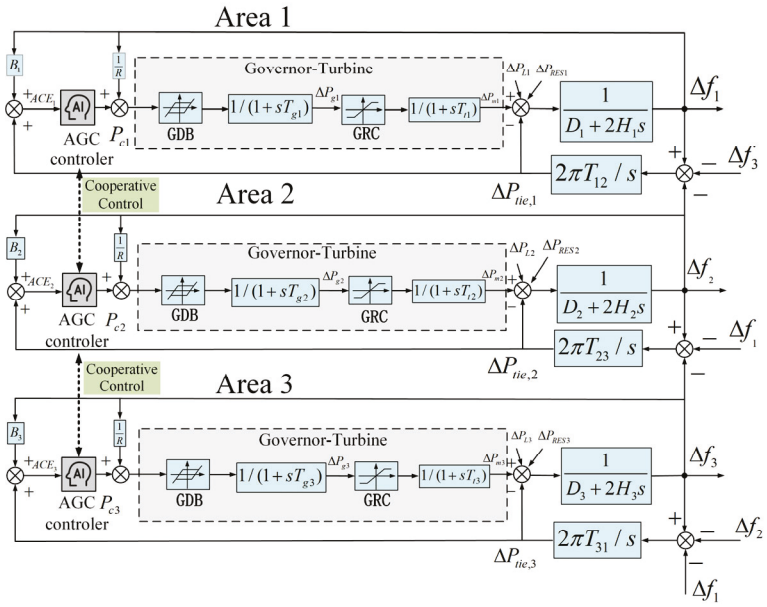


Figure 1. Multi-area interconnected power system.

In a multi-region interconnected power system, AGC controllers in each region not only regulate locally based on the ACE information within their respective regions, but also collaborate with AGC controllers in other regions. This collaboration ensures optimal cross-region power exchange and frequency regulation through the sharing of information between interconnected regions, effectively addressing the challenges posed by fluctuating and intermittent renewable energy sources.

3. Framework for AGC Based on MADRL Algorithm with the LECTR Mechanism

3.1. Action Space

The actions of each agent determine the output of the unit in the area, and the action space is shown below:

$$a_i = [A_{oder-i}] \tag{6}$$

where a_i is the action of the i-th agent and A_{oder-i} is the regulation command of the i-th agent.

3.2. State Space

The agent generates control actions by sensing information regarding the state of the power system environment. The combination of state information constitutes the state space of the agent, which in this paper, includes the following:

$$S_i = [ACE_i, \Delta f_i, P_{\mathrm{tie},i}] \tag{7}$$

where ACE_i represents the ACE value for i-th region, Δf_i represents the frequency deviation for i-th region, and $P_{tie,i}$ represents the tie line deviation for i-th region.

3.3. Reward Function

To achieve optimal AGC performance in this system, minimizing the ACE is crucial. The reward function is designed to account for both system frequency deviation and tie-line power. If the ACE becomes excessively large during the training process, the reward function value is assigned a more negative value. The scaling factor ε determines the relative impact of ACE and power output variations on the reward and is set to 0.5. Additionally, the term $\Delta P_{oder-i}{}^2 = \left(P_i - P_i'\right)^2$ is introduced as part of the reward to guide the algorithm in avoiding large fluctuations in the generation command.

$$r_i^t = -\sum_{i=1}^{n} \varepsilon (B_i \Delta f_i + \Delta P_{\text{tie},i})^2 + (1-\varepsilon)\left(P_i - P_i'\right)^2 + A$$
$$\begin{cases} A = 0 & |ACE_i| < 5\ MW \\ A = -10 & |ACE_i| \geq 5\ MW \end{cases} \tag{8}$$

3.4. Overall Training Framework

As shown in Figure 2, the proposed method is divided into two main procedures: the first procedure focuses on centralized training of the agents. The agents include an actor network $\chi(o;\theta_i)$ and a critic network $M(o,a;\varphi_i)$. In the centralized training procedure, the actor network $\chi(o;\theta_i)$ observes the state o_i and sends generation commands $a_i, i \in [1,n]$ to the generators in their respective areas. Subsequently, the actor network receives the updated state of the system following the interaction, which is expressed as $o_i', i \in [1,n]$. At each time step, the reward value $r_i, i \in [1,n]$ for the action taken in each area is calculated using a specific reward function. Finally, the data (o_i, a_i, r_i, o_i') will be added to the experience pool. The critic network samples data from the experience pool to evaluate the effectiveness of new actions, which subsequently updates the actor network. This process facilitates the training of multi-agent systems. The second procedure involves agents that completed their training (i.e., the expert agent j) providing action suggestions for power generation commands to the agent in the newly added region (i.e., the novice agent i). This approach accelerates the the novice agent i's learning of control strategies for cooperative control within the interconnected power system. After offline training optimization, the agents are deployed in an interconnected power system to enable efficient real-time control.

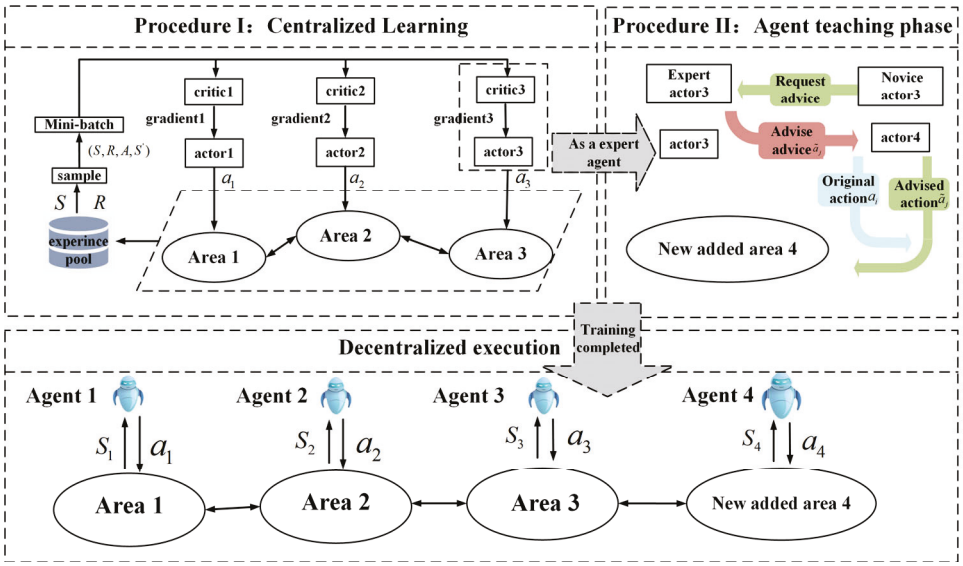


Figure 2. Data-driven AGC based on the MADRL algorithm with the LECTR mechanism.

4. Training for Agent Based on the LECTR Mechanism

The data-driven AGC method, based on the LECTR mechanism, incorporates this mechanism to enhance the convergence speed of newly added area agents. Additionally, it introduces a double-target critic network with a delayed update strategy to address the issue of overestimation in the target critic network's value. In the following subsections, we will present the enhanced MADRL algorithm and outline the specific steps for implementing the LECTR mechanism.

4.1. MADRL with a Double Target Critic Network Delay Update Strategy

The purpose of the improved MADRL algorithm presented in this paper is to facilitate updates to the parameters of the actor network parameters, maximizing the cumulative expected return J.

$$J(\theta_i) = E_{O\sim D, a\sim\chi}\left[\sum_{t=0}^{T}\gamma^t r_i^t\right] \tag{9}$$

where γ is the reward discount factor, suggesting that agents are more focused on the long-term performance of the overall reward.

In the improved MADRL algorithm, the learning process involves training a centralized critic network that has access to the policies of all agents. This centralized critic network is represented as a centralized state value function.

$$M(o, a_1, \cdots, a_n; \varphi_i) \tag{10}$$

where o represents the overall observation value, and o_i represents the local observations of each i-th agent. $\chi(o;\theta_i)$ represents the action computed by the actor network for a given state o_i.

During the update of the parameters for the i-th agent, the gradient descent methods are typically employed. The parameters of the actor network are updated by iterating in the direction opposite to the gradient. This approach allows us to gradually improve the performance of the agent.

$$\nabla_{\theta_i} J = E_{o,a_{i\sim D}}\left[\nabla_{\theta_i}\chi(o;\theta_i)\,\nabla_{a_i} M(O, a_1, \cdots, a_n; \varphi_i)_{|a_i=\chi(o;\theta_i)}\right] \tag{11}$$

The experience replay area D here includes $(o, a_1, \ldots, a_n, r_1, \ldots, r_n, o')$ of all agents.

Then, we minimize the loss function, which can be expressed as the difference between the target value and the evaluation value $M(o, a; \varphi_i)$. The parameters of the critic network can be adjusted.

$$y_i = r_i + \gamma M^-\left(o', a_1', \cdots, a_n'; \varphi_i^-\right)|_{a_i'=\chi^-(o_i';\theta_i^-)} \tag{12}$$

$$L = \frac{1}{M}\sum_{i=1}^{M}(y_i - M(o, a_1, \cdots, a_n; \varphi_i))^2 \tag{13}$$

where $M^-\left(o, a; \varphi_i^-\right)$ and $\chi\left(o_i'; \theta_i^-\right)$ are the target critic and actor networks. The target critic network and actor network initially replicate the parameters of the original critic and actor networks during the offline training process. Subsequently, the parameters of the target networks are updated with a delay, which enhances the stability of the updates for both the critic and actor networks.

To address the issue of target critic network value overestimation in the traditional MADRL algorithm, a double-target critic network $M^-\left(o, a; \varphi_i^-\right)$ is employed to mitigate the overestimation of the state value function. It is essential to consider the information from all agents in MADRL. Consequently, during training, all agents should have access to comprehensive state information, allowing them to observe the entire state space.

In addition, regularization techniques are introduced to smooth the target critic network value and prevent overfitting. Normally distributed random noise, denoted as ε, is added during the update of the critic network to enhance stability against fluctuations. The improved method for calculating the target value is presented below:

$$\varepsilon \sim clip(N(0,\sigma), -c, c) \tag{14}$$

$$y_i = r_i + min_{j=1,2}\gamma M^{-}\left(o', a_1' + \varepsilon, \cdots, a_n' + \varepsilon; \varphi_i^{-}\right) \tag{15}$$

Then, the parameters of the target networks are updated with a delay, which enhances the stability of the updates for both the critic network and the actor network. The updates for the actor network, critic network, target actor network, and target critic network are as follows:

$$\begin{array}{ll} \varphi_i = \varphi_i - \alpha^{\varphi_i} \nabla_{\varphi_i} L(\varphi_i) & \varphi_i^{-} = \tau\varphi_i + (1-\tau)\varphi_i^{-} \\ \theta_i = \theta_i + \alpha^{\theta_i} \nabla_{\theta_i} J(\theta_i) & \theta_i^{-} = \tau\theta_i + (1-\tau)\theta_i^{-} \end{array} \tag{16}$$

where α^{φ_i} and α^{θ_i} represent the learning rates for the critic and actor networks, while τ denotes the soft update rate for the target networks.

4.2. The Application of the LECTR Mechanism in Expandable Power System

This subsection outlines the procedure for executing a cooperative multi-region load frequency control task after novice agent i received guidance from expert agent j. The entire process is further divided into two phases (see Figure 3).

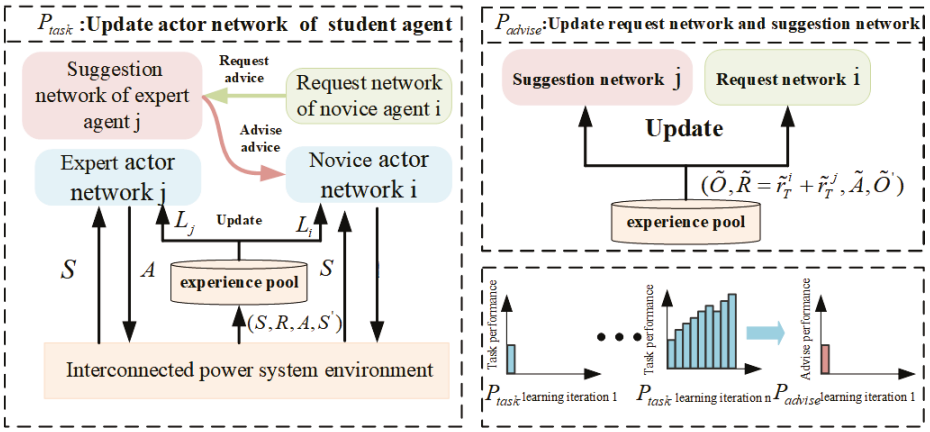


Figure 3. LeCTR consists of two iterated phases.

Phase I: In each learning iteration, the actor networks of the expert agent and the novice agent interact with the power system environment to update their actor network parameters θ_i and θ_j based on the actions suggested by the expert agent. This process utilizes the improved MADRL algorithm L_i and L_j (L_i stands for the learning algorithm of the novice agent algorithm and L_j for the learning algorithm of expert agent algorithm). We call this phase P_{task}.

Phase II: This phase primarily focuses on updating the suggestion network of the expert agent and request network of the novice agent based on the advising-level rewards generated during the process. We refer to this phase as P_{advise}.

The agent in the LeCTR mechanism can assume the role of a novice agent, an expert agent, or both simultaneously. Additionally, the agent is capable of seeking advice regarding its own state while providing guidance to teammates in different states. The LeCTR mechanism uses distinct advising-level observations for the request network of the novice agent and the suggestion network of the expert agent. The request network

of the novice agent $\overset{\sim}{\chi}_N^i\left(\tilde{O}_N^i;\overset{\sim}{\theta}_N^i\right)$ for agent i decides when to request advice using observation $\tilde{O}_N^i = < o^i, M^i(o^i,a^i) >$ where s^i and $M^i(o^i,a^i;\varphi_i)$ are calculated by the critic network. Through $\tilde{O}_N^i$, agent i observes a measure of its local task-level observation and actor network state. Similarly, the expert agent j's suggestion network $\overset{\sim}{\chi}_E^j\left(\tilde{O}_E^j;\overset{\sim}{\theta}_E^j\right)$ uses advising-level observation $\tilde{O}_E^j = < o^i, M^i(o^i,a^i;\varphi_i), M^j(o^i,a^i;\varphi_j) >$ to decide when/what to advise. $\tilde{O}_E^j$ provides expert agent j with a measure of the task-level state/knowledge of novice agent i (via o^i and $M^i(o^i,a^i;\varphi_i)$ and of its own task-level knowledge given the student's context (via $M^j(o^i,a^i;\varphi_j)$). The novice perspective action of the agent is $\tilde{a}_N^i = \overset{\sim}{\chi}_N^i\left(\tilde{O}_N^i;\overset{\sim}{\theta}_N^i\right) \in$ {request advice, do not request advice}. Meanwhile, expert agent j decides what to advise: either an action from action space of novice agent i, or a special no-advice action $\tilde{a}_\varnothing$. Thus, the expert perspective action for agent j is $\tilde{a}_E^j = \overset{\sim}{\chi}_E^j\left(\tilde{O}_E^j;\overset{\sim}{\theta}_E^j\right) \cup \tilde{a}_\varnothing$. Given no advice, novice agent i executes the originally intended action a^i. However, given advice $\tilde{a}_E^j$, novice agent i executes action $\tilde{a}_E^j$. Following advice execution, agents collect task-level experiences and update their actor network.

In Phase I, we set the reward function to evaluate the contribution of the actor network output actions to stabilize the power system frequency. In Phase II, we need to set up relevant advising-level reward functions to evaluate the contribution of the outputs of the suggestion network and the request network to accelerate the learning of the newly added area agents. Since request network $\overset{\sim}{\chi}_N^i$ and suggestion network $\overset{\sim}{\chi}_E^j$ must coordinate to help student i learn, they receive identical advising-level rewards $\tilde{r}_E^i = \tilde{r}_N^j$. In this paper, we set up the advising-level reward function as follows:

$$max_a M_E\left(o^i, a; \varphi_j\right) - M_E\left(o^i, a^i; \varphi_j\right) \tag{17}$$

The above proposal-level reward function measures the strategic deviation between the action a_i chosen by the novice agent i in state o_i and the optimal action evaluated by the expert agent j. The proposed reward function measures the deviation between the optimal action and the optimal action evaluated by the expert agent j. By quantifying the difference in the value of the critic network, the expert agent learns to estimate the 'cognitive error' of its teammates in a given state and decides whether or not to intervene accordingly. This setup allows the expert agent to improve the learning collaboration between them during the teaching process, so that they not only focus on their own task benefits, but also understand and contribute to the learning process of their teammates.

When the expert agent outputs the suggested actions, $\overset{\sim}{\chi}_E^j$ and $\overset{\sim}{\chi}_N^i$ will be rewarded, otherwise the reward is zero. The parameter-updating methods of the suggestion network and the request network are referred to in the literature [22].

In order to facilitate collaborative learning among agents, the LeCTR framework employs a novel teaching mechanism that supports dynamic role switching by structurally modeling observations, actions, and strategies at the instructional level. Specifically, $\overset{\sim}{\chi}$ is $< \overset{\sim}{\chi}_N^i, \overset{\sim}{\chi}_N^j, \overset{\sim}{\chi}_E^i, \overset{\sim}{\chi}_E^j >$; $\tilde{O}$ is $< \tilde{O}_N^i, \tilde{O}_N^j, \tilde{O}_E^i, \tilde{O}_E^i >$; $\tilde{A}$ is $< \tilde{a}_N^i, \tilde{a}_N^j, \tilde{a}_E^i, \tilde{a}_E^j >$; $\tilde{r}$ is $r_E^j + r_N^j$; and $\overset{\sim}{\theta}$ is the parameter of strategy $\overset{\sim}{\chi}$. $\tilde{N}$ is the experience pool of data related to the training of the request network and the suggestion network; and $M\left(\tilde{S}, \tilde{A}; \overset{\sim}{\theta}\right)$ is the critic network for evaluating the actions of the suggestion network and the request network. With the unified modeling described above, LeCTR allows agents to simultaneously request assistance

as a 'novice agent' and provide feedback as an 'expert agent' at any time step, enabling bi-directional switching of collaborative behaviors.

The training process of the LECTR mechanism and algorithmic flow of algorithm for training agents are shown in Figure 4.

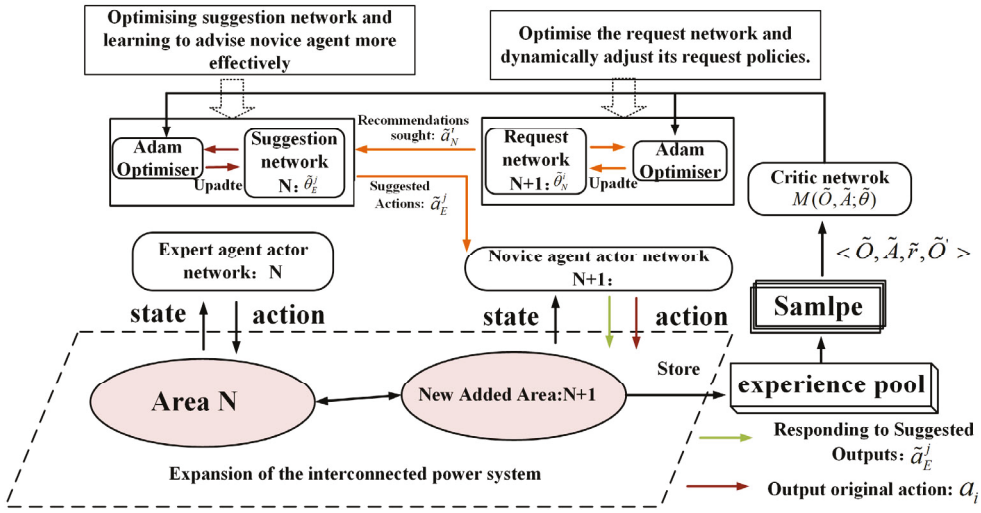


Figure 4. The training process of the LECTR mechanism.

5. Case Study

In this section, we first establish a simulation of a three-area power system to evaluate the control performance of the improved MADRL algorithm compared to other control algorithms, including deep Q-networks (DQN) [24] and the multi-agent deep deterministic policy gradient (MADDPG) [25]. Subsequently, we demonstrate the advantages of the improved MADRL with the LECTR mechanism in accelerating the learning process of the newly added agent and improving the control performance in an expanded interconnected power system.

5.1. Experimental Environment

The simulations were carried out using the deep learning framework PaddlePaddle, with the following hardware configuration: an AMD Ryzen 7 2700 eight-core processor operating at 3.20 GHz, an NVIDIA GeForce RTX 2060 GPU, and a total of 16 GB of RAM. The sampling period of the controller during the simulation is 4 s, and the total duration of the disturbance is 1500 s. We set the baseline capacity of the system to 5000 MVA. The characteristics of the power system model presented in this paper are listed in Table 1.

Table 1. Parameters of the interconnected power system.

Parameter	T_g (s)	T_t (s)	D (p.u./Hz)	H (p.u./Hz)	T_{ij} (p.u./Hz)	R (Hz/p.u.)
Area 1	0.10	0.35	1.7	24	0.014	0.5
Area 2	0.09	0.32	1.5	19	0.07	0.3
Area 3	0.08	0.33	2.7	22	0.03	0.2
Expanded area 4	0.10	0.35	1.4	17	0.019	0.6

For the DQN algorithm, the reward discount factor γ and the learning rate α were set to 0.99 and 0.0005, respectively. MADDPG utilized a learning rate of 0.001 for both the actor and critic network, a reward discount factor γ of 0.99, and a soft update rate τ of 0.01. In the proposed method, the normally distributed random noise ε was set to 0.1, and the time interval for delayed update was set to 2. The learning rates of the actor network and

critic network were set to 0.002, and a reward discount factor γ and soft update rate τ were set to 0.98 and 0.005. The number of training iterations for all algorithms was set to 30,000.

5.2. Three-Area Power System Disturbance Simulation

5.2.1. Step Load Disturbance

As shown in Figure 5, a step load disturbance is introduced to simulate the load in the power system, which experiences irregular and sudden increases and decreases. The transition process of the improved MADRL algorithm occurs in the shortest time, and the ACE of the improved MADRL algorithm remains at 0 after the step change is applied. At 300 s, 500 s, and 900 s, the absolute values of the maximum ACE changes for the three algorithms DQN, MADDPG, and the improved MADRL are (0.007 p.u., 0.0052 p.u., and 0.0032 p.u.), (0.0100 p.u., 0.0082 p.u., and 0.00526 p.u.), and (0.0066 p.u., 0.0035 p.u., and 0.0023 p.u.), respectively. The improved MADRL reduces the absolute values of the maximum ACE changes compared to the other algorithms by (21.28–53.46%), (23.28–56.85%), and (26.53–54.32%).

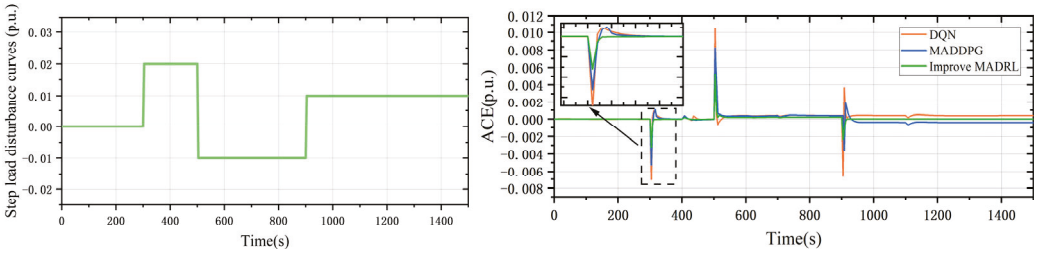


Figure 5. Step load disturbance curves and the ACE variations step load disturbance in a three-area power system.

5.2.2. Random Renewable Energy Disturbance

Renewable energy sources exhibit considerable randomness and fluctuations. To examine the impact of these stochastic variations in renewable energy on the interconnected power system, we treat renewable energy as a random disturbance without accounting for its secondary frequency regulation capabilities. Figure 6 presents the data for renewable energy sources in a three-area system.

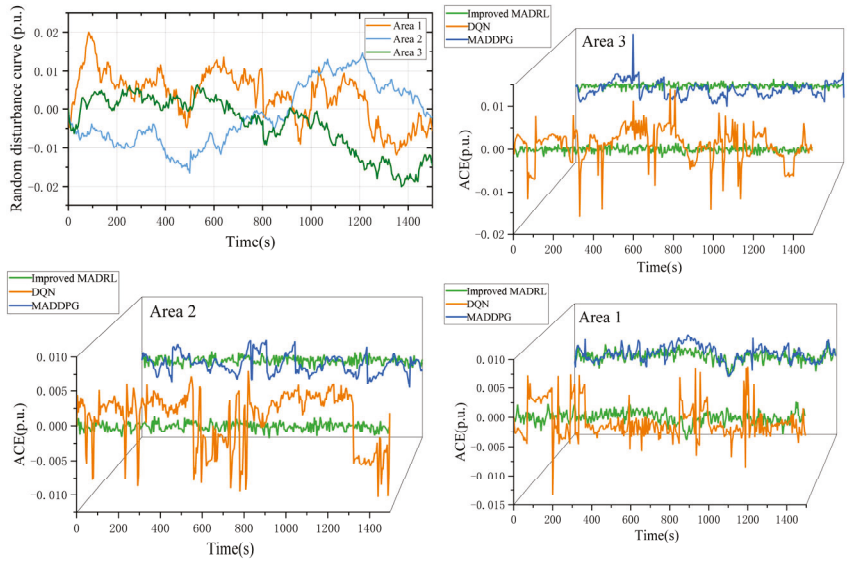


Figure 6. Random disturbance curve and the ACE variations under random disturbance in a three-area power system.

Figure 6 shows that the mean absolute ACE of the improved MADRL algorithm is significantly lower than that of other algorithms, while maintaining ACE within a reasonable range across multiple power system areas. The MADDPG algorithm can reduce the ACE to within 0.005 p.u. However, there are still regions exhibiting unsatisfactory performance. This is because the improved MADRL algorithm introduces a double-target critic network, which enhances the stability of the algorithm's convergence and prevents over-rewarding. Consequently, the improved MADRL algorithm demonstrates greater adaptability to power system environments characterized by a high proportion of renewable energy sources, resulting in superior control performance. In contrast, DQN is a single-agent algorithm that employs discrete generation control commands. As the interconnected power system expands, the dimensionality of the action space increases exponentially, leading to challenges in both exploration and convergence for the DQN algorithm. As a result, the DQN algorithm exhibits the poorest control performance, resulting in the highest average fluctuations in ACE.

Figure 7 shows the power output of the generator with different algorithms in Area 1. It can be seen that the improved MADRL algorithm has the best stability in the face of renewable energy disturbances, followed by MADDPG. Due to the strong stochastic variation of the output power of the renewable energy sources, the DQN has difficulties keeping up with the load for a short period of time.

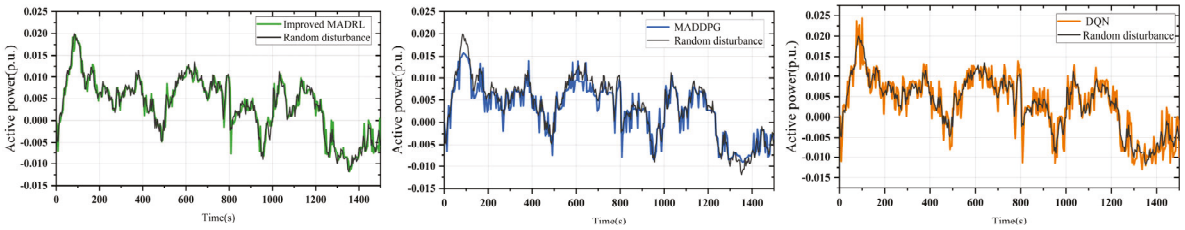


Figure 7. Output curve of the Area 1 unit under random disturbance.

The comparison of specific data is presented in Table 2. The power system data indicate that the mean absolute ACE of other algorithms was 2.5 to 6.10 times higher than that of the improved MADRL algorithm. Furthermore, the improved MADRL algorithm reduces the maximum variation in absolute ACE by 66.08% to 80.83% and achieves a reward value that is 72.61% to 132.14% higher than that of the other algorithms. Therefore, the improved MADRL algorithm demonstrates the best control performance.

Table 2. Numerical results of regional system performance comparisons.

Method	Reward	Mean Absolute ACE [p.u.]	Largest Variation in Absolute ACE [p.u.]
DQN	−1.95	0.003084164	0.013206667
MADDPG	−1.45	0.001495223	0.007463333
Improved MADRL	−0.84	0.000595075	0.002533333

5.3. Extension of Power System Disturbance Simulation

This section of the simulation extends the power system to a fourth area to evaluate the control and learning performance of the enhanced MADRL with the LECTR mechanism in a highly stochastic power system environment.

5.3.1. Comparison of Offline Training Speed

Figure 8 shows the reward convergence curves of the newly added regional agents trained offline under the guidance of four different algorithms. The proposed method achieves convergence within 6833 rounds, demonstrating improvements in convergence

speed of 58.73%, 67.95%, and 75.01% compared to the other three algorithms (improved MADRL, MADDPG, and DQN), respectively.

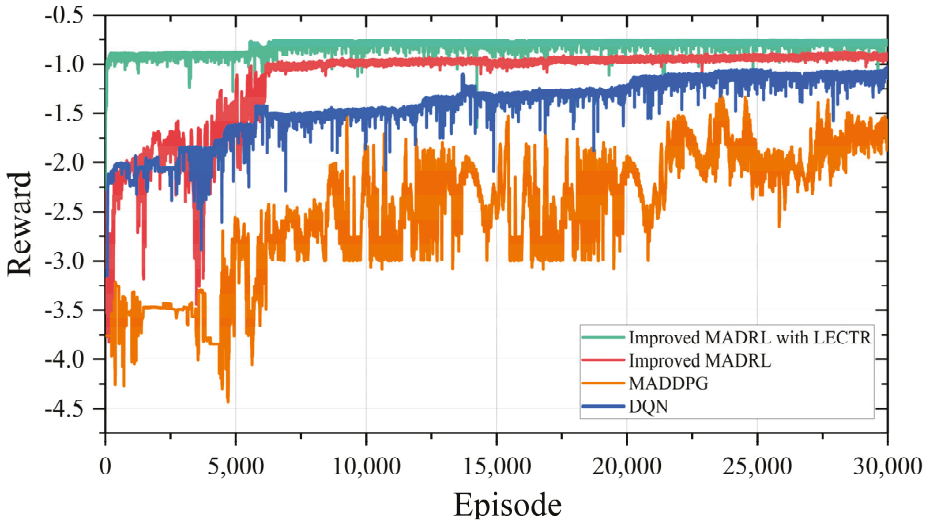


Figure 8. Reward convergence curves of different algorithms.

This is because we use a trained expert agent from the original power system region to provide action suggestions, which the novice agent in the newly joined area selectively accepts during the training process. This method ensures that the novice agent explores the power system environment through stochastic actions while assimilating the suggested actions from the expert agent's perspective and effectively translating them into local empirical knowledge. Consequently, this enables the novice agent to learn how to make improved control decisions in a scalable power system environment, thereby reducing the time required for independent learning.

For the other algorithms, there are serious challenges in dealing with the expanding interconnected power system. Each agent in the newly joined area must be retrained individually, which increases the training complexity of the multi-agent algorithms. As a result, the convergence of rewards under these algorithms becomes slower.

5.3.2. Step Load Disturbance

Figure 9 illustrates the change in ACE of the four algorithms following a step disturbance in the extended power system. It is evident that the improved MADRL with the LECTR mechanism recovers to 0 p.u. more rapidly after the disturbance. At 200 s, 600 s, and 900 s, the improved MADRL with the LECTR mechanism reduces the absolute values of the maximum ACE change compared to the other algorithms by 21.28% to 53.46%, 23.28% to 56.85%, and 26.53% to 54.32%, respectively.

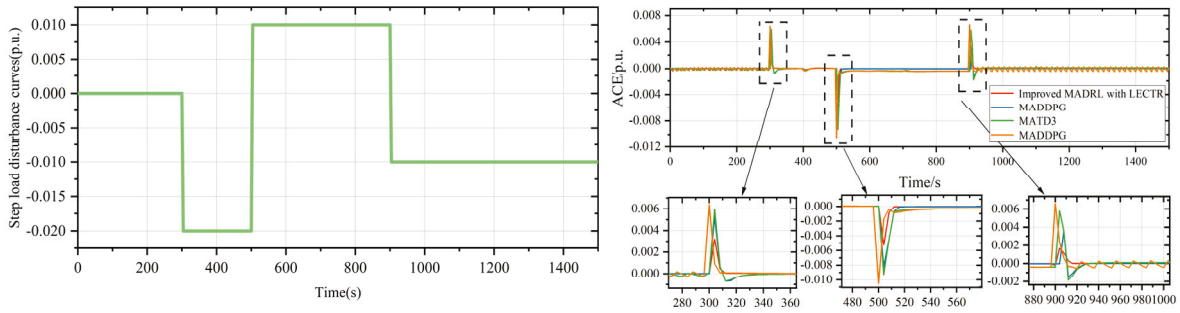


Figure 9. Step load disturbance curves and the ACE variations under step load disturbance in an expanded power system.

5.3.3. Random Renewable Energy Disturbance

Figure 10 shows the disturbance data of renewable energy sources, such as wind power, in the newly extended area. It also compares the control strategies developed by the agent in the fourth area using four different algorithms: the improved MADRL with the LECTR mechanism, improved MADRL, MADDPG, and DQN, based on ACE metrics. The results indicate that the control performance of the improved MADRL with the LECTR mechanism is superior not only to that of DQN and MADDPG, but also shows further enhancement compared to the improved MADRL.

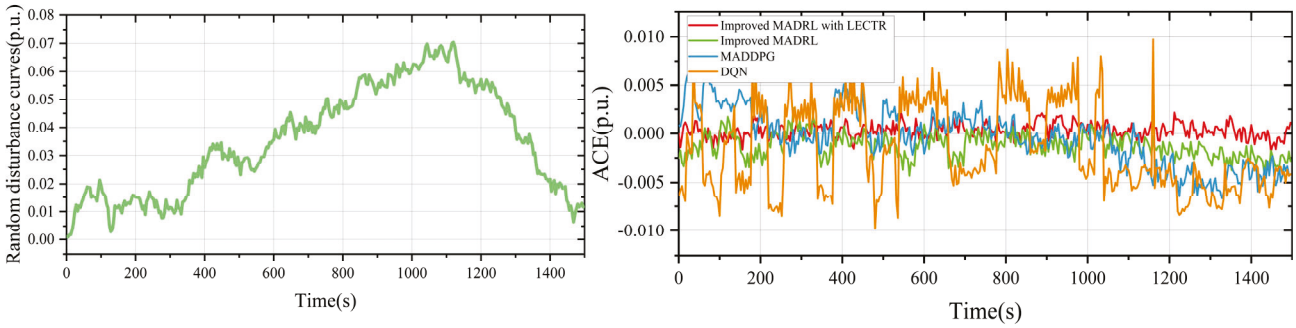


Figure 10. ACE variations under random disturbance in an expanded power system.

The comparative data for each algorithm are presented in Table 3. The improved MADRL with the LECTR mechanism reduces the mean absolute ACE by 54.93% to 84.80%, decreases the largest variation in absolute ACE by 50.03% to 78%, and achieves a reward value that is 25.33% to 150.66% higher than that of other algorithms.

Table 3. Numerical results of four-area system performance comparisons.

Method	Reward	Mean Absolute ACE [p.u.]	Largest Variation in Absolute ACE [p.u.]	Episode Number of Convergence
Improved MADRL with LECTR	−0.75	0.000658	0.00216	6833
Improved MADRL	−0.94	0.00146	0.00435	16558
MADDPG	−1.25	0.00234	0.00669	21324
DQN	−1.88	0.00433	0.00982	27345

During the expansion of power system regions, it is essential to integrate new agents into the existing multi-agent framework to develop innovative coordination control strategies for the expanded power system area. Simulations demonstrate that our proposed improved MADRL with LECTR algorithm does not require re-centralized training of all regional agents, while maintaining excellent convergence and control performance. The improved MADRL with the LECTR mechanism offers a valuable reference for data-driven AGC in more flexibly interconnected power systems.

6. Conclusions

To achieve real-time frequency response control in extended power systems, we propose a MADRL framework based on the LECTR mechanism for the dynamic optimization of AGC.

(1) The LECTR mechanism is introduced to facilitate the joint development of control strategies when interconnected power system regions are expanded. The LECTR mechanism enhances the learning speed of agents in the newly integrated region by 58.73% to 75.01% and reduces the average ACE by 54.93% to 84.80% by enabling

peer-to-peer action suggestions from agents in the original region to those in the new region.

(2) In a fixed-area power system environment, the proposed method effectively reduces ACE fluctuations and demonstrates superior control performance.

Author Contributions: Methodology, Y.S. (Yuexing Shi); software, F.Y., B.Z. and Y.S. (Yunwei Shen); formal analysis, X.S.; investigation, Y.S. (Yunwei Shen); data curation, D.L.; writing—review and editing, B.Z. All authors have read and agreed to the published version of the manuscript.

Funding: This research was funded by "National Natural Science Foundation of China", grant number "52377111" and "National Natural Science Foundation of China", grant number "52407122".

Data Availability Statement: The data presented in this study are available on request from the corresponding author due to privacy reasons.

Conflicts of Interest: Xinyi Shao was employed by the Shanghai Electric Power Company. The remaining authors declare that the research was conducted in the absence of any commercial or financial relationships that could be construed as a potential conflict of interest. The authors declare that this study received funding from "National Natural Science Foundation of China", grant number "52377111" and "National Natural Science Foundation of China", grant number "52407122". The funder was not involved in the study design, collection, analysis, interpretation of data, the writing of this article, or the decision to submit it for publication. The authors declare that the research was conducted in the absence of any commercial or financial relationships that could be construed as potential conflicts of interest.

References

1. Wang, H.; Zhang, Z.; Wang, Q. Generating adversarial deep reinforcement learning -based frequency control of island city microgrid considering generalization of scenarios. *Front Energy Res.* **2024**, *12*, 1377465. [CrossRef]
2. Basit, M.; Dilshad, S.; Badar, R.; Rehman, S.M.S. Limitations, challenges, and solution approaches in grid-connected renewable energy systems. *Int. J. Energy Res.* **2020**, *44*, 4132–4162. [CrossRef]
3. Xu, D.; Zhou, B.; Wu, Q.; Chung, C.; Li, C.; Huang, S.; Chen, S. Integrated modelling and enhanced utilization of power-to-ammonia for high renewable penetrated multi-energy systems. *IEEE Trans Power Syst.* **2020**, *35*, 4769–4780. [CrossRef]
4. Liu, Z.; Li, J.; Zhang, P.; Ding, Z.; Zhao, Y. An AGC dynamic optimization method based on proximal policy optimization. *Front. Energy Res.* **2022**, *10*, 947532. [CrossRef]
5. Kazemi, M.V.; Sadati, S.J.; Gholamian, S.A. Adaptive frequency control of microgrid based on fractional order control and a data-driven control with stability analysis. *IEEE Trans. Smart Grid.* **2022**, *13*, 381–392. [CrossRef]
6. Barakat, M. Novel chaos game optimization tuned-fractional-order PID fractional-order Pi Controller for load–frequency control of interconnected power systems. *Prot. Control. Mod. Power Syst.* **2022**, *7*, 16. [CrossRef]
7. El-Bahay, M.H.; Lotfy, M.E.; El-Hameed, M.A. Effective participation of wind turbines in frequency control of a two-area power system using Coot Optimization. *Prot. Control. Mod. Power Syst.* **2023**, *8*, 14. [CrossRef]
8. Karanam, A. and Shaw. B. A new two-degree of Freedom Combined PID controller for automatic generation control of a wind integrated interconnected power system. *Prot. Control. Mod. Power Syst.* **2022**, *7*, 20. [CrossRef]
9. Guo, J. A novel proportional-derivative sliding mode for load frequency control. *IEEE Access.* **2024**, *12*, 127417–127425. [CrossRef]
10. Saha, D.; Saikia, L.C.; Rahman, A. Cascade Controller based modeling of a four area thermal: Gas AGC system with dependency of wind turbine generator and pevs under restructured environment. *Prot. Control. Mod. Power Syst.* **2022**, *7*, 47. [CrossRef]
11. Singh, V.P.; Kishor, N.; Samuel, P. Distributed multi-agent system-based load frequency control for multi-area power system in smart grid. *IEEE Trans. Ind. Electron.* **2017**, *64*, 5151–5160. [CrossRef]
12. Yu, T.; Wang, H.Z.; Zhou, B.; Chan, K.W.; Tang, J. Multi-agent correlated equilibrium Q(λ) learning for coordinated smart generation control of interconnected power grids. *IEEE Trans Power Syst.* **2015**, *30*, 1669–1679. [CrossRef]
13. Zhang, Q.; Dehghanpour, K.; Wang, Z.; Qiu, F.; Zhao, D. Multi-agent safe policy learning for power management of networked microgrids. *IEEE Trans. Smart Grid.* **2021**, *12*, 1048–1062. [CrossRef]
14. Xi, L.; Wu, J.; Xu, Y.; Sun, H. Automatic Generation Control Based on Multiple Neural Networks with Actor-Critic Strategy. *IEEE Trans. Neural Networks Learn. Syst.* **2021**, *32*, 2483–2493. [CrossRef] [PubMed]
15. Yu, T.; Zhou, B.; Chan, K.W.; Chen, L.; Yang, B. Stochastic Optimal Relaxed Automatic Generation Control in Non-Markov Environment Based on Multi-Step *Q*(*λ*). *IEEE Trans. Power Syst.* **2011**, *26*, 1272–1282. [CrossRef]

16. Xi, L.; Chen, J.; Huang, Y.; Xu, Y.; Liu, L.; Zhou, Y.; Li, Y. Smart generation control based on multi-agent reinforcement learning with the idea of the Time Tunnel. *Energy* **2018**, *153*, 977–987. [CrossRef]
17. Daneshfar, F.; Bevrani, H. Load–frequency control: A GA-based multi-agent reinforcement learning. *IET Gener. Transm. Distrib.* **2010**, *4*, 13. [CrossRef]
18. Kamruzzaman, M.d.; Duan, J.; Shi, D.; Benidris, M. A Deep Reinforcement Learning-Based Multi-Agent Framework to Enhance Power System Resilience Using Shunt Resources. *IEEE Trans. Power Syst.* **2021**, *36*, 5525–5536. [CrossRef]
19. Li, J.; Yu, T. Deep Reinforcement Learning Based Multi-Objective Integrated Automatic Generation Control for Multiple Continuous Power Disturbances. *IEEE Access* **2020**, *8*, 156839–156850. [CrossRef]
20. Yang, F.; Huang, D.; Li, D.; Lin, S.; Muyeen, S.M.; Zhai, H. Data-driven load frequency control based on multi-agent reinforcement learning with attention mechanism. *IEEE Trans. Power Syst.* **2023**, *38*, 5560–5569. [CrossRef]
21. Xi, L.; Yu, L.; Xu, Y.; Wang, S.; Chen, X. A novel multi-agent DDQN-AD method-based distributed strategy for automatic generation control of Integrated Energy Systems. *IEEE Trans. Sustain. Energy* **2020**, *11*, 2417–2426. [CrossRef]
22. Omidshafiei, S.; Kim, D.-K.; Liu, M.; Tesauro, G.; Riemer, M.; Amato, C. Learning to teach in cooperative multiagent reinforcement learning. *Proc. AAAI Conf. Artif. Intell.* **2019**, *33*, 6128–6136. [CrossRef]
23. Li, J.; Zhou, T.; Cui, H. Brain-inspired deep meta-reinforcement learning for active coordinated fault-tolerant load frequency control of multi-area grids. *IEEE Trans. Autom Sci Eng.* **2024**, *21*, 2518–2530. [CrossRef]
24. Yin, L.; Yu, T.; Zhou, L. Design of a novel smart generation controller based on deep Q learning for large-scale interconnected power system. *J. Energy Chem.* **2018**, *144*, 04018033. [CrossRef]
25. Yan, Z.; Xu, Y. Data-driven load frequency control for stochastic power systems: A deep reinforcement learning method with Continuous Action Search. *IEEE Trans. Power Syst.* **2019**, *34*, 1653–1656. [CrossRef]

Disclaimer/Publisher's Note: The statements, opinions and data contained in all publications are solely those of the individual author(s) and contributor(s) and not of MDPI and/or the editor(s). MDPI and/or the editor(s) disclaim responsibility for any injury to people or property resulting from any ideas, methods, instructions or products referred to in the content.

symmetry

MDPI

Article

Optimal Flexibility Dispatching of Multi-Pumped Hydro Storage Stations Considering the Uncertainty of Renewable Energy

Xinyi Chen [1], Pan Wu [1], Hongyu He [1], Bingbing Song [1], Kangping Qin [1], Xiaobi Teng [1], Fan Yang [2,*] and Dongdong Li [2]

[1] State Grid East China Branch, Shanghai 200120, China; chen_xy@ec.sgcc.com.cn (X.C.); wu_p@ec.sgcc.com.cn (P.W.); he_hy@ec.sgcc.com.cn (H.H.); song_bb@ec.sgcc.com.cn (B.S.); qin_kp@ec.sgcc.com.cn (K.Q.); teng_xb@ec.sgcc.com.cn (X.T.)
[2] College of Electric Power Engineering, Shanghai University of Electric Power, Shanghai 200090, China; lidongdong@shiep.edu.cn
* Correspondence: yangfan@shiep.edu.cn

Abstract: With the continuous increase in the penetration rate of renewable energy, the randomness and flexibility demand in the power system continues to increase. The main grid side of the power system vigorously develops pumped hydro storage (PHS) resources. However, the current PHS station scheduling method of a fixed time period and fixed power has lost a certain flexibility supply. In this paper, an optimal dispatching model of multi-pumped hydro storage stations is proposed to supply flexibility for different regions of the state grid in east China. Firstly, the credible predictable power (CPP) of renewable energy is calculated and the definition of flexibility demand of a power system is given. The calculation model for flexibility demand is established. Secondly, considering the regional allocation constraint in the state grid in east China, a non-centralized model of multi-PHS within the dispatch scope is established. In the model, the constraints of storage capacity of different hydropower conversion coefficients of each PHS station is considered. The flexibility supply model of PHS stations to each region of the state grid in east China is established to realize reasonable flexibility allocation. Then, by combining the PHS station models and the flexibility demand calculation model, the optimal dispatching model for the flexibility supply of multi-PHS stations is established. Finally, based on the network dispatching example, the effectiveness and superiority of the proposed strategy are verified by a case study.

Keywords: pumped hydro storage (PHS) station; flexibility; flexible scheduling; power system; renewable energy

1. Introduction

With the "dual carbon" goal proposed, the installed capacity of renewable energy resources in the power system will continue to increase. As a result, the penetration rate of new energy continues to increase. The superposition of renewable energy resources and load fluctuations leads to an increase in the risk of instability in the power system. Therefore, for the stable operation of the power system, the power system needs to have a stronger ability to cope with uncertainty and volatility. The "symmetry" between electricity production (power generation) and electricity consumption can be regarded as an ideal state, namely that the two are fully matched in quantity and highly synchronized in time. In order to achieve this state, the power system needs flexible scheduling strategies and efficient energy storage technology to cope with the instability of intermittent energy, such as wind and solar energy, on the power generation side, as well as the random fluctuations of load on the power side.

At present, scholars have adopted various methods to deal with the uncertainty of new energy in the optimization scheduling process. The predicted power is utilized directly in most instances for calculating when developing the day-ahead dispatch. References [1–3]

predict the power of renewable energy resources (RERs) through different methods, which eventually improves the accuracy of RERs' prediction in long- and short-time scales. On this basis, a more appropriate dispatch can be developed. However, these studies ignore the degree of fluctuations of RERs.

In addition, in order to measure the ability of the power system to cope with volatility, the concept of "power system flexibility" was proposed. In 2008, the International Energy Agency (IEA) proposed the concept of "power system flexibility", which reflects the ability of a power system to cope with large fluctuations in demand and supply. The stronger the flexibility, the stronger the ability to cope with fluctuations within the system; that is, the stronger the ability to maintain system stability [4]. Power system flexibility is defined in [5] as the ability of a system to call on its own resources to meet the load changes in the grid. In [6,7], power system flexibility is the ability to respond to load fluctuations at various time scales and maintain the standard level of system reliability. Therefore, there is still no unified definition of power system flexibility, but in general, the flexibility of the power system is the ability to dispatch various flexible resources in the power system and maintain system stability per unit time.

By the end of 2022, the total installed capacity of PHS stations approved under construction was 121 million kilowatts in China. However, at present, there is no commercial consensus on the dispatch of PHS units in the power system, especially the coordinated dispatch with other units. At the same time, the potential for the flexibility supply of PHS stations themselves is not sufficient. Therefore, some studies have focused on the more adequate dispatch of PHS stations. In [8], the authors study the optimal operation evaluation criteria, considering factors such as energy diversification and allocation, based on the research results of PHS-based energy systems in recent years. In [9], the authors establish an operation dispatching model with the goal of minimizing the running cost of the PV-PHS system. In [10], the authors combined PHS with residential buildings to study the technical and economic feasibility. In [11], the authors conducted a study on the optimal dispatch and management of seawater PHS stations with the goal of maximizing operating profits. However, the common limitation of these studies is that they all aim for optimal dispatching with the goal of economic optimization, and do not consider the flexibility balance between supply and demand in the dispatching process.

In [12–15], the lowest cost is taken as the optimization goal, so that the combined operation of wind power and pumped storage combined unit model is established. In [16], the authors examined the dispatching of PHS resources in coordination with other resources. In [17], the authors proposed a novel deterministic PSH model that considers the transition time and trajectory between three states of PHS units in look-ahead dispatch. In [18], the authors proposed a novel coordination strategy of wind and PHS units for a fast and reliable self-healing process. In these studies, the operation and dispatch models of PHS stations are established, but the reserved time constraints between the working conditions of PHS stations and the storage capacity constraints of different hydropower conversion coefficients are not considered. At the same time, only one PHS station is considered in these studies to provide or absorb power to the grid, or model pumped storage power plants intensively. The issue of multiple PHS units and supply flexibility for multiple regions is not considered. In actual operation, when the multi-PHS stations supply flexibility to multiple regions, it is necessary to consider the regional allocation constraints.

In order to address the shortcomings in the current research, the main objectives of this study are as follows:

(1) CPP is calculated based on predictive data of RERs. In view of the current problem of inconsistent definition of the flexibility of power systems, this study defines the flexibility demand of power system as the change in net load per unit time, and propose a formula model for calculating flexibility demand at multiple time scales;

(2) Design the refined operation model of PHS stations. This study summarizes the PHS unit models in previous studies and combines the actual operation characteristics of PHS stations to further refine the operation models of PHS stations.

(3) Propose the optimal flexibility dispatching model of multi-PHS stations. Based on the optimal matching of the flexibility supply of PHS stations and the flexibility demand of each region, the objective function is established. To integrate the different regional allocation constraints of different PHS stations to different regions, the flexibility supply of PHS stations to different regions was quantified, and the flexibility supply model of PHS stations was established. The effectiveness of the proposed method is verified by a case study.

2. Optimal Flexibility Dispatching Model of Multi-PHS Stations Considering the Uncertainty of Renewable Energy

In this study, an optimal flexible scheduling model for multi-PHS stations considering the uncertainty of renewable energy is proposed. On the basis of considering the uncertainty of the renewable energy forecast, the net load series is calculated, and then the flexibility demand is obtained. According to the actual operation characteristics of PHS stations, a refined operation model of PHS stations is established. Considering the power allocation constraints caused by the actual situation, the flexibility supply of different regions is calculated. Finally, the flexibility demand and supply are best matched to achieve the optimal flexible dispatching, and the economy of the flexibility supply mode is compared with that of the thermal power flexibility supply. The overall research framework is shown in Figure 1.

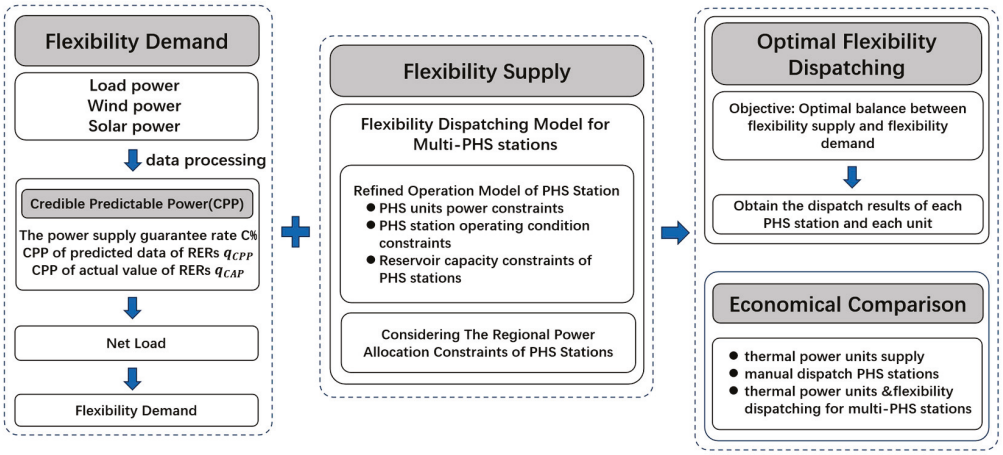


Figure 1. Overall research block diagram.

3. Flexibility Demand of Power System

In this study, power system flexibility is defined as the ability of the power system to cope with power changes and maintain stability, and flexibility demand is defined as the amount of change per unit time of net load. At the same time, the forecasted uncertainty of renewable energy is considered. Flexibility has both upward and downward directions, and the values and characteristics of flexibility are different. For the demand for flexibility in different directions, the flexible supply in different directions needs to be balanced with it.

3.1. Calculation of CPP

The CPP of RERs is defined as the minimum level of output that renewable energy forecasts can reach with a certain probability C%. This probability C% is also referred to as the power supply guarantee rate. This value represents a high-confidence prediction of energy output, reflecting the overall characteristics of renewable energy. The formula for calculating the CPP of RERs is as follows:

$$F(x) = \int_{-\infty}^{x} \hat{f}(s)ds \tag{1}$$

$$q = F^{-1}(x)|_{x=1-C\%} \tag{2}$$

where $F(x)$ is the cumulative distribution function of the dataset, the dataset is predicted data or actual value of RERs, $\hat{f}(s)$ is the probability density function of the dataset, $F^{-1}(x)$ is the inverse function of $F(x)$, q is the CPP of the dataset within power supply guarantee rate C%, and C% is the percentage of confidence that ensures RERs can reliably output as planned.

Applying (1) and (2) and using the predicted data of RERs, the CPP of the predicted data of RERs q_{CPP} can be calculated. Applying (1) and (2) and using the actual value of RERs, the Credible Actual Power (CAP) q_{CAP} can be calculated, i.e., CPP of actual value of RERs.

Furthermore, the incorporating ratio of RERs participating in dispatching is given by:

$$\beta = \frac{q_{CAP}}{q_{CPP}} \tag{3}$$

In the dispatching process, all forecasted renewable energy power is replaced by P^{new}.

$$P^{new} = \beta \cdot P^{new_h} \tag{4}$$

where P^{new} is the renewable energy power used for dispatching, including wind power P_t^{wind} and solar power P_t^{solar}; P^{new_h} is the original forecast data obtained from the wind or solar plants.

3.2. Formula Model for Calculation of Power System Flexibility Demand

3.2.1. Net Load Time Series Calculations

The net load is the power of the power system load demand minus the output power of renewable energy, and the net load can reflect the superposition fluctuation of load and renewable energy. The net load, at the same time, depends on the load demand power and the renewable energy output power at that time. The net load of the power system is calculated as follows:

$$P_t^{net} = P_t^{load} - P_t^{wind} - P_t^{solar} \tag{5}$$

where P_t^{net} is the net load value at time t. P_t^{load}, P_t^{wind}, and P_t^{solar} are the required load power, the output power of wind power, and the output power of photovoltaics at time t, respectively.

3.2.2. The Flexibility Demand

The flexibility demand at different time scales is the amount of change in the net load per unit time, and the flexibility demand at different time scales is also different. The flexibility demand at different time scales is calculated as follows:

$$P_t^{flex} = P_{t+a}^{net} - P_t^{net} \tag{6}$$

where P_t^{flex} is the flexibility demand of the t period. P_{t+a}^{net} is the predicted net load value corresponding to the next scheduling period; if the sampling interval of the forecast data is the same as the time of the scheduling period, a takes 1.

The value of the flexibility demand calculated according to Equation (6) is divided into positive and negative values, which are used to distinguish the direction of the flexibility demand, with a positive value indicating an upward flexibility demand and a negative value indicating a downward flexibility demand. The following formulas can be used to distinguish between upward and downward flexibility demand:

$$P_{t,s}^{flex_up} = \begin{cases} P_{t,s}^{flex}, \ P_{t,s}^{flex} > 0 \\ 0, \ P_{t,s}^{flex} \leq 0 \end{cases} \tag{7}$$

$$P_{t,s}^{flex_dn} = \begin{cases} 0, \ P_{t,s}^{flex} > 0 \\ P_{t,s}^{flex}, \ P_{t,s}^{flex} \leq 0 \end{cases} \tag{8}$$

where $P_{t,s}^{flex_up}$ and $P_{t,s}^{flex_dn}$ are the upward flexibility demand and the downward flexibility demand for period t under time scale s, respectively.

4. Flexibility Dispatching Model for Multi-PHS Stations

4.1. Set Dispatching Variables

- Power generation/pumping condition status variables $U_{i,t}^{gen}/U_{i,t}^{pm}$: Boolean variables. Indicate the power generation/pumping status of the ith PHS unit in the t period. A value of 0 indicates that the PHS station is not in the power generation/pumping condition, and a value of 1 indicates that it is in the power generation/pumping condition.
- Generating power $P_{i,t}^{gen}$: Real variables. Indicate the power generated by the ith PHS unit in the t period.
- The amount of water remaining in the upstream/downstream reservoir $E_{n,t}^{up}/E_{n,t}^{dn}$: Real variables. Indicate the water volume of the upstream/downstream reservoir of the nth PHS station in the t period.
- Number of power generation/pumping starts $K_{i,d}^{gen}/K_{i,d}^{pm}$: Integer variables. Indicate the number of power generation/pumping conditions started on day d for the ith PHS unit. $K_{i,d}^{gen}$ represents the number of power generation conditions started on day d for the ith PHS unit. $K_{i,d}^{pm}$ represents the number of pumping conditions started on day d for the ith PHS unit. This variable can be calculated and represented by the power generation/pumping condition state variable.

4.2. Refined Operation Model of PHS Station

In order to make the PHS station more accurate in the dispatching process, we must fully consider the various operation characteristics of the PHS station in the actual operation. In this study, we designed a refined operation model of the PHS station. The PHS unit has the characteristics of fast start and stop, fast climbing speed, etc. PHS units can be converted under three working conditions: power generation, pumping, and shutdown, corresponding to the state of transmitting power, absorbing power, and neither emitting nor absorbing power. As a result, PHS stations are able to provide flexibility in both upward and downward directions. However, the PHS units in the same PHS station cannot be in both power generation and pumping conditions at the same time. None of the PHS units in the entire dispatch scope can be in power generation and pumping conditions at the same time. Since the PHS unit cannot directly jump from the pumping condition to the power generation condition, nor can it jump from the power generation condition to the pumping condition, when the pumping and power generation conditions are converted, an interval of dispatching period is required.

A PHS station is usually equipped with multiple PHS units and has an upstream reservoir and a downstream reservoir. PHS units in the same PHS station share the same upstream and downstream reservoirs. The volume of the upstream reservoir determines the time when the PHS station can generate electricity, and the amount of water in the downstream reservoir determines the time when it can be pumped. However, the basic downstream reservoir capacity is much larger than the upstream reservoir capacity, so in most cases, the effective reservoir capacity of the upstream reservoir of the PHS station is mainly considered. At the same time, there is a dynamic equilibrium relationship between the upper and downstream reservoirs of PHS stations, and different PHS stations have different hydropower conversion coefficients due to the different heights of the drop between the upstream reservoir and the downstream reservoir. The constraints contained in the refined operation model of PHS station are as follows:

1. PHS units power constraints

(1) Power generation constraint:

$$P_{i,min}^{gen} \le P_{i,t}^{gen} \le P_{i,max}^{gen} \tag{9}$$

where $P_{i,min}^{gen}$ is the minimum stable power generation power of the ith PHS unit, and $P_{i,max}^{gen}$ is the maximum power generation power of the ith PHS unit, $i = 1, 2, \cdots$.

(2) Pumping power constraint:

$$P_i^{pm} = P_{i,t}^{pm} \tag{10}$$

where P_i^{pm} is the rated pumping power of the ith PHS unit.

2. PHS station operating condition constraints

(1) Different working conditions are not simultaneous constraints:

$$U_{i,t}^{gen} + U_{j,t}^{pm} \le 1 \tag{11}$$

where $j = 1, 2, \cdots$, and m is the number of PHS units within the dispatch scope.

(2) Condition conversion reservation time constraints:

$$\begin{cases} U_{i,t}^{gen} \le 1 - U_{i,t-1}^{pm} \\ U_{i,t}^{pm} \le 1 - U_{i,t-1}^{gen} \end{cases} \tag{12}$$

(3) Prevent the operating condition changes sudden constraints:

$$\begin{cases} \left(1 - U_{i,t-1}^{gen}\right) \cdot U_{i,t-2}^{gen} + \left(1 - U_{i,t-1}^{gen}\right) \cdot U_{i,t}^{gen} \le 1 \\ \left(1 - U_{i,t-2}^{gen}\right) \cdot U_{i,t-1}^{gen} + \left(1 - U_{i,t}^{gen}\right) \cdot U_{i,t-1}^{gen} \le 1 \end{cases} \tag{13}$$

$$\begin{cases} \left(1 - U_{i,t-1}^{pm}\right) \cdot U_{i,t-2}^{pm} + \left(1 - U_{i,t-1}^{pm}\right) \cdot U_{i,t}^{pm} \le 1 \\ \left(1 - U_{i,t-2}^{pm}\right) \cdot U_{i,t-1}^{pm} + \left(1 - U_{i,t}^{pm}\right) \cdot U_{i,t-1}^{pm} \le 1 \end{cases} \tag{14}$$

(4) Specified time shutdown constraints:

$$U_{i,t}^{gen} + U_{i,t}^{pm} = 0 \tag{15}$$

(5) The maximum number of starts under the same working condition in one day constraints:

$$K_{i,start,min}^{gen} \le K_{i,d}^{gen} \le K_{i,start,max}^{gen} \tag{16}$$

$$K_{i,start,min}^{pm} \le K_{i,d}^{pm} \le K_{i,start,max}^{pm} \tag{17}$$

where $K_{i,start,min}^{gen}$ and $K_{i,start,max}^{gen}$ are the minimum and maximum number of starts of the ith PHS unit in a day, respectively. $K_{i,start,min}^{pm}$ and $K_{i,start,max}^{pm}$ are the minimum and maximum number of pumping starts in a day for the ith PHS unit, respectively.

$$K_{i,d}^{gen} = \sum_{t=1}^{T} \left(1 - U_{i,t-1}^{gen}\right) \cdot U_{i,t}^{gen} \tag{18}$$

$$K_{i,d}^{pm} = \sum_{t=1}^{T} \left(1 - U_{i,t-1}^{pm}\right) \cdot U_{i,t}^{pm} \tag{19}$$

where T is the number of time slots dispatched.

(6) Minimum running time constraint for power generation:

$$\left(X_{i,t-1}^{gen,on} - T_i^{gen,on}\right) \cdot \left(U_{i,t-1}^{gen} - U_{i,t}^{gen}\right) \ge 0 \tag{20}$$

where $X_{i,t-1}^{gen,on}$ is the continuous operation time of the ith PHS unit in the t period. $T_i^{gen,on}$ is the minimum continuous operation time of the ith PHS unit under power generation conditions. The formula for calculating $X_{i,t-1}^{gen,on}$ is as follows:

$$X_{i,t}^{gen,on} = \left(1 - U_{i,t-1}^{gen}\right) \cdot U_{i,t}^{gen} + U_{i,t-1}^{gen} \cdot U_{i,t}^{gen} \cdot \left(1 + X_{i,t-1}^{gen,on}\right) \tag{21}$$

(7) Minimum running time constraint for pumping:

$$\left(X_{i,t-1}^{pm,on} - T_i^{pm,on}\right) \cdot \left(U_{i,t-1}^{pm} - U_{i,t}^{pm}\right) \geq 0 \tag{22}$$

where $X_{i,t-1}^{pm,on}$ is the continuous pumping time of the ith PHS unit in the t period. $T_i^{pm,on}$ is the minimum continuous operation time of the ith PHS unit under pumping conditions. The formula for calculating $X_{i,t}^{pm,on}$ is as follows:

$$X_{i,t}^{pm,on} = \left(1 - U_{i,t-1}^{pm}\right) \cdot U_{i,t}^{pm} + U_{i,t-1}^{pm} \cdot U_{i,t}^{pm} \cdot \left(1 + X_{i,t-1}^{pm,on}\right) \tag{23}$$

(8) PHS unit start-up constraint:

$$\sum_{i=1}^{I_n} U_{i,t}^{gen} - \sum_{i=1}^{I_n} U_{i,t-1}^{gen} \leq 1 \tag{24}$$

$$\sum_{i=1}^{I_n} U_{i,t}^{pm} - \sum_{i=1}^{I_n} U_{i,t-1}^{pm} \leq 1 \tag{25}$$

where I_n is the number of PHS units in the nth PHS station.

3. Reservoir capacity constraints of PHS stations

(1) Upstream reservoir and downstream reservoir constraints:

$$\begin{cases} E_{n,min}^{up} \leq E_{n,t}^{up} \leq E_{n,max}^{up} \\ E_{n,min}^{dn} \leq E_{n,t}^{dn} \leq E_{n,max}^{dn} \end{cases} \tag{26}$$

where $E_{n,min}^{up}$ and $E_{n,max}^{up}$ are the minimum capacity and maximum capacity of the upstream reservoir, respectively. $E_{n,min}^{dn}$ and $E_{n,max}^{dn}$ are the minimum capacity and maximum capacity of the downstream reservoir, respectively.

(2) The dynamic balance of upper and lower storage capacity constraints:

$$\begin{cases} E_{n,t}^{up} = Q_{n,t}^{pm} - Q_{n,t}^{gen} + E_{n,t-1}^{up} \\ E_{n,t}^{dn} = -Q_{n,t}^{pm} + Q_{n,t}^{gen} + E_{n,t-1}^{up} \end{cases} \tag{27}$$

where $Q_{n,t}^{pm}$ and $Q_{n,t}^{gen}$ are the amount of pumped water stored and the power generation displacement in the t period of the nth PHS station, respectively.

Under the power generation condition of the PHS unit, the gravitational potential energy of the water is converted into electrical energy, and under the pumping condition, the electrical energy is converted into the gravitational potential energy of the water. Therefore, there exists the following relationship between power generation and pumping power of PHS stations and the amount of drainage and pumped water:

$$\begin{cases} P_{n,t}^{gen} = \eta_n^{gen} \cdot Q_{n,t}^{gen} \\ P_{n,t}^{pm} = \eta_n^{pm} \cdot Q_{n,t}^{pm} \end{cases} \tag{28}$$

where $P_{n,t}^{gen}$ is the total power generated in the t period of the nth PHS station, and its value is equal to the sum of the power generated by all PHS units in the t period of the nth PHS station. $P_{n,t}^{pm}$ is the total pumped power of the nth PHS station in the t period, and its

value is equal to the sum of the pumping power of all PHS units in the t period in the nth PHS station. η_n^{gen} and η_n^{pm} are the water-electricity conversion coefficient under the power generation condition and the water-electricity conversion coefficient under the pumping condition of the nth PHS station, respectively.

The water-electricity conversion coefficient η_n^{gen} of the PHS station under power generation conditions indicates a power generation capacity of 1 m^3 water conversion per unit of water consumed under power generation conditions, and the calculation formula is as follows:

$$\eta_n^{gen} = \frac{\eta_n^{tur} \cdot Q^{gen} \cdot h_n^{gen} \cdot \rho \cdot g}{e} \tag{29}$$

where η_n^{tur} is the average turbine efficiency of the nth PHS station. Q^{gen} is the unit of water volume, the value is 1 m^3. ρ is the density of water, usually 1000 kg/m^3. h_n^{gen} is the height of the drop between the upstream reservoir drainage outlet and the downstream reservoir of the nth PHS station; in $m.$, e is the unit of electricity and the value is $e = 1\,\text{MWh} = 3.6 \times 10^9$ J. Therefore, the water-electricity conversion coefficient of the PHS station under the power generation condition mainly depends on the height of the drop between the upstream reservoir drainage outlet and the downstream reservoir of the PHS station.

The water-electricity conversion coefficient η_n^{pm} under the pumping condition of the PHS station represents the amount of electricity consumed by pumping 1 m^3 of water to the upstream reservoir under the pumping condition, and the calculation formula is as follows:

$$\eta_n^{pump} \cdot \eta_n^{pm} \cdot e = h_n^{pm} \cdot Q^{pm} \cdot \rho \cdot g \tag{30}$$

$$\eta_n^{pm} = \frac{h_n^{pm} \cdot Q^{pm} \cdot \rho \cdot g}{\eta_n^{pump} \cdot e} \tag{31}$$

where η_n^{pump} is the average pump efficiency of the nth PHS station. h_n^{pm} is the height of the drop from the downstream reservoir pumping port to the upstream reservoir of the nth PHS station; in $m.$, Q^{pm} is the unit of water volume and the value is 1 m^3.

4.3. Flexibility Supply for Different Regions

The flexibility supply of the PHS station to different regions is calculated by the final dispatch power of each PHS station. The dispatching power generation and pumping power of each PHS station are calculated by the working condition of each unit of each PHS station and the power generation and pumping power.

The final dispatch power generation/pumping power of each PHS station is determined by the power generation/pumping state variable and the power generation/pumping power. $P_{n,t}^{gen,end}$ and $P_{n,t}^{pm,end}$ are the dispatch generation power and pumping power of the nth PHS station during the t period, respectively. The calculation formulas are as follows:

$$P_{n,t}^{gen,end} = \sum_{i=1}^{I_n} U_{i,t}^{gen} \cdot P_{i,t}^{gen} \tag{32}$$

$$P_{n,t}^{pm,end} = \sum_{i=1}^{I_n} U_{i,t}^{pm} \cdot P_{i,t}^{pm} \tag{33}$$

The formulas for calculating the upward and downward flexibility supply obtained by each region in each dispatching period are as follows:

$$F_{t,r}^{up,supply} = \sum_{n=1}^{N} p_{n,r} \cdot P_{n,t}^{gen,end} \tag{34}$$

$$F_{t,r}^{dn,supply} = \sum_{n=1}^{N} p_{n,r} \cdot P_{n,t}^{pm,end} \tag{35}$$

where $p_{n,r}$ is the allocation ratio of the pumped power distribution from the nth PHS station to area r.

The flexibility supply variables obtained by each region in each dispatching period can be calculated as shown in Figure 2.

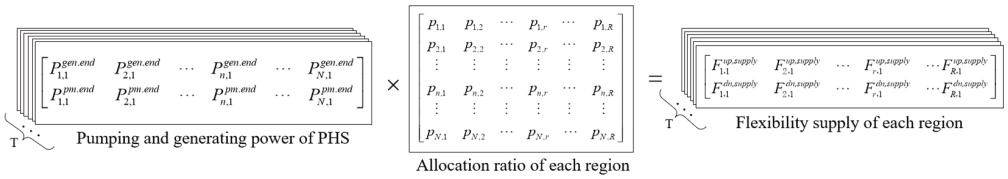


Figure 2. Schematic diagram of the flexibility supply variables.

In order to prevent the oversupply flexibility of PHS stations and the reverse increase in flexibility demand, the flexibility supply needs to meet the constraints of preventing excessive flexibility supply:

(1) Upward flexibility supply constraints: The upward flexibility supply of PHS stations to each region cannot exceed the upward flexibility demand of this region; otherwise, there will be an excess of upward flexibility supply. The expression is as follows:

$$P_{t,r}^{flex_up} - F_{t,r}^{up,supply} \geq 0 \tag{36}$$

where $P_{t,r}^{flex_up}$ is upward flexibility demand in the t period of r area. $F_{t,r}^{up,supply}$ is t period upward flexibility supply to the r area.

(2) Downward flexibility supply constraints: The downward flexibility supply of PHS stations to each region cannot exceed the downward flexibility demand of this region; otherwise, there will be excessive downward flexibility supply. The expression is as follows:

$$F_{t,r}^{dn,supply} - P_{t,r}^{flex_dn} \geq 0 \tag{37}$$

where $F_{t,r}^{dn,supply}$ is t period downward flexibility supply to the r area. $P_{t,r}^{flex_dn}$ is downward flexibility demand in the t period of r area.

4.4. Objective Function

In order to achieve the optimal supply flexibility of PHS stations, it is necessary to best match the flexibility supply of PHS stations with the flexibility demand of each region. That is, the difference between the flexibility supply of PHS stations to each region and the flexibility demand of each region needs to be as small as possible. In this study, the matching degree between the flexibility supply of PHS stations and the flexibility demand for each region is quantified by the difference between the flexibility supply of PHS stations and the flexibility demand of each region.

The objective function considers the influence of PHS stations on the flexibility supply of different regions in different modes, and the flexibility supply of PHS stations to each region needs to be calculated according to a certain allocation ratio.

The difference between upward flexible demand and upward flexible supply is calculated as follows:

$$F_{diff}^{up} = \sum_{r=1}^{R} \sum_{t=1}^{T} \left(P_{t,r}^{flex_up} - F_{t,r}^{up,supply} \right) \tag{38}$$

where F_{diff}^{up} is the deviation between upward flexibility demand and upward flexibility supply within the dispatching scope, i.e., the upward flexibility demand after the PHS supply and the upward flexibility. R is the total number of regions within the dispatching scope.

The difference between downward flexibility demand and downward flexibility supply is calculated as follows:

$$F_{diff}^{dn} = \sum_{r=1}^{R} \sum_{t=1}^{T} \left(F_{t,r}^{dn,supply} - P_{t,r}^{flex_dn} \right) \tag{39}$$

where F_{diff}^{dn} is the difference between the downward flexibility demand and the downward flexibility supply within the dispatching scope, i.e., the downward flexibility demand after the PHS supply and the downward flexibility.

Based on the above formula of flexibility supply and demand, considering the flexibility supply of PHS, including upward flexibility supply and downward flexibility supply, the optimal matching of flexibility supply and demand in each region by each PHS station is taken as the objective function of day-ahead dispatching, and its expression is as follows:

$$minF = min\left(F_{diff}^{up} + F_{diff}^{dn}\right) \tag{40}$$

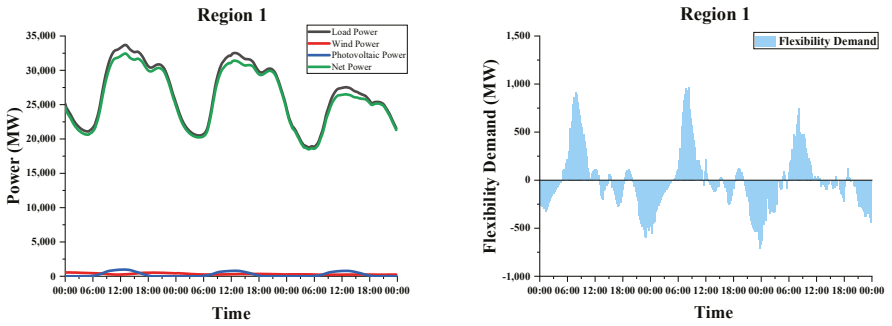
The value of the decision variable that enables the objective function to be minimized is the dispatch result that supplies the optimal flexibility for PHS.

5. Materials and Methods

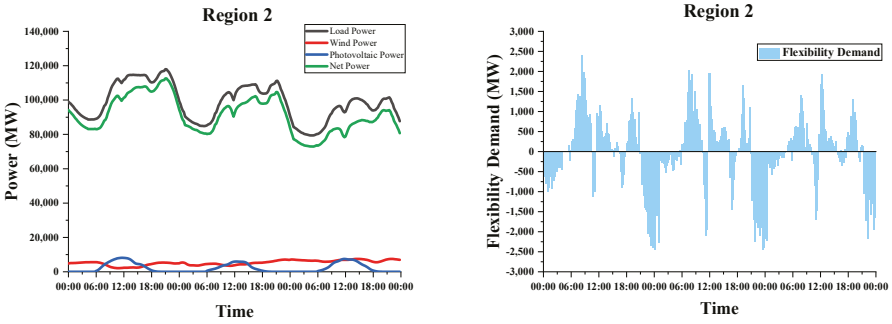
In order to verify the effectiveness of the model established in this study, a regional power grid in East China was used as an example system for simulation analysis. There are 4 regions in this dispatching scope, with a total of 10 PHS stations including 48 PHS units, with a total installed capacity of 13,700 MW. Different PHS stations have different flexibility supply patterns for each region, so the pumped and power generation power are allocated according to different proportions. The total installed capacity of wind power is 29,553.9 MW, and the total installed capacity of photovoltaic is 34,922.5 MW. The peak daily load of the system is 344,522 MW.

5.1. Flexibility Demand

The 3-day flexibility demand is calculated based on the 3-day renewable energy and load forecast data, as can be seen in Figure 3. The flexibility demand above the horizontal axis of the coordinate system is the upward flexibility demand. The flexibility demand below the horizontal axis is the downward flexibility demand. And the flexibility demand in different directions needs to be met by the flexibility supply in the corresponding direction. However, too much flexibility supply will lead to an inverse increase in the demand for flexibility, so the best match between flexibility supply and demand is required.

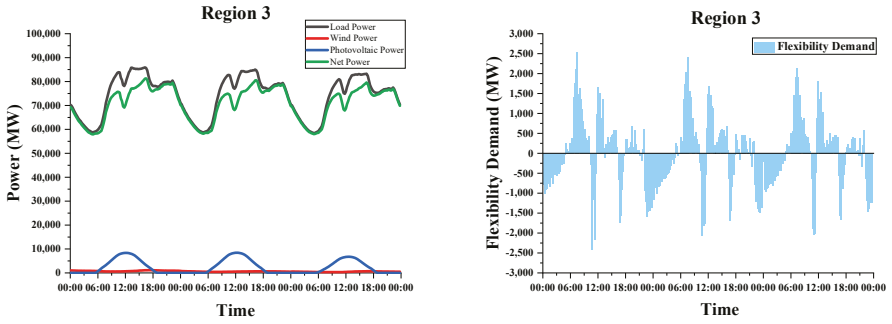


(**a**) Region 1

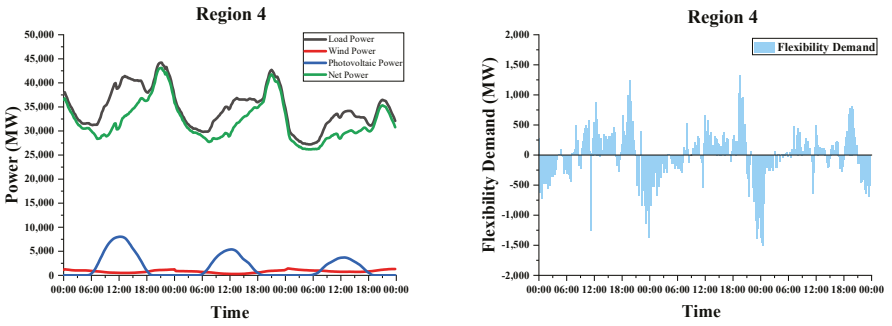


(**b**) Region 2

Figure 3. *Cont.*



(**c**) Region 3



(**d**) Region 4

Figure 3. Forecast data curves and flexibility demand of regions.

5.2. Flexibility Supply

The main parameters of the PHS station include the number of units and the power of a single unit, as shown in Table 1.

Table 1. Parameters of each PHS station.

PHS Station Number	Number of Units	Single Generating Power (MW)	Single Pumping Power (MW)
1	6	300	315
2	4	300	312
3	4	375	380
4	6	350	380
5	4	250	275
6	4	150	165
7	6	300	315
8	4	300	330
9	4	250	270
10	6	300	269

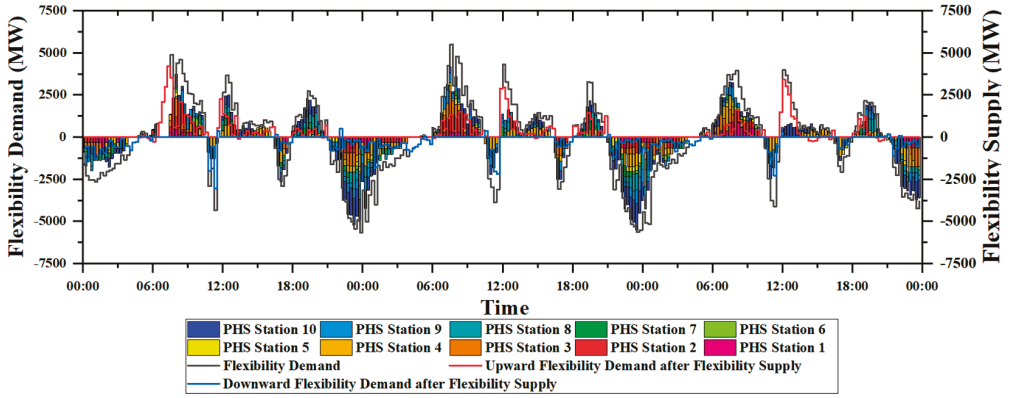
Due to factors such as the price model of PHS stations and the contracts signed between grid operators and PHS stations, the flexibility supply patterns of PHS stations to each region are also different, and the different regions have different regional constraints.

Table 2 shows the distribution ratio of each PHS station to each region under different regional allocation constraints.

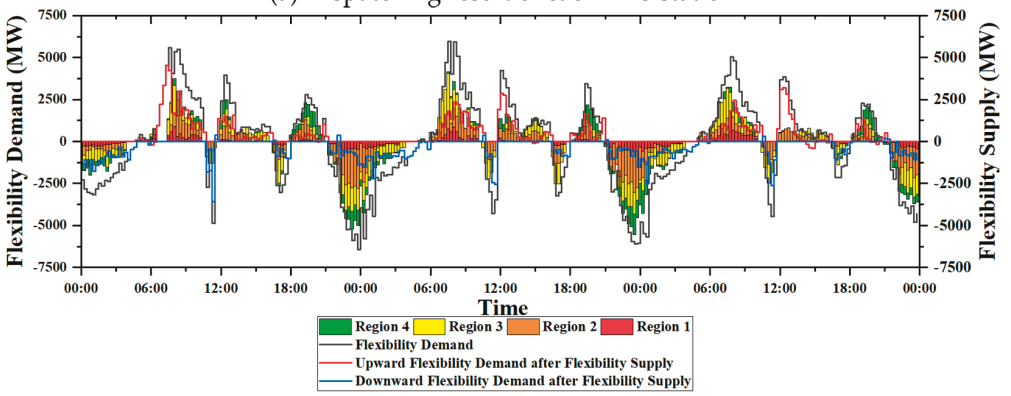
The simulation dispatching results of each PHS station are shown in Figure 4, where the horizontal axis represents the time, the vertical axis represents the generation power or pumping power of each PHS station, the positive power represents the generation power, and the negative power represents the pumping power.

Table 2. PHS station allocation ratio to each region.

PHS Station Number	Allocation Ratio (%)			
	Region 1	Region 2	Region 3	Region 4
1	33.33	27.78	27.78	11.11
2	41.67	0	58.33	0
3	12.67	0	87.33	0
4	0	0	100	0
5	50	0	0	50
6	50	0	0	50
7	27	18	0	55
8	0	0	0	100
9	0	100	0	0
10	0	100	0	0



(**a**) Dispatching result of each PHS station



(**b**) Dispatching result in each region

Figure 4. Dispatching result of dispatching scope.

The dispatching results show that the optimized dispatching model for PHS flexibility can realize the output dispatching of PHS stations, and conform to the operation characteristics of PHS stations, for example, the power generation and pumping conditions are different in the same time period, the multiple cycles of power generation and pumping in the dispatching period, and the limited number of starts and stops in one day is not exceeded.

Figure 4a shows the matching of flexibility demand and flexibility supply in the whole dispatching scope. The black curve represents the flexibility demand in the whole dispatching scope, the red curve represents the upward flexibility demand after the flexibility supply of the PHS station, the blue curve represents the downward flexibility demand after the flexibility supply of the PHS station, and the different colors in the histogram represent the flexibility supply of different PHS stations. Figure 4b shows the flexibility

supply of PHS stations to each region, and the different colors in the histogram represent the flexibility supply of PHS stations to each region.

The simulation results show that the histogram can basically cover the area enclosed by the black curve and the coordinate axis, and the flexibility supply by the PHS station in this dispatching scope can basically meet the overall flexibility demand. At the same time, the upward and downward flexible supply of PHS electricity has basically not exceeded the limit. There is a constraint to prevent the oversupply of flexibility in the constraints of the flexibility dispatching model of the PHS station, because the solver is used to solve the optimization problem. The convergence accuracy is set to 0.01% in order to prevent the solution time from being too long. In order to find a feasible solution and make the strict constraints feasible, the solver automatically adds relaxation in the solution process, so in some cases, the flexibility oversupply constraint is violated in a few periods in the simulation results, but the degree of violation is acceptable.

Figure 5 shows the supply and demand of flexibility in each region. The black curve represents the flexibility demand of each region, the red curve and blue curve represent the upward and downward flexibility demand after the PHS station flexibility supply to each region, respectively. The histogram represents the flexibility supply of PHS stations to each region. This flexibility supply is calculated by the allocation ratio under regional constraints.

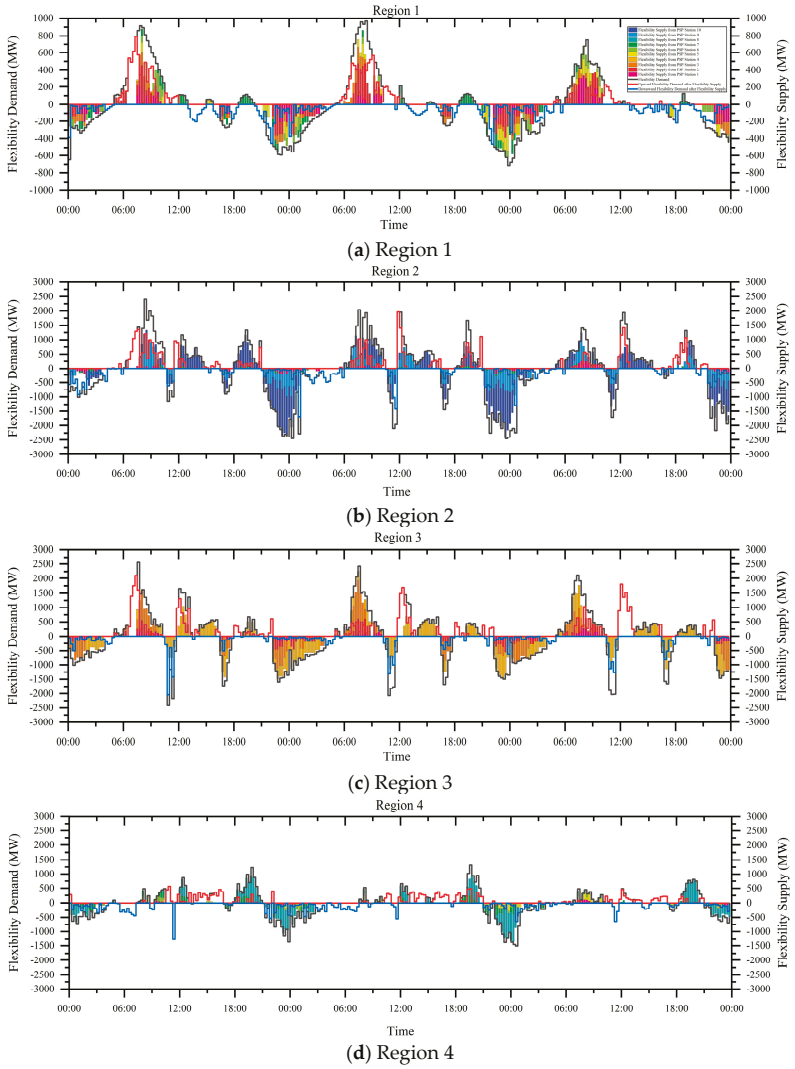


Figure 5. The flexibility supply of PHS stations to each region.

Through the flexibility supply and demand of each region, it can be deduced that the matching of flexibility supply and flexibility demand in each region can be completely matched in most cases Moreover, it can be observed that some dispatching periods are limited by the actual operating conditions of PHS stations, and it is difficult to achieve a complete match between flexibility supply and demand.

5.3. Flexibility Supply Costs

In order to quantify the economics of the dispatch model proposed in this study, the following three dispatching modes are set up, along with the flexibility supply from PHS stations and thermal power units.

Case1: All flexibility supply is from thermal power units. Figure 6 shows the flexibility supply of the thermal power units, the upward flexibility of the thermal power unit is the region enclosed by the red curve and the 0 coordinate axis, and the downward flexibility of the supply is the area enclosed by the blue curve and the 0 coordinate axis.

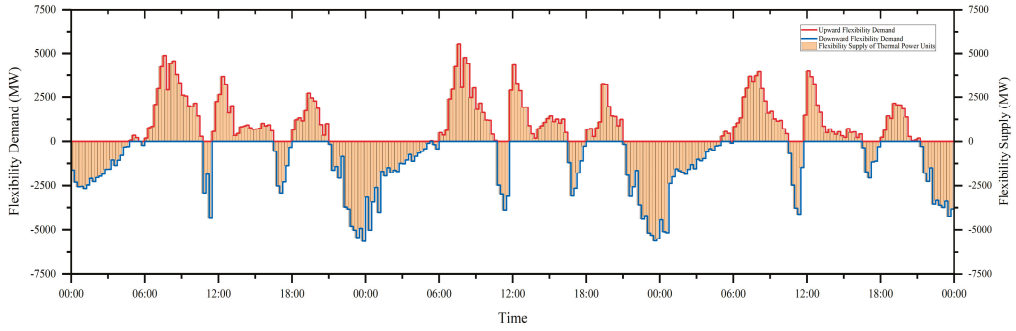


Figure 6. Case1 dispatching result.

Case2: The supply flexibility of PHS stations is added, manual dispatching to dispatch PHS stations is used, and the remaining flexibility supply is derived from thermal power units. Figure 7 shows the flexibility supply of manually dispatched PHS stations, the histogram represents the flexibility supply of each PHS station, and the area enclosed by the red curve, the blue curve and the 0 coordinate axis shows the flexibility supply of thermal power units required. The area enclosed by the blue curve above the zero axis and the 0 axis is the reverse increase in the downward flexibility demand caused by the operation of the PHS unit, and the area enclosed by the red curve below the zero axis and the 0 axis is due to the reverse increase in the upward flexibility demand caused by the operation of the PHS units.

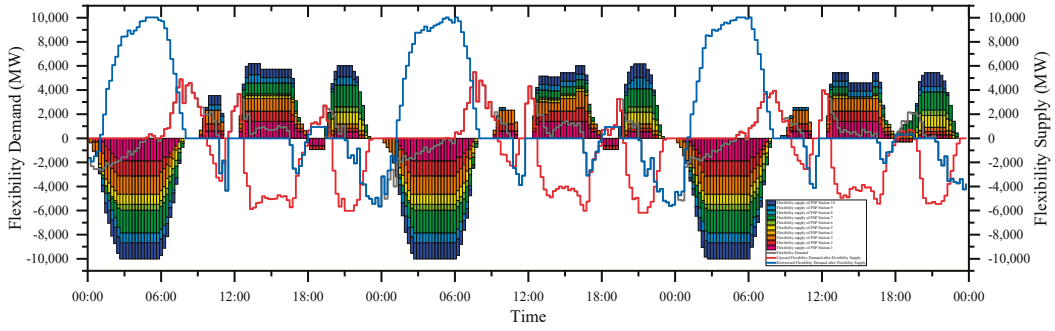


Figure 7. Case2 dispatching result.

Case3: PHS stations supply flexibility is added, and the PHS station flexibility optimization dispatching model proposed in this study is used to dispatch PHS stations. Figure 8 shows the flexible supply of PHS stations using the model proposed in this study. The histogram represents the flexibility supply of PHS stations, and the area enclosed by

the red curve, the blue curve, and the 0 coordinate axis shows the flexibility of thermal power units supply required.

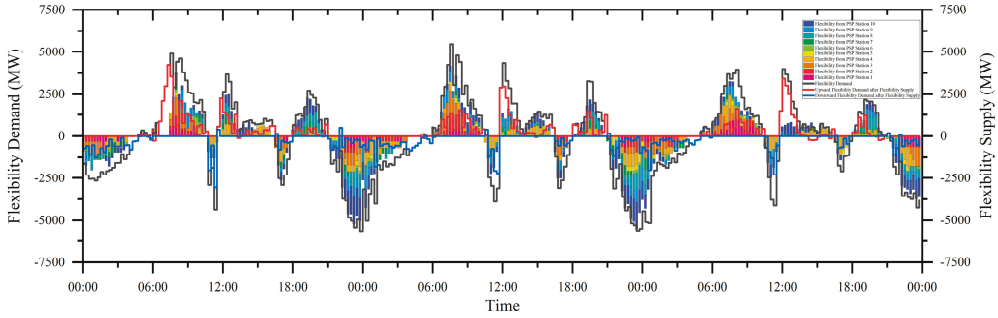


Figure 8. Case3 dispatching result.

The economics are evaluated by quantifying the cost of power generation for the flexibility supply of each case. The method of quantifying the cost of flexible supply is simplified as follows:

(1) Thermal power units: When the supply is indicative of an upward flexibility, it is necessary to climb up the slope to increase power generation, that is, to increase the power generation on the basis of the original power generation plan, and the flexibility supply cost is positive. The downward flexibility supply causes the need to climb down to reduce the power generation capacity, that is, the power generation is reduced on the basis of the original power generation plan, and the cost of flexibility supply is negative.

(2) PHS unit: When the supply is indicative of an upward flexibility, it needs to generate electric energy under the power generation condition, and the flexibility supply cost is positive. When the supply of a downward flexibility is required, it needs to consume electricity in pumping conditions, and the cost of flexible supply is positive.

The cost of flexibility supply of thermal power units is set to be 0.35 CNY/kWh, and the cost of flexibility supply of PHS units is 0.35 CNY/kWh under pumping conditions and 0.21 CNY/kWh under power generation conditions.

The economic comparison in different cases is shown in Table 3. Through comparison, it is found that the cost of flexibility supply only through thermal power resources is obviously higher, and the cost of flexibility supply is significantly lower after adding PHS resources. In Case3, the PHS stations have more flexibility supply, which greatly reduces the flexible supply pressure on the thermal power station. At the same time, the PHS station's dispatching strategy in this study greatly reduces the cost of power generation and dispatching. Therefore, the optimal scheduling strategy proposed and the PHS power station model established in this paper are effective.

Table 3. Economic comparison.

Case	Resource Type	Upward Flexibility Supply (MW)	Downward Flexibility Supply (MW)	Cost of Flexibility Supply (CNY)
Case1	Thermal units	3,663,015.68	3,655,076.08	6.4033×10^8
Case2	PHS stations	542,103	686,743	9.4668×10^7
	Thermal units	781,093.17	662,304.99	
Case3	PHS stations	138,256.82	175,022	2.5680×10^7
	Thermal units	208,252.24	172,739.11	

6. Conclusions

With the continuous improvement of the penetration rate of renewable energy in the power system. The flexibility demand of power systems is also increasing, it is more difficult

to balance the supply and demand of power system flexibility, and flexible resources are required to play a greater role. In recent years, PHS resources have not only been vigorously developed, but also possess the advantages of pollution-free, low-cost, and fast regulation. In this study, according to the actual operation characteristics of PHS units, a refined operation model of PHS is established. The optimal dispatching model for PHS flexibility is established with the goal of optimal matching of flexibility supply and flexibility demand in the different flexibility supply patterns of multi-PHS stations. The results show that the proposed method can realize the optimal flexibility of multi-PHS power station supply to multiple regions in East China. At the same time, this method can satisfy the matching of flexibility supply and flexibility demand, and make the PHS stations' dispatching more reasonable. This optimal flexibility dispatching method improves the utilization rate and flexible supply of PHS power stations and demonstrates favorable economic characteristics.

Author Contributions: Conceptualization, X.C. and P.W.; methodology, H.H. and B.S.; software, K.Q. and X.T.; validation, X.C.; investigation, X.C. and X.T.; writing—original draft preparation, F.Y.; writing—review and editing, X.C., X.T. and D.L.; supervision, H.H. and B.S. All authors have read and agreed to the published version of the manuscript.

Funding: The work is sponsored by Science and Technology Project of East China Branch of State Grid (Grant No.: SGHD0000DKJS2310440).

Data Availability Statement: The data presented in this study are available on request from the corresponding author due to privacy reasons.

Conflicts of Interest: Xinyi Chen, Pan Wu, Hongyu He, Bingbing Song, Kangping Qin and Xiaobi Teng were employed by The State Grid East China Branch. The remaining authors declare that the research was conducted in the absence of any commercial or financial relationships that could be construed as a potential conflict of interest.

References

1. Wang, W.; Dou, F.; Cheng, J.; Jiang, Z.; Shi, L.; Wu, F. A modeling method for a wind and photovoltaic joint power probability model. *Power Syst. Prot. Control.* **2020**, *48*, 22–29. [CrossRef]
2. Wang, S.; Yu, J. Joint Conditions Probability Forecast Method for Wind Speed and Wind Power. *Proc. CSEE* **2011**, *31*, 7–15. [CrossRef]
3. Liu, Y.; Li, W.; Liu, C.; Zhang, D. Mixed Skew Distribution Model of Short-term Wind Power Prediction Error. *Proc. CSEE* **2015**, *35*, 2375–2382. [CrossRef]
4. IEA. *Empowering Variable Renewables-Options for Flexible Electricity Systems*; International Energy Agency: Paris, France, 2008. [CrossRef]
5. Lannoye, E.; Flynn, D.; O'mally, M. Evaluation of power system flexibility. *IEEE Trans. Power Syst.* **2021**, *27*, 922–931. [CrossRef]
6. Holttinen, H.; Tuohy, A.; Milligan, M.; Lannoye, E.; Silva, V.; Müller, S.; Sö, L. The flexibility workout: Managing variable resources and assessing the need for power system modification. *IEEE Power Energy Mag.* **2013**, *11*, 53–62. [CrossRef]
7. Lu, Z.; Li, H.; Qiao, Y. Power System Flexibility Planning and Challenges Considering High Proportion of Renewable Energy. *Autom. Electr. Power Syst.* **2016**, *40*, 147–158. [CrossRef]
8. Mahfoud, R.J.; Alkayem, N.F.; Zhang, Y.; Zheng, Y.; Sun, Y.; Alhelou, H.H. Optimal operation of pumped hydro storage-based energy systems: A compendium of current challenges and future perspectives. *Renew. Sust. Energ. Rev.* **2023**, *178*, 113267. [CrossRef]
9. Kusakana, K. Optimal operation scheduling of grid-connected PV with ground pumped hydro storage system for cost reduction in small farming activities. *Energy Storage* **2018**, *16*, 133–138. [CrossRef]
10. Lin, S.; Ma, T.; Javed, M.S. Prefeasibility study of a distributed photovoltaic system with pumped hydro storage for residential buildings. *Energy Convers. Manag.* **2020**, *222*, 113199. [CrossRef]
11. Cavazzini, G.; Benato, A.; Pavesi, G.; Ardizzon, G. Techno-economic benefits deriving from optimal scheduling of a Virtual Power Plant: Pumped hydro combined with wind farms. *J. Energy Storage* **2021**, *37*, 102461. [CrossRef]
12. Zhang, G.; Chen, Y.; Zhang, J.; Tang, N.; Niu, Y. Research on optimization of day-ahead dispatching of wind power-photovoltaic-hydropower-thermal power-pumped storage combined power generation system. *Acta Energiae Solaris Sin.* **2020**, *41*, 79–85.
13. Zou, J.; Lai, X.; Wang, N. Mitigation of wind curtailment by coordinating with pumped storage. *Proc. CSEE* **2015**, *39*, 2472–2477. [CrossRef]
14. Ma, Z.; Wang, D.; Zhang, H.; Wang, Y.; Dong, H. Two-stage optimal dispatching based on wind-photovoltaic—Pumped storage-thermal power combined power generation system. In Proceedings of the 2019 IEEE 3rd Conference on Energy Internet and Energy System Integration (EI2), Changsha, China, 8–10 November 2019; pp. 1714–1719. [CrossRef]

15. Zhao, J.; He, Y.; Fang, Y.; Weng, Y.; Ma, W.; Xiao, S.; Liang, Y. Multi-Source Optimal Dispatch Considering Ancillary Service Cost of Pumped Storage Power Station Based on Cooperative Game. *Energy Rep.* **2021**, *7*, 173–186. [CrossRef]
16. Xia, S.; Ding, Z.; Du, T.; Zhang, D.; Shahidehpour, M.; Ding, T. Multitime Scale Coordinated Scheduling for the Combined System of Wind Power, Photovoltaic, Thermal Generator, Hydro Pumped Storage, and Batteries. *IEEE Trans. Ind. Appl.* **2020**, *56*, 2227–2237. [CrossRef]
17. Wang, S.; Liu, J.; Chen, H.; Bo, R.; Chen, Y. Modeling State Transition and Head-Dependent Efficiency Curve for Pumped Storage Hydro in Look-Ahead Dispatch. *IEEE Trans. Power Syst.* **2021**, *36*, 5396–5407. [CrossRef]
18. Golshani, A.; Sun, W.; Zhou, Q.; Zheng, Q.P.; Wang, J.; Qiu, F. Coordination of Wind Farm and Pumped-Storage Hydro for a Self-Healing Power Grid. *IEEE Trans. Sustain. Energy* **2018**, *9*, 1910–1920. [CrossRef]

Disclaimer/Publisher's Note: The statements, opinions and data contained in all publications are solely those of the individual author(s) and contributor(s) and not of MDPI and/or the editor(s). MDPI and/or the editor(s) disclaim responsibility for any injury to people or property resulting from any ideas, methods, instructions or products referred to in the content.

symmetry

MDPI

Article

Data-Driven Dynamic Security Partition Assessment of Power Systems Based on Symmetric Electrical Distance Matrix and Chebyshev Distance

Hang Qi, Ruiyang Su, Runjia Sun * and Jiongcheng Yan

School of Electrical Engineering, Shandong University, Jinan 250061, China; qi_hang@mail.sdu.edu.cn (H.Q.); 202214639@mail.sdu.edu.cn (R.S.); yanjc@mail.sdu.edu.cn (J.Y.)
* Correspondence: sunrunjia@sdu.edu.cn

Abstract: A rapid dynamic security assessment (DSA) is crucial for online preventive and restoration decision-making. The deep learning-based DSA models have high efficiency and accuracy. However, the complex model structure and high training cost make them hard to update quickly. This paper proposes a dynamic security partition assessment method, aiming to develop accurate and incrementally updated DSA models with simple structures. Firstly, the power grid is self-adaptively partitioned into several local regions based on the mean shift algorithm. The input of the mean shift algorithm is a symmetric electrical distance matrix, and the distance metric is the Chebyshev distance. Secondly, high-level features of operating conditions are extracted based on the stacked denoising autoencoder. The symmetric electrical distance matrix is modified to represent fault locations in local regions. Finally, DSA models are constructed for fault locations in each region based on the radial basis function neural network (RBFNN) and Chebyshev distance. An online incremental updating strategy is designed to enhance the model adaptability. With the simulation software PSS/E 33.4.0, the proposed dynamic security partition assessment method is verified in a simplified provincial system and a large-scale practical system in China. Test results demonstrate that the Chebyshev distance can improve the partition quality of the mean shift algorithm by approximately 50%. The RBFNN-based partition assessment model achieves an accuracy of 98.96%, which is higher than the unified assessment with complex models. The proposed incremental updating strategy achieves an accuracy of over 98% and shortens the updating time to 30 s, which can meet the efficiency of online application.

Keywords: Chebyshev distance; dynamic security assessment; incremental updating; power grid partition; preventive and restoration decision-making; radial basis function neural network; symmetric electrical distance matrix

1. Introduction

Dynamic security assessment (DSA) evaluates the security and stability of the power system under specified operating conditions (OCs) and anticipated faults [1]. It can provide valuable information for preventive and restoration control decision-making [2,3]. With the integration of renewable energy and frequent extreme weather events, the uncertainty of the OCs has increased significantly. Preventive and restoration control decision-making needs to be performed online to adapt to fast-varying OCs. A rapid DSA is required. However, the traditional DSA method based on time-domain simulation is computationally complex [4]. It cannot meet the high assessment efficiency for massive candidate schemes generated during the control decision-making process.

The data-driven DSA method utilizes machine learning to directly learn the map between the input and the dynamic security of power systems [5,6]. It can realize an online assessment due to its high efficiency. The input features are fundamental to data-driven DSA. For a specific fault type, the dynamic security of the power system is closely related

to the pre-fault OCs and fault locations. Therefore, the DSA inputs need to incorporate both OCs and the fault location information. To ensure high evaluation efficiency, the DSA typically employs steady-state features as inputs [7–9]. Pre-fault OCs can be represented by steady-state power flow features, such as the node injection power, voltage, and line transmission power [10,11]. For fault locations, the traditional DSA method constructs a dedicated assessment model for each fault. It has high assessment accuracy [12,13]. However, an increase in fault locations can lead to a large scale of DSA model sets and high maintenance costs.

Existing DSA methods with a unified assessment model adapted to fault locations can be divided into three categories. The first category leverages machine learning techniques to handle multiple fault locations. Assuming that each OC corresponds to a single anticipated fault, Refs. [14,15] employ transfer learning to build DSA models for multiple faults, of which the accuracy is over 97%. However, they do not include fault location information in the inputs and cannot assess different fault locations under the same OCs. Ref. [16] employs multi-label learning to construct a single DSA model for multiple faults, and improves the DSA accuracy to 99%. The number of considered fault locations is determined by training sample labels. Therefore, the DSA model has no generalization performance in unseen fault locations. The second category employs discrete encoding methods such as binary [17], integer [18–21], and one-hot encoding [22,23] to represent fault location features. DSA models distinguish different fault locations through these discrete encodings and are generally able to achieve an assessment accuracy of more than 97%. However, discrete encoding fails to reflect the physical differences between fault locations. The discrete encoding-based DSA model has poor generalization performance in unseen fault locations. The third category constructs electrical coordinates to represent fault locations [24,25]. The electrical coordinate is composed of the electrical distance to preselected reference nodes. It can reflect the electrical differences among fault locations. The electrical coordinate-based DSA model has high generalization performance and obtains an assessment accuracy of 98%.

The mapping relationship among OCs, fault locations, and the system dynamic security is strongly nonlinear. To ensure high assessment accuracy, the training set needs to cover a wide variation range of OCs and anticipated fault locations. The size of the training set is thereby large. The learning for massive samples containing a nonlinear map requires a machine learning model with strongly nonlinear fitting capabilities. Typically, increasing the structural complexity of machine learning models can enhance nonlinear fitting capabilities, e.g., long short-term memory (LSTM) neural networks [26], convolutional neural networks (CNNs) [27], and recurrent neural networks (RNNs) [28]. However, these highly complex models face issues such as high training costs, overfitting risks, poor interpretability, and difficulties in model updating. They are hard to update timely to support online preventive and restoration control decision-making.

According to the principle of Occam's Razor in machine learning, the models with simple structures are preferentially adopted within acceptable training errors. Therefore, this paper proposes a dynamic security partition assessment method of the power system. Instead of a single high-complexity unified assessment model, multiple low-complexity partition assessment models are employed without an accuracy loss. The aim is to achieve an accurate and incrementally updated DSA using low-complexity models. The contributions of this paper are as follows:

(1) A self-adaptive power grid partition method that strictly accounts for electrical connections is proposed based on the mean shift algorithm. The node locations are represented by a symmetric electrical distance matrix, and the Chebyshev distance is introduced to measure the differences between node location features.
(2) To build the input feature set for DSA, high-level steady-state features of OCs are extracted based on a stacked denoising autoencoder (SDAE). Meanwhile, the symmetric electrical distance matrix is modified to represent fault locations in local regions, which reduces the redundancy of fault location features.

(3) Multiple DSA models are constructed for fault locations in each local region. The model structure is the radial basis function neural networks (RBFNN) integrated with the Chebyshev distance, which can achieve a close assessment accuracy to complex models. Moreover, an incremental updating strategy is designed to enhance the adaptability of the DSA model.

The rest of this paper is organized as follows: Section 2 introduces a self-adaptive power grid partition method that strictly accounts for electrical connections. The input feature set for DSA is constructed in Section 3. Section 4 constructs DSA models for fault locations in each local region and designs an incremental updating strategy. Test results for a simplified provincial system and a larger-scale practical system in China are presented in Section 5. Conclusions are drawn in Section 6.

2. Power Grid Partition with a Strict Consideration of Electrical Connections

2.1. Description of the Power Grid Partition Problem for DSA

The impacts of different fault locations on the power system dynamic security have local similarities. That is, fault locations with tight electrical connections have similar effects on the dynamic security and vice versa. The tightness of electrical connections is typically quantified as the impedance-based electrical distance [29,30]. Therefore, the nodes with close electrical distances should be within the same region, while nodes with distant distances are in separate regions. Constructing dedicated models for each region can reduce the difficulty of training DSA models.

The impedance-based electrical distance between nodes in a power grid is typically defined as the equivalent impedance [30]:

$$d_{ij} = Z_{ii} + Z_{jj} - 2Z_{ij} \tag{1}$$

where d_{ij} represents the electrical distance between nodes i and j; Z_{ii} and Z_{jj} denote the self-impedances of nodes i and j, respectively; and Z_{ij} denotes the mutual impedance between nodes i and j.

To quantify the quality of the power grid partition, an evaluation index of electrical modularity Q_e is defined as Equation (2) based on complex network theory and the concept of weighted modularity [31].

$$Q_e = \frac{1}{2M}\sum_{i=1}^{n}\sum_{j=1}^{n}\left(w_{ij} - \frac{W_i W_j}{2M}\right)\cdot\delta(i,j) \tag{2}$$

$$M = \frac{1}{2}\sum_{i=1}^{n}\sum_{j=1}^{n} w_{ij} \tag{3}$$

where n denotes the number of nodes in the power grid; W_i denotes the sum of edge weights of node i; $\delta(i, j) \in \{0, 1\}$ denotes whether nodes i and j belong to the same region; $\delta(i, j) = 1$ indicates the same partition, while 0 indicates different regions; and M denotes the sum of the edge weights among all nodes. The edge weight w_{ij} between nodes i and j is represented by electrical distance. A higher Q_e indicates a better partition quality.

Clustering algorithms are common methods for partitioning power grids [32,33], which can be categorized into prototype, density, and hierarchical clustering. Prototype clustering, e.g., the K-means algorithm, requires a predetermination of the partition number [34], while hierarchical clustering has high computational complexity in large-scale power grids. Without specifying the partition number, the mean shift algorithm in density clustering can achieve a self-adaptive power grid partition with low computational costs [35,36]. Therefore, the mean shift algorithm is adopted in this paper.

Considering the characteristics of the DSA, the symmetric electrical distance matrix and Chebyshev distance are integrated into the mean shift algorithm for the power grid

partition. The mean shift-based power grid partition is introduced from four aspects: feature representation, algorithm structure, partition steps, and distance metric.

2.2. Feature Representation of the Node Location Based on a Symmetric Electrical Distance Matrix

Clustering algorithms rely on input features to distinguish electrical differences among node locations. Therefore, the feature representation of a node location is supposed to reflect these electrical differences.

The symmetric electrical distance matrix, denoted as $\boldsymbol{D}$, is composed of the electrical distance between any two nodes. It can be represented as follows:

$$\boldsymbol{D} = \begin{pmatrix} d_{11} & \cdots & d_{1n} \\ \vdots & \ddots & \vdots \\ d_{n1} & \cdots & d_{nn} \end{pmatrix} \tag{4}$$

$\boldsymbol{D}$ is a n-order and symmetric matrix due to the symmetry of the electrical distance (i.e., $d_{ij} = d_{ji}$). Each row of the matrix $\boldsymbol{D}$ is a feature vector of the corresponding node location. For example, the location of node i can be represented as an n-dimensional feature vector $\boldsymbol{x}_i = (d_{i1}, d_{i2}, \ldots, d_{in})$, which is called the "electrical coordinate" of node i. Ref. [24] pointed out that the electrical coordinate can effectively reflect the electrical differences among nodes. Therefore, the electrical coordinates are selected as the node location features for the mean shift algorithm.

The row vector can be further called the full-dimensional electrical coordinate since the matrix $\boldsymbol{D}$ in Equation (4) is a complete symmetry matrix of the order $n \times n$. If $\boldsymbol{D}$ is an incomplete and unsymmetric matrix of the order $n \times k$ ($k < n$), the feature vector of node i is a k-dimensional electrical coordinate, denoted as $\boldsymbol{x}_i = (d_{i1}, d_{i2}, \ldots, d_{ik})$. The electrical coordinate is composed of the electrical distances to preselected reference nodes. Its dimension is equal to the number of reference nodes. The reference nodes of the full-dimensional electrical coordinate include all nodes in the whole power grid.

The symmetric electrical distance matrix is sensitive to changes in the power grid topology. It needs to be recalculated when the outage of a branch occurs. The common recalculation method is to modify the node admittance matrix and obtain the new node impedance matrix by inversion. The new symmetric electrical distance matrix is obtained by Equation (1). The computation time is high due to matrix inversion. To improve the recalculation efficiency, the branch addition method is adopted.

As shown in Figure 1, Z_0 is the line impedance of line l_{ij}. Disconnecting line l_{ij} is equivalent to adding a new line of $-Z_0$ to line l_{ij}. The new node impedance matrix $\boldsymbol{Z}'$ can be represented as follows:

$$\boldsymbol{Z}' = \boldsymbol{Z} - \frac{\boldsymbol{Z}\boldsymbol{A}_{\mathrm{M}}(\boldsymbol{Z}\boldsymbol{A}_{\mathrm{M}})^{T}}{\boldsymbol{A}_{\mathrm{M}}^{\mathrm{T}}\boldsymbol{Z}\boldsymbol{A}_{\mathrm{M}} - Z_0} \tag{5}$$

where $\boldsymbol{A}_{\mathbf{M}}$ is a n-order column vector, which can be represented as [0, …, 1, …, −1, …,0]. Its i-th element is 1, and the j-th element is −1. Without the complex matrix inversion, the new node impedance matrix can be obtained rapidly. The recalculation efficiency of the symmetric electrical distance matrix is thereby improved significantly.

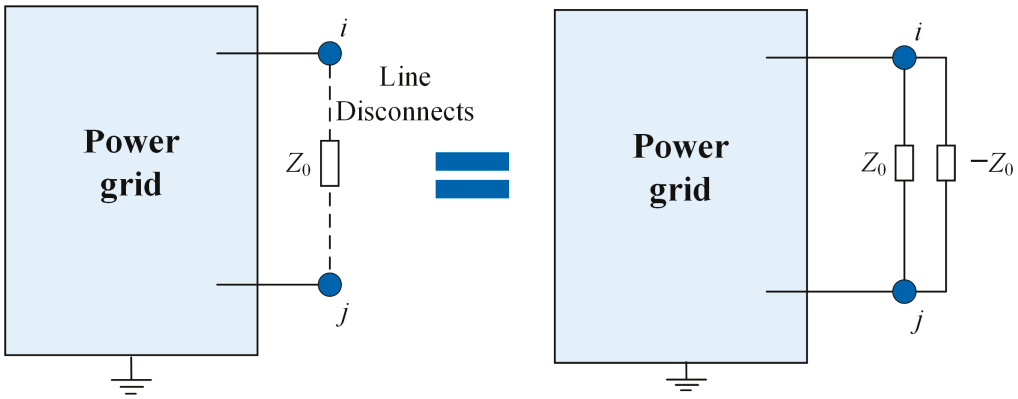


Figure 1. Diagram of the branch addition method.

2.3. Mean Shift Algorithm

The underlying assumption of the mean shift algorithm is that sample points in different clusters follow different probability density distributions [37,38]. Each sample point performs iterations along the direction of the steepest increase in density and converges to the region with the highest local density. Sample points converging to the same region belong to the same cluster. With the two-dimensional feature plane in Figure 2 as an example, the iteration process of density centers for sample points is elaborated as follows. The colored circle represents the distribution of the sample point in the feature plane. The arrow represents the direction of the shift vector.

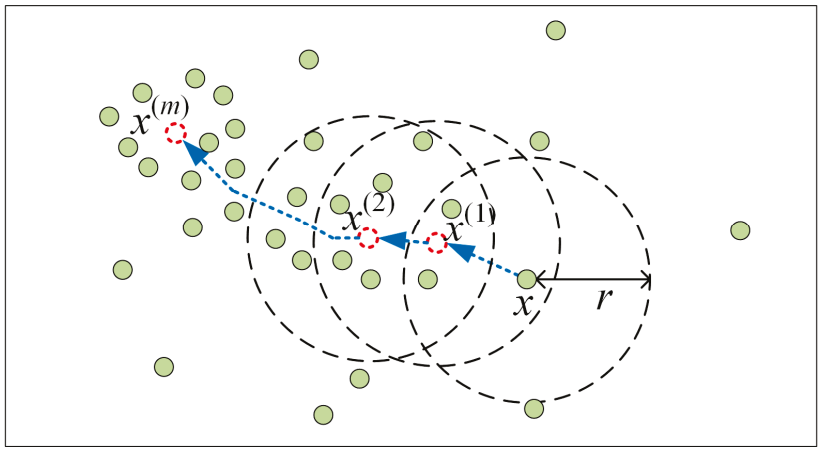


Figure 2. Diagram of the density center iteration.

A sample point x is randomly selected as the initial density center. Based on all sample points within a circle centered at x with radius r, the shift vector $\boldsymbol{xx}^{(1)}$ is calculated. The direction of the shift vector is toward the steepest increase in the density of sample distribution. The endpoint $x^{(1)}$ of the vector $\boldsymbol{xx}^{(1)}$ is selected as the new density center, and a new shift vector $\boldsymbol{x}^{(1)}\boldsymbol{x}^{(2)}$ is calculated. The above process is repeated until the final shift vector $||\boldsymbol{x}^{(m-1)}\boldsymbol{x}^{(m)}||$ is less than a predefined threshold. The iteration process converges, and the endpoint $x^{(m)}$ is considered the converged density center for sample point x. The shift vector $\boldsymbol{M(x)}$ for sample point x is calculated as follows [35]:

$$\boldsymbol{M}(\boldsymbol{x}) = \left[\sum_{\boldsymbol{x_i}\in S_x} G\left(\frac{\boldsymbol{x_i}-\boldsymbol{x}}{\sigma}\right)(\boldsymbol{x_i}-\boldsymbol{x})\right] \Big/ \sum_{\boldsymbol{x_i}\in S_x} G\left(\frac{\boldsymbol{x_i}-\boldsymbol{x}}{\sigma}\right) \tag{6}$$

$$G\left(\frac{\boldsymbol{x_i}-\boldsymbol{x}}{\sigma}\right) = \frac{1}{\sqrt{2\pi}\sigma} e^{-\frac{\|\boldsymbol{x_i}-\boldsymbol{x}\|^2}{2\sigma^2}} \tag{7}$$

where $\boldsymbol{x}$ represents the feature vector of the sample point x, i.e., electrical coordinate; $\boldsymbol{S_x}$ denotes the high-dimensional spherical region around the sample point x; $G((\boldsymbol{x_i}\text{-}\boldsymbol{x})/\sigma)$ represents the Gaussian weight [39]; and σ is the bandwidth of the Gaussian weight. After one shift, the feature vector of the density center point $x^{(1)}$ can be represented as follows:

$$\boldsymbol{x}^{(1)} = \boldsymbol{x} + \boldsymbol{M}(\boldsymbol{x}) = \sum_{\boldsymbol{x_i} \in S_x} \left[G\left(\frac{\boldsymbol{x_i} - \boldsymbol{x}}{\sigma} \right) \boldsymbol{x_i} \right] \Big/ \sum_{\boldsymbol{x_i} \in S_x} G\left(\frac{\boldsymbol{x_i} - \boldsymbol{x}}{\sigma} \right) \tag{8}$$

The density center iteration is performed for all sample points until the iteration process of all sample points converges. The clusters are determined according to the converged density centers of sample points. Sample points converging to the same region are divided into the same cluster, while those in different regions are divided into different clusters.

2.4. Self-Adaptive Power Grid Partition Based on the Mean Shift Algorithm

The power grid partition based on the mean shift algorithm is self-adaptive without specifying the partition number beforehand. The detailed partition steps are as follows:

(1) Compute symmetric electrical distance matrix, extract the electrical coordinate of each node, and set the iteration termination threshold d_s and aggregation threshold d_a;
(2) Calculate the shift vector $\boldsymbol{M(x)}$ of each node;
(3) Move each node according to its shift vector $\boldsymbol{M(x)}$;
(4) Repeat Steps (2) and (3) until $||\boldsymbol{M(x)}|| < d_s$ and the density center iteration process for each node has converged;
(5) If the distance between the converged density centers of two nodes is less than d_a, these two nodes are aggregated to the same cluster, i.e., the same region; otherwise, these two nodes are assigned to different regions.

Step (1) involves feature input and parameter setting. Steps (2) to (4) constitute the density center iteration process for each node. Step (5) is the node aggregation process. To ensure the topological connectivity of each local region after partitioning, a hierarchical aggregation method is adopted in Step (5).

The node aggregation process considering topological connectivity is shown in Figure 3. The point denotes the node; the blue point denotes the aggregation center node. lines represent topological connections between nodes, numbers on the points indicate the connectivity level of each node to the aggregation center node, green denotes division into the same region, and white denotes separation into different regions. One-level connectivity indicates a direct connection, while two-level connectivity indicates connection through one intermediate node. Firstly, as shown in Figure 3a, a node is randomly selected as an aggregation center node, i.e., the blue point. Nodes that are 1-level connected to the blue point are identified based on the adjacency matrix. If the distance between the converged density centers of the 1-level connected node and the blue point is less than d_a, these two nodes are partitioned into the same region; otherwise, these two nodes belong to different regions. Then, as shown in Figure 3b, 2-level connected nodes that are directly connected to 1-level connected nodes in the current region are identified. The distance between the converged density centers of 2-level connected nodes and the blue point is calculated, and the nodes within the same region are screened. The node aggregation process continues until no more higher-level connected nodes within the same region can be found. The above process is performed repeatedly for another unpartitioned node until all nodes are partitioned. The aggregation process of the power grid is terminated.

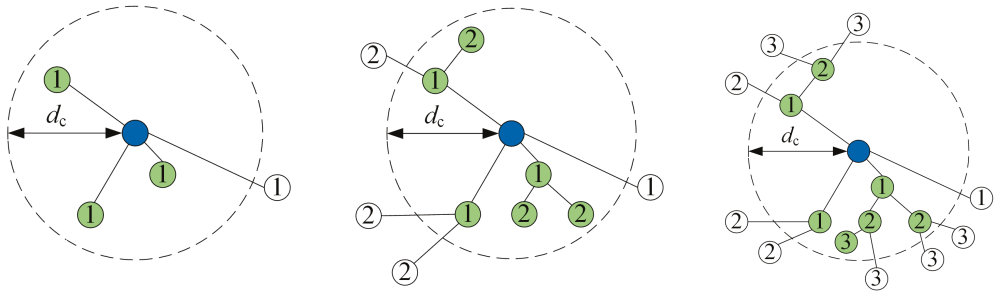


Figure 3. Node aggregation process considering topological connectivity. (**a**) Aggregation of 1-level connected nodes; (**b**) aggregation of 2-level connected nodes; and (**c**) aggregation of 3-level connected nodes.

In large-scale power systems, the computation cost of the mean shift algorithm is high, and the power grid partition efficiency is decreased. To boost the partition efficiency, this paper makes the following two improvements: (1) Reduce the number of nodes to be clustered. The generator bus belongs to a one-degree node, which is only connected to one terminal bus. To enhance partition efficiency, generator buses do not participate in clustering. They are directly partitioned into the same region as the connected terminal buses. (2) Adopt parallel computation. In the mean shift algorithm, the density center iteration for each node is independent of others and only depends on the initial node distribution. It can be accelerated by parallel computation and is not affected by each other.

During the clustering process, small regions consisting of a few nodes may be formed. Constructing a DSA model for each small region can increase the number of models, occupying many computation and storage resources. To reduce the number of DSA models, the partition results of the power grid need to be fine-tuned. Small regions are aggregated into the adjacent regions.

2.5. Chebyshev Distance between Node Location Features

In clustering algorithms, the distance metric between features, a.k.a. feature distance, is a crucial factor affecting the quality of power grid partition. To achieve a power grid partition that strictly considers the electrical distance, the feature distance is supposed to reflect the electrical distance between nodes. Typically, clustering algorithms use the Euclidean distance to measure distances between sample points. However, the Euclidean distance between electrical coordinates is not equivalent to the electrical distance between nodes. In this paper, the Chebyshev distance is selected as the distance metric for further improving the quality of the power grid partition.

With electrical coordinates, the feature distance $dist(\boldsymbol{x}_i, \boldsymbol{x}_j)$ between nodes i and j can be represented in the following norm form:

$$dist(\boldsymbol{x_i}, \boldsymbol{x_j}) = \left\|\boldsymbol{x_i} - \boldsymbol{x_j}\right\|_p, p > 0 \tag{9}$$

where p represents the norm, $p = 2$ is the Euclidean distance, and $p = \infty$ is the Chebyshev distance. As shown in Equation (9), the feature distance $dist(\boldsymbol{x}_i, \boldsymbol{x}_j)$ is determined by the electrical coordinate $\boldsymbol{x}$ and p-norm. Ref. [40] has proven that the Chebyshev distance between full-dimensional electrical coordinates is equivalent to the electrical distance. That is, Equation (10) holds.

$$dist(\boldsymbol{x_i}, \boldsymbol{x_j}) = \left\|\boldsymbol{x_i} - \boldsymbol{x_j}\right\|_\infty = \max\left(d_{i1} - d_{j1}, d_{i2} - d_{j2}, \cdots, d_{in} - d_{jn}\right) = d_{ij} \tag{10}$$

Therefore, full-dimensional electrical coordinates and the Chebyshev distance are employed in the mean shift algorithm to achieve the power grid partition by strictly considering electrical connections. The application of the Chebyshev distance in the mean

shift algorithm includes the determination of the high-dimensional spherical region in Equation (6), the distance metric in Equation (7), the length calculation of $||\boldsymbol{M}(x)||$ in Step 4 of Section 2.4, and the distance metric between converged density centers in Step 5 of Section 2.4.

3. Construction of the Input Feature Set for DSA

Multiple DSA models are constructed for the anticipated fault locations in each local region. For a specific fault type and a power grid with a fixed topology, the dynamic security of the power system is determined by pre-fault OCs and fault locations. Input data must include OCs and fault location information. In this paper, pre-fault OCs are represented by steady-state power flow features, which are widely used by existing research. Anticipated fault locations are represented by electrical coordinates.

3.1. Feature Extraction of OCs Based on SDAE

The steady-state power flow features are used to represent pre-fault OCs. These features include the active and reactive power of each generator, the active and reactive power of each load, the voltage magnitude and phase angle of each bus, and the active and reactive transmission power on each line. It is noted that the OCs are intended to describe the operating status of the whole power system rather than a local region. Therefore, steady-state power flow features across the whole power system are adopted. These features are generally high-dimensional and exhibit feature redundancy, deteriorating the training accuracy and efficiency of the data-driven DSA model. Thus, high-level features must be extracted from high-dimensional steady-state features.

SDAE is an unsupervised multilayer neural network that extracts abstract high-level features by stacking multiple denoising autoencoders (DAEs) [41,42]. It has a robust feature extraction capability. In this section, SDAE is adopted as an extractor for steady-state power flow features, and the extracted high-level features are used as inputs of each DSA model for different local regions.

Each DAE in the SDAE consists of an encoder and a decoder. The training objective is to minimize the error between the input of the encoder and the reconstruction output of the decoder. The loss function L_D of DAE can be represented as follows [43]:

$$\min L_D = \frac{1}{2}\sum_{i=1}^{N}\|\boldsymbol{F}_i - \boldsymbol{z}_i\|^2 \tag{11}$$

where N represents the number of training samples; the i-th training sample feature vector, denoted as $\boldsymbol{F}_i$, serves as the encoder input; and $\boldsymbol{z}_i$ is the reconstructed feature vector, which serves as the decoder output. The encoder output is the high-level features extracted by DAE. In the SDAE, the DAE in the first layer uses steady-state power flow features as input for training. The outputs of the first layer serve as inputs of the next layer. The SDAE is trained layer by layer. The outputs of the final layer serve as the high-level features, which are used as one part of the DSA model inputs.

3.2. Redundancy Analysis of Electrical Coordinates for Fault Locations in a Local Region

The full-dimensional electrical coordinate of the order n is used to represent the node location in the mean shift-based power grid partition. However, it is redundant for DSA to represent fault locations in the local region. As shown in Figure 4, Regions A and B are two interconnected local regions with l tie lines. A_i and B_i are the nodes at both ends of the tie lines. The electrical distance between nodes P_1 and Q_1 is calculated as follows:

$$d_{\mathrm{P_1Q_1}} = Z_{\mathrm{P_1P_1}} + Z_{\mathrm{Q_1Q_1}} - 2Z_{\mathrm{P_1Q_1}} \tag{12}$$

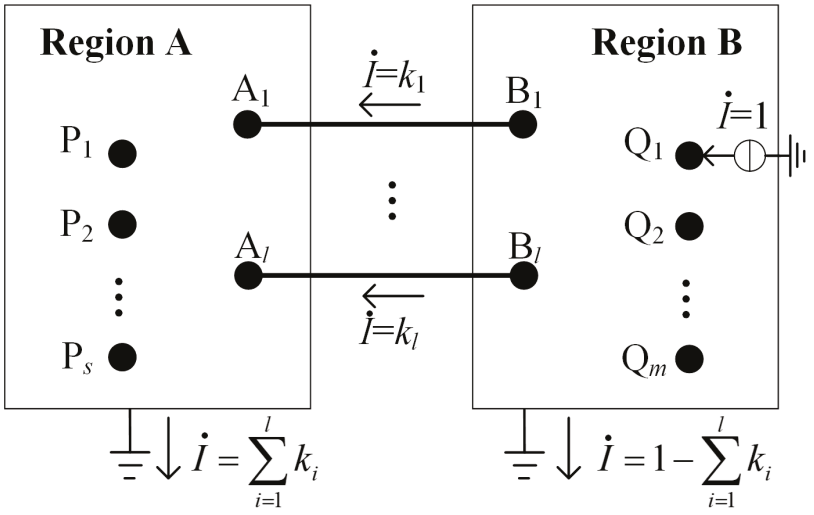


Figure 4. Diagram of two interconnected local regions.

Based on the physical meanings of the mutual impedance, $Z_{P_1Q_1}$ is numerically equal to the voltage at node P with a unit current injected into node Q_1 and no current injected into other nodes, denoted as $Z_{P_1Q_1} = \dot{U}_{P_1}\big|_{\dot{I}_{Q1}=1}$. With a unit current injected into node Q_1, the currents on tie lines are denoted as $k_1, k_2, \ldots, k_l$. According to the superposition theorem, the voltage at node P_1 is equal to the sum of the voltages at node P_1 with region B removed and currents $k_1, k_2, \ldots, k_l$, respectively, injected at nodes $A_1, \ldots, A_l$. It can be represented as follows:

$$Z_{P_1Q_1} = \dot{U}_{P_1}|_{\dot{I}_{Q1}=1} = \sum_{i=1}^{l} U_{P_1}{}'|_{\dot{I}_{Ai}=k_i} = \sum_{i=1}^{l} k_i Z_{P_1A_i}{}' \tag{13}$$

where $Z_{P1Ai'}$ represents the mutual impedance between node P_1 and A_i after region B and the tie lines are removed. Substituting Equation (13) into Equation (12) yields the following equation:

$$d_{P_1Q_1} = -2\sum_{i=1}^{l} k_i Z_{P_1A_i}{}' + Z_{P_1P_1} + Z_{Q_1Q_1} \tag{14}$$

Assume there are m reference nodes located in region B, denoted as $Q_1, \ldots, Q_m$. The currents on tie lines are denoted as $k_{i1}, k_{i2}, \ldots, k_{il}$ when a unit current is injected into node Q_i. The m-dimensional electrical coordinate composed of the electrical distances between node P and m node Q_i, denoted as $\boldsymbol{x}_P$, can be represented as follows:

$$\boldsymbol{x}_P = \begin{bmatrix} d_{PQ_1} & d_{PQ_2} & \cdots & d_{PQ_m} \end{bmatrix}^T = \begin{pmatrix} -2k_{11} & \cdots & -2k_{1l} & 1 \\ \vdots & \ddots & \vdots & \vdots \\ -2k_{m1} & \cdots & -2k_{ml} & 1 \end{pmatrix} \begin{pmatrix} Z_{PA_1}{}' \\ Z_{PA_2}{}' \\ \vdots \\ Z_{PA_l}{}' \\ Z_{PP} \end{pmatrix} + \begin{pmatrix} Z_{Q_1Q_1} \\ Z_{Q_2Q_2} \\ \vdots \\ Z_{Q_mQ_m} \end{pmatrix} \tag{15}$$

Equation (15) can be rewritten into the following form:

$$\boldsymbol{x}_P = \boldsymbol{K}_{(m\times(l+1))} \cdot \boldsymbol{Z}_{(l+1)} + \boldsymbol{C}_m \tag{16}$$

where $\boldsymbol{K}_{(m\times(l+1))}$ is a constant matrix of order $m \times (l+1)$; $\boldsymbol{C}_m$ is an m-dimensional constant vector; and $\boldsymbol{Z}_{(l+1)}$ is an $(l+1)$-dimensional vector related to nodes P, $A_1, \ldots, A_l$. The m-dimensional electrical coordinate of the node in region A is only related to $\boldsymbol{Z}_{(l+1)}$. Due to the sparse electrical connections between regions A and B, the number of tie lines is small. The feature dimension m is greater than $l+1$, resulting in feature redundancy.

To reduce the feature redundancy, the electrical coordinate reference nodes of the fault location in the local region should be selected within that region. The symmetric electrical distance matrix is modified as shown in Equation (17), where $\boldsymbol{D}_{\mathrm{A}}$ and $\boldsymbol{D}_{\mathrm{B}}$ are used to represent the fault locations occurring at regions A and B.

$$\boldsymbol{D} = \begin{pmatrix} \boldsymbol{D}_{\mathrm{A}} & 0 \\ 0 & \boldsymbol{D}_{\mathrm{B}} \end{pmatrix} = \left(\begin{array}{ccc:ccc} d_{\mathrm{A}_1\mathrm{A}_1} & \cdots & d_{\mathrm{A}_1\mathrm{P}_s} & & & \\ \vdots & \ddots & \vdots & & & \\ d_{\mathrm{P}_s\mathrm{A}_1} & \cdots & d_{\mathrm{P}_s\mathrm{P}_s} & & & \\ \hdashline & & & d_{\mathrm{B}_1\mathrm{B}_1} & \cdots & d_{\mathrm{B}_1\mathrm{Q}_m} \\ & & & \vdots & \ddots & \vdots \\ & & & d_{\mathrm{Q}_m\mathrm{B}_1} & \cdots & d_{\mathrm{Q}_m\mathrm{Q}_m} \end{array} \right) \tag{17}$$

The dimension of steady-state power flow features can be significantly reduced by the feature extraction of SDAE. The dimension of electrical coordinates can also be reduced using block matrices from the symmetric electrical distance matrix to represent fault locations in local regions. Consequently, the dimension of input features for DSA does not drastically increase with the growth of the system scale. The proposed input feature representation method for DSA is applicable in large-scale power systems.

4. Dynamic Security Partition Assessment

The DSA model is constructed based on the RBFNN due to its flexible distance metric. It can leverage the electrical coordinates and Chebyshev distance to distinguish similar samples. To improve the adaptability of DSA model, an incremental updating strategy is designed to ensure its high assessment accuracy for different non-linear transient changes.

4.1. Construction of the RBFNN-Based DSA Model for a Local Region

The anticipated fault locations in the same region have similar impacts on the system dynamic security. The nonlinearity of the input–output map within the training set for each local region is reduced. The map is suitable to be learned by shallow models. RBFNN is a three-layer feedforward neural network with a single hidden layer. It has a simple structure, high training efficiency, and an interpretable decision-making process [44]. It can approximate any continuous function with arbitrary precision. Therefore, multiple DSA models are constructed based on the RBFNN for the anticipated fault locations in each local region.

As shown in Figure 5, the input to the RBFNN consists of OC and anticipated fault location features. Each neuron in the RBFNN hidden layer corresponds to a center vector obtained from the training set by the clustering algorithm. The radial basis function $\Phi()$ measures the difference between the sample and the center vector, which is the activation function of the hidden layer neurons. The Gaussian function is a widely used radial basis function, which can be represented as follows [39]:

$$\phi(\boldsymbol{F}_i, \boldsymbol{F}_{\mathrm{c}}) = \frac{1}{\sqrt{2\pi}\sigma} e^{-\frac{dist(\boldsymbol{F}_i, \boldsymbol{F}_{\mathrm{c}})^2}{2\sigma^2}} \tag{18}$$

where $\boldsymbol{F}_i$ is the feature vector of the i-th sample and $\boldsymbol{F}_{\mathrm{c}}$ is the center vector of the hidden layer neuron.

The feature vector is defined as $\boldsymbol{F} = (\boldsymbol{o}, \boldsymbol{x})$, where $\boldsymbol{o}$ are high-level steady-state features of OCs, and $\boldsymbol{x}$ is the electrical coordinate of the anticipated fault location. The OC features represented by steady-state features are typically treated as Euclidean data, which are measured by the Euclidean distance. The anticipated fault location features, represented by electrical coordinates, are non-Euclidean data, which are measured by the Chebyshev distance. Considering these two types of feature distance metrics, $dist(\boldsymbol{F}_i, \boldsymbol{F}_{\mathrm{c}})$ is defined as follows:

$$dist(\boldsymbol{F}_i, \boldsymbol{F}_{\mathrm{c}}) = \alpha \|\boldsymbol{o}_i - \boldsymbol{o}_{\mathrm{c}}\|^2 + \beta \|\boldsymbol{x}_i - \boldsymbol{x}_{\mathrm{c}}\|^{\infty} \tag{19}$$

where α and β are weight coefficients and $\alpha + \beta = 1$.

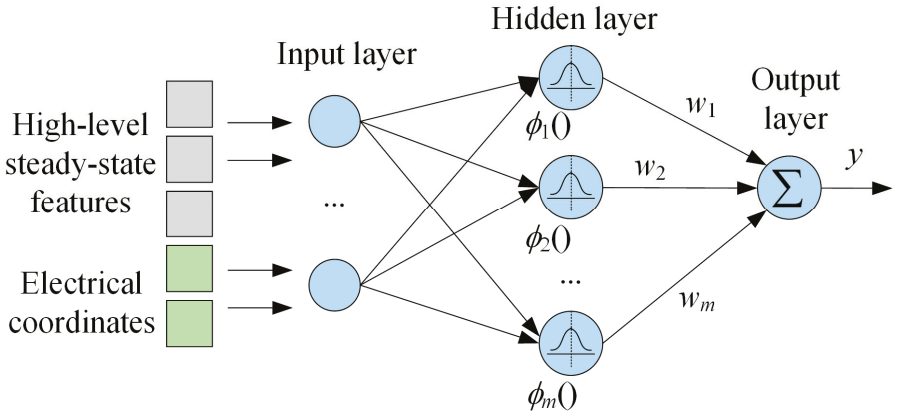


Figure 5. Structure of the RBFNN.

Both the mean shift-based grid partition and RBFNN employ the Chebyshev distance, which focuses on the maximum value and disregards other values. The mean shift algorithm and RBFNN expect to measure differences between locations according to electrical distance, and the Chebyshev distance between full-dimensional electrical coordinates is equivalent to the electrical distance. Therefore, the Chebyshev distance is sufficient in this paper.

The Chebyshev distance between electrical coordinates is impacted by the power grid topology. If there is an island region in the power grid, the electrical coordinate and Chebyshev distance will be infinite. Both the mean shift algorithm and RBFNN cannot handle infinite feature values. To ensure the feasibility of the methods proposed in this paper, island regions need to be identified based on the adjacency matrix and removed.

4.2. Online Incremental Update of the DSA Model

The typical mode of current data-driven DSA methods is "offline training, online assessment". However, the OCs of the power grid are constantly changing, and the training set generated offline cannot fully cover actual OCs and anticipated fault locations. During the online assessment, significant differences between the samples to be evaluated and the training set may lead to low generalization accuracy of the DSA model. To enhance the assessment accuracy of the DSA model, it is significant to generate new training samples to update the DSA model online. This section designs an online incremental updating method of the DSA model based on distance metrics and RBFNN. The new sample set for model updating is denoted as X_{new}. The detailed model updating steps are as follows:

(1) The new OCs and anticipated fault locations are obtained based on real-time and future prediction information. High-level steady-state features and electrical coordinates are extracted, and an unlabeled new sample set is generated.
(2) The minimum feature distance between the new sample and the RBFNN hidden layer center vectors is calculated according to Equation (19). If the minimum exceeds the predefined threshold D_t, a dynamic security label of the new sample is obtained based on a time-domain simulation and stored in X_{new}. If the minimum is lower than D_t, the new sample is abandoned.
(3) Central samples of X_{new} are obtained based on the mean shift algorithm and Equation (19).
(4) New neurons in the RBFNN hidden layer are added with central samples from X_{new} as the center vectors. The weights between the new neurons and the output layer are trained based on X_{new}, while the other structures and weights remain unchanged.

With the above incremental updating method, the DSA model can efficiently acquire knowledge from the new sample set. Moreover, it can avoid catastrophic forgetting during the model updating process. By repeatedly performing incremental updates, the rolling

update of the DSA model can be achieved, ensuring that the model consistently maintains high generalization accuracy.

4.3. Framework of the Dynamic Security Partition Assessment

The mode of "offline training, rolling update, online assessment" for the dynamic security partition assessment is adopted. The assessment framework is illustrated in Figure 6. It mainly includes three blocks: offline training, rolling updating, and online assessment. Each block is elaborated as follows:

(1) Offline training provides initial training data and a model for DSA. The power grid is firstly partitioned into several regions based on the mean shift algorithm. Multiple training sets for each region are generated, which include high-level steady-state features extracted by SDAE and a block symmetric electrical distance matrix. Multiple DSA models are constructed based on the RBFNN and each training set. The OC features of the RBFNN models in each region are the same.

(2) Rolling updating periodically performs an update of DSA models to guarantee high DSA performance all the time. During the rolling updating stage, new training samples are generated periodically. DSA models are updated online and incrementally based on the proposed updating method. The number of DSA models is not increased, while catastrophic forgetting can be avoided. In this block, T represents the model updating cycle.

(3) Online assessment gives the final assessment results. Combinations of OCs and anticipated faults are obtained, and the region where the fault is located is first determined. Next, the steady-state features and electrical coordinates of the combination are extracted. Finally, the DSA model corresponding to the fault location is adopted to obtain the assessment results.

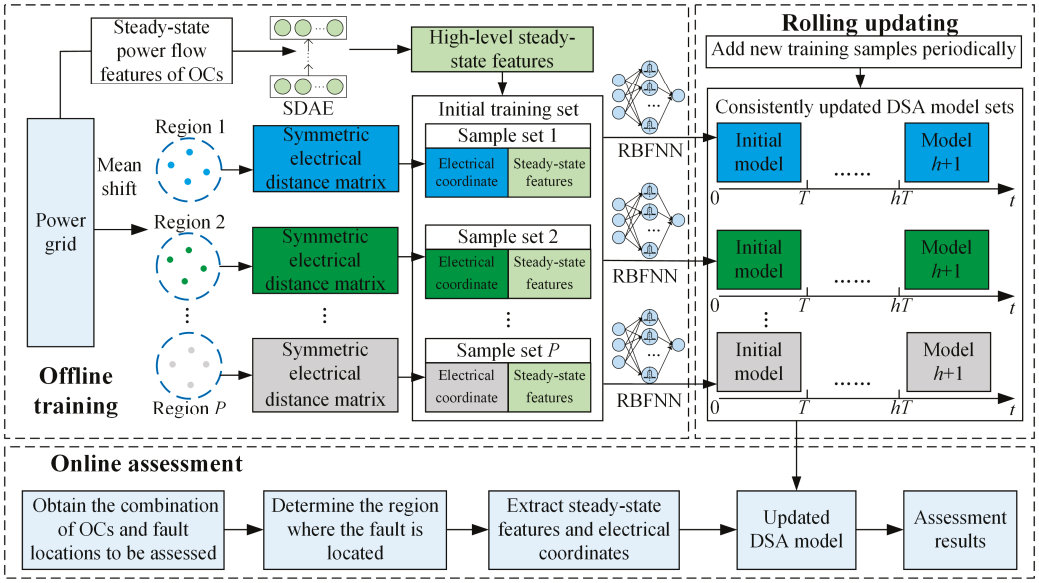


Figure 6. Framework of the dynamic security partition assessment.

The quality of input data is crucial for the data-driven DSA. Poor data may arise in two stages. (1) In the offline training stage, insufficient training samples and class imbalance may occur. To generate sufficient samples for model training, a wider range of OCs and more anticipated fault locations can be simulated by a time-domain simulation. The oversampling technique can be employed to increase the number of samples in minority classes. (2) In the online assessment stage, the acquired OC data may contain noise. This paper employs SDAE to process OC features, which exhibit strong robustness to noise. The high-level features extracted by SDAE are used as inputs of the RBFNN, reducing the impact of noise on the assessment results of the RBFNN.

The comprehensive flow chart of the proposed data-driven dynamic security partition assessment is shown in Figure 7. It includes the power grid partition, sample generation, DSA model construction, model updating, and online assessment. The DSA of the power system depends on communication and big data technology. It is vulnerable to false data injection attack (FDIA), which injects false information into the cyber system of power grid and can result in the misjudgments of DSA model. To reduce the risk of FDIA, false data detection is performed for new training samples before the model update. The false data are identified and eliminated, and then the DSA model is updated online for new preprocessed training samples.

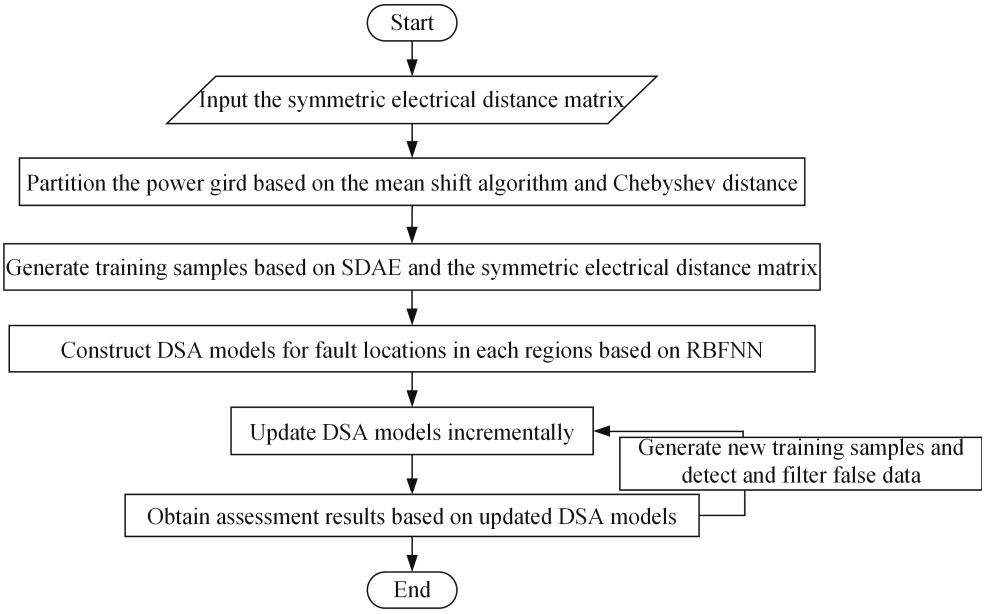


Figure 7. Flow chart of the dynamic security partition assessment.

The power system DSA includes transient rotor angle stability, voltage stability, and frequency stability assessments. The proposed partition assessment method is applicable to the above three scenarios. In this paper, the transient rotor angle stability assessment is adopted as the application scenario. The output of each regional DSA model provides the transient angle stability results of the whole power system under a combination of OCs and anticipated fault locations. The power system is defined as unstable when the maximum rotor angle difference between synchronous generators exceeds 180° during the transients.

The power grid is partitioned into multiple regions and dedicated DSA models are constructed for fault locations in each region. Each DSA model requires the input of global OC information, and the output is the global dynamic security results for the entire power system. These global data are typically consolidated at the provincial power dispatch center and not shared among the different grid regions. Therefore, the construction, storage, calling, and updating of DSA models are usually carried out at the provincial power dispatch center. The central computing resources are limited. When central computing resources are insufficient, distributed computing technology can be employed. The power dispatch center assigns updating tasks for DSA models to the computing resources in each region, and then the updated model parameters are sent back to the power dispatch center.

5. Experimental Results and Discussions

The effectiveness of the proposed dynamic security partition assessment method is verified in a simplified provincial power system in China. The example system includes 112 buses, 32 generators, and three HVDC links. The transmission power of three HVDC links are 8 GW, 8 GW, and 4 GW. Nine wind farms are integrated into the system. The

simulation software is PSSE 34. Numerical simulation and machine learning are performed on a server with 64 GB of RAM and a 24-core Intel Xeon Gold 6148 CPU (2.40 GHz).

5.1. Test of Power Grid Partition

The power grid is partitioned based on the mean shift algorithm integrated with the symmetric electrical distance matrix and Chebyshev distance. The symmetric electrical distance matrix is a 112-order matrix. The radius of the high-dimensional spherical region is set to the average value of the symmetric electrical distance matrix. The bandwidth σ in the Gaussian weight is set to 20. The iteration termination threshold d_s is set to 0.01. The aggregation threshold d_a is a key factor in the partition quality. The electrical modularity Q_e under different aggregation thresholds d_a is shown in Figure 8. The Q_e reaches the maximum when d_a = 1.6. Therefore, d_a is determined to be 1.6.

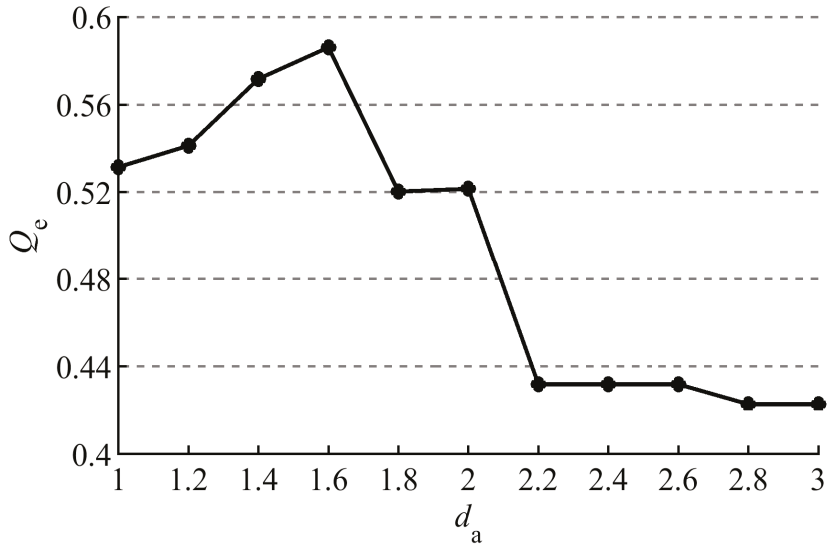
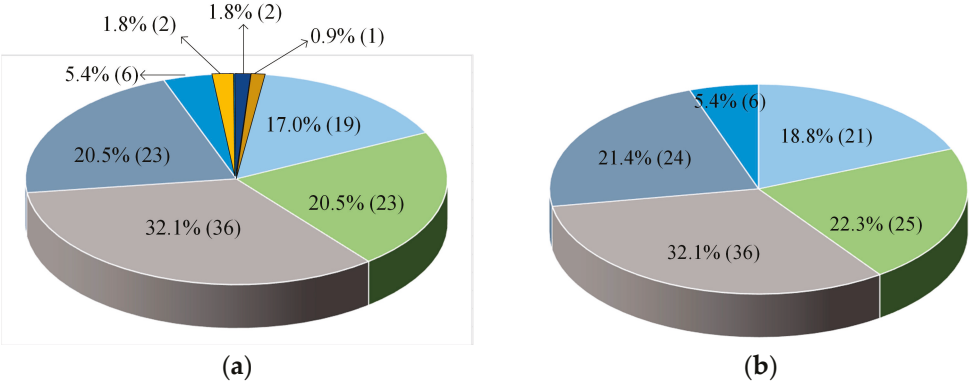


Figure 8. Electrical modularity Q_e under different aggregation thresholds d_a.

The number of buses in different regions before fine-tuning is shown in Figure 9a. Different colors represent different regions. "32.1% (36)" denotes that the region includes 36 buses and accounts for 32.1% of the total bus count. During fine-tuning process, three small regions where the node number is less than five are aggregated into adjacent regions. The number of buses in different regions after fine-tuning is shown in Figure 9b. Three small regions are aggregated into adjacent regions. The distributions of the remaining five regions are shown in Figure 10. Different colors represent different regions. The number represents the region number.



(**a**) (**b**)

Figure 9. The number of buses in different regions of a simplified provincial system in China before and after fine-tuning. (**a**) Before fine-tuning and (**b**) after fine-tuning.

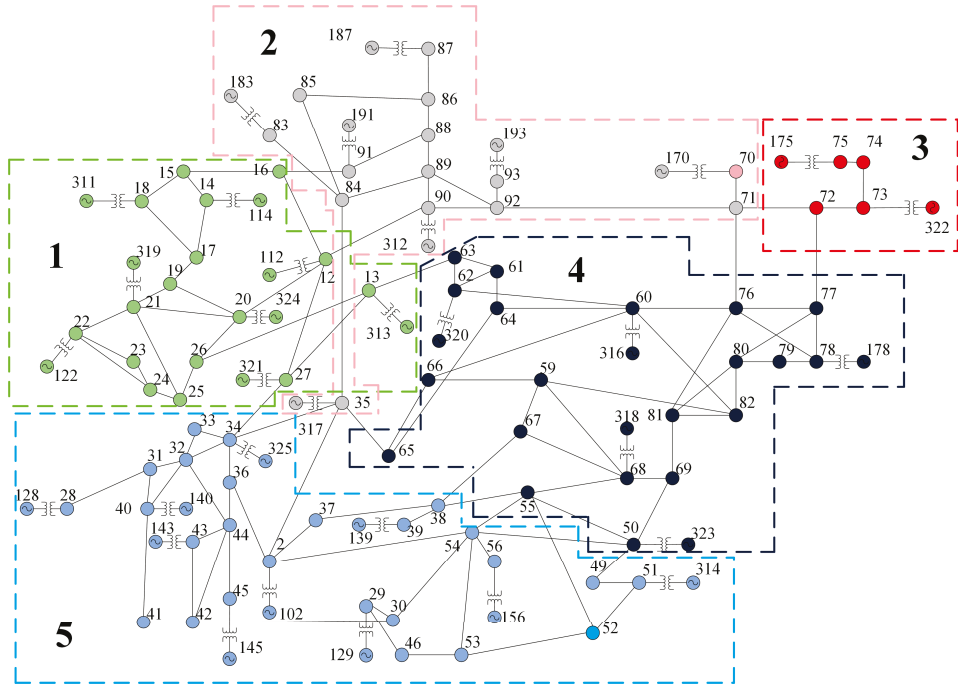


Figure 10. Distributions of partitioned regions.

To verify the effectiveness of the Chebyshev distance, mean shift algorithms with different distance metrics are compared in Figure 11. The distance metrics include Chebyshev, Euclidean, Manhattan, and cosine distances. The results show that the power grid partition quality with the Chebyshev distance metric is the best. It demonstrates that the Chebyshev distance is applicable to the mean shift-based power grid partition.

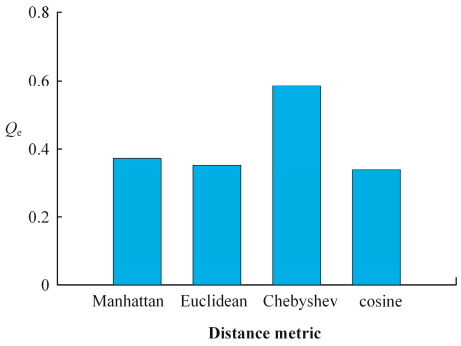


Figure 11. Comparisons of different distance metrics in the mean shift algorithm.

5.2. Test of Dynamic Security Partition Assessment

Multiple DSA models are constructed for anticipated fault locations in each local region. To generate the dataset for DSA, the time-domain simulations are performed as follows. The power of each load in the system fluctuates randomly between 80% and 120%. The outputs of the generators are adjusted based on load levels and spinning reserve capacity. A total of 1000 OCs are obtained. The anticipated faults are N-1 three-phase short circuits on 10%, 20%, . . ., 90% of each line. The fault duration is 0.25 s. For each fault location, 100 OCs are randomly selected. Following the above simulation settings, a dataset including 92,700 samples is generated, which includes 50,514 stable samples and 42,186 unstable samples. The number of anticipated fault locations and samples in each region is shown in Table 1. It is worth noting that the proposed partition method discovers a special region 3, where no stable samples exist. It indicates that the instability risk of transient rotor angle caused by faults in region 3 is high. Due to the lack of stable samples,

the faults in region 3 are considered to cause instability without building the specified DSA model.

Table 1. The number of anticipated fault locations and samples in each region.

Region No.	The Number of Anticipated Fault Locations	The Number of Samples	The Number of Stable Samples	The Number of Unstable Samples
1	207	20,700	6709	13,991
2	144	14,400	5628	8772
3	27	2700	0	2700
4	261	26,100	17,687	8413
5	288	28,800	20,490	8310
Total	927	92,700	50,514	42,186

The steady-state power flow features to represent OCs are extracted by SDAE. The structure of SDAE is (50, 40, 30). The dimension of the extracted high-level features is 30. The symmetric electrical distance matrix of each region is used to represent the regional fault locations. Except for region 3, the samples in other regions are randomly divided into training and test samples at 3:1, respectively. Then, four RBFNN-based DSA models are constructed on the training samples in regions 1, 2, 4, and 5. The hyper-parameters of RBFNN are shown in Table 2. Center vectors of hidden-layer neurons are obtained from training samples based on the default K-means algorithm.

Table 2. Hyperparameters of the RBFNN.

Parameter Type	Value	Parameter Type	Value
Hidden-layer neurons	100	Optimizer	Adam
$-1/2\sigma^2$ of RBF kernel	1	Learning rate	0.001
Distance metric for OC features	Euclidean distance	Training epochs	100
Distance metric for fault location features	Chebyshev distance	Training strategy	Mini-batch
α in Equation (19)	0.5	Batch size	300
β in Equation (19)	0.5		

Figure 12 presents the comparison results of partition assessment and unified assessment with different machine learning models. The unified assessment constructs one model for fault locations in all regions. The machine learning models for comparison include RBFNN, CNN, deep belief network (DBN) [45], gated recurrent unit (GRU) [13], RNN [28], random forest (RF) [46], and extreme gradient boosting (XGBoost) [47]. The structures of the above machine learning models are shown in Table 3. As shown in Figure 12, the accuracy of the partition assessment is higher than the unified assessment, whatever the machine learning model is. It demonstrates that the proposed partition assessment method is effective.

Table 3. Structures of machine learning models.

Models	Structure
CNN	Conv (10, 3) + MaxPooling (2) + Conv (10, 3) + GlobalMaxPooling () + Dense (50)
DBN	(100, 100, 50)
GRU	GRU (50, 20) + Dense (50)
RNN	RNN (50, 20) + Dense (50)
RF	n_estimators = 100
XGBoost	n_estimators = 100

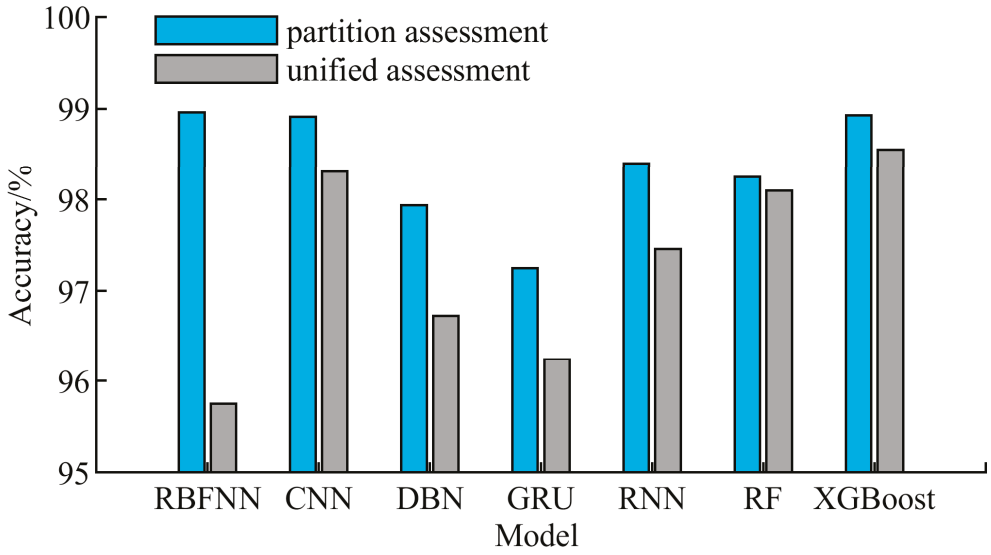


Figure 12. Comparisons of partition and unified assessments.

Table 4 further shows the comparison of the results from different machine learning models for the partition assessment. The accuracy of RBFNN is close to CNN, RNN, and XGBoost. It demonstrates that the constructed RBFNN-based DSA model can achieve a close assessment performance to complex models.

Table 4. Comparison of different machine learning models for the partition assessment.

Region	RBFNN	CNN	DBN	GRU	RNN	RF	XGBoost
1	99.38%	99.04%	98.98	97.82	98.86	98.86	99.32
2	98.44%	98.44%	95.91	96.92	97.36	95.69	97.94
3	\	\	\	\	\	\	\
4	99.25%	99.13%	98.71	98.50	98.81	98.71	99.25
5	98.64%	98.54%	97.51	95.88	98.21	98.68	98.86
Total	98.96%	98.91%	97.94	97.25	98.40	98.25	98.93

The model for fault locations in region 1 is denoted as "Model 1". With Model 1 as an example, the effectiveness of the proposed incremental updating method of the DSA model is verified. A total of 4600 new samples are generated. The OCs and fault locations in new samples are not included in old samples. Samples are divided as shown in Figure 13. Old and new samples are divided into training and test samples at 3:1. The proposed incremental updating method is compared with retraining and continued training. Model 1 with incremental updating is trained on new training samples, and 26 new neurons in the hidden layer are added. The incremental updating is achieved by the freeze of a layer in Keras. The model with retraining is trained on old and new training samples. The training epochs are set to 100. The continued training is designed to train the initial model with new training samples. An assessment of the accuracy of the updated Model 1 on old and new test samples and updating time are shown in Table 5.

Table 5. Comparisons of the retraining and incremental updating of Model 1.

Updating Strategy	Accuracy on Old Test Samples	Accuracy on New Test Samples	Updating Time
Retraining	99.04%	99.17%	500 s
Continued training	92.12%	99.22%	97 s
Incremental updating	99.46%	98.48%	30 s

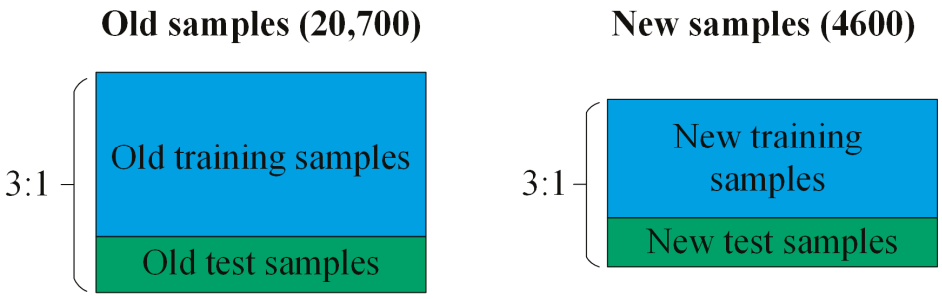


Figure 13. The division of samples.

The assessment accuracy with continued training on old test samples is significantly lower than the other two. It demonstrates that continued training leads to catastrophic forgetting of old knowledge. The accuracy with incremental updating on old test samples is the highest, while the assessment accuracy on new test samples is close to the other two. Moreover, the incremental updating process takes only 30 s. Test results demonstrate that the proposed incremental updating method has high updating performance and efficiency while avoiding catastrophic forgetting of old knowledge.

5.3. Tests on a Large-Scale Practical Power System in China

The practical power system is a regional system in China. It includes 2624 buses, 527 generator buses, 919 load buses, 2349 AC lines, two DC lines with 800 kV, eight DC lines with 500 kV, and 1634 transformers.

The power grid is partitioned based on the mean shift algorithm. The number of buses in different regions before fine-tuning is shown in Figure 14a. During the fine-tuning process, two small regions are aggregated into adjacent regions. The power grid is finally partitioned into three regions. The clustering results of buses in the three-dimensional feature space are shown in Figure 15, where d_{10} represents the electrical coordinate feature of the tenth dimension. Different colors represent different clusters.

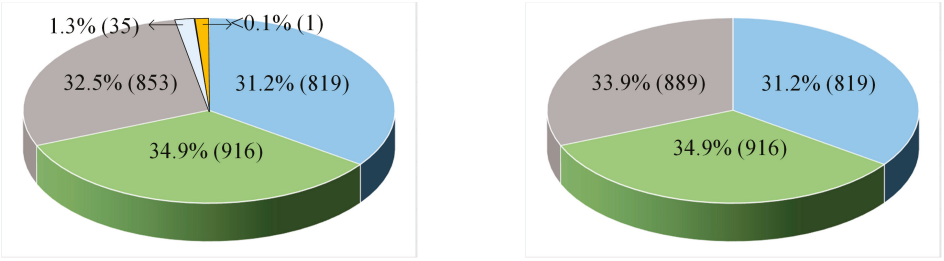


Figure 14. The number of buses in different regions of a practical system in China before and after fine-tuning. (**a**) Before fine-tuning and (**b**) after fine-tuning.

To generate the dataset, the time-domain simulations are performed as follows. The level of each load fluctuates randomly between 80% and 120%. The outputs of the generators are adjusted based on the load levels and spinning reserve capacity. A set of 7000 OCs is obtained. The anticipated faults are N-1 three-phase short circuits on each bus except for generator buses. The fault duration is set to 0.25 s. For each anticipated fault location, 50 OCs are randomly selected. A total of 104,850 samples are generated. The sample distribution in each region is shown in Table 6.

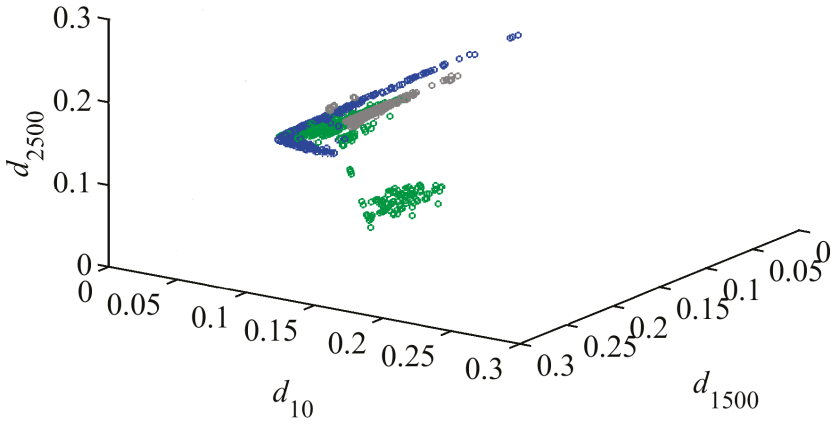


Figure 15. Cluster results in the three-dimensional feature space.

Table 6. Distribution of samples in each region.

Region	Samples	Stable Samples	Unstable Samples
1	33,400	22,121	11,279
2	34,650	22,777	11,873
3	36,800	22,721	14,079
Total	104,850	67,619	37,231

Figure 16 presents a comparison of the results from partition and unified assessments with RBFNN. The accuracy of the partition assessment is significantly higher than that of the unified assessment. It demonstrates that the proposed dynamic security partition method is applicable to large-scale power systems.

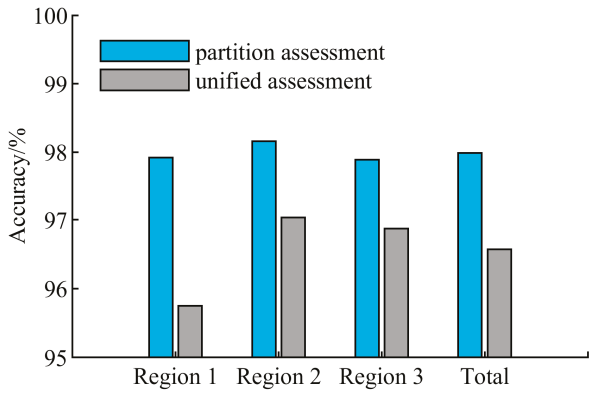


Figure 16. Accuracy of the partition and unified assessments based on RBFNN.

6. Conclusions

This paper proposes a data-driven dynamic security partition assessment method for power systems, aiming to develop accurate and incrementally updated DSA models with simple structures. By the mean shift algorithm integrated with a symmetric electrical distance matrix and Chebyshev distance, the power grid is partitioned strictly considering electrical connections. Multiple DSA models are constructed based on the RBFNN and Chebyshev distance, achieving high assessment accuracy with a simple model structure. DSA models are updated online based on the incremental updating strategy, which achieves high updating efficiency and avoids catastrophic forgetting during the updating process. The case study demonstrates that the partition assessment has higher accuracy than the unified assessment. In the partition assessment, the RBFNN-based assessment models have close accuracy to deep learning and ensemble learning models. The proposed incremental updating method can greatly reduce the updating time while maintaining high accuracy.

In addition to pre-fault operating conditions and fault locations, the topology is also a significant factor affecting the dynamic security of the power system. In this paper, the input feature set of the DSA model does not include power grid topology information. The DSA model must be reconstructed to adapt to the change of the power grid topology. The topological change can be reflected by the symmetric electrical distance matrix. A feature representation method of the topology will be studied based on the symmetric electrical distance matrix. Furthermore, the construction of a low-complexity DSA model considering OCs, fault locations, and topology is also the focus of future research.

Author Contributions: Conceptualization, H.Q. and R.S. (Runjia Sun); methodology, H.Q.; software, R.S. (Ruiyang Su); validation, H.Q., R.S. (Ruiyang Su) and R.S. (Runjia Sun); formal analysis, J.Y.; investigation, H.Q.; data curation, J.Y.; writing—original draft preparation, H.Q.; writing—review and editing, R.S. (Runjia Sun); supervision, R.S. (Runjia Sun). All authors have read and agreed to the published version of the manuscript.

Funding: This research was funded by National Natural Science Foundation of China under Grant 52307111 and Shandong Provincial Natural Science Foundation under Grant ZR2023QE273.

Data Availability Statement: The data presented in this study are available on request from the corresponding author, as the data in this study relate to the actual power grids and are classified data.

Conflicts of Interest: The authors declare no conflicts of interest.

Abbreviations

Abbreviation	**Description**
DSA	dynamic security assessment
OC	operating condition
LSTM	long short-term memory neural network
CNN	convolutional neural network
RNN	recurrent neural network
SDAE	stacked denoising autoencoder
RBFNN	radial basis function neural network
DAE	denoising autoencoder
DBN	deep belief network
GRU	gated recurrent unit
RF	random forest
XGBoost	extreme gradient boosting
Notation	**Description**
Z_{ii}/Ω	self-impedance
Z_{ij}/Ω	mutual impedance
d_{ij}	electrical distance
Q_e	electrical modularity
N	the number of nodes
W_i	the sum of the edge weights of node i
$\boldsymbol{D}$	symmetric electrical distance matrix
$\boldsymbol{x}_i$	electrical coordinate
X	sample point
$\boldsymbol{M(x)}$	shift vector for sample point x
$\boldsymbol{S_x}$	high-dimensional spherical region
$G(\,)$	Gaussian weight
σ	bandwidth of the Gaussian weight
d_s	iteration termination threshold
d_a	aggregation threshold
$dist(\boldsymbol{x_i}, \boldsymbol{x_j})$	feature distance between $\boldsymbol{x}_i$ and $\boldsymbol{x}_j$

L_D	loss function of DAE
N	number of training samples
$\boldsymbol{F}_i$	i-th training sample feature vector
$\boldsymbol{z}_i$	reconstructed feature vector
$\boldsymbol{F}_c$	center vector of the hidden layer neuron
$\boldsymbol{o}$	high-level steady-state features of OCs
α, β	weight coefficients
X_{new}	new sample set for model updating

References

1. Hatziargyriou, N.; Milanovic, J.; Rahmann, C.; Ajjarapu, V.; Canizares, C.; Erlich, I.; Hill, D.; Hiskens, I.; Kamwa, I.; Pal, B.; et al. Definition and classification of power system stability–revisited & extended. *IEEE Trans. Power Syst.* **2020**, *36*, 3271–3281.
2. Liu, T.; Liu, Y.; Liu, J.; Wang, L.; Xu, L.; Qiu, G.; Gao, H. A bayesian learning based scheme for online dynamic security assessment and preventive control. *IEEE Trans. Power Syst.* **2020**, *35*, 4088–4099. [CrossRef]
3. Li, Z.; Xue, Y.; Wang, H.; Hao, L. Decision support system for adaptive restoration control of transmission system. *J. Mod. Power Syst. Clean Energy* **2021**, *9*, 870–885. [CrossRef]
4. Lara, J.D.; Henriquez-Auba, R.; Ramasubramanian, D.; Dhople, S.; Callaway, D.S. Revisiting power systems time-domain simulation methods and models. *IEEE Trans. Power Syst.* **2023**, *39*, 2421–2437. [CrossRef]
5. Lal, M.D.; Varadarajan, R. A review of machine learning approaches in synchrophasor technology. *IEEE Access* **2023**, *11*, 33520–33541. [CrossRef]
6. Li, H.; Li, C.; Liu, Y. Machine learning-based frequency security early warning considering uncertainty of renewable generation. *Int. J. Electr. Power Energy Syst.* **2022**, *134*, 107403. [CrossRef]
7. Mohammadi, H.; Khademi, G.; Dehghani, M.; Simon, D. Voltage stability assessment using multi-objective biogeography-based subset selection. *Int. J. Electr. Power Energy Syst.* **2018**, *103*, 525–536. [CrossRef]
8. Li, H.; Li, C.; Liu, Y. Maximum frequency deviation assessment with clustering based on metric learning. *Int. J. Electr. Power Energy Syst.* **2020**, *120*, 105980. [CrossRef]
9. Huang, J.; Guan, L.; Su, Y.; Yao, H.; Guo, M.; Zhong, Z. System-scale-free transient contingency screening scheme based on steady-state information: A pooling-ensemble multi-graph learning approach. *IEEE Trans. Power Syst.* **2021**, *37*, 294–305. [CrossRef]
10. Liu, X.; Min, Y.; Chen, L.; Zhang, X.; Feng, C. Data-driven transient stability assessment based on kernel regression and distance metric learning. *J. Mod. Power Syst. Clean Energy* **2020**, *9*, 27–36. [CrossRef]
11. An, J.; Yu, J.; Li, Z.; Zhou, Y.; Mu, G. A data-driven method for transient stability margin prediction based on security region. *J. Mod. Power Syst. Clean Energy* **2020**, *8*, 1060–1069. [CrossRef]
12. Liu, X.; Zhang, X.; Chen, L.; Xu, F.; Feng, C. Data-driven transient stability assessment model considering network topology changes via mahalanobis kernel regression and ensemble learning. *J. Mod. Power Syst. Clean Energy* **2020**, *8*, 1080–1091. [CrossRef]
13. Ren, C.; Xu, Y.; Zhang, R. An interpretable deep learning method for power system transient stability assessment via tree regularization. *IEEE Trans. Power Syst.* **2021**, *37*, 3359–3369. [CrossRef]
14. Ren, C.; Xu, Y. Transfer learning-based power system online dynamic security assessment: Using one model to assess many unlearned faults. *IEEE Trans. Power Syst.* **2019**, *35*, 821–824. [CrossRef]
15. Ren, C.; Xu, Y.; Dai, B.; Zhang, R. An integrated transfer learning method for power system dynamic security assessment of unlearned faults with missing data. *IEEE Trans. Power Syst.* **2021**, *36*, 4856–4859. [CrossRef]
16. Ren, C.; Yuan, H.; Li, Q.; Zhang, R.; Xu, Y. Pre-fault dynamic security assessment of power systems for multiple different faults via multi-label learning. *IEEE Trans. Power Syst.* **2022**, *38*, 5501–5511. [CrossRef]
17. Moulin, L.S.; Da Silva, A.A.; El-Sharkawi, M.A.; Marks, R.J. Support vector machines for transient stability analysis of large-scale power systems. *IEEE Trans. Power Syst.* **2004**, *19*, 818–825. [CrossRef]
18. AL-Masri, A.N.; Ab Kadir, M.Z.A.; Hizam, H.; Mariun, N. A novel implementation for generator rotor angle stability prediction using an adaptive artificial neural network application for dynamic security assessment. *IEEE Trans. Power Syst.* **2013**, *28*, 2516–2525. [CrossRef]
19. He, M.; Zhang, J.; Vittal, V. Robust online dynamic security assessment using adaptive ensemble decision-tree learning. *IEEE Trans. Power Syst.* **2013**, *28*, 4089–4098. [CrossRef]
20. Diao, R.; Vittal, V.; Logic, N. Design of a real-time security assessment tool for situational awareness enhancement in modern power systems. *IEEE Trans. Power Syst.* **2009**, *25*, 957–965. [CrossRef]
21. Beiraghi, M.; Ranjbar, A.M. Online voltage security assessment based on wide-area measurements. *IEEE Trans. Power Delivery* **2013**, *28*, 989–997. [CrossRef]
22. Sun, M.; Konstantelos, I.; Strbac, G. A deep learning-based feature extraction framework for system security assessment. *IEEE Trans. Smart Grid* **2018**, *10*, 5007–5020. [CrossRef]
23. Zhang, T.; Sun, M.; Cremer, J.L.; Zhang, N.; Strbac, G.; Kang, C. A confidence-aware machine learning framework for dynamic security assessment. *IEEE Trans. Power Syst.* **2021**, *36*, 3907–3920. [CrossRef]

24. Qi, H.; Li, C.; Liu, Y.; Zhang, L.; Zhang, Q.; Fan, H. Location representation of single-position fault for power system transient stability intelligent assessment. In Proceedings of the 2020 IEEE Sustainable Power and Energy Conference (iSPEC), Chengdu, China, 23–25 November 2020; pp. 2435–2441.
25. Ren, Z.; Li, L.; Qi, H.; Yang, J.; Li, C.; Xu, W. Data-driven dynamic security assessment based on expanded electrical coordinate system. In Proceedings of the 2022 IEEE International Conference on Power Systems and Electrical Technology (PSET), Aalborg, Denmark, 13–15 October 2022; pp. 316–322.
26. Wu, Y.; Wang, Q.; Guo, N.; Yingjie Tian, Y.; Li, F.; Su, X. Efficient multi-source self-attention data fusion for fdia detection in smart grid. *Symmetry* **2023**, *15*, 1019. [CrossRef]
27. Yan, R.; Geng, G.; Jiang, Q.; Li, Y. Fast transient stability batch assessment using cascaded convolutional neural networks. *IEEE Trans. Power Syst.* **2019**, *34*, 2802–2813. [CrossRef]
28. Hagmar, H.; Tong, L.; Eriksson, R.; Tuan, L.A. Voltage instability prediction using a deep recurrent neural network. *IEEE Trans. Power Syst.* **2020**, *36*, 17–27. [CrossRef]
29. Mao, X.; Zhu, W.; Wu, L.; Zhou, B. Comparative study on methods for computing electrical distance. *Int. J. Electr. Power Energy Syst.* **2021**, *130*, 106923. [CrossRef]
30. Arianos, S.; Bompard, E.; Carbone, A.; Xue, F. Power grid vulnerability: A complex network approach. *Chaos* **2008**, *19*, 1–16. [CrossRef]
31. Zhao, C.; Zhao, J.; Wu, C.; Wang, X.; Xue, F.; Lu, S. Power grid partitioning based on functional community structure. *IEEE Access* **2019**, *7*, 152624–152634. [CrossRef]
32. Ganganath, N.; Wang, J.V.; Xu, X.; Cheng, C.; Tse, C.K. Agglomerative clustering-based network partitioning for parallel power system restoration. *IEEE Trans. Ind. Inf.* **2017**, *14*, 3325–3333. [CrossRef]
33. Zhong, L.; Zhu, M.; Chen, S.; Shi, M.; Zhang, X.; Chen, D. Double-layer K-means++ clustering method for evaluation of dispatchable potential of massive regional 5G base stations. *IEEE Access* **2022**, *10*, 82870–82882. [CrossRef]
34. Ren, L.; Yong, B. Wind turbines fault classification treatment method. *Symmetry* **2022**, *14*, 688. [CrossRef]
35. Yamasaki, R.; Tanaka, T. Properties of mean shift. *IEEE Trans. Pattern Anal. Mach. Intell.* **2019**, *42*, 2273–2286. [CrossRef]
36. Zhang, Z.; Wang, C.; Wu, Q.; Dong, X. Optimal dispatch for cross-regional integrated energy system with renewable energy uncertainties: A unified spatial-temporal cooperative framework. *Energy* **2024**, *292*, 130433. [CrossRef]
37. Comaniciu, D.; Meer, P. Mean shift: A robust approach toward feature space analysis. *IEEE Trans. Pattern Anal. Mach. Intell.* **2002**, *24*, 603–619. [CrossRef]
38. Cheng, Y. Mean shift, mode seeking, and clustering. *IEEE Trans. Pattern Anal. Mach. Intell.* **1995**, *17*, 790–799. [CrossRef]
39. Ghassabeh, Y.A. A sufficient condition for the convergence of the mean shift algorithm with Gaussian kernel. *J. Multivar. Anal.* **2015**, *135*, 1–10. [CrossRef]
40. Ren, Z.; Qi, H.; Li, C.; Qu, H.; Yang, J.; Xu, W. Research on distance preservation ability of fault location features for data-driven dynamic security assessment. In Proceedings of the 2022 IEEE 6th Conference on Energy Internet and Energy System Integration (EI2), Chengdu, China, 11–13 November 2022; pp. 1120–1125.
41. Su, T.; Liu, Y.; Zhao, J.; Liu, J. Probabilistic stacked denoising autoencoder for power system transient stability prediction with wind farms. *IEEE Trans. Power Syst.* **2020**, *36*, 3786–3789. [CrossRef]
42. Duan, B.; Han, L.; Gou, Z.; Yang, Y.; Chen, S. Clustering mixed data based on density peaks and stacked denoising autoencoders. *Symmetry* **2019**, *11*, 163. [CrossRef]
43. Yan, J.; Li, C.; Liu, Y. Insecurity early warning for large scale hybrid AC/DC grids based on decision tree and semi-supervised deep learning. *IEEE Trans. Power Syst.* **2021**, *36*, 5020–5031. [CrossRef]
44. Alhmoud, L.; Nawafleh, Q.; Merrji, W. Three-phase feeder load balancing based optimized neural network using smart meters. *Symmetry* **2021**, *13*, 2195. [CrossRef]
45. Wu, S.; Zheng, L.; Hu, W.; Yu, R.; Liu, B. Improved deep belief network and model interpretation method for power system transient stability assessment. *J. Modern Power Syst. Clean Energy* **2020**, *8*, 27–37. [CrossRef]
46. Liu, S.; Liu, L.; Fan, Y. An integrated scheme for online dynamic security assessment based on partial mutual information and iterated random forest. *IEEE Trans. Smart Grid* **2020**, *11*, 3606–3619. [CrossRef]
47. Zhang, S.; Zhang, D.; Qiao, J.; Wang, X.; Zhang, Z. Preventive control for power system transient security based on XGBoost and DCOPF with consideration of model interpretability. *CSEE J. Power Energy Syst.* **2021**, *7*, 279–294.

Disclaimer/Publisher's Note: The statements, opinions and data contained in all publications are solely those of the individual author(s) and contributor(s) and not of MDPI and/or the editor(s). MDPI and/or the editor(s) disclaim responsibility for any injury to people or property resulting from any ideas, methods, instructions or products referred to in the content.

symmetry

MDPI

Article

Assessment of the Renewable Energy Consumption Capacity of Power Systems Considering the Uncertainty of Renewables and Symmetry of Active Power

Kaijian Ou [1], Shilin Gao [2,*], Yuhong Wang [2], Bingjie Zhai [2] and Wei Zhang [2]

[1] Guangdong Provincial Key Laboratory of Intelligent Operation and Control for New Energy Power System, Guangzhou 510663, China; oukj@csg.cn
[2] College of Electrical Engineering, Sichuan University, Chengdu 610065, China; yuhongwang@scu.edu.cn (Y.W.); zhaibingjie1@stu.scu.edu.cn (B.Z.); zhangwei32106@stu.scu.edu.cn (W.Z.)
* Correspondence: gaoshilin@scu.edu.cn

Abstract: The rapid growth of renewable energy presents significant challenges for power grid operation, making the efficient integration of renewable energy crucial. This paper proposes a method to evaluate the power system's capacity to accommodate renewable energy based on the Gaussian mixture model (GMM) from a symmetry perspective, underscoring the symmetrical interplay between load and renewable energy sources and highlighting the balance necessary for enhancing grid stability. First, a 10th-order GMM is identified as the optimal model for analyzing power system load and wind power data, balancing accuracy with computational efficiency. The Metropolis–Hastings (M-H) algorithm is used to generate sample spaces, which are integrated into power flow calculations to determine the maximum renewable energy integration capacity while ensuring system stability. Short-circuit ratio calculations and N-1 fault simulations validate system robustness under high renewable energy integration. The consistency between the results from the M-H algorithm, Gibbs sampling, and Monte Carlo simulation (MCS) confirms the approach's accuracy.

Keywords: symmetry in renewable energy integration; active power symmetry; probabilistic assessment; Gaussian mixture models; Metropolis–Hastings algorithm

1. Introduction

Symmetry in renewable energy integration refers to the balanced incorporation of renewable sources like wind and solar into the power grid, emphasizing equilibrium between variable supply and consistent demand to ensure stability. Lately, sources of renewable energy, including wind and solar, known for their lack of carbon emissions, have swiftly become part of the electrical grid [1,2]. They have occupied an important position in the energy systems of many countries. As of 2021's close, the worldwide installed capacity for solar and wind energy reached 1674 GW, with European nations like Germany, Denmark, Norway, and Sweden extensively adopting these green energy solutions [3]. However, the increasing complexity and dynamic nature of modern power systems, driven by the integration of renewable energy, have been widely recognized [4,5]. The generation of renewable energy typically exhibits strong randomness, intermittency, and volatility [6]. The integration of a high proportion of renewable energy complicates the operational characteristics of power systems. Characteristics such as low disturbance rejection, low inertia, and low short-circuit capacity inherent in power systems will pose significant challenges to their balance capacity, support capacity, regulation ability, and safety and stability [7–9]. Stability, in this context, is vital because it ensures that the grid can reliably accommodate fluctuations in energy supply and demand without compromising the continuous delivery of electricity or the security of the power network. Hence, to lower

the renewable energy reduction rate and guarantee the system's safe functioning, it is critically important to precisely evaluate the system's capacity to absorb renewable energy.

Symmetry in renewable energy integration refers to the balanced incorporation of renewable sources like wind and solar into the power grid, emphasizing equilibrium between variable supply and consistent demand to ensure stability. Lately, sources of renewable energy, including wind and solar, known for their lack of carbon emissions, have swiftly become part of the electrical grid [1,2]. They have occupied an important position in the energy systems of many countries. As of 2021's close, the worldwide installed capacity for solar and wind energy reached 1674 GW, with European nations like Germany, Denmark, Norway, and Sweden extensively adopting these green energy solutions [3–5]. However, the generation of renewable energy typically exhibits strong randomness, intermittency, and volatility [6]. The integration of a high proportion of renewable energy complicates the operational characteristics of power systems. Characteristics such as low disturbance rejection, low inertia, and low short-circuit capacity inherent in power systems will pose significant challenges to their balance capacity, support capacity, regulation ability, and safety and stability [7–9]. Stability, in this context, is vital because it ensures that the grid can reliably accommodate fluctuations in energy supply and demand without compromising the continuous delivery of electricity or the security of the power network. Hence, to lower the renewable energy reduction rate and guarantee the system's safe functioning, it is critically important to precisely evaluate the system's capacity to absorb renewable energy.

In the field of power systems, assessing the absorption capacity of renewable energy is a significant research topic. Currently, the most commonly used analytical methods include typical day analysis and time series production simulation [10]. The typical day analysis method, as described in references [11,12], mainly evaluates the power system's capacity to absorb renewable energy based on the peak load's regulating margin on a typical day. However, this method does not fully consider the randomness and volatility of renewable energy output and load, resulting in conservative calculation outcomes [13]. In contrast, time series production simulation, as shown in reference [14], can more comprehensively simulate the operation of power systems, but its large data requirements, heavy computational load, and lengthy optimization solution time limit its practical application efficiency. Furthermore, the output of renewable energy is random. To comprehensively analyze the impact of system uncertainty factors on renewable energy absorption, it is necessary to use probabilistic analysis methods to precisely calculate the flow distribution of the system in a safe operating state.

Currently, the most common probabilistic analysis methods in the field of power system research are divided into two categories: analytical methods and simulation methods. Among them, the analytical method calculates the probability distribution of the output by processing the convolution between random variables. However, the assumption that input random variables are independent results in lower computational accuracy of the analytical method. The MCS method, as the most representative simulation method, achieves high computational accuracy with a sufficiently large sampling size [15]. However, due to the high computational cost of the MCS method, it has gradually become a standard for verifying the accuracy of other methods [16,17]. The M-H algorithm, an iterative sampling algorithm derived from the Metropolis algorithm, exhibits good sampling performance and high computational efficiency. It significantly increases the computation speed [18,19].

This paper addresses the effectiveness and precision required in assessing the renewable energy absorption capacity within power system operations. In simulating input random variables, it first constructs probability models of the load and wind power using the GMM, then employs the M-H algorithm to obtain a sample space from the probability density function of the input random variables. An assessment model for renewable energy absorption capacity is built under the constraints of safe system operation, taking into account the dynamic characteristics and complexity of the power system and enhancing the efficiency and accuracy of random variable simulation with the M-H algorithm. The model identifies renewable energy access points and initial outputs based on the network's

topology and uses power flow calculations to determine the maximum capacity of renewable energy that can be integrated for each sample set under the constraints of system safety, statistically analyzing the capacity for renewable energy integration. Finally, the model's reliability and practicality are validated by analyzing the short-circuit ratio of renewable energy sites and performing N-1 fault simulations. The effectiveness of the proposed model in improving the precision of renewable energy absorption assessments and reducing computational complexity is verified through simulation experiments under various scenarios and conditions.

2. Probabilistic Modeling of Load and Wind Power

In the study of probabilistic assessment of renewable energy integration capacity, probabilistic modeling of uncertain factors is the primary issue to be addressed. The accuracy of this modeling directly affects the precision of probabilistic load flow calculations, which in turn determines the accuracy of the renewable energy integration capacity assessment results. The main uncertain factors affecting the integration capacity of renewable energy are the randomness of the load and the fluctuating nature of renewable energy. Currently, in power system studies considering load randomness, loads are mostly treated as following a normal distribution. However, actual load power distributions in general systems do not strictly follow a normal distribution but exhibit a multimodal nature. Some scholars have discovered the advantages of using a weighted GMM in modeling and have applied it to probabilistic load modeling, achieving excellent modeling results.

For the probabilistic modeling of wind power in renewable energy, existing methods can be divided into two categories: the first category establishes a probabilistic model of wind speed, and the second establishes a probabilistic model of wind power. Numerous studies have shown that measured wind speed data approximately follow a Weibull distribution. Based on the inherent relationship between wind speed and wind power, the probabilistic distribution of wind power can thus be derived. However, further research observations indicate that the probability distribution curve of measured wind speed data does not completely conform to a Weibull distribution. Some researchers have proposed using a probabilistic modeling method based on a weighted Gaussian mixture distribution. Compared to single distribution models, mixture distribution models offer greater flexibility in fitting curves, significantly improving the accuracy of wind power modeling.

GMM describes the joint probability distribution of a random vector x, represented as the convex sum of several Gaussian distributions [20]. The set of adjustable parameters for GMM is denoted by $\Omega = \{\omega_m, \boldsymbol{\mu_m}, \boldsymbol{\sigma_m}; m = 1, 2, \ldots, M\}$. The formula for GMM is outlined below:

$$f_{\mathrm{X}}(x) = f_{\mathrm{X}}(x) = \sum_{m=1}^{M} \omega_m N_m(x; \boldsymbol{\mu_m}, \boldsymbol{\sigma_{\mathbf{m}}}) \tag{1}$$

$$\sum_{m=1}^{M} \omega_m = 1, \omega_m > 0 \tag{2}$$

$$N_m(x; \boldsymbol{\mu}_m, \boldsymbol{\sigma}_m) = \frac{e^{-\frac{1}{2}(x-\boldsymbol{\mu}_m)^T \boldsymbol{\sigma}_m^{-1}(x-\boldsymbol{\mu}_m)}}{(2\pi)^{W/2}\det(\boldsymbol{\sigma}_m)^{1/2}} \tag{3}$$

In this context, $f_{\boldsymbol{\mathrm{X}}}(x)$ represents the joint probability density function of x; ω_m stands for the weight coefficient; $N_m(\cdot)$ symbolizes the multi-dimensional Gaussian distribution, termed as the m-th Gaussian component within the GMM; $\det(\cdot)$ symbolizes the determinant of a matrix; M indicates the total count of Gaussian components; and $\boldsymbol{\mu_m}$ and $\boldsymbol{\sigma_m}$ are the mean vector and covariance matrix of the m-th Gaussian component, respectively.

Figure 1 illustrates a GMM with four Gaussian components. In this diagram, the GMM's probability density function (depicted by the black line) is a convex sum of the probability density functions of four Gaussian distributions (shown by red, blue, green, and purple lines). By tuning the parameter set Ω, GMM can effectively model the probability density function of any random variable.

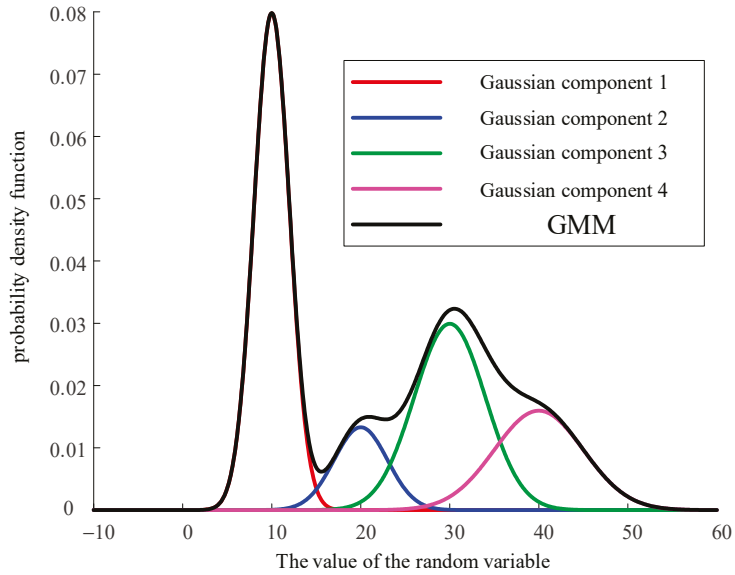


Figure 1. Schematic diagram of GMM.

In Figure 1, the Gaussian components from 1 to 4 have weight coefficients set at 0.4, 0.1, 0.3, and 0.2, respectively. Identifying the parameter set Ω for the GMM falls under the category of typical parameter estimation issues. Utilizing x, which represents the historical data of the load and wind power, one can establish the load's Gaussian mixture model.

For analyzing power load and wind power using a GMM, the historical records of actual power consumption and wind power can be viewed as a series of observations. These observations reflect the power consumption and wind power in the power system over different periods. However, these data are not complete because it is not possible to directly observe which specific power value belongs to which category of power consumption or generation. Some data remain unrecorded or unobservable. In a GMM, this unobservable membership information is referred to as hidden variables or missing data. Let the category to which the input random variable belongs be Z, and then the complete data are (X, Z). If there are past observations of a random variable, these past observations can be used to establish a Gaussian mixture probability model for the variable through parameter estimation. Currently, the expectation–maximization (EM) algorithm is one of the main algorithms used for parameter estimation in GMMs. Using the EM algorithm to determine the parameters of the GMM for load and wind power is a classic and effective method. This algorithm optimizes the parameter set Ω through an iterative process, which includes the mean (μ), covariance matrix (Σ), and weight coefficients (π) for each Gaussian component [21]. First, these parameters are initialized, which can be performed randomly or through heuristic methods. The core of the EM algorithm consists of two main steps: the expectation step (E-step) and the maximization step (M-step). In the E-step, the hidden variables are estimated by calculating the probability that each data point belongs to each Gaussian component, referred to as responsibility. This is calculated as follows:

$$\gamma_{ik} = \frac{\pi_k \cdot N(x_i|\mu_k, \Sigma_k)}{\sum_{j=1}^{K} \pi_j \cdot N(x_i|\mu_j, \Sigma_j)} \tag{4}$$

where γ_{ik} represents the probability that data point x_i belongs to the kth Gaussian component, π_k is the weight coefficient of the kth Gaussian component, and $N(x_i|\mu_k, \Sigma_k)$ is the probability density function of the kth Gaussian component.

$$\pi_k^{\text{new}} = \frac{1}{N} \sum_{i=1}^{N} \gamma_{ik} \tag{5}$$

$$\mu_k^{\text{new}} = \frac{\sum_{i=1}^{N} \gamma_{ik} x_i}{\sum_{i=1}^{N} \gamma_{ik}} \tag{6}$$

$$\Sigma_k^{\text{new}} = \frac{\sum_{i=1}^{N} \gamma_{ik} (x_i - \mu_k^{\text{new}})(x_i - \mu_k^{\text{new}})^T}{\sum_{i=1}^{N} \gamma_{ik}} \tag{7}$$

where π_k^{new} is the updated weight coefficient, μ_k^{new} is the updated mean, Σ_k^{new} is the updated covariance matrix, and N is the total number of data points.

The E-step and M-step are repeated until the parameters converge, i.e., the change in parameters is less than a predefined threshold. Through this iterative process, the EM algorithm can effectively determine the parameters of the GMMfor load and wind power, thereby establishing a more accurate probabilistic model. This model can better reflect the randomness and volatility of load and wind power, thus improving the accuracy of renewable energy consumption capacity assessment.

3. Acquisition of Input Variables Sample Space

The M-H algorithm is an iterative sampling method derived from the Metropolis algorithm, known for its excellent sampling performance and high computational efficiency. This algorithm simulates transitions between system states based on a state transition probability matrix, derived from the Markov chain Monte Carlo (MCMC) method. It overcomes the limitations of the traditional MCS method, which can only model static scenarios, by allowing dynamic simulation of random variables transitioning between different states.

In the context of power systems, assuming that the first-order Markov chain is $X = \{x_l, x_2, \ldots, x_t, \ldots, x_N\}$, where N is the data length of the historical power series, x_t is the state value of the t-th data corresponding to dividing the historical sequence into S states, consists of S states forming the state space $E = \{E_l, E_2, \ldots, E_S\}$, each moment of historical data corresponds to a state, and there are S possibilities for each state to transition to the next state, which can be known according to the Markov property (the present state is solely connected to the immediate preceding state and is unrelated to any states prior to that), calculated as follows:

$$p_{ij} = P_r\{x_{t+1} = E_j \mid x_t = E_i\} = n_{ij} / \sum_{k=1}^{S} n_{ik} \tag{8}$$

In the formula, p_{ij} and n_{ij} are the probability of transferring from state E_i to state E_j and the number of transfers, respectively, and the transitions between the states form the state transfer probability matrix $\boldsymbol{P}$, according to which the cumulative state transfer probability matrix $\boldsymbol{Q}$ can be formed, and $\boldsymbol{P}$ and $\boldsymbol{Q}$ are shown in Equations (5) and (6).

$$\boldsymbol{P} = \begin{bmatrix} p_{11} p_{12} \cdots p_{1S} \\ p_{21} p_{22} \cdots p_{2S} \\ \vdots \quad \vdots \quad \cdots \quad \vdots \\ p_{S1} p_{S2} \cdots p_{SS} \end{bmatrix} \tag{9}$$

$$\boldsymbol{Q} = \begin{bmatrix} p_{11} & p_{11} + p_{12} & \cdots & p_{11} + p_{12} + p_{1S} \\ p_{21} & p_{21} + p_{22} & \cdots & p_{21} + p_{22} + p_{2S} \\ \vdots & \vdots & \ddots & \vdots \\ p_{S1} & p_{S1} + p_{S2} & \cdots & p_{S1} + p_{S2} + p_{SS} \end{bmatrix} \tag{10}$$

Assuming that the original power state sequence satisfies the $f(x)$ distribution, and the initial state x satisfies $f(x) > 0$, according to the proposed probability distribution $g(y|x)$ (denoting the probability of sampling a known x to obtain y), sampling an alternative state y, the acceptance probability of y is calculated as follows:

$$h(x, y) = \min\left\{1, \frac{f(y)g(x|y)}{f(x)g(y|x)}\right\} \tag{11}$$

where x is the current state, y is the alternative state, f is the target probability density function, and g is the proposed probability density function. When Equation (7) satisfies the symmetry condition, i.e., $g(y|x) = g(x|y)$, it can be simplified as follows:

$$h(x, y) = \min\left\{1, \frac{f(y)}{f(x)}\right\} \tag{12}$$

We accept the alternative state with probability $h(x, y)$ as the state value at the next moment, otherwise keep the original state unchanged. Applying the M-H algorithm to extract load and wind power sample spaces in power systems can accurately simulate the dynamics and random behavior of load and wind power changes over time. This method significantly enhances the modeling and analysis of power systems, especially in evaluating and planning for the integration of variable renewable energy sources and other load management strategies.

4. Evaluation of Renewable Energy Consumption Capacity Considering Safety and Stability Constraints

4.1. Assessment Model for Renewable Energy Consumption Capacity

This paper employs a probabilistic assessment method that fully considers the uncertainties of load and wind power. Since the fluctuations in load and wind power result in varying amounts of wind power accommodation and the ultimate integration capacity of wind power is constrained by system operating conditions, the evaluation model proposed in this paper is based on the following concept: taking into account the impact of uncertain factors, the model assesses the maximum renewable energy integration capacity under the static security constraints of the power system.

(1) Objective Function

The assessment of renewable energy integration capacity typically selects either the system operating cost or the amount of renewable energy integration as the objective function. The former optimizes the system's economic operating cost, considering various safety constraints, and determines the optimal integration of renewable energy by minimizing the system's operating cost. The latter directly aims to maximize the amount of renewable energy integration, determining the system's maximum integration capacity while ensuring all operational indicators remain within safe operating limits. According to the evaluation model's concept, this paper uses the maximum renewable energy integration as the objective function.

$$\max\left(P_w + \sum_{i \in C} \Delta P_{wi}\right) \tag{13}$$

where P_w represents the initial power of renewable energy integration, ΔP_{wi} denotes the additional renewable energy integration capacity in the ith increment, and C signifies the number of increments in renewable energy power.

(2) Constraints

To ensure the safe and stable operation of the power system, the operational data of each node and branch within the system must meet safety operation constraints. These constraints are divided into equality constraints and inequality constraints. The equality constraints represent the power balance equations at the nodes. The formula is expressed as follows:

$$\begin{aligned} P_i &= U_i \sum_{j=1}^{n} U_j \left(G_{ij} \cos \delta_{ij} + B_{ij} \sin \delta_{ij}\right) \\ Q_i &= U_i \sum_{j=1}^{n} U_j \left(G_{ij} \sin \delta_{ij} + B_{ij} \cos \delta_{ij}\right) \end{aligned} \tag{14}$$

The inequality constraints include the active and reactive power output constraints of conventional generators, node voltage magnitude constraints, node voltage phase angle constraints, and branch power transmission constraints. The inequality constraints are expressed as follows:

$$\begin{gathered} {P_{Gi}}^{\min} < P_{Gi} < {P_{Gi}}^{\max} \\ {Q_{Gi}}^{\min} < Q_{Gi} < {Q_{Gi}}^{\max} \\ {U_i}^{\min} < U_i < {U_i}^{\max} \\ \left|\delta_i - \delta_j\right| < \left|\delta_i - \delta_j\right|_{\max} \\ |F_k| \le F_{k_{\max}} \quad k \in \Omega \end{gathered} \tag{15}$$

where ${P_{Gi}}^{\max}$ and ${Q_{Gi}}^{\max}$ are the maximum active and reactive power outputs of the conventional generator at node i; ${P_{Gi}}^{\min}$ and ${Q_{Gi}}^{\min}$ are the minimum active and reactive power outputs of the conventional generator at node i; U_i is the voltage magnitude at node i; ${U_i}^{\max}$ is the maximum voltage magnitude at node i; ${U_i}^{\min}$ is the minimum voltage magnitude at node i; δ_i is the voltage phase angle at node i; δ_j is the voltage phase angle at node j; F_k is the active power flow through branch k; $F_{k_{\max}}$ is the maximum allowable power flow through branch k; and Ω represents the set of all branches in the system.

The mathematical model of renewable energy consumption capacity assessment in this paper can be simplified as the following nonlinear optimization model:

$$\begin{cases} \max f(s) = P_{\mathrm{w}} + \sum\limits_{i \in C} \Delta P_{\mathrm{w}i} \\ \text{s.t.} g(s) = 0 \\ h_{\min} \leqslant h(s) \leqslant h_{\max} \end{cases} \tag{16}$$

where s is all state and control variables; P_w is initial power of renewable energy access; ΔP_{wi} is third increase of renewable energy access capacity; C is number of renewable energy power increases; $g(s)$ is trend equation of the system; and $h(s)$ is inequality constraints determined by the static safety constraints of the system, with a lower limit of $h_{\min}$ and an upper limit of $h_{\max}$. Equation (16) integrates key components from the preceding equations—specifically, the objective function in Equation (13) that maximizes renewable energy integration while keeping state variables within safety limits, and the constraints in Equations (14) and (15) that establish power balance and operational limits—into a comprehensive nonlinear optimization model; with the trend equation g(s) capturing the system's dynamic behavior as renewable energy capacity increases and linking directly to the constraints to ensure that as ΔP_{wi} increases, the system remains within predefined operational boundaries, while the inequality constraints h(s) derived from Equations (14) and (15) further ensure the system operates within safe limits, thus providing a rigorous framework for assessing the maximum renewable energy integration capacity while maintaining system stability and security.

4.2. Short-Circuit Ratio Verification

For a long time, short-circuit ratio, as a static analysis method, has provided an important reference for the planning and operation of power grids due to its simplicity and intuition. The multi-site short-circuit ratio for renewable energy, as suggested in the referenced literature [21], presents a more comprehensive M_{RSCR} calculation formula that removes all assumptions inherent in the traditional CIGRE short-circuit ratio derivation. This approach accounts for both amplitude and phase differences among electrical quantities across various nodes. It also considers the impact of reactive power from renewable energy generation equipment, making it applicable for evaluating and calculating volt-

age strength in diverse scenarios of multi-renewable energy site access systems. Figure 2 shows the simplified equivalent model of i (i = 1, 2, …, n) renewable energy stations simultaneously connected to the AC system.

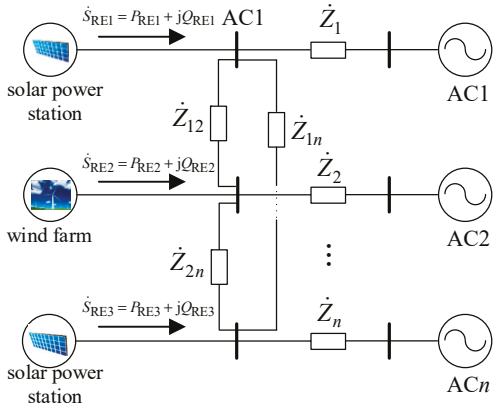


Figure 2. Streamlined model of an AC system interfacing with various renewable energy stations.

In Figure 2, $\dot{S}_{REi}$, P_{REi}, Q_{REi}, and $\dot{U}_{REi}$ represent the apparent power, active power, reactive power, and voltage at the bus of renewable energy generation equipment/station i, respectively. $\dot{Z}_{ij}$ denotes the equivalent impedance between grid-connected points i and j, while $\dot{Z}_{ij}$ indicates the system-side equivalent impedance between the main grid-equivalent power source i and its associated grid-connected point j. The renewable energy grid-connected buses in Figure 2 can symbolize either the grid-side access points of renewable energy power generation equipment or the grid-connection points of renewable energy stations. Assuming the currents injected into the AC system by each renewable energy grid-connected bus are $\dot{I}_1$, $\dot{I}_2$, …$\dot{I}_n$, then the nodal voltages at each grid-connected bus $\dot{U}_{REl}$, $\dot{U}_{RE2}$,…, $\dot{U}_{REn}$, $\dot{S}_{REn}$ can be expressed as follows:

$$\begin{bmatrix} \dot{U}_{REl} \\ \dot{U}_{RE2} \\ \vdots \\ \dot{U}_{REn} \end{bmatrix} = \begin{bmatrix} \dot{Z}_{eq11} & \dot{Z}_{eq12} & \cdots & \dot{Z}_{eq1n} \\ \dot{Z}_{eq21} & \dot{Z}_{eq22} & \cdots & \dot{Z}_{eq2n} \\ \vdots & \vdots & & \vdots \\ \dot{Z}_{eqn1} & \dot{Z}_{eqn2} & \cdots & \dot{Z}_{eqnn} \end{bmatrix} \begin{bmatrix} \dot{I}_1 \\ \dot{I}_2 \\ \vdots \\ \dot{I}_n \end{bmatrix} \tag{17}$$

In the equation, $\dot{Z}_{eqij}$ denotes the element located in the i-th row and j-th column of the equivalent impedance matrix $\dot{Z}_{eqij}$ at the bus where renewable energy sources are interconnected with the AC grid. The short-circuit ratio is used to measure the relative magnitude between the system's nominal voltage and the voltage generated by the equipment upon integration into the system. Reflecting on the physical significance described, the maximum renewable source connection ratio (M_{RSCR}) at the i-th renewable energy interconnection bus within the system is defined as follows:

$$M_{RSCRi} = \frac{\left|\dot{U}_{\mathbf{N}i}\right|}{\left|\dot{U}_{\mathbf{RE}i}\right|} = \frac{\left|\dot{U}_{\mathbf{N}i}\right|}{\left|\dot{Z}_{\mathbf{eq}ii}\dot{I}_i + \sum_{j=1,j\neq i}^{n} \dot{Z}_{\mathbf{eq}j}\dot{I}_j\right|} \tag{18}$$

where $\dot{U}_{\mathbf{N}i}$ is the nominal voltage at the i-th grid-connected bus node; $\dot{U}_{REi}$ is the voltage produced by the renewable energy generation equipment at node i, with the subscript RE denoting the renewable energy power station; and $\dot{I}_i$ is the short-circuit current supplied by the i-th renewable energy power station. The actual operating voltage at the i-th grid-connected bus node, $\dot{U}_i$ is derived by multiplying both the numerator and denominator of Equation (18) by $\left|\dot{U}_i^* / \dot{Z}_{eqii}\right|$, calculated as follows:

$$\begin{aligned} M_{RSCR_i} &= \frac{\left|\dot{U}_i^* \dot{U}_{Ni} / \dot{Z}_{eqii}\right|}{\left|\dot{U}_i^* \dot{I}_i + \sum_{j=1,j\neq i}^{n} \frac{\dot{Z}_{eqij}}{\dot{Z}_{eqi}} \dot{U}_i^* \dot{I}_j\right|} \\ &= \left|\frac{\dot{U}_i^* \dot{U}_{Ni}}{\dot{Z}_{eqii}}\right| / \left|\dot{S}_{REi} + \sum_{j=1,j\neq i}^{n} \Pi_{\cdot ij} \dot{S}_{REj}\right| \end{aligned} \tag{19}$$

where $\dot{S}_{REi}$ represents the actual apparent power of renewable energy injected at the *i*-th renewable energy grid-connected bus node; $\Pi_{\cdot ij} = \dot{Z}_{eqij}\dot{U}_i^* / \dot{Z}_{eqii}\dot{U}_j^*$ is the complex power conversion factor between renewable energy grid-connected buses *i* and *j*, indicating the phase and amplitude differences among the electrical quantities at each grid-side access point of renewable energy generation equipment or at each renewable energy station grid-connected node. Depending on the specific requirements, the M_{RSCRG} (maximum renewable source connection grid ratio) for the grid-side access point of the renewable energy generation equipment or the M_{RSCRS} (maximum renewable source connection station ratio) for the grid-connected point of the renewable energy station can be determined using Equation (19). It is noted that, when considering the connection of just a single renewable energy power station to the AC system, the corresponding renewable energy station short-circuit ratio (R_{SCR}) is defined as follows:

$$R_{SCR} = \left|\dot{U}^* \dot{U}_N / \dot{Z}_{eq}\right| / \left|\dot{S}_{RE}\right| \tag{20}$$

where $\dot{Z}_{eq} = R + jX$ represents the system-side equivalent impedance from the grid-side access point of the renewable energy generation equipment or the connection point of the renewable energy station.

In this paper, this quantitative index is used to carry out safety and stability verification of the maximum capacity of renewable energy field station access under the condition of satisfying the system safety operation constraints.

4.3. Assessment Process for Considering Safety and Stability Constraints in the Consumption Capacity Evaluation

Based on the above analysis, a set of probabilistic assessment methods for renewable energy consumption capacity and an assessment flow system for system security and stability analysis can be derived, as shown in Figure 3.

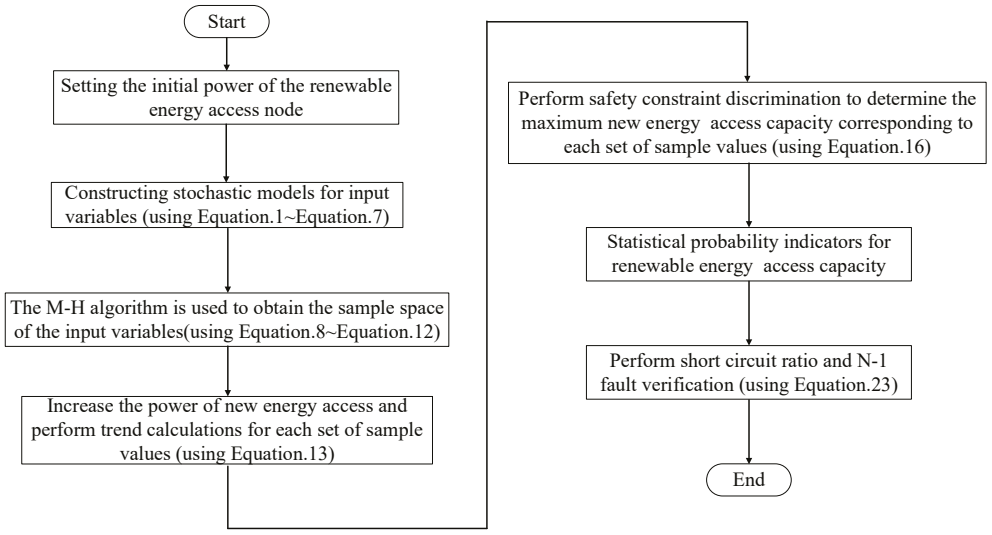


Figure 3. Flowchart of the evaluation method.

5. Case Analysis

5.1. Probabilistic Modeling of Load

While higher-order GMM models tend to offer greater accuracy, balancing modeling precision with computational efficiency is crucial. Thus, this paper opts for a 10th-order Gaussian mixture model for load modeling and calculation. The load's probability density function is defined as follows:

$$f_{\mathrm{L}}(x) = \omega_1 \frac{1}{\sqrt{2\pi}\sigma_1} \mathrm{e}^{-\frac{(x-\mu_1)^2}{2\sigma_1^2}} + \omega_2 \frac{1}{\sqrt{2\pi}\sigma_2} \mathrm{e}^{-\frac{(x-\mu_2)^2}{2\sigma_2^2}} + \ldots + \omega_{10} \frac{1}{\sqrt{2\pi}\sigma_{10}} \mathrm{e}^{-\frac{(x-\mu_{10})^2}{2\sigma_{10}^2}} \tag{21}$$

In this paper, the 5th-order Gaussian mixture model, the 8th-order Gaussian mixture model, the 10th-order Gaussian mixture model, the 12th-order Gaussian mixture model, the 15th-order Gaussian mixture model, and the normal distribution are selected to fit the probability density curves of the load measured data, respectively. The selection of these specific model orders is based on a balance between model accuracy and computational efficiency. The 5th-order model was chosen as it provides a simple yet reasonably accurate fit, capturing the basic structure of the data. The 8th-order model was introduced to improve upon the 5th-order, addressing some of the complexities in the data that the lower-order model might miss. The 10th-order model, identified through preliminary analysis, was expected to provide the best overall fit, balancing accuracy and computational demands. The 12th-order model was added to examine the effects of a slight increase in model complexity beyond the 10th-order, though it introduces some risk of overfitting, particularly evident in its slight overestimation of the highest peak. Finally, the 15th-order model was included to explore the impact of higher complexity on the model's accuracy and computational cost. These selections allow for a comprehensive comparison of the fitting effects, providing insights into the trade-offs between model complexity, accuracy, and computational efficiency.

Figure 4 shows the probability density distribution curves of the load measured data and the six selected fitting models. As can be seen from Figure 4, the probability density distribution curve of the load measured data contains two peaks. The 5th-order GMM and the normal distribution both underestimate these two peaks of the original data. The 8th-order GMM improves the fit over the 5th-order, providing a better approximation to the lower peak, but it still slightly underestimates this peak. The 10th-order GMM achieves the best overall fit, accurately capturing both peaks with minimal deviation from the original data. The 12th-order Gaussian mixture model, while offering a good fit, slightly overestimates the highest peak, which reduces its overall accuracy compared to the 10th-order model. The 15th-order GMM also overestimates the highest peak, though it is in good agreement with the rest of the distribution. To verify the accuracy of these models more convincingly, the fitting indexes of each model were analyzed.

The metrics for evaluating a model's fit to reality are root mean square error (RMSE), summed squared error (SSE), and coefficient of determination (R^2). The closer the RMSE and SSE are to 0, the better the model fits the original data, and the closer R^2 is to 1, the better the ability to explain the original data, and the formula is as follows:

$$\begin{aligned} \mathrm{RMSE} &= \sqrt{\frac{1}{n}\sum_{i=1}^{n}(\hat{x}_i - x_i)^2} \\ \mathrm{SSE} &= \sum_{i=1}^{n}(\hat{x}_i - x_i)^2 \\ R^2 &= \frac{\sum_{i=1}^{n}(\hat{x}_i - \overline{x}_i)^2}{\sum_{i=1}^{n}(x_i - \overline{x}_i)^2} \end{aligned} \tag{22}$$

where $\hat{x}_i$ is sample data; x_i is raw data; $\overline{x}_i$ is average of raw data.

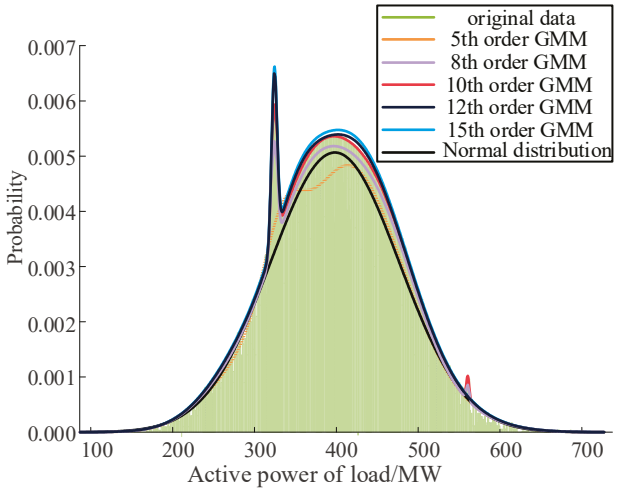


Figure 4. Probability density distribution curve of active power of load.

Table 1 illustrates that, when weighing simulation accuracy against computational expense, the 10th-order GMM emerges as the optimal modeling method.

Table 1. Accuracy evaluation index of load model.

Fit Model	RMSE	SSE	R^2
normal distribution	0.000753	0.000318	0.963
5th-order Gaussian distribution	0.000560	0.000127	0.988
8th-order Gaussian distribution	0.000382	0.000106	0.991
10th-order Gaussian distribution	0.000159	0.000048	0.995
12th-order Gaussian distribution	0.000147	0.000027	0.993
15th-order Gaussian distribution	0.000132	0.000013	0.982

5.2. Probabilistic Modeling of Wind Power

Based on the analysis above, given the satisfactory fitting performance of the 10th-order Gaussian mixture model, the probability model for wind power output is also adopted as a 10th-order Gaussian mixture model. A probability model of the GMM is established using actual output power data from a wind farm.

The wind power model based on the Gaussian mixture distribution demonstrates better accuracy in fitting the probability density curves of the load-measured data compared to models that utilize the Weibull distribution. Both the Weibull distribution and GMM were used to fit the original data, with the fitting curves displayed in Figure 5. Clearly, although the probability distribution of wind power is similar to the Weibull distribution, the Weibull distribution fails to capture the smaller fluctuations in wind power. This limitation is evident in Figure 5, where the Weibull distribution underestimates the short-term variations that arise due to local atmospheric conditions or turbulence. In contrast, the Gaussian mixture distribution, due to its flexible and versatile structure, accurately models these fluctuations. A comprehensive analysis of Figure 5 and Table 2 confirms that the Gaussian mixture distribution is more suitable for fitting the probability distribution of wind power than the Weibull distribution.

Table 2. Evaluation of wind power model accuracy.

Fit Model	RMSE	SSE	R^2
Weibull distribution	0.000533	0.000258	0.9677
10th-order Gaussian distribution	0.000163	0.000052	0.9989

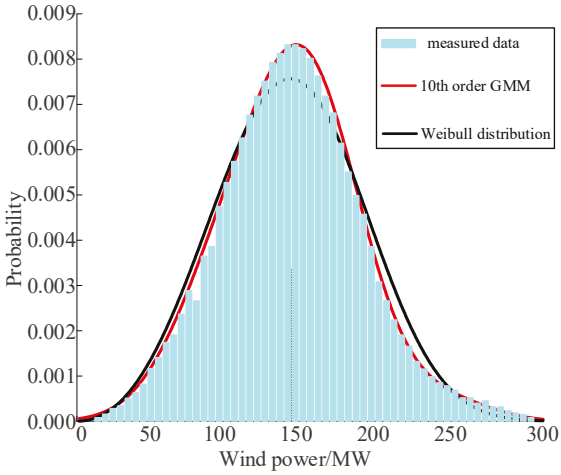


Figure 5. Probability distribution of wind power based on different models.

5.3. Validity Test of Renewable Energy Consumption Capacity Assessment Method

To validate the effectiveness of the proposed methodology, we applied the Metropolis–Hastings (M-H) algorithm to a modified IEEE 39-bus system to evaluate its ability to integrate renewable energy sources. The method's accuracy was subsequently corroborated using Monte Carlo simulation (MCS) as a benchmark. Additionally, Gibbs sampling was employed to provide a further comparison and validation of the results. In this simulation, the active and reactive power at nodes 21 and 23 followed Gaussian mixture distributions, derived from actual load data measurements. Moreover, the conventional generator at node 36 was replaced by a wind farm, with the farm's output modeled as a random variable also adhering to a Gaussian mixture distribution. To further analyze the impact of stochastic variations in load and wind on the system's capacity to accommodate renewable energy, node 35 was designated as a renewable energy access point with a power factor of 0.94, and the capacity for renewable energy was incrementally increased by 2 MW in each calculation iteration. The modified IEEE 39-bus system is shown in Figure 6.

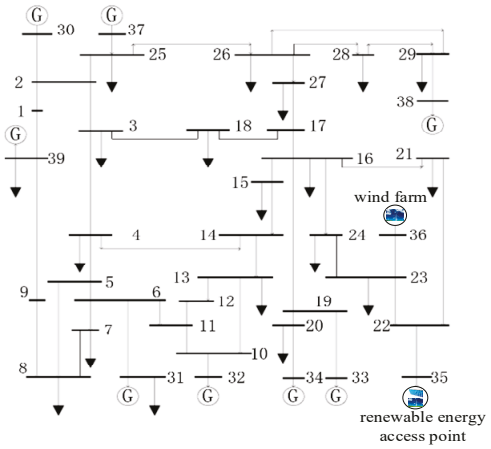


Figure 6. The modified IEEE 39-Bus System.

A sampling space for active load and wind power was created by sampling from the load and wind power variables' probability density functions. These samples were then used sequentially to adjust the power at the renewable energy access points, determining the maximum capacity of renewable energy that could be safely supported. Finally, kernel density estimation was employed to illustrate the probability density curves for renewable energy absorption.

As shown in Figures 7 and 8, the probability density curves generated by the Metropolis–Hastings (M-H) algorithm, the Monte Carlo simulation (MCS) method, and

the Gibbs sampling method are nearly identical, indicating that all three methods provide a consistent and accurate assessment of the fluctuations in renewable energy consumption in response to changes in load and wind power. This comparison highlights the reliability of the M-H algorithm, which was validated against the well-established MCS method and further corroborated by the Gibbs sampling approach. Table 3 presents the probabilistic statistical indicators of renewable energy consumption obtained from all three assessment methods, further confirming the accuracy and consistency of the M-H algorithm in evaluating renewable energy integration.

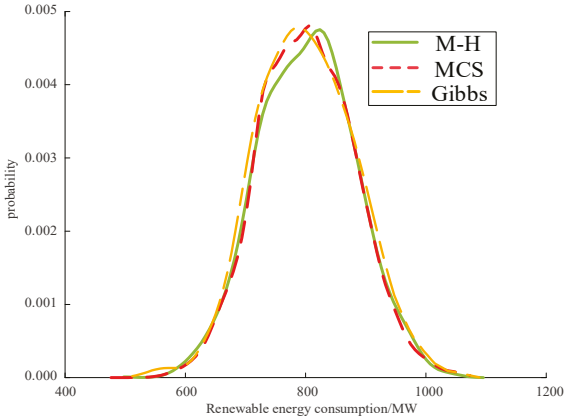


Figure 7. Probability density distribution curve of renewable power consumptive amount.

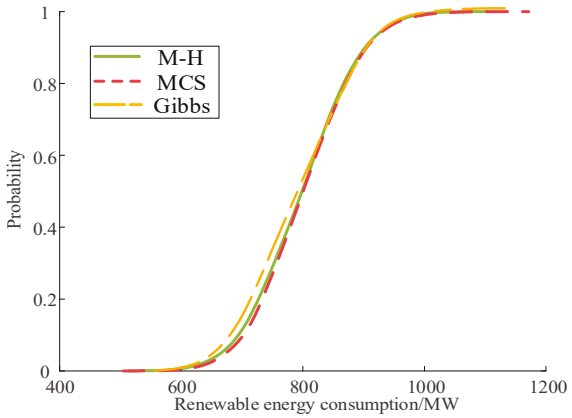


Figure 8. Cumulative distribution curve of renewable power consumptive amount.

Table 3. Statistical indicators of three assessment methods.

Algorithm	Number of Samples	Execution Time/ms	Mean/MW	Standard Deviation/MW	Maximum/MW	Min/MW
MCS	10,000	0.324	801.14	79.49	1088.94	518.04
M-H	2000	0.169	800.71	80.83	1054.87	535.96
Gibbs	2000	0.175	798.39	75.67	1035.28	558.37

As can be seen from Table 3, when the sampling scale of the MCS method is 10,000 and the sampling scale of the M-H algorithm is 2000, the probability indices of the M-H algorithm and the results of the MCS method are very close to each other, which verifies the accuracy of the proposed method and determines the maximum renewable energy carrying capacity of this system to be 1054.87 MW. Additionally, the Gibbs sampling method, with a sampling scale of 2000, also produces consistent results. Notably, the M-H algorithm not only achieves high accuracy but also requires the least execution time among the methods compared, demonstrating its efficiency and effectiveness.

When the renewable energy field station output in the system is 1054.87 MW, its R_{SCR} can be calculated according to Equation (20) as follows:

$$R_{SCR} = \left|\dot{U}^{*}\dot{U}_{N}/\dot{Z}_{eq}\right| / \left|\dot{S}_{RE}\right| = 2.79 \tag{23}$$

This result not only satisfies the condition of $R_{SCR} > 2.5$ proposed in the literature [16], indicating that the system still maintains high voltage stability and safety margin under a larger proportion of renewable energy access, but also further confirms the validity and reliability of the proposed evaluation method.

In order to assess the security and robustness of the power system under maximum renewable energy access conditions, an N-1 fault validation is necessary. This process simulates the power system's ability to respond and adjust in the event of failure of any single component (e.g., substation, transmission line, etc.) to ensure that the stability of the power system is not affected by a single point of failure. Under the maximum renewable energy access capacity, this paper simulates an N-1 fault on lines 4–14 in the IEEE 39-bus system, whose fault type is a three-phase ground fault with a fault onset time of 2 s. After the fault, the changes in each generator parameter are shown in Figures 9–11.

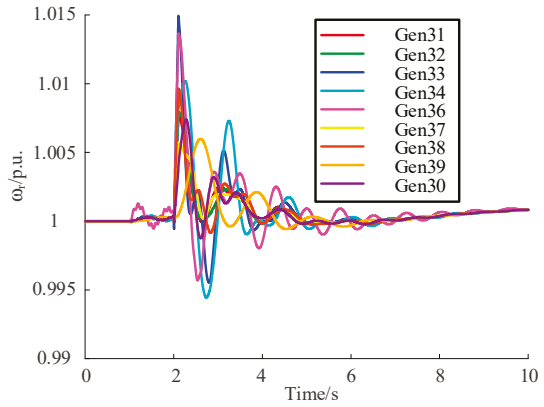


Figure 9. Variation of generator speeds.

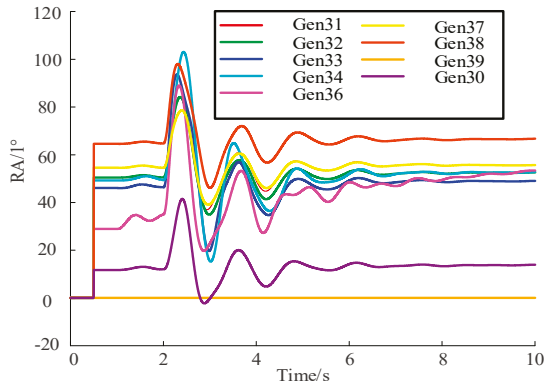


Figure 10. Variation of power angles.

After the N-1 fault simulation of the modified IEEE 39-bus system, the analysis of the three parameter variation plots shows that the response of each generator in the system exhibits significant transient fluctuations after the occurrence of a three-phase ground fault. Firstly, Figure 9 demonstrates that the rotational speed undergoes a brief overshoot and then stabilizes after the fault, which reflects that the generators have sufficient inertia and regulation to resist the transient perturbations. Figure 10 shows that the generators' power angle differences increase significantly during the initial phase of the fault, posing a brief challenge to system stability, but gradually return to a more stable state after the fault is cleared. Figure 11 shows that the voltages of all generators show a sharp drop, followed

by a gradual recovery of the voltage to a level close to the pre-fault level. It shows that the system has the ability to cope with N-1 faults and maintain stable operation under the calculated maximum carrying capacity of the renewable energy source.

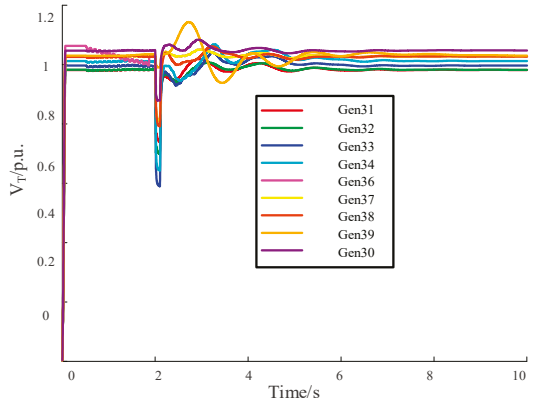


Figure 11. Variations in generator terminal voltage.

Figure 12 represents a power system that integrates renewable energy and conventional power sources, transmitting electricity externally through DC transmission. The system consists of 102 nodes, with the 500 kV main grid comprising 42 nodes. It includes three DC transmission lines: LCC1, LCC2, and LCC3, each with a transmission capacity of 800 MW. Through these three DC transmission channels, the system stably transmits a total of 2400 MW of electricity. To further validate the effectiveness of the proposed methodology, the M-H algorithm was applied to the system to assess its capacity for integrating renewable energy. The method's accuracy was subsequently verified using both MCS and Gibbs sampling as benchmarks. In this simulation, the active and reactive power of the loads on bus 1B-1 were modeled using a GMM derived from actual load data measurements. Similarly, the output of the wind power plant WTGA-5 was also modeled using a GMM, as shown in Figure 5. To analyze the impact of stochastic variations in load and wind power on the system's ability to accommodate renewable energy, Gen1B-1 was designated as a renewable energy access point with a power factor of 0.94. The renewable energy capacity was incrementally increased by 2 MW in each calculation iteration.

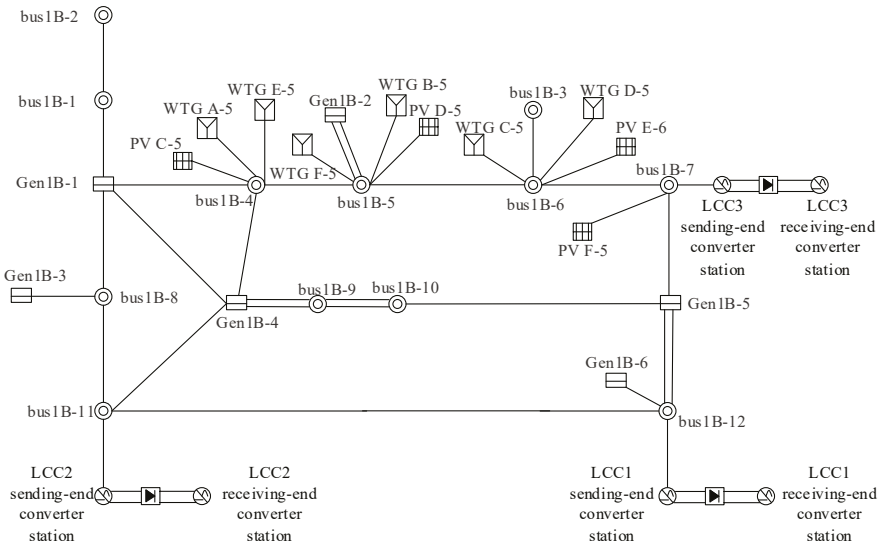


Figure 12. The AC–DC hybrid system.

To more intuitively understand the system's performance under different conditions, we performed kernel density estimation on the results of the three algorithms and plotted the probability density distribution curves and cumulative distribution curves. As shown in Figures 13 and 14, the probability density curves of the M-H algorithm, Gibbs sampling, and the MCS method basically overlap, indicating that the M-H algorithm can achieve accuracy comparable to both the MCS method and Gibbs sampling.

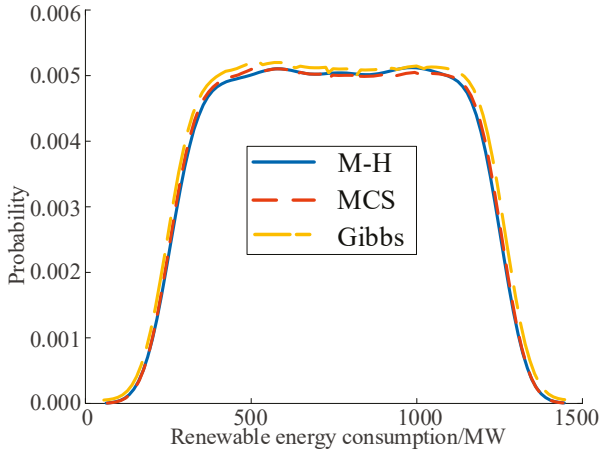


Figure 13. Probability density distribution curve of renewable power consumptive amount.

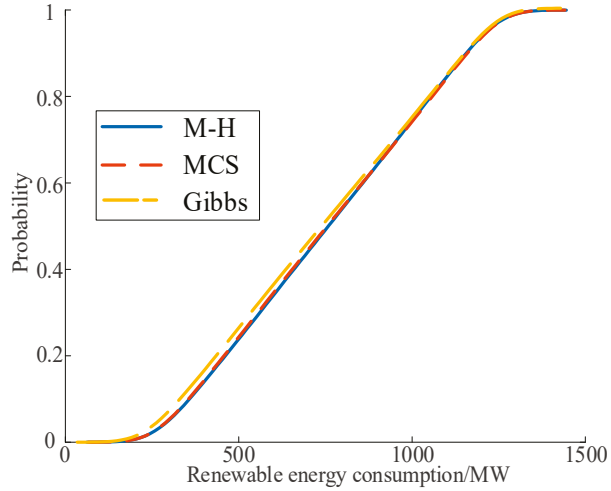


Figure 14. Cumulative distribution curve of renewable power consumptive amount.

As seen in Table 4, all three methods yield very similar statistical indicators, further validating the effectiveness of the M-H algorithm. Notably, Table 4 also shows that the M-H algorithm has the shortest execution time, making it more efficient than both the MCS method and Gibbs sampling.

Table 4. Statistical indicators of three assessment methods.

Algorithm	Number of Samples	Execution Time/ms	Mean/MW	Standard Deviation/MW	Maximum/MW	Min/MW
MCS	10,000	0.379	756.58	289.31	1253.11	254.43
M-H	2000	0.182	757.88	286.69	1250.91	256.38
Gibbs	2000	0.237	758.39	291.67	1259.28	259.15

When the renewable energy field station output in the system is 1250.91 MW, its R_{SCR} can be calculated according to Equation (20) as follows:

$$R_{SCR} = \left|\dot{U}^{*}\dot{U}_{N}/\dot{Z}_{eq}\right| / \left|\dot{S}_{RE}\right| = 2.74 \quad (24)$$

This result also satisfies the condition of RSCR > 2.5 proposed in the literature [16].

Similarly, under the maximum renewable energy access capacity, this paper simulates an N-1 fault on bus 1B-8 in the AC–DC hybrid system shown in Figure 12. The fault type is a three-phase ground fault with a fault onset time of 2 s. After the fault, the changes in bus voltages, generator active power, and generator speed are shown in Figures 15–17. After the N-1 fault simulation of the AC–DC hybrid system, Figure 15 shows that the bus voltage fluctuates transiently when the fault occurs, which is manifested as an instantaneous drop, and then gradually recovers and tends to stabilize, and recovers to a level close to the pre-fault level, which indicates that the system has a good voltage recovery capability and steady-state performance; Figure 16 shows that the active power of each generator fluctuates to varying degrees at the time of the fault occurrence, especially that some of the generators (e.g., Gen1B-4 and Gen1B-6) showed a significant drop in active power and then a rapid recovery, after the fault is cleared, the active power of the generators gradually recovers and tends to a new steady state, which indicates that the system is able to re-distribute the power load after the fault and gradually return to a steady state; Figure 17 shows that the generator speed remains basically unchanged before and after the fault, showing a horizontal straight line, which indicates that the generator speed is not significantly affected in the simulation of the N-1 fault, indicating that the system has strong inertia and regulation ability, and is able to effectively resist the transient shocks caused by the fault, and maintain the stable operation of the generator. In summary, the simulation results show that the AC–DC hybrid system exhibits good voltage recovery capability, power load redistribution capability, and generator stability under N-1 fault, which verifies the safety and robustness of the system under the maximum renewable energy access capacity.

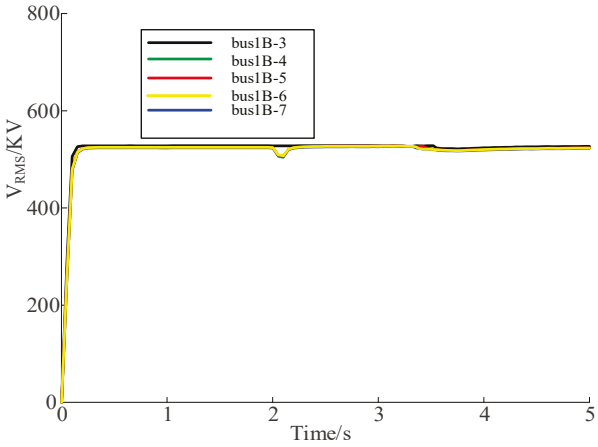


Figure 15. Bus voltage variations for each bus.

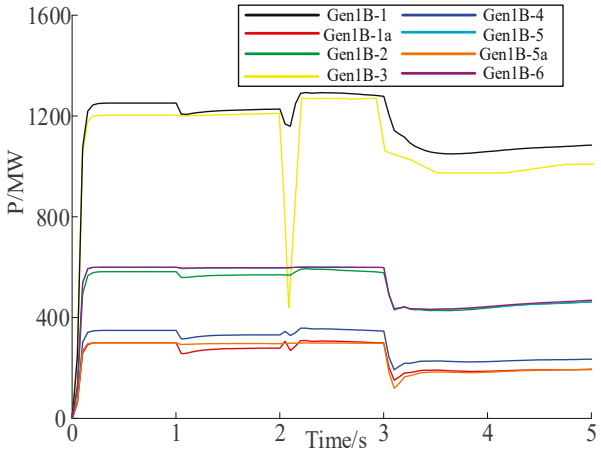


Figure 16. Active power variations for each generator.

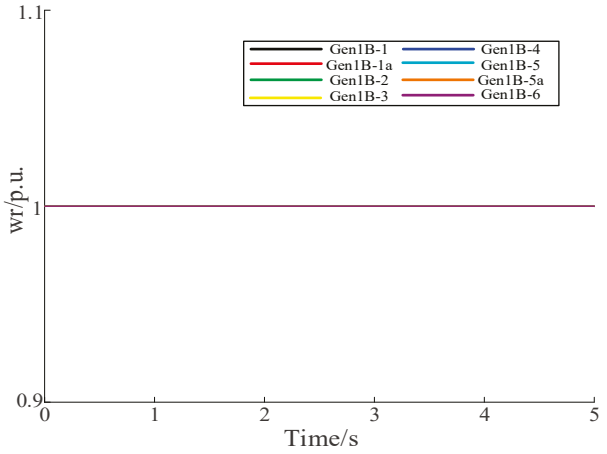


Figure 17. Speed variations for each generator.

6. Conclusions

This paper proposes a probabilistic assessment method for evaluating the renewable energy integration capacity, considering the uncertainty of renewables and the symmetry of active power. The proposed method achieves high simulation accuracy for the uncertainties of node injection powers, such as load and wind power. Compared to existing renewable energy integration assessment methods, the proposed method has the following characteristics:

1. Through the simulation of the random characteristics of load and wind power and the calculation of probabilistic load flow, the proposed method can comprehensively and accurately reflect the changes in renewable energy integration capacity influenced by the operating state of the power system and its uncertainties.
2. A 10-order GMM is used to construct the probabilistic model for load. The research results show that the RMSE and SSE of the 10-order Gaussian distribution load fitting model are 0.000159 and 0.000048, respectively, with a R^2 reaching 0.995. Compared to other fitting models, this approach provides more accurate load modeling. Similarly, the 10-order Gaussian distribution wind power fitting model has an RMSE and SSE of 0.000163 and 0.000052, respectively, with an R^2 reaching 0.994. Compared to the Weibull distribution, this model offers more precise wind power modeling.
3. During the simulation calculations on both the 102 nodes system and IEEE 39-bus system with renewable energy integration, the maximum renewable energy integration capacities were determined to be 1250.91 MW and 1054.87 MW, respectively. The results of different simulation case studies also show that the probability metrics

obtained by the M-H algorithm, Gibbs sampling, and the MCS method are basically the same, verifying the accuracy of the proposed method.

4. Under the maximum renewable energy integration capacity in different scenarios, it was found through short-circuit ratio and N-1 fault validation that the system can consistently meet stability requirements.

While the proposed method offers a comprehensive and accurate assessment of renewable energy integration capacity, it is not without limitations. One limitation is the computational intensity associated with high-order Gaussian mixture models, which may lead to increased processing times in larger systems or more complex scenarios. Additionally, the method's reliance on accurate probabilistic models means that its effectiveness is contingent upon the quality of the input data, which can be challenging in cases of sparse or highly variable data. To address these limitations, future research could explore the development of more efficient computational techniques or hybrid models that balance accuracy with computational demand. Additionally, extending the methodology to incorporate other types of uncertainties, such as those related to grid infrastructure or market conditions, could further enhance its applicability. Researchers might also consider the integration of machine learning techniques to improve the accuracy of input data modeling and reduce dependency on large datasets.

In conclusion, the proposed probabilistic assessment method represents a significant step forward in renewable energy integration analysis, offering a robust framework for future studies while highlighting areas for continued improvement.

Author Contributions: Conceptualization, K.O. and S.G.; investigation, B.Z. and W.Z.; methodology, K.O. and B.Z.; software, W.Z. and Y.W.; data curation, K.O. and S.G.; validation, K.O. and W.Z.; formal analysis, B.Z. and Y.W.; resources, S.G. and Y.W.; writing—original draft preparation, K.O. and S.G.; writing—review and editing, W.Z. and K.O.; visualization, Y.W. and W.Z.; supervision, Y.W. and S.G.; project administration, Y.W. and S.G.; funding acquisition, B.Z. and S.G. All authors have read and agreed to the published version of the manuscript.

Funding: This research was supported by the Guangdong Provincial Key Laboratory of Intelligent Operation and Control for New Energy Power System (GPKLIOCNEPS-2023-KF-01).

Data Availability Statement: Data are contained within the article.

Conflicts of Interest: The authors declare no conflicts of interest.

References

1. Liu, X.; Wang, L.; Cao, Y.; Ma, R.; Wang, Y.; Li, C.; Liu, R.; Zou, S. Renewable Scenario Generation Based on the Hybrid Genetic Algorithm with Variable Chromosome Length. *Energies* **2023**, *16*, 3180. [CrossRef]
2. Hui, J.; Tai, K.; Yan, R.; Wang, Y.; Yuan, M.; Zheng, Z.; Gao, S.; Liao, J. Frequency Coordination Control Strategy for Large-Scale Wind Power Transmission Systems Based on Hybrid DC Transmission Technology with Deep Q Network Assistance. *Appl. Sci.* **2024**, *14*, 6817. [CrossRef]
3. Liu, X.; Zou, P.; You, J.; Wang, Y.; Wu, J.; Zheng, Z.; Gao, S.; Hao, W. Advanced Primary Frequency Regulation Optimization in Wind Storage Systems with DC Integration Using Double Deep Q-Networks. *Electronics* **2024**, *13*, 2249. [CrossRef]
4. Cavus, M.; Allahham, A.; Adhikari, K.; Giaouris, D. A Hybrid Method Based on Logic Predictive Controller for Flexible Hybrid Microgrid with Plug-and-Play Capabilities. *Appl. Energy* **2024**, *359*, 122752. [CrossRef]
5. Akbulut, O.; Cavus, M.; Cengiz, M.; Allahham, A.; Giaouris, D.; Forshaw, M. Hybrid Intelligent Control System for Adaptive Microgrid Optimization: Integration of Rule-Based Control and Deep Learning Techniques. *Energies* **2024**, *17*, 2260. [CrossRef]
6. Zhang, J.; Wang, J.; Cao, Y.; Li, B.; Li, C. A Coordinated Control Strategy of Multi-Type Flexible Resources and Under-Frequency Load Shedding for Active Power Balance. *Symmetry* **2024**, *16*, 479. [CrossRef]
7. Yin, R.; Kara, E.C.; Li, Y.; DeForest, N.; Wang, K.; Yong, T.; Stadler, M. Quantifying flexibility of commercial and residential loads for demand response using setpoint changes. *Appl. Energy* **2016**, *177*, 149–164. [CrossRef]
8. Wang, G.; Yang, Y.; Hu, T.; Yu, W.; Han, X. Analysis of key influencing factors for multi-mode Solar Heat Pump Systems. *J. Renew. Sustain. Energy* **2022**, *14*, 053703. [CrossRef]
9. Unsal, D.B.; Aksoz, A.; Oyucu, S.; Guerrero, J.M.; Guler, M. A Comparative Study of AI Methods on Renewable Energy Prediction for Smart Grids: Case of Turkey. *Sustainability* **2024**, *16*, 2894. [CrossRef]

10. Hu, X.; Min, H.; Dai, S.; Cai, Z.; Yang, X.; Ding, Q.; Yang, Z.; Xiao, F. Research on Maintenance Strategies for Different Transmission Sections to Improve the Consumption Rate Based on a Renewable Energy Production Simulation. *Energies* **2022**, *15*, 9262. [CrossRef]
11. Bordonaro, A.; Gaglio, S.; Lo Re, G.; Martorella, G.; Peri, D. On-board energy consumption assessment for symbolic execution models on embedded devices. In Proceedings of the 2020 25th IEEE International Conference on Emerging Technologies and Factory Automation (ETFA), Vienna, Austria, 8–11 September 2020.
12. Lou, B.; Liang, Y.; Gao, X. Energy Consumption Assessment and energy-saving management in tourist resorts. *Int. J. Heat Technol.* **2021**, *39*, 195–204. [CrossRef]
13. Cerjan, M.; Petričić, A.; Delimar, M. HIRA Model for Short-Term Electricity Price Forecasting. *Energies* **2019**, *12*, 568. [CrossRef]
14. Deng, X.; Li, Y.; Liu, H.; Zhao, Y.; Yang, Y.; Xu, X.; Cheng, X.; de Wit, B. Examining Energy Consumption and Carbon Emissions of Microbial Induced Carbonate Precipitation Using the Life Cycle Assessment Method. *Sustainability* **2021**, *13*, 4856. [CrossRef]
15. Shu, Z.; Jirutitijaroen, P.; da Silva, A.M.L.; Singh, C. Accelerated State Evaluation and Latin hypercube sequential sampling for composite system reliability assessment. *IEEE Trans. Power Syst.* **2014**, *29*, 1692–1700. [CrossRef]
16. García-Miguel, P.L.C.; Zarilli, D.; Alonso-Martinez, J.; Plaza, M.G.; Gómez, S.A. Optimal Operation and Market Integration of a Hybrid Farm with Green Hydrogen and Energy Storage: A Stochastic Approach Considering Wind and Electricity Price Uncertainties. *Sustainability* **2024**, *16*, 2856. [CrossRef]
17. Zhang, J.; Wang, B.; Ma, H.; Li, Y.; Yang, M.; Wang, H.; Ma, F. A Fast Reliability Evaluation Strategy for Power Systems under High Proportional Renewable Energy—A Hybrid Data-Driven Method. *Processes* **2024**, *12*, 608. [CrossRef]
18. Hastings, W.K. Monte Carlo sampling methods using Markov chains and their applications. *Biometrika* **1970**, *57*, 97–109. [CrossRef]
19. Borkar, V.S. Equation of state calculations by Fast Computing Machines. *Resonance* **2022**, *27*, 1263–1269. [CrossRef]
20. Sun, H.; Xu, S.; Xu, T.; Guo, Q.; He, J.; Zhao, B.; Yu, L.; Zhang, Y.; Li, W.; Zhou, Y.; et al. Definition and index of short-circuit ratio of new energy multi-field station. *Proc. CSEE* **2021**, *41*, 497–506.
21. Dang, D.; Liu, Y.; Lee, S.-K. State Evaluation of Electrical Equipment in Substations Based on Data Mining. *Appl. Sci.* **2024**, *14*, 7348. [CrossRef]

Disclaimer/Publisher's Note: The statements, opinions and data contained in all publications are solely those of the individual author(s) and contributor(s) and not of MDPI and/or the editor(s). MDPI and/or the editor(s) disclaim responsibility for any injury to people or property resulting from any ideas, methods, instructions or products referred to in the content.

MDPI AG
Grosspeteranlage 5
4052 Basel
Switzerland
Tel.: +41 61 683 77 34

Symmetry Editorial Office
E-mail: symmetry@mdpi.com
www.mdpi.com/journal/symmetry



Disclaimer/Publisher's Note: The title and front matter of this reprint are at the discretion of the Guest Editors. The publisher is not responsible for their content or any associated concerns. The statements, opinions and data contained in all individual articles are solely those of the individual Editors and contributors and not of MDPI. MDPI disclaims responsibility for any injury to people or property resulting from any ideas, methods, instructions or products referred to in the content.

MDPI

Academic Open
Access Publishing

mdpi.com

ISBN 978-3-7258-8722-4